Properties and evolution of cratonic lithosphere

by

Timothy McIntyre

A thesis submitted in partial fulfillment of the requirements for the degree of

Doctor of Philosophy

Department of Earth and Atmospheric Sciences
University of Alberta

Abstract

Resolving important fundamental questions about the petrogenesis of cratonic lithosphere is difficult in ancient cratons that have long and complex histories. Several properties of cratons are poorly constrained and our understanding of their petrogenesis largely remains ambiguous. In the Archean Earth, the diversity of tectonic environments that gave rise to the building blocks of cratonic lithosphere and the timing of its amalgamation into coherent cratons is uncertain due to our limited understanding of the tectonic regimes that operated during this Eon. Equally unclear is the petrogenetic melting environment that gave rise to the highly refractory composition of cratonic lithospheric mantle. Finally, our understanding of the thermal evolution and thickness of cratons is limited by poor constraints on the abundances of heat producing elements in cratonic mantle throughout its depth. In this thesis, three studies are presented that focus on contributing insight into the timing of the onset of plate tectonics and the petrogenetic environments that gave rise to the earliest cratonic crust, the petrogenetic melting environment of lithospheric mantle that underpins the Proterozoic portion of the North Atlantic Craton, and lastly, an improved estimate of the heat producing element abundances in the various lithologies that comprise cratonic lithosphere.

In the first study, Chapter 2, the geochronology and petrogenesis of Archean crustal components of the Nagssugtoqidian orogen (NO), West Greenland were evaluated. The Qorlortoq gneiss, a component of this heterogeneous crust, was found to have much older ages than the surrounding gneiss. This allowed for new insights into the evolution of the Archean lithosphere comprising the NO. Measurements of U-Pb and Lu-Hf in zircon from the Qorlortoq gneiss yielded an age of 3177 ± 12 Ma with a weighted mean εHf of 1.7 ± 0.5. The hiatus in crustal production between this and the younger Archean components of the NO (<2.87 Ga) imply a local tectonic regime dominated

by stagnant lid or only episodic subduction. The crust in the NO provides a complimentary Archean history to regional studies, allowing for a better understanding of the timing and processes that led to the formation of the North Atlantic Craton in the Archean.

The second study, Chapter 3, focuses on the contributions of hydrous vs anhydrous melting regimes to generating the refractory compositions of cratonic lithospheric mantle in the Paleoproterozoic. This was done through a detailed geochronological and geochemical evaluation of a Paleoproterozoic orogenic peridotite – the Ussuit peridotite, West Greenland. The Ussuit peridotite was found to have formed in a sub-arc environment and provides potential geochemical proxies for comparison with mantle xenoliths. Re-Os isotope geochronology of the Ussuit peridotites dates the melting event responsible for their highly depleted compositions to ~2 Ga, which overlaps the Paleoproterozoic production of local and global oceanic arc-lithosphere incorporated into cratons in the Paleoproterozoic. Combined with geochemical similarities with Paleoproterozoic cratonic mantle xenoliths, this suggests the Ussuit peridotite could have equivalents in the cratonic lithosphere of other regions and that highly depleted sub-arc lithospheric mantle may constitute a fundamental component of the Proterozoic keels beneath cratons.

Heat production is a fundamental, but poorly constrained, property of the lithospheric mantle that is required to model the thermal structure of the cratonic lithosphere. In the final study, Chapter 4, heat producing element (K, Th, and U) concentrations in cratonic mantle roots were measured in the spectrum of minerals that make up cratonic peridotites. These new data were produced via laser ablation ICP-MS and together with a literature compilation of robust data were used to place better constraints on heat production in the cratonic lithospheric mantle. The resulting magnitude of heat generation in depleted peridotitic lithosphere was found to be between 0.00004 and 0.006

$\mu W/m^3$. This new estimate is significantly lower than previous published estimates, that are in common use and can range up to 0.084 $\mu W/m^3$, 1 to 3 orders of magnitude higher than the new estimate. Depending on model assumptions, using this new value for mantle heat production produces modelled estimated thicknesses of cratonic lithosphere as much as 10 to 80 km thinner than estimates that rely on some previous measurements of heat producing elements.

Preface

This thesis comprises three research articles produced from the PhD research of Timothy McIntyre that was done under the supervision of Dr. D. Graham Pearson. The research was funded through the Canada Research Excellence Chair and the Collaborative Research and Training Experience Program grants held by Dr. D. Graham Pearson together with a National Research Council of Canada Post Graduate Doctoral Scholarship held by Timothy McIntyre.

Chapter 2 of this thesis has been published as "McIntyre, T., Waterton, P., Vezinet, A., Szilas, K., & Pearson, D. G. (2021). Extent and age of Mesoarchean components in the Nagssugtoqidian orogen, West Greenland: Implications for tectonic environments and crust building in cratonic orogenic belts. Lithos, 396–397, 106182." Sample collection was done by T. McIntyre and P. Waterton. Data collection and processing were done by T. McIntyre and A. Vezinet. Initial writing of the manuscript was done by T. McIntyre. Co-authors, P. Waterton, A. Vezinet, K. Szilas, and D.G. Pearson added valuable contributions to the discussion that further improved the implications of the work. D.G. Pearson was the principal investigator and involved conceptualization of the project and revision of the manuscript.

Chapter 3 of this work will be published as "McIntyre, T., Waterton, P., Li, L., Gong, B., Zha, X., Szilas, K., & Pearson D. G. (20XX). Juvenile lithospheric mantle formed beneath oceanic arcs underpins mobile belts cratonized during Paleoproterozoic supercontinent assembly." Samples were collected by T. McIntyre and P. Waterton. Data collection was done by T. McIntyre, L. Li, B. Gong, and X. Zha. D.G. Pearson is the principal investigator and was involved in the conceptualization of the project and added valuable contributions to revisions of the manuscript.

Chapter 4 of this thesis has been published as "McIntyre, T., Kublik, K., Currie, C., & Pearson, D. G. (2021). Heat generation in cratonic mantle roots—New trace element constraints from mantle

xenoliths and implications for cratonic geotherms. *Geochemistry, Geophysics, Geosystems*, *22*, e2021GC009691." Data collection and the initial writing of the manuscript were done by T. McIntyre. K. Kublik and C. Currie aided the development of geothermal models and provided valuable contributions to the discussion. D.G. Pearson was the principal investigator of the work, provided the samples, added valuable insight and contributions to the manuscript, and involved in the conceptualization of the project.

Acknowledgements

I would like to give a big thank you to my supervisor, Graham Pearson, for guidance in the writing of these manuscripts and support through the years I have worked with him. I would also like to thank him for putting in long hours editing the various manuscripts in this thesis, especially in final months of writing. Thank you to the amazing laboratory support staff that have helped me in the lab; Sarah Woodland, Yan Luo, Chiranjeeb Sarkar, Mark Labbe, and Andrew Locock. I would also like to thank Pedro Waterton for his support in the lab but more importantly for spending three weeks camped in the field in West Greenland during the start of winter when it was well below 0 ℃ and snowing.

Table of Contents

List of Tables

List of Figures

Appendix D

Chapter 1
An introduction to cratons and their petrogenetic complexities

1.1 Introduction

Cratons are recognized as the thick (>150 km) portions of lithosphere that have been stable for approximately a billion years or more (Pearson et al., 2021). In the pursuit of knowledge, understanding how cratons formed and our planet evolved through time is a superlative goal that furthers our understanding of the natural universe. Moreover, the deep refractory lithospheric keels of cratons are instrumental in the stabilization of continents (Jordan, 1978; Pearson et al., 2021) and development of important mineral deposits (e.g. Boyd & Gurney, 1986; Hoggard et al., 2020). Without the emergence and stabilization of continents that harbored the earliest organism (e.g. Allwood et al., 2006; Eickmann et al., 2018) and comprise the land masses we inhabit, Earth may not have nurtured the diversity of life we see today.

In the context of economic resources, the diamondiferous deep cratonic lithosphere incorporated into and brought to the surface by kimberlites provides the world's natural diamond supply (Boyd & Gurney, 1986). Cratons are additionally fundamental to the development of base metal deposits (Hoggard et al., 2020). Their rigid impenetrable keels deflect upwelling asthenosphere causing the focusing of magma into thinner lithosphere at cratonic boundaries (Sleep et al., 2002). These cratonic boundaries are the loci of thick sedimentary deposits which are important sources of sulfur and volatile components necessary for upgrading the metal tenures of circum-cratonic magmas (Hoggard et al., 2020). As such, understanding the processes that led to the formation and stabilization of thick refractory cratonic lithosphere is fundamental to our understanding of the natural world and the discovery and development its natural resources.

Cratons are complex amalgamations of lithospheric blocks formed in different tectonic environments whose mantle lithosphere has been subject to billions of years of metasomatism (Fig. 1-1; Pearson et al., 2021). Moreover, Earths' geodynamic environments have changed through time. For example, the timing of the development of a global network of mobile tectonic plates is unclear, but likely transitioned to such a global geodynamic regime from one largely dominated by stagnant lid tectonics sometime in the Archean (**Chapter 2**; Palin et al., 2020; Bauer et al., 2020). The formation of a global network of plates with subductions zones is critical for the amalgamation of continental lithospheric segments and their stabilization through thickening by lateral accretion (Wang et al., 2018; Pearson et al., 2021). These lithospheric segments, pre-cratonization, are referred to here as "proto-cratonic lithosphere". That the timing of the onset of global plate tectonics is unresolved, blurs our understanding of when cratons stabilized and which petrogenetic environments formed the various lithospheric components of the earliest cratonic lithosphere.

Similar to geodynamic and crustal complexities, secular cooling of earth has convoluted our understanding of the petrogenetic environment in which the refractory compositions of cratonic lithospheric mantle (CLM) formed. In the Phanerozoic, low mantle potential temperatures characterizing convective upper mantle (~1315 ºC; Walter, 2014) are only able to produce melt residues similar to those of the CLM in forearc and sub-arc environments where hydrous fluids facilitate greater degrees of mantle melting (cf. Baker & Stopler, 1994; Hirose & Kawamoto, 1995; Falloon et al., 1999; Pickering-Witter & Johnston, 1999; Kubo, 2002; Condamine & Médard, 2014; Mitchell & Grove, 2015; Wang et al., 2016). In the Paleoproterozoic and earlier Earth, mantle potential temperatures were much higher, possibly approaching 1550 ºC under mid-ocean ridges and up to ~1700 ºC in plume environments (Herzberg et al., 2010; Walter, 2014). At these

mantle potential temperatures, residues from anhydrous polybaric melting may reach the refractory compositions that in the Phanerozoic are only be found in subduction zone settings (e.g. Bernstein et al., 1998; Herzberg & Rudnick, 2012; Lee & Chin, 2014; Pearson & Wittig, 2014). To a large extent, the uncertainty in the petrogenesis of CLM is due to our uncertainty in the roles of hydrous vs anhydrous melting in generating the refractory compositions of this domain (**Chapter 3**).

Thermal erosion and metasomatism have also restricted our understanding of the petrogenesis of CLM and hence that of cratonic lithosphere as a whole. Cratons have been subject to incipient rifting or fragmented and reconstituted via lateral accretion (e.g. van Gool et al., 2002; Wardle, et al., 2002a,b; St-Onge et al., 2009). Through transformative metasomatic processes, some cratons have had their deep lithospheric keels removed or been extensively metasomatized (e.g. Pearson et al., 2003; Menzies et al., 2007; Griffin et al., 2009; Wang et al., 2015; Artemieva, 2019; Liu et al., 2021). Moreover, it is unclear if the samples we have available to us, largely xenoliths sampled from lithosphere penetrated by melts, are representative of the broader lithospheric mantle or are the metasomatized wall rocks of lithospheric melt conduits (e.g. **Chapter 4**; O'Reilly & Griffin, 2013; Pearson & Wittig, 2014). These issues contribute to the overall uncertainties in our understanding of the formation and evolution of cratons.

Finally, uncertainty exists in some properties used in constraining the geothermal gradients withing cratons. For example, values for heat generation in cratonic mantle roots varies greatly between different studies (e.g. **Chapter 4**; Rudnick et al., 1998; Michaut & Jaupart, 2004; Michaut et al., 2007; Hieronymus & Goes, 2010; Hasterok & Chapman, 2011; Jaupart & Mareschal, 2015; Goes et al., 2020). This has led to a poor understanding of the thermal structure of cratons important for understanding their thickness and evolution through time (Jaupart & Mareschal, 2015).

Further studies are warranted regarding the onset of plate tectonics, the tectonic environments involved in the production of the earliest crust, the involvement of hydrous vs anhydrous melting regimes in developing the most refractory compositions of cratons, and the heat production within cratonic mantle roots today that can be used in modelling to understand their current and past thermal state. This thesis is a contribution towards these goals.

1.2 Geochronological approaches to understanding craton petrogenesis

Understanding the geodynamic diversity of environments that gave rise to the crust of cratons, through isotopic and geochronological studies, has been instrumental in understanding the processes of craton formation. For instance, crustal studies of the Laurentian (Hoffman, 1988), Siberian (Rosen, 2002), and Kaapvaal (Reid, 1997; Robb et al., 1999) cratons show significant production of juvenile continental crust in the Paleoproterozoic, i.e., crust with isotopic characteristics showing derivation from melting of asthenospheric mantle with limited or no crustal recycling of older lithosphere. Ultimately these juvenile crustal sections were amalgamated into supercratons (Ionov, et al., 2015a,b; Pearson et al., 2021). Studies of the crust in these regions were instrumental in understanding the timing of melt depletion recorded in mantle xenoliths from these cratons (Janney et al., 2010; Ionov, et al., 2015a,b; Liu et al., 2018; Pearson et al., 2021). Together these data show the cratonization of Paleoproterozoic mobile belts (Janney et al., 2010; Ionov, et al., 2015a,b; Liu et al., 2018; Pearson et al., 2021) into thick, strong continental lithosphere - cratons.

Applying a similar approach to the Archean is more challenging due to the common occurrence of crust-mantle decoupling in the cores of cratonic lithosphere (Pearson et al., 2021). However, such approaches will be important in developing our understanding of cratonic evolution. New methods, such as split-stream laser ablation multi-collector ICPMS for measurements of U-Pb and other

tracer isotopes (Lu-Hf and Sm-Nd) in pertinent crustal phases, have led to a greater understanding of the processes involved in the formation of proto-cratonic components and their eventual amalgamation into cratonic lithosphere. For example, in the North Atlantic Craton (NAC), combined U-Pb and Lu-Hf isotopic systematics of zircon from across crustal terranes shows local tectonic quiescence until at least 3.2 Ga (Næraa et al., 2012) possibly implying the onset of plate tectonics, and hence a mechanism for lateral accretion and thickening of cratonic lithosphere, that was much later than implied from some other studies (cf. Palin et al., 2020; Reimink et al., 2021). Similarly, split-stream U-Pb and Lu-Hf isotopic systematics of zircon from kimberlites, in combination with studies of paleogeothermal gradients, suggest that large components of the NAC formed via stagnant lid tectonics as late as 3.0 Ga (Gardiner et al., 2019; Yakymchuk et al., 2020). These approaches allow for a better understanding of the processes leading to the formation of proto-cratonic lithosphere and the timing of its eventual amalgamation into a craton.

In the context of crustal studies, **Chapter 2** focuses on the Archean components of the Nagssugtoqidian orogen that in part form a portion of the North Atlantic craton that has a very different geochronological history from its core. The compositional diversity of crustal components across these regions highlights changing geodynamic environments and supports other studies that infer the formation of the NAC in the late Mesoarchean/Neoarchean by lateral accretion (Friend & Nutman, 2005; Wittig et al., 2010).

Arguably, the most useful geochronological tool in understanding the timing of cratonic stabilization has been the Re-Os isotopic system. Os is compatible during mantle melting whereas Re is not (Walker et al., 1989; Pearson et al., 2021). This causes the "freezing" of Os isotopic compositions in the restites of mantle melting. Studies of Re-Os isotopic systematics in mantle xenoliths shows distinct peaks in the formation of CLM through time (Fig. 1-2; Pearson et al.,

2021) providing important insight into the longevity of cratonic mantle lithosphere. Comparing Re-Os model ages (T_{RD} and T_{MA}; Walker et al., 1989) to crustal sections of cratons has been instrumental in understanding their petrogenesis, particularly for Proterozoic CLM, as noted above (e.g. Janney et al., 2010; Ionov, et al., 2015a,b; Liu et al., 2018).

Chapter 3 seeks to build on our understanding of the petrogenesis of Paleoproterozoic CLM through a geochemical and geochronological study of a Paleoproterozoic mantle tectonite. Mantle tectonites provide complimentary information to mantle xenoliths due to their different histories post melting, i.e., mantle xenoliths reside in the mantle and are subject to secondary processes in that domain, including affects from their transporting host rock, whereas mantle tectonites reside in the crust and are subject to different secondary processes. **Chapter 3** shows that melting events in a Paleoproterozoic mantle tectonite overlap the age of juvenile crust from local and global mobile belts responsible for cratonization in the Paleoproterozoic. Combining the geochemical similarities between this mantle tectonite and Paleoproterozoic mantle xenoliths, the likely contributions of hydrous vs anhydrous melting in the formation of Paleoproterozoic CLM are evaluated.

1.3 Modelling the thermal structure of cratons to understand their petrogenesis

The current paradigm is that cratons were thickened via lateral compression to their current thickness of >150 km (Wang et al., 2018; Pearson et al., 2021). Thermochemical erosion of cratons through melt induced weakening (e.g. Wang et al., 2015; Celli et al., 2020) may remove the base of cratons (e.g. Menzies et al., 2007; Liu et al., 2021) or change their compositions internally (e.g. Griffin et al., 2009; Artemieva, 2019). Where not affected by such processes, deep refractory roots may be preserved, implying a highly refractory character for CLM that has not been affected by

metasomatism (Griffin et al., 2009; Artemieva, 2019). As such, the thermal structure of cratons has implications for initial state of cratons and their subsequent modification.

Our understanding of the thermal structure of the lithosphere comes from xenoliths thermobarometry, tomography, and steady-state geothermal modelling (Jaupart & Mareschal, 2015). Xenoliths are important direct samples of the lithosphere, but sampling by kimberlites may be subject to numerous biases (**Chapter 4**). As such, modelling, i.e., tomography and steady-state geotherms, is critical in our understanding of the thermal structure of cratons including their thickness (Jaupart & Mareschal, 2015). Yet models are only as good as the assumptions on which they are built. Many properties of cratons used in such models are based on uncertain assumptions due to limited access to samples from the deep lithosphere (Jaupart & Mareschal, 2015). Importantly, this has led to a poor understanding of the thickness of cratons and consequently their temperature at depth (Jaupart & Mareschal, 2015).

Heat generation in the lithospheric mantle portion of cratons, from the decay of K, U, and Th, is a poorly constrained parameter that can have significant impacts on modelled geotherms (Fig. 1-3). **Chapter 4** uses in situ measurements of K, U, and Th in cratonic mantle xenoliths to better constrain heat generation. This method has not been previously used for this purpose. The new database presented in **Chapter 4** is the most robust data thus far assembled for HPE in cratonic mantle peridotites. The data indicate that models based on earlier bulk-rock HPE data likely significantly overestimate heat generation in cratonic mantle roots. The new constraints allow for better modelling to understand lithospheric thickness and the potential impacts of metasomes on geotherms in the cratonic lithosphere.

Mid ocean ridge   Subduction   Plume subcretion

Time

Mantle potential temperature

Proto-cratonic lithosphere

LAB   LAB   LAB

Chapter 2: Petrogenesis of Archean continental crust

Latteral accretion

Juvenile cratonic lithosphere

Cratonic mantle components
Juvenile CLM:
Oceanic lithosphere
Sub-arc lithosphere
Plume residues

LAB

Modified and unmodified cratonic lithospehre

Proto- & old cratonic lithosphere

LAB   LAB   LAB

Chapter 3: Petrogenesis of Paleoproterozoic proto-CLM

Latteral accretion

Evolved cratonic lithosphere

Cratonic mantle components
Old-CLM
Prestine
Subduction modified
Plume modified
Aesthenospheric melt modified

Juvenile CLM:
Oceanic lithosphere
Sub-arc lithosphere
Plume residues

LAB

Chapter 4: Thermal properties of mature CLM

Fig. 1-1 Schematic illustration of the complexities of cratonic petrogenesis and the frame of reference of the chapters in this study. The earliest initial crust building events may have been in the early Archean or late Hadean, as such crust is extent today (e.g. Nutman et al., 1993; Nutman et at., 1996; Stern & Bleeker, 1998), though no reliable Re-Os model ages record extensive CLM of this age (Fig. 1-2; Pearson et al., 2021). In the Archean, tectonic amalgamation of Archean proto-cratonic blocks likely took place (Friend & Nutman, 2005; Wittig et al., 2010; Pearson & Wittig, 2014; Pearson et al., 2021). Punctuated later episodes were responsible for the addition of new lithosphere to cratons and the modification of old cratonic lithosphere (Fig. 1-2; Janney et al., 2010; Wittig et al., 2010; Ionov, 2015a,b; Liu et al., 2018, 2021; Pearson et al., 2021). Plume impingement, rifting, incipient rifting, transient asthenospheric and lithospheric melts, and sub-arc metasomatism all contributed to further producing the complexities of the heterogeneous cratonic lithosphere.
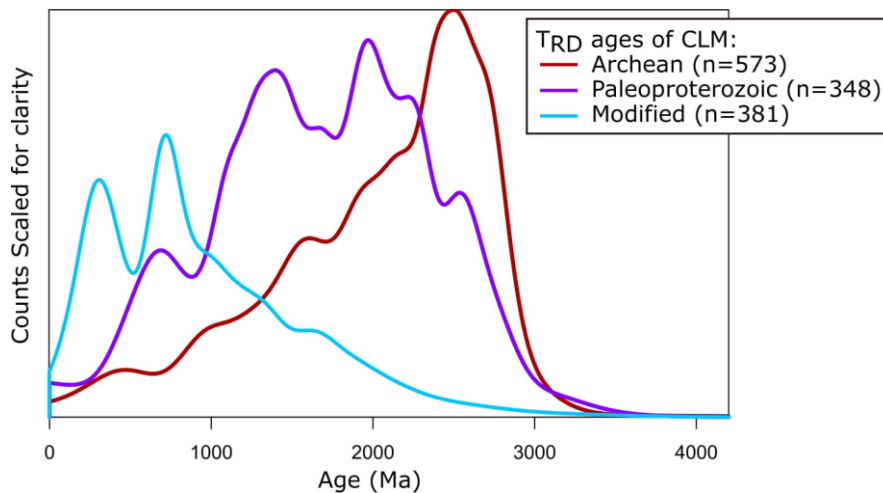
Fig. 1-2. T_{RD} model ages for cratonic mantle samples globally from Pearson et al. (2021). The ages show punctuated peaks in the production of CLM, a protracted formation of CLM to the late Proterozoic, and the modification of CLM with T_{RD} ages displaced to younger ages. Bandwidth is 100 Ma.
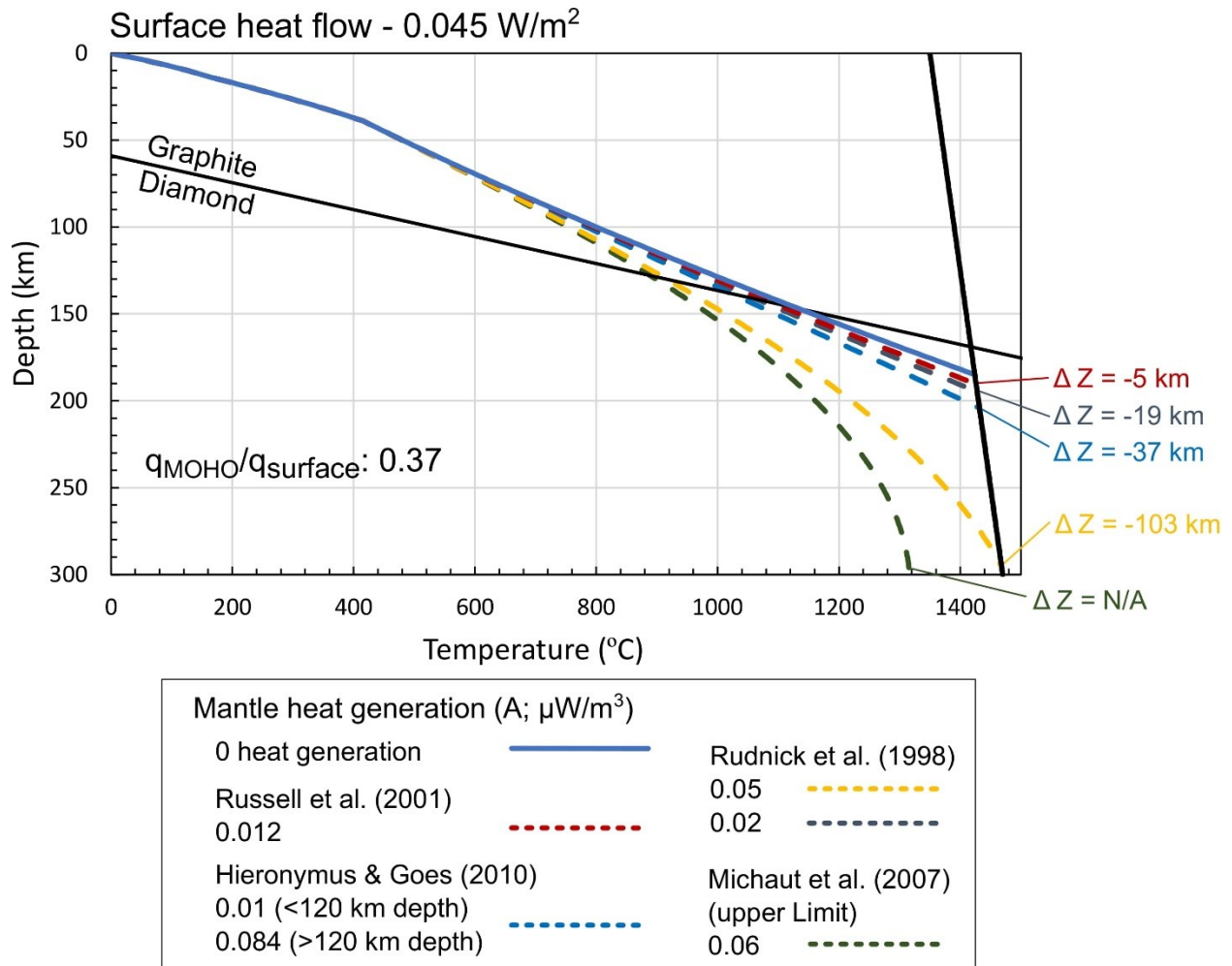
Fig. 1-3. Comparison of model geotherms using common CLM heat generating values discussed in Chapter 4. The model uses temperature and pressure dependent thermal conductivity (details given in Appendix A). $q_{moho}/q_{surface}$ refers to the ratio of heat flow (q) across the Moho and surface of the earth. ΔZ compares the depth geotherms intersect the mantle adiabat [$T_{adiabat}$ = 1350 ºC + 0.4*(depth in km)] between using a mantle heat generation of 0 µW/m³ and common literature estimates. Negative values indicate a greater depth to the lithosphere asthenosphere boundary for geotherms that use heat generation estimates from the literature compared with geotherms using no heat generation as an estimate

10

Chapter 2

Extent and age of Mesoarchean components in the Nagssugtoqidian orogen, West Greenland: implications for tectonic environments and crust building in cratonic orogenic belts

T. McIntyre[1], P. Waterton[1,2], A. Vezinet[1], K. Szilas[2], & D.G. Pearson[1]

[1]Department of Earth & Atmospheric Sciences, University of Alberta, Edmonton, Alberta, Canada

[2]Department of Geosciences and Natural Resource Management, University of Copenhagen, Copenhagen, Denmark

Abstract

The Nagssugtoqidian orogen (NO),which forms the northern margin of the North Atlantic craton in West Greenland, largely comprises ~2870 to 2720 Ma juvenile continental crust reworked during Paleoproterozoic orogenic events. Sparse evidence of components older than 3100 Ma in the area (U–Pb zircon ages and bulk-rock Sm–Nd isotopes) have hinted at a unit called the Qorlortoq gneiss but were not substantiated by regional studies. Here we report the "rediscovery" of the Qorlortoq gneiss, documented through a new geochemical and geochronological dataset of this orthogneiss and related components, which include ultramafic cumulate enclaves and late basaltic dykes. Laser Ablation Split Stream (LASS) U-Pb/Lu-Hf isotopic analyses of zircon from the gneiss give a U–Pb disconcordia upper-intercept age of 3177 ± 12 Ma and weighted mean εHf(t) of 1.7 ± 0.5, indicating a juvenile protolith extracted from a depleted mantle source.

Ultramafic enclaves of cumulate origin make up a key component of the Qorlortoq gneiss. Their trace element systematics indicate a parental melt with tholeiitic affinities, sourced from depleted mantle beneath relatively thin lithosphere (<80 km), that was subsequently contaminated by crustal assimilation. Re–Os isotope systematics of the cumulates and their relationship with the younger Qorlortoq dykes place the age of these cumulates close to that of the Qorlortoq gneiss.

The age of the Qorlortoq gneiss makes it the oldest known component in the NO by ~300 Ma. The extended timescale between episodes of crustal production in this area, could indicate a geodynamic environment characterized by stagnant-lid or episodic mobile-lid tectonics, at least on a regional scale. These constraints provide important information about the diversity and nature of Archean geodynamic environments.

2.1 Introduction

The Paleoproterozoic Nagssugtoqidian orogen (NO), West Greenland, is largely constructed of juvenile Archean crust younger than 2900 Ma that was reworked during the major Nagssugtoqidian orogenesis at ~1850 Ma (Kalsbeek & Nutman, 1996; Connelly & Mengel, 2000; Connelly et al., 2000). Despite the Archean components of the NO being important building blocks of the northern margin of the North Atlantic craton (NAC) in West Greenland (Fig. 2-1), they have not received wide attention. Their petrogenesis, role in crust building, and broader regional significance are poorly understood (Whitehouse et al., 1998; Connelly & Mengel, 2000; Hollis et al., 2006).

Archean magmatic rocks from the NO are fundamentally different in age relative to other components of the NAC in the adjacent Nuuk region to the south. Whereas the Nuuk region has punctuated crustal age peaks at 3880 to 3630 Ma, 3200 Ma, 3000 Ma, and 2850 Ma, the distribution of which is explained by the amalgamation of terranes forming under different geodynamic environments (Nutman, 1996; Friend & Nutman, 2005; Amelin et al., 2011; Fisher & Vervoort, 2018; Gardiner et al., 2019; Steenfelt et al., 2021), the predominant Archean rocks of the NO are younger and formed continuously from 2870 to 2720 Ma (Kalsbeek & Nutman, 1996; Connelly & Mengel, 2000). Because of the difference in ages and the limited studies on the intervening area between the Nagssugtoqidian and Nuuk regions, how these two regions are linked

remains unclear (cf. Connelly & Mengel, 2000; Steenfelt et al., 2020). However, on the basis of disparate age distributions and radiogenic isotopic systematics (e.g. Whitehouse et al., 1998; Gardiner et al., 2019), there is likely a change in the processes of crustal generation between these two areas of Archean crust. Understanding the link between them therefore has important implications for the regional geological environment, Archean geodynamics, and understanding cratonic assembly during the late Archean.

Past research has revealed only sparse evidence in the Nagssugtoqidian region of a lithological component older than 2900 Ma. Any such older rocks are important because of their potential to provide important information on how the Archean rocks of the NO are related to the rest of the NAC. In a regional Sm-Nd study of Nagssugtoqidian gneisses (Whitehouse et al., 1998), two samples – considered to reflect low degrees of metamorphic disturbance – gave depleted mantle model ages of 3040 and 3150 Ga. It was argued that this signature reflects partial melting of a ~3100 Ma or older juvenile felsic source. In addition, limited unpublished U-Pb analyses of gneiss-hosted zircon from the Qorlortoq valley (Fig. 2-1), cited in some studies (Manatschal et al., 1998; van Gool et al., 2002; van Gool & Marker, 2007), revealed some ~3100 to 3150 Ma ages, which were used to define the Qorlortoq unit. The age of the Qorlortoq unit is similar to that of the 3200 Ma peak in the Nuuk region, within the core of the NAC, which is related to renewed magmatism and the addition of juvenile components to the crust following a ~400 Ma episode of no magmatic activity (Næraa et al., 2012; Gardiner et al., 2019). If the Qorlortoq unit similarly recorded the formation of juvenile crust with similar characteristics to that in the Nuuk region, it could provide an important link between Nagssugtoqidian orogenic belt and the Nuuk region as well as provide important information about geodynamic process occurring at that time. However, an attempt to reproduce the results of the unpublished zircon data, which indicated that the Qorlortoq unit is

older than 3100 Ma failed to produce ages older than 2900 Ma, and the Qorlortoq unit was dropped from regional geological nomenclature (van Gool & Marker, 2007).

In this study, we report age determinations of new samples from a portion of the Qorlortoq valley (Fig. 2-1), which we show is largely composed of 3177 Ma leucocratic orthogneiss hosting numerous ultramafic enclaves and is cut by late basaltic dykes. These rocks record fundamental information on the formation of early continental crust in a period when significant changes have been interpreted to have occurred in Earth's geodynamic processes (Næraa et al., 2012; Kirkland et al., 2021). We report bulk-rock major and trace element data of various lithologies in the Qorlortoq complex (gneiss, ultramafic enclaves, and basaltic dykes), laser ablation split-stream U-Pb and Lu-Hf isotopic systematics of zircon from the felsic gneiss, and Re-Os isotopic characteristics of the ultramafic enclaves and dykes. Finally, we discuss possible scenarios for the building of the Qorlortoq crust and its relationship with other Nagssugtoqidian blocks and the broader NAC.

2.2 Regional geology

2.2.1 The Nagssugtoqidian orogen

The Nagssugtoqidian orogen (NO), West Greenland, comprises the northern margin of the North Atlantic craton (NAC) and is largely composed of Archean gneisses and supracrustal belts with subordinate similar Paleoproterozoic units (Fig. 2-1), all of which were reworked during Paleoproterozoic orogenesis. The broad sequence of crustal magmatism and metamorphic events is: 1) Initial juvenile crust produced at ~3177 Ma (this study); 2) A predominant period of juvenile crust building between 2870 and 2810 Ma followed by crustal reworking during orogenesis from 2790 to 2690 Ma (Kalsbeek & Nutman, 1996; Connelly & Mengel, 2000; Connelly et al., 2006; Hollis et al., 2006). 3) A 645 Ma period of tectonic quiescence (Fig. 2-2; Kalsbeek & Nutman,

1996). 4) Rifting at 2045 Ma to produce an intra-cratonic basin (Kalsbeek & Manatschal, 1999; van Gool et al., 2002; Mayborn & Lesher, 2006). 5) Minor Paleoproterozoic crustal building from 1950 to 1870 Ma (Kalsbeek & Nutman, 1996; Whitehouse et al., 1998; Connelly *et al.*, 2000). 6) Final reassembly of the rifted Archean segments during continental collision between 1873 and 1775 Ma – i.e. the Nagssugtoqidian orogeny (van Gool et al., 2002; Connelly et al., 2000). These events are summarized in Fig. 2-2.

The ~3177 Ma Qorlortoq gneiss records the oldest crust known in the Nagssugtoqidian area but appears minor in its presently exposed aerial extent based on a paucity of detrital zircons of this age (Fig. 2-2). By contrast, 2870 to 2720 Ma felsic orthogneiss appears to represent the most volumetrically significant crustal component in the NO (Kalsbeek & Nutman, 1996; Connelly & Mengel, 2000). A high-grade orogenic episode between 2720 and 2790 Ma is recorded by migmatitic melts and overgrowths on zircon in older gneisses, and synkinematic granitic and tonalitic gneisses (Connelly & Mengel, 2000; Hollis et al., 2006; Thrane & Connelly, 2006). Some positive εNd values are observed in the gneisses formed between 2810 and 2870 Ma (Whitehouse et al., 1998), and there is a high abundance of 2720 to 2790 Ma migmatitic melts and metamorphic overgrowths on zircon in older gneisses and associated metasedimentary belts. As such, the 2870 to 2810 Ma gneisses are considered to be juvenile crust produced in a subduction zone environment, followed by the collisional convergence of island arcs or island arcs colliding with continental lithosphere (Connelly & Mengel, 2000). Sharp contacts between older gneisses and younger 2690 to 2720 Ma, less deformed, granitic bodies are interpreted to mark the end of Archean orogenesis and accompanying lithospheric thickening (Connelly & Mengel, 2000).

With the exception of minor ~2500 Ma granitic dykes of unknown origin found south of the Sisimiut area (Nutman et al., 1999; Connelly & Mengel, 2000), Archean crustal generation and orogenesis was followed by a ~650 Ma period in which crust production appeared to cease, along with any perceptible reworking or tectonism (Fig. 2-2).

The earliest known Paleoproterozoic event in the NO area is rifting of the Archean gneisses, marked by the intrusion of the Kangâmiut dyke swarm at ~2045 Ma (Figs. 2-1 and 2-2), to form a narrow inter-cratonic oceanic basin between two southern and northern rifted blocks (Kalsbeek & Manatschal, 1999; van Gool et al., 2002; Mayborn & Lesher, 2006). Juvenile arc volcanism between the rifted Archean blocks, occurring between 1950 and 1873 Ma, is marked by the Arfersiorfik quartz-diorite suite and Sisimiut charnockites (Fig. 2-1; Kalsbeek & Nutman, 1996; Connelly et al., 2000). Collisional convergence of the original rifted Archean blocks, and the Rae craton to the north of the NAC, was responsible for the Nagssugtoqidian orogeny and occurred between 1873 Ma and 1820 Ma (van Gool et al., 2002; Connelly et al., 2000). This episode resulted in up to granulite-facies metamorphism in some areas (Connelly et al., 2000). Late pegmatitic intrusions and metamorphic zircon and monazite indicate that temperatures remained high until at least 1775 Ma (Connelly et al., 2000).

2.2.2 The Qorlortoq unit and samples

Gneiss, similar to the Qorlortoq gneiss, outcrops erratically throughout the Qorlortoq valley, (Fig. 2-1; van Gool & Marker, 2007; Manatschal et al., 1998), but is not shown on recent geological maps. The samples in this study are from the most easterly part of the Qorlortoq valley (Figs. 2-1 and 2-3), an area that is not well explored. The gneiss is leucocratic and composed of hornblende, biotite, plagioclase, and quartz. Mildly deformed amphibolite (basaltic) dykes cut through the area and form sharp contacts with gneiss (Fig. 2-4). These dykes are common in Qorlortoq gneisses but

16

absent in younger Archean gneisses (Kalsbeek and Manatschal, 1999; van Gool and Marker, 2007), providing a diagnostic feature for the Qorlortoq gneiss. They range in width from centimeters to a few meters, tend to strike in the direction of the gneissic foliation, and are composed of hornblende, plagioclase, and olivine. Locally, these dykes can comprise up to 25% of the outcrop. Numerous elliptical ultramafic enclaves are hosted in the gneiss and range in diameter from a few meters to up to 50 m's (Figs. 2-3 and 2-4). These become increasingly amphibole-rich near their margins and contacts with their host gneisses are typically highly irregular (Fig. 2-4). The enclaves are dominantly olivine, amphibole, and orthopyroxene with varying proportions of spinel. We term these units the Qorlortoq gneiss, basaltic dykes, and cumulates (the last for reasons discussed below). East of samples GR16-265 to 267 (Fig. 2-3) there is an inferred lithological boundary because the gneisses to the east are paragneisses and do not contain ultramafic enclaves or basaltic dykes.

2.3 Methods

2.3.1 In-situ measurements

In-situ analyses of major elements in minerals from the cumulate rocks were made by EPMA at the Electron Microprobe Laboratory, University of Alberta, Canada. A 2 μm beam size was used with an accelerating voltage of 20 kV and beam current of 30 nA. On- and off-peak counting times were 20-40s for all elements. Interference corrections were applied to Ti for interference by Ba, and to Mn for interference by Cr. Matrix corrections were done using ZAF or Phi-Rho-Z algorithms. Analytical details and standards used, along with sample data, are given in Appendix C.

2.3.2 Major and trace elements

Major and minor element concentrations were determined by X-ray fluorescence at Franklin Marshall College, US. Six replicate analyses of MUH-1 were done to monitor accuracy and precision (Appendix C). Relative standard deviation (RSD) on most major and minor elements was <5%, except for K_2O (17 % RSD), consistent with the intermediate precision previously estimated for MUH-1 analyzed using this method (Waterton et al., 2020a). Most oxides were accurate to within 5% of the reference values (GeoREM: Jochum et al., 2005) for MUH-1, except for K_2O and Na_2O (both ~25% greater than the references). The poor precision and accuracy of the alkali metals is due to their very low abundance in MUH-1. However, the analysis of K_2O and Na_2O using this method has previously been shown to be precise and accurate for reference material with higher concentrations (OKUM and BHVO; Waterton et al., 2020a). LOI is also likely to be imprecise for samples with low volatile contents (Waterton et al., 2020a).

Trace elements were measured by inductively coupled mass spectrometry (ICPMS) at the Arctic Resources Laboratory (ARL), University of Alberta, Canada. 0.1 ± 0.01 g aliquots of sample were dissolved in Savillex PFA beakers with 4 mL of 28.7 M HF and 1 mL of 15.4 M HNO_3 at 150 ºC for 72 hrs. The samples were evaporated to near dryness and re-dissolved in 15.4 M HNO_3 three times. The final solution was spiked with In as an internal standard and diluted to 3.5% HNO_3. This solution was measured with a Nu Attom ICPMS equipped with a Peltier cooled quartz spray chamber. Reference material OKUM, MUH-1 and BCR-2 were measured to assess the accuracy of the analyses. Compared with compiled analyses of the reference materials from GeoReM (Jochum et al., 2005) most significant elements used in this study were within 10% of the reference values (Appendix C). However, Sc was 12% higher than the reference values for Sc in OKUM. This inaccuracy in the Sc data does not impact the interpretations made in this study. Typical

precision of the analyses using this method is better than 10% (2σ relative; Waterton et al., 2017). Limits of detection were taken as the mean of two procedural blanks plus three times the standard deviation. All trace element analyses are given in Appendix C.

2.3.3 Laser ablation split-stream analyses of U-Pb/Lu-Hf isotopes in zircon

Zircons from two Qorlortoq gneiss (GR16-256 and GR16-261) were measured by laser ablation split-stream (LASS) analyses for U-Pb and Lu-Hf isotopes (complete analyses in Appendix C). The analyses were preformed at the ARL. Zircons were mounted in epoxy and polished to a half grain thickness for ablation using a RESOlution ArF 193nm excimer laser ablation system equipped with an S-155 Laurin Technic 2-volume ablation cell. U-Pb measurements were made on a Thermo Scientific Element XR sector field ICP-MS and Lu-Hf measurements on a Neptune Plus MC-ICP-MS. Methods and instrumentation parameters are described in Vezinet et al. (2018).

The zircons typically range from 75 to 250 μm in length and are subrounded. Cathodoluminescent imaging shows the zircons to have complex internal oscillatory zoning with different growth domains (Fig. 2-5). The 33 μm diameter laser spot size used in the analyses allows for different domains to be targeted. Penetration of different domains with significantly different ages is easily seen in the time resolved signal of ^{207}Pb/^{206}Pb ratios and such analyses were filtered out. All Hf data were selected from the same time-interval as the selected U-Pb isotopic measurement, via simultaneous observation of the time-integrated Hf and Pb isotope data.

Data reduction was performed with the program Iolite following Paton et al. (2010) and Fisher et al. (2017). Analyses of U and Pb isotopes were calibrated using the 1830 ± 1 Ma reference zircon LH94-15 (Simonetti et al., 2005) which bracketed every 7 to 10 unknown analyses. Downhole fractionation of U and Pb isotopes were modelled as smoothed cubic spline functions fitted to analyses of LH94-15. ^{202}Hg was measured to estimate the isobaric interference of ^{204}Hg on ^{204}Pb.

^{202}Hg signals were typically 2080 to 2380 cps. The corrected ^{204}Pb signal of the Qorlortoq zircon varied from below detection to comprising 0.04 % of the ^{206}Pb signal. At these low level (where ^{206}Pb/^{204}Pb>1500), no correction for common Pb was made. Isobaric interferences and mass bias corrections applied to Hf isotopic measurements are discussed in Fisher et al. (2011, 2017). The data were filtered for quality control following Vezinet et al. (2018): 2 relative standard deviations of the ^{206}Pb/^{207}Pb signal that is <1 %; >15s integration time of the sample signal; concordance of >95% and <105% ([((^{208}Pb/^{238}U age)/(^{207}Pb/^{206}Pb age)-1)*100]); 2 times propagated error of the εHf values lower than 3ε-units. Uncertainties in εHf values are calculated by propagating analytical uncertainty with uncertainty in the age of the zircon, estimate of CHUR (Bouvier et al., 2008), and ^{176}Lu decay constant (Söderlund et al., 2004).

Reference material Plešovice (Sláma et al., 2008), FC-1 (Paces and Miller, 1993; Woodhead and Hergt, 2005), MUN-1, and MUN-3 (Fisher et al., 2011) were measured as secondary standards with the unknown samples to assess accuracy (Appendix C). The weighted mean ^{207}Pb/^{206}Pb age of FC-1 zircon was 1100 ± 3 Ma, within error of the reference value of 1099. ± 0.6 Ma (Fig. B2-1). Concordia ages for analyses of Plešovice from the two analytical sessions were 330 ± 2 Ma and 329 ± 2 Ma (Fig. B2-2). Concordia ages for FC-1 were 1106 ± 6 Ma and 1090 ± 6 Ma (Fig. B2-2). The measured ^{176}Hf/^{177}Hf ratio for Plešovice in this study was 0.282491 ± 0.000011 and for FC-1 was 0.282197 ± 0.000016, both within error of the reference values (Fig. B2-1). The measured ^{176}Hf/^{177}Hf ratio for MUN-1 and MUN-3 was 0.282136 ± 0.000011 and 0.282149 ± 0.000027, respectively, both within error of the reference value 0.282135 ± 0.000008 (Fisher et al., 2011).

2.3.4 Re-Os isotopes and platinum group elements

Re-Os isotopes and PGEs were measured by isotope dilution at the ARL. Complete details are given in Pearson & Woodland (2000) and only briefly summarized here. 1 g of sample was dissolved in inverse aqua regia (6 mL 15.4 M HNO_3 and 3.5 mL 10.6 M HCl) with isotopic spike at 260 ºC and 100 bars for 16 hrs in an Anton-Paar high-pressure Asher. The spike was enriched in isotopes ^{190}Os, ^{191}Ir, ^{99}Ru, ^{106}Pd, ^{194}Pt, and ^{185}Re. Os was separated from the matrix by solvent extraction and microdistillation. Os measurements were made with a Thermo Triton Plus thermal ionization mass spectrometer in negative ion mode on the secondary electron multiplier. PGEs and Re were separated from the matrix by anion exchange chromatography using Biorad® AG1-X8 resin and measured in solution using a Nu Attom ICPMS equipped with a Peltier cooled quartz spray chamber.

Six repeat analyses of OKUM were done to monitor accuracy and precision and gave values (Appendix C): Os 0.84 ± 0.06 ppb, Ir 0.92 ± 0.03 ppb, Ru 4.93 ± 0.05 ppb, Pt 11.86 ± 0.35 ppb, Pd 12.01 ± 0.16 ppb, Re 0.49 ± 0.02 ppb. Measured $^{187}Os/^{188}Os$ ratios in OKUM were 0.265 ± 0.013. There are unknown interferences on ^{101}Ru and ^{100}Ru, causing some samples to not plot on a mixing line between spike and natural Ru in $^{101}Ru/^{99}Ru$ vs $^{100}Ru/^{99}Ru$ space. In some cases, this is associated with increases in $^{100}Ru/^{99}Ru$ over time during analysis (McIntyre et al., 2019). Although ^{101}Ru is not used in calculations and not all analyses display both phenomenon, analyses in which $^{100}Ru/^{99}Ru$ increase with time only occur where there are extreme deviations from the spike-natural isotope mixing line in $^{101}Ru/^{99}Ru$ vs $^{100}Ru/^{99}Ru$ space. As a result, no data in this study are given for analyses in which Ru do not plot on this mixing line. This includes one analyses of Ru in OKUM yielding 8.08 ± 0.21 ppb (>3 ppb above the long-term average from the ARL; Appendix C). Disregarding this, all analyses are within uncertainty of the compiled values for

OKUM in GeoReM (Jochum et al., 2005) and within uncertainty of the long term average values for the ARL (n = 56; Appendix C). Six procedural blank measurements were also made (Appendix C). One blank measurement was relatively high (P1135) in Pt (230 ppt), Pd (75 ppt), and Re (14 ppt) and is considered an outlier. Several other blank measurements gave signals, after correction for relevant oxide molecular interferences, that were zero. In the blanks Os was 9 ± 6 ppt, Ir 8 ± 8 ppt (two analyses were less than oxide interference), three Ru analyses were below oxide interferences except one with 169 ± 6 ppt, Pt was 21 ± 14 ppt, three Pd analyses were less than the oxide interferences while the remainder gave 6 ± 8 ppt, and Re analyses were 0.3 ± 0.1 ppt.

2.4 Results

2.4.1 In-situ major elements of the cumulates

Olivine MgO and FeO concentrations in the cumulate rocks range from 43.5 to 49.0 wt% and 9.6 to 16.4 wt%, respectively, corresponding to olivine Mg #'s of 83 to 90. Olivine Mg #'s are correlated with bulk rock Mg #'s. The concentration of CaO in the olivines is < 0.01 wt% in all analyses, Mn ranges 0.14 to 0.24 wt%, and NiO ranges from 0.38 to 0.47 wt%.

In the spinel, Cr #'s (Cr/(Cr+Al)) range from 0.19 to 0.81 and Fe #'s (Fe^{2+}/(Mg+Fe^{2+})) range from 0.3 to 0.85. These variations in Cr # vs Fe # space follow trends of low temperature (~550 ºC) chromite in equilibrium with olivine (Fig. B2-3). Some spinels have been largely altered to Cr-rich magnetite and have Fe^{3+} #'s (Fe^{3+}/(Fe^{3+}+Al+Cr) up to 0.52.

Orthopyroxene MgO contents range from 30.8 to 34.4 wt% and are dominantly enstatite (83 to 90 %) with lesser ferrosilite (10 to 17 %). Like olivine, the orthopyroxene Mg#'s are correlated with bulk-rock Mg #'s. The CaO content of the orthopyroxene is low, from 0.08 to 0.41 wt%.

2.4.2 Bulk-rock major and trace elements

Two Qorlortoq gneiss samples were measured for major and trace elements. These samples are felsic in composition with concentrations of SiO_2 of ~70 wt%, Al_2O_3 of ~16.5 wt%, Na_2O of ~4.6 wt%, K_2O of 2.0 and 0.9 wt%, and $FeO + MnO + MgO + TiO_2$ of ~4 wt% (Appendix C). Together these data fall within the sodic tonalite-trondhjemite-granodiorite (TTG) classification criteria of Moyen & Martin (2012), consistent with their tonalitic modal mineralogy.

The ultramafic rocks display high concentrations of MgO (30.0 to 45.9 wt%) and FeO (10.2 to 12.8 wt%), and low concentrations of Al_2O_3 (1.01 to 5.71 wt%), TiO_2 (0.05 to 0.23 wt%), and CaO (0.03 to 5.74 wt%) (Appendix C). Concentrations of SiO_2 range from 41.3 to 46.6 wt%. MgO forms good correlations with most major and trace elements (Figs. 2-6 and B2-4), including some fluid mobile elements (e.g. Sr), indicating that these elements were relatively immobile during metamorphism (Pearce, 1996). High FeO contents (>10%) and mixing lines between olivine (MgO 48 wt%, CaO 0.02 wt%, and Al_2O_3 0 wt%) and magma compositions (Fig. 2-6) identify the ultramafic rocks as cumulates (Szilas et al., 2015; McIntyre et al., 2019).

Primitive-normalized trace element patterns for most of the ultramafic rocks are flat, with negative Nb anomalies and slightly enriched light REEs and Th (Fig. 2-7). The most Mg-rich samples however are extremely depleted in middle REEs, giving a U-shaped trace element pattern and positive high field strength element anomalies (HFSE) (Fig. 2-7).

One sample of the basaltic dykes that crosscut the Qorlortoq gneiss was analyzed (the Qorlortoq dykes). This sample is a relatively evolved basalt with MgO of 6.3 wt% and SiO_2 of 51 wt% (Appendix C). Primitive mantle normalized trace element patterns are largely flat in heavy REEs, depleted in light REEs, and have negative Zr anomalies (Fig. 2-7).

2.4.3 U-Pb/Lu-Hf isotopes of zircon in the Qorlortoq gneiss

U-Pb analyses of the zircons are given in Appendix C. Those from sample GR16-261 define a discordia with an upper intercept of 3177 ± 12 Ma (MSDW (concordance + equivalence) = 0.52) (Fig. 2-8 A). Sample GR16-256 gives a concordia age of 3150 ± 28 Ma (MSWD (concordance + equivalence) = 2.6) that is slightly displaced below concordia (Fig. 2-8 A). The data from this sample do not define a single age population (probability of fit = 2.4×10^{-4}), plot along the discordia defined by GR16-261 (Fig. B2-5) and have $^{207}Pb/^{206}Pb$ ages identical to that of GR16-261 (Fig. 2-8 B). For these reasons, it is likely that zircon crystals from GR16-256 suffered minor Pb loss and the age of both samples is taken to be that of GR16-261 – 3177 ± 12 Ma. Together these rocks mark the oldest components in the Nagssugtoqidian orogen (Fig. 2-2).

The above age (3177 Ma) is used to calculate the initial εHf values for the Qorlortoq gneiss using the Lu-Hf decay constant of Söderlund et al. (2004) and CHUR value of Bouvier et al. (2008), propagating the uncertainties in age of the sample, ^{176}Lu decay constant, and CHUR composition into the calculation. Both samples define a single population with a weighted mean εHf of 1.75 ± 0.54 (MSWD = 0.47) (Fig. 2-8 C). This value falls along a trend typical of crustal evolution in West Greenland on an Hf isotope evolution diagram (Fig. 2-9).

2.4.4 Platinum group elements and Re-Os isotopes of Qorlortoq cumulates and dyke

The ultramafic enclaves are characterized by relatively homogenous bulk-rock Os and Ir concentrations of 1.98 ± 0.72 ppb and 1.53 ± 0.61 ppb, respectively. In contrast, Pt and Pd are highly variable (0.25 to 8.31 ppb and 0.15 to 9.38 ppb, respectively). Primitive mantle normalized PGE patterns are variable, with PPGEs (Pt and Ir) being both depleted and enriched relative to IPGEs (Os, Ir, and Ru; Fig. B2-6). In addition, Os/Ir ratios are variable and are non-chondritic. The variable PPGE characteristics and relatively high IPGs concentrations (>1 ppb) are typical of

Archean ultramafic cumulates in West Greenland as a whole (Coggon et al., 2013; Szilas et al., 2015, 2017; Rizo et al., 2016; McIntyre et al., 2019). A basaltic dyke crosscutting the Qorlortoq gneiss has extremely low PGE concentrations and high Re concentrations relative to the cumulates (Fig. B2-6 and Appendix C), consistent with basalts with similar MgO concentrations (e.g. Philipp et al., 2001). The complete bulk-rock PGE dataset is given in supplementary Appendix C.

The Os isotopic composition of the ultramafic cumulates are generally unradiogenic ($^{187}Os/^{188}Os$ ratios between 0.1084 and 0.1142), with a few exceptions (values up to 0.2807) and have T_{MA} and T_{RD} model ages broadly of Meso- and Neoarchean age (Table 2-1). These ages largely overlap with the host gneiss (3177 Ma) and crustal building and orogenesis in the area between 2720 and 2870 Ma. The rocks do not produce a Re-Os isochron, with many samples displaced to high $^{187}Os/^{188}Os$ and low $^{187}Re/^{188}Os$ (Fig. B2-7) indicating that Re was partially redistributed during metamorphism.

2.5 Discussion:

2.5.1 Qorlortoq Ultramafic Cumulates

2.5.1.1 The composition and nature of the parental melt to the ultramafic cumulates

Ultramafic rocks of cumulate origin are an integral part of the Eoarchean and Mesoarchean terranes that comprise the North Atlantic Craton (Nutman, et al., 1996; Rollinson et al., 2002; Rollinson, 2007; Coggon et al., 2013; Szilas et al., 2015, 2017; McIntyre et al., 2019). For the ultramafic cumulates that comprise part of the Qorlortoq gneiss region, the composition of the parental melt can be estimated by extrapolating linear trends between an element of unknown concentration and the concentration of an element whose concentration is known in the melt. In the cumulates, the MgO content of the melt can be estimated from the intersection, in FeO_t vs MgO space, of bulk-

rock melts calculated to be in equilibrium with olivine in the rocks (Fig. 2-10). However, the measured olivine chemistry in the Qorlortoq cumulates has been affected by significant metamorphic re-equilibration on a mineral scale, possibly with amphibole; CaO in the olivine is <0.01 wt% (average LOD) atypical of igneous olivine (CaO > 0.2 wt% (Sobolev et al., 2007)). In contrast to mineral chemistry, bulk-rock MgO and FeO concentrations are resistant to metamorphic alteration in ancient igneous rocks (Szilas et al., 2015; McIntyre et al., 2019). Thus, the pre-metamorphic olivine composition of the cumulates was deduced from the intersection of the bulk-rock analyses with the idealized composition of olivine with varying Mg #, giving an estimate for the olivine composition that has 48.2 wt% MgO, 10.2 wt% FeO, and Mg # of 89 (Fig. 2-10). The intersection of the bulk-rock with melt in equilibrium with this olivine gives a parental melt to the cumulates of 15.9 wt% MgO (Fig. 2-10).

The extended range of major and trace element concentrations in the parental melt was determined by extrapolating elements in the cumulates to a MgO content of 15.9 wt% (complete element list is given in Appendix C). Unlike other elements, high field strength elements (HFSE) do not form good correlations with MgO, largely due to low concentrations and scatter in high MgO rocks (Fig. B2-4). This is typical of highly refractory Archean cumulates with little interstitial melt where there are large positive and erratic spikes in HFSEs (cf. Szilas et al., 2017; Waterton et al., 2020b), the reason for which is likely due to the accumulation of HFSE-rich phases precipitated from the melt (e.g. Waterton et al., 2020b) or assimilated from the crust. Excluding these high MgO rocks, MgO correlates reasonably well with Ta (Fig. B2-4) and HFSEs were extrapolated to a Ta concentration of 0.05 ppm.

This method assumes that the cumulates formed from a melt that did not fractionate significantly between different enclaves. This is supported by modelling the fractional crystallization of the

estimated parental melt to the cumulates using MELTS (Gualda et al., 2012; Ghiorso & Gualda, 2015). The results demonstrate that fractional crystallization plus variable mineral proportions during different stages of crystallization are unlikely to account for the linear trends seen in the bulk-rock data, as this would require a fortuitous mixing of different components (Fig. 2-10). Thus, the bulk-rock data show mixing between largely olivine and melt with relatively constant composition.

The resulting estimated parental melt to the cumulates is a relatively siliceous basalt that has a primitive-normalized trace element pattern that is flat in heavy REEs, slightly enriched in light REEs, and has negative Nb, Ta, and Ti anomalies (Appendix C and Fig. 2-7). The alkali, MgO, and FeO contents and Zr/Ti and Nb/Y ratios of the melt indicate a tholeiitic affinity (Fig. B2-8). The melt has clearly undergone some crustal contamination as is evident from some modal orthopyroxene in the cumulates, recalculated high SiO_2 content of the melt (51.4 wt% at 15.9 wt% MgO), and high Th/Nb ratio (0.22; Fig. 2-11). In contrast, Nb/Yb, Nb/Y, Zr/Y, and Zr/Nb ratios of the melt are very similar to depleted MORB (Fig. 2-11) indicating the mantle source experienced prior melt removal. In trace elements discrimination diagrams the parental melt plots in the fields of Archean intra-plate basalts, albeit, with more crustal contamination than most (higher Th relative to Nb; Fig. 2-11). The melt is distinct from Archean basalts interpreted to be of arc origin in that it has lower Nb/Y and Nb/Yb (Fig. 2-11), indicating the source for the cumulates was less enriched than for Archean arc basalts. Thus, we interpret the crustal contamination signature to result from crustal assimilation rather than crustal recycling in a subduction zone. Although an oceanic vs continental setting cannot be differentiated as Archean oceanic basalts can have significant crustal contamination (e.g. Pearce, 2008), the crustal contamination likely precludes an

27

oceanic spreading center origin. Thus, the Qorlortoq ultramafic cumulates formed from intraplate basalts sourced from depleted mantle that underwent crustal contamination on ascent.

2.5.1.2 Age of the ultramafic cumulates

The age of the cumulate enclaves in the context of regional processes occurring at that age is important in understanding their origin, considering the very ancient ages of many ultramafic bodies in the NAC (Bennett et al., 2002; Coggon et al., 2013; Rizo et al., 2016; McIntyre et al., 2019). Gneiss-hosted ultramafic enclaves can often be shown to predate their host because of intrusive tonalitic dykes identical in age to their host gneiss (Nutman et al. 1996; Szilas et al., 2017). For the Qorlortoq cumulates, no definitive intrusive relationships were found between enclave and host gneiss, making the age of the cumulates difficult to decipher. There is no clear Re-Os isochron defined by these rocks (Fig. B2-7), likely indicating variable Re mobility. Assuming a Re/Os ratio of zero to obtain a minimum age constraint, the oldest Re-Os T_{RD} age of the cumulates is 2941 ± 358 Ma (Table 2-1), overlapping with the host gneiss age (3177 Ma). This could be consistent with the Qorlortoq cumulate enclaves predating their host, like ultramafic enclaves in other gneiss complexes. If these cumulates do predate the host gneiss, the lack of associated basaltic enclaves in the gneiss may indicate that the cumulates were the most refractory portions of a basaltic crust that largely melted to produce the Qorlortoq gneiss. However, the large uncertainty of the T_{RD} ages does not preclude the cumulates forming during younger events, for example, the cumulates being coeval with the Qorlortoq dykes.

A scenario where the ultramafic cumulates are genetically related to the Qorlortoq dykes is disregarded based on distinct differences in trace element geochemistry between the cumulates and dykes, which include higher Zr/Nb and lower Nb/Th ratios in the cumulates relative to the dykes, reflecting higher degrees of crustal contamination in the parental melt of the cumulates

(Fig. 2-11). If the enclaves are not genetically related to the Qorlortoq dykes, they likely predate them. The ultramafic enclaves are highly deformed; they are elliptical and have highly irregular contacts with the host gneiss (Fig. 2-4). In addition, the enclaves are small (≤50 m) relative to younger dunite-bearing complexes (e.g. Guillou-Frottier et al., 2014) or the original inferred size of Archean disaggregated gneiss hosted ultramafic enclaves (e.g. Nutman, 1996; Szilas et al., 2017). We therefore interpret the exposed dunite enclaves as the broken-up fragments of a larger ultramafic complex. In contrast, the dykes, although deformed, are not typically disaggregated and have more regular contacts with the gneiss (Fig. 2-4). On these grounds the cumulates are interpreted to pre-date the Qorlortoq dykes, which, based on geochemical similarities to other basalts in the NO area, are interpreted as being associated with other magmatism between 2820 and 2790 Ma (see Section 2.5.2). Because of their inferred intraplate setting discussed above, the ultramafic cumulates likely predate the main episode of arc-volcanism that occurred between 2820 and 2870 Ma (Connelly & Mengel, 2000).

Although these time constraints are important, they do not link the ultramafic cumulates to any tectonic event. There is little known magmatic activity in the area older than 2870 Ma, with the exception the Qorlortoq gneiss (Fig. 2-2). Thus, the precise age of the cumulates remains unknown.

2.5.2 Origin of the Qorlortoq dykes

The chemical characteristics of the Qorlortoq dyke sample analyzed in this study – flat primitive mantle normalized HREE patterns, low Th/Nb ratios, and depleted LREEs relative to HREEs (Figs. 2-7 and 2-11) – are characteristics of a tholeiitic melt, with minor crustal contamination, that was derived from a depleted mantle source. The tholeiitic nature of the magma, the occurrence of the dykes within continental crust in combination with limited crustal contamination suggests eruption through attenuated continental lithosphere. Thus, the Qorlortoq dykes could be related to

the 2045 Ma Kangâmiut dyke swarm (Fig. 2-1), as has previously been suggested based on similar mineralogy, their size and their spatial distribution within their host gneisses (van Gool & Marker, 2007). However, the most northern known extent of the Kangâmiut dykes is ~50 km south of the Qorlortoq gneiss (Fig. 2-1). The other Archean gneisses proximal to the Qorlortoq gneiss and throughout the central and northern part of the NO are not cut by extensive dyke swarms. The relative abundance of Qorlortoq dykes in the Qorlortoq gneisses compared to in the 2870 to 2720 Ma gneisses, suggests that they either predate the formation of the younger gneisses, or predate their juxtaposition with the Qorlortoq gneiss, possibly during the Archaean or during the Nagssugtoqidian orogeny. Furthermore, the trace element composition of the Qorlortoq dyke analyzed here is clearly distinct from the Kangâmiut dykes in that it has lower LREE/HREE, Th/Nb, Nb/Yb, and Zr/Y ratios (Fig. 2-11). Specifically, the very low Zr/Y ratio (1.3) shown by the Qorlortoq dyke is rare in most Phanerozoic basalts (Li et al., 2015) or Archean basalts (Fig. 2-11). Taken together, this evidence indicates that the Qorlortoq dykes are not genetically related to the Kangâmiut dykes.

The extremely low Zr/Y ratio of the Qorlortoq dyke has been observed in Archean mafic rocks from West Greenland - the Archean Kangilinaaq amphibolites (Fig. 2-11) - which occur in the northern part of the NO (Fig. 2-1; Hollis et al., 2006). The similar unusually low Zr/Y ratios and other trace element characteristics (Figs. 2-11) potentially indicate that the Qorlortoq dyke and Kangilinaaq amphibolites were generated from the same mantle source, at similar times. We therefore tentatively correlate the Qorlortoq dykes with the Kangilinaaq amphibolites located within the same orogen. The Kangilinaaq amphibolites are interpreted to be coeval with metasediments with which they are intercalated, which were found to be ~2790 to 2820 Ma in age

(Hollis et al., 2006). Thus, the Kangilinaaq amphibolites formed during regional volcanism at ~2800 Ma (Hollis et al., 2006) and we suggest that the Qorlortoq dykes likely formed at this time.

2.5.3 Qorlortoq Gneiss

The Nagssugtoqidian orogen (NO) has generally been described as Archean crust reworked during Paleoproterozoic collision between the North Atlantic craton (NAC) and a lesser-known craton to the north, underlying the Rinkian fold and thrust belt (Fig. 2-1; van Gool et al., 2002; van Gool & Marker, 2007). A more comprehensive understanding of the relationship between the Archean components of the NO and the NAC is needed here to describe the significance of the Qorlortoq gneiss. Our new 3177 Ma U-Pb zircon age of the Qorlortoq gneiss and the accompanying suprachondritic εHf values are similar to those in the Akia terrane and broader Nuuk region (Fig. 2-9) to the south of the Nagssugtoqidian area (Fig. 2-1), which formed at a time when the production of continental crust in these areas transitioned from dominantly intra-crustal reworking characterized by subchondritic crustal εHf to juvenile crustal production with suprachondritic εHf (Fig. 2-9; Næraa et al., 2012; Gardiner et al., 2019). The post-3200 Ma change in the Hf isotopic record in West Greenland has been interpreted to reflect a transition from stagnant-lid to mobile-lid tectonics (Næraa et al., 2012) or renewed magmatism in a stagnant-lid tectonic setting (Gardiner et al., 2019; Yakymchuk et al., 2020; Steenfelt et al., 2021). Thus, two important questions are how and whether the Archean rocks of the NO are related to those in the NAC immediately to the south and if any geodynamic setting can be inferred from the age and geochemical characteristics of the Qorlortoq gneiss.

2.5.3.1 Characteristics and origin of the Qorlortoq gneiss

Tonalites are the products of partial melting of mafic protoliths (Moyen & Martin, 2012). Thus, the suprachondritic εHf in zircons from the Qorlortoq gneiss indicates that its protolith was

juvenile mafic crust extracted from moderately depleted mantle and, extrapolating these εHf values to the West Greenland depleted mantle curve of Næraa et al. (2012; Fig. 2-9), yields a two-stage depleted model age of ~3300 Ma (using a $^{176}Lu/^{177}Hf$ ratio of 0.024 and Lu-Hf decay constant is from Söderlund et al. (2004)). Similarly, using the depleted mantle curve of Fisher & Vervoort (2018) (mantle depletion at 3800 Ma) would yield younger model ages of ~3220 Ma. Unlike the Akia terrane, where the protolith of some of the gneisses have been interpreted to be up to Eoarchean in age (Gardiner, et al., 2019), there is no indication that the Qorlortoq gneiss formed from the melting of long-lived crust.

2.5.3.2 *Relationship of the Nagssugtoqidian orogen to the North Atlantic craton and significance of the Qorlortoq gneiss*

Detrital zircon from Archean supracrustal belts are useful in determining spatial relationships between different terranes because their catchment areas can sample large aerial extents of crust, unlike individual igneous samples. The Akia terrane is the most proximal, well studied terrane to the NO (Fig. 2-1). There is a strong contrast in the detrital zircon record between the Archean rocks of the Akia terrane and the NO (Fig. 2-9). Detrital zircon from Archean supracrustal belts of the Akia terrane have a strong ~3000 Ma peak, reflecting the dominant age of orthogneisses in that area (Fig. 2-9; Kirkland et al., 2018; Gardiner, et al., 2019; Steenfelt et al., 2021; Yakymchuk et al., 2020). By contrast, a compilation of detrital zircon ages from the Archean NO rocks show no significant peak until after 2900 Ma (Fig. 2-9). This difference suggests that the Archean rocks of these areas are at most distally related at the time of deposition, although it could also reflect different catchment areas for the sediments. However, magmatic zircon age distributions support the interpretation that the Akia Terrane and NO have different geological histories. Except for the Qorlortoq gneiss, there is no magmatic zircon evidence for gneisses older than 2900 Ma in the

Nagssugtoqidian orogen, and the NO lacks a ~3000 Ma magmatic event (e.g. Kalsbeek et al., 1987; Kalsbeek & Nutman, 1996; Connelly & Mengel, 2000; Thrane & Connelly, 2006). In contrast, no magmatic ages from the Akia terrane overlap the 2870 to 2820 Nagssugtoqidian gneisses (Kirkland et al., 2018; Gardiner, et al., 2019; Steenfelt et al., 2021; Yakymchuk et al., 2020), although metamorphism overlapping this age is observed in the northern Akia Terrane and Alanngua Complex (Kirkland et al., 2018; Steenfelt et al., 2021).

The significant difference in the age peaks in the detrital and magmatic zircon record between the Akia terrane and Nagssugtoqidian Archean crust give two possibilities for the relationship between the basement of these areas (Connelly & Mengel, 2000). Either the Archean rocks of the NO represent remnants of diachronous subduction-related magmatism and growth along the margin of the older Akia terrane or they form an allochthonous terrane, accreted to the Akia terrane (Connelly & Mengel, 2000). Recently, Steenfelt et al. (2021) suggested the presence of a terrane separate from the Akia terrane that was accreted to its northern margin, which they termed the Tuno terrane (Fig. 2-1). These authors suggest the Archean rocks of the NO may be part of this terrane based on finding a ~2820 Ma gneiss in the area defined by the Tuno terrane (Fig. 2-1) (i.e. having a similar age to the Archean NO gneisses; Kalsbeek & Nutman, 1996; Connelly & Mengel, 2000). However, this gneiss also contained xenocrystic zircon with $^{207}Pb/^{206}Pb$ ages of ~2966 Ma, distinct from all previously reported ages in the NO (Fig. 2-2).

The inclusion of Akia aged zircon in magmatic rocks with ages similar to the Archean components of the NO, suggest that these magmatic rocks assimilated Akia aged crust on the northern boundary of the Akia terrane. In addition, other orthogneisses from the proposed Tuno terrane have metamorphic U-Pb zircon ages of ~3000 Ma (Yakymchuk et al., 2020), overlapping the age of

granulite facies metamorphism in the Akia Terrane (Waterton et al., 2020b; Yakymchuk et al., 2020). Finally, detrital zircon from Archean supracrustal belts in the Tuno terrane contain age peaks overlapping both the Akia terrane and Archean components of the NO (Fig. 2-9; Nutman et al., 2004; Gardiner et al., 2019). This raises an alternative interpretation to the Tuno terrane of Steenfelt et al. (2021) whereby the bimodal age peaks in the Tuno area, related to both Akia and Nagssugtoqidian basement, could indicate diachronous subduction-related magmatism along the northern margin of the Akia terrane after 2900 Ma. Subduction related growth is likely to be accompanied by accretion of exotic crust. If the hypothesis is correct, the Qorlortoq gneiss studied here, together with other older exotic terranes in the area (e.g. ~3600 Ma Aasivik terrane (Figs. 2-1; Rosing et al., 2001)) whose ages are missing from the detrital zircon record (Figs. 2-2 and 2-9), would represent crust accreted to the growing margin of the Akia terrane. In this model, the post-2900 Ma Archean rocks in the Nagssugtoqidian orogen are possibly a combination of magmatic rocks produced along the subduction front and accreted ocean island arcs.

Addressing the total original extent of the Qorlortoq gneiss in this setting is hindered by the preliminary nature of our investigation and a lack of additional data. There is presently no evidence for other Qorlortoq gneiss-aged components within the NO. This may imply significant reworking or recycling of the Qorlortoq gneiss or mafic crust related to its protolith during the late Archean, from which a small block of Qorlortoq gneiss survived. Alternatively, the Qorlortoq gneiss may extend eastwards under the Greenland Ice Sheet and only its western margin is exposed. Although depleted mantle model ages up to 3190 Ma from bulk-rock Sm-Nd systematics in 2870 to 2720 Ma gneisses of the NO implies recycling of an earlier, 3190 Ma continental source (Whitehouse *et al.*, 1998), bulk-rock Sm-Nd isotopes are sensitive to alteration in high grade metamorphic terranes (e.g. Amelin, 2009; Hammerli et al., 2019). In contrast, a lack of detrital zircon related to

the Qorlortoq gneiss, absence of older inherited zircon cores and zircon xenocrysts in younger gneisses, and older crust likely implies that the protolith of the late Archean NO gneisses was mafic. We recommend that future work focus on U-Pb/Hf in zircon of the late Archean NO gneisses to assess the age and nature of recycled components in those gneisses and to evaluate whether they could be derived from reworked Qorlortoq gneiss, related mafic crust, or some other unrelated crust.

2.5.3.3 Implications for Archean geodynamic processes

The 3177 ± 12 Ma age of the Qorlortoq gneiss determined here is ~300 Myr older than the main peak in crustal building observed in the magmatic and detrital zircon record of Archean Nagssugtoqidian crust (Fig. 2-2). Modern subduction margins shows punctuated pulses of magmatism and bimodal εHf values on temporal scales of about tens of millions of years and lasting hundreds of millions of years (e.g. Kemp et al., 2009). The lack of crust younger than the Qorlortoq gneiss in this intervening time is therefore inconsistent with continuous mobile-lid tectonic process in the NO region throughout the Mesoarchean, albeit unless there was significant recycling of continental crust. The apparent limited production of continental crust at ~3177 Ma followed by no additional record of crustal production between 3177 and 2870 Ma might instead reflect a stagnant lid tectonic regime, similar to that suggested by some to have occurred between 3600 Ma and 3200 Ma in the Nuuk region (Fig. 2-9; Næraa et al., 2012; Gardiner, et al., 2019), or as late as 3000 Ma in the Akia Terrane (Yakymchuk et al., 2020). Alternatively, the Qorlortoq gneiss may have been produced during a short, punctuated episode of subduction (e.g. O'Neill et al., 2007) followed by accretion to a continental margin 300 Myr later. Thus, the Qorlortoq gneiss is interpreted to have formed by within-plate volcanism (e.g. Yakymchuk et al., 2020) or in a short-lived subduction episode (e.g. O'Neill et al., 2007), followed by local stagnant-lid tectonics, or

simply tectonic quiescence, until ~2870 Ma, at which time it was juxtaposed against the late Meso- and Neoarchean rocks of the Nagssugtoqidian area by subduction. In any event, there is no evidence for continual mobile lid tectonics between 3177 Ma and 2870 Ma recorded in the Qorlortoq gneiss and spatially related rocks.

Recently, the transition to mobile lid tectonics at 3200 Ma in the Akia terrane hypothesised by Næraa et al. (2012) has been challenged based on Hf isotopic characteristics of zircon and a high paleogeothermal gradient in the 3000 Ma Akia terrane crust that do not support an origin by subduction processes (Gardiner, et al., 2019; Yakymchuk et al., 2020; Waterton et al., 2020b). Thus, the results of this study and others provide no clear evidence that continental crust in the northern part of the NAC formed by continuous mobile-lid tectonics between 3200 Ma and 2900 Ma. In such a model, the post-2900 Ma prolonged production of juvenile Archean crust with bimodal εHf (Fig. 2-9) and εNd (Whitehouse et al., 1998) and inferred Neoarchean amalgamation of terranes in the area (Friend & Nutman, 2005), record the subsequent onset of mobile-lid tectonics in the late Meso- to Neoarchean in rocks on the northern margin of the NAC. If this interpretation is correct, the transition to mobile-lid tectonics in the northern NAC occurred during a period commonly inferred to mark the onset of global mobile-lid tectonics, albeit up to 300 Myr later or more than some estimates (cf. Palin et al., 2020).

2.6 Conclusions

The discovery and dating of the Qorlortoq gneiss, documented here, provides important constraints on the geodynamic setting of the Nagssugtoqidian area in the Archean. The detrital and magmatic zircon record of the Akia terrane and late Meso- and Neoarchean component of the NO implies post-2900 Ma Archean growth by subduction along the northern margin of the Akia terrane. We

interpret the Qorlortoq gneiss as an exotic fragment of older crust accreted during this process. The significant age hiatus between the Qorlortoq gneiss and other Archean rocks of the Nagssugtoqidian provides no evidence for continual mobile-lid tectonics during this period, consistent with findings from other studies of the Akia terrane (Gardiner et al., 2019; Yakymchuk et al., 2020).

The Qorlortoq igneous ultramafic cumulates documented in this study were produced via crustal contamination of high-MgO intra-plate basalts sourced from a depleted mantle. The lack of basaltic enclaves in the gneiss and Mesoarchean T_{RD} ages of the cumulates may suggest that these cumulates are refractory/un-melted portions of the mafic/ultramafic protocrust that melted to produce the Qorlortoq gneiss. Un-melted material of the most refractory protocrust may have become entrained in the melt and exists today as xenoliths and rafts of ultramafic rocks within the Qorlortoq gneiss. The depleted mantle trace element characteristics of the cumulates and suprachondritic εHf in zircon from the host gneiss supports this hypothesis. Despite this, an origin for the cumulates as products from late intrusions between 2870 and 3177 Ma cannot be explicitly ruled out. Whatever the ultimate origin, this type of material could have formed the major portion of the early cratonic crust.

Trace element geochemical characteristics of the Qorlortoq dykes are distinct from the Kangâmiut dykes indicating that these dyke swarms are unrelated. Uniquely low Zr/Y ratios of the Qorlortoq dykes are identical to those of the Kangilinaaq amphibolites in the northern Nagssugtoqidian area placing important time constraints on the age of the dykes at ~2800 Ma. Trace element systematics indicate that the dykes were sourced from a depleted mantle and suffered very little crustal contamination despite forming in continental crust, implying eruption through attenuated

lithosphere, in contrast to the thick lithosphere extant beneath the southern portion of the NO and northern edge of the North Atlantic Craton (Sand et al., 2009).

Acknowledgements

2.7 Tables and Figures

Table 2-1 Re-Os isotope compositions of the Qorlotoq cumulate enclaves and dyke.

Sample	Os (ppb)	2σ	Re (ppb)	2σ	$^{187}Re/^{188}Os$	2σ	$^{187}Os/^{188}Os$	2σ	T_{MA} (Ma)	2σ	T_{RD} (Ma)	2σ
Qorlortoq cumulates enclaves												
GR16-252	2.36	0.02	0.009	0.016	0.0182	0.0005	0.11039	0.00018	2787	357	2669	329
GR16-255	3.21	0.02	0.0099	0.0006	0.0148	0.0009	0.10980	0.00015	2849	360	2751	337
GR16-258	2.19	0.02	0.0620	0.0014	0.136	0.003	0.11272	0.00015	3441	608	2353	295
GR16-259	2.38	0.02	0.0245	0.0006	0.050	0.001	0.11264	0.00021	2671	373	2363	297
GR16-260	1.09	0.01	0.0352	0.0009	0.162	0.005	0.12980	0.00018	-46	189	-28	117
GR16-262	0.33	0.01	0.0501	0.0011	0.74	0.02	0.28068	0.00054				
GR16-264	2.04	0.02	0.0293	0.0008	0.0252	0.0007	0.10909	0.00027	3054	399	2847	349
GR16-265	1.85	0.02	0.0264	0.0007	0.069	0.002	0.11046	0.00018	3164	456	2661	328
GR16-266	1.86	0.02	0.0071	0.0002	0.0184	0.0005	0.10872	0.00018	3026	384	2897	353
GR16-267	1.84	0.02	0.0020	0.0007	0.005	0.002	0.10840	0.00019	2977	367	2941	358
GR16-268	2.48	0.02	0.0120	0.0007	0.023	0.001	0.11089	0.00020	2752	358	2603	322
GR16-275	2.51	0.02	0.0253	0.0006	0.048	0.001	0.11421	0.00020	2422	342	2149	275
GR16-277	1.56	0.01	0.0137	0.0003	0.042	0.001	0.11763	0.00023	1861	273	1678	227
Qorlortoq basaltic dyke												
GR16-257	0.047	0.037	0.49	0.02	187	147	21.07	0.80	6387	4790		

*T_{MA} and T_{RD} ages use primitive upper mantle (Meisel et al., 2001; Walker et al., 2002) and the decay constant used for ^{187}Re was 1.6689x10^{-11} (Selby et al., 2007). Uncertainties are propagated after Sambridge & Lambert (1997).
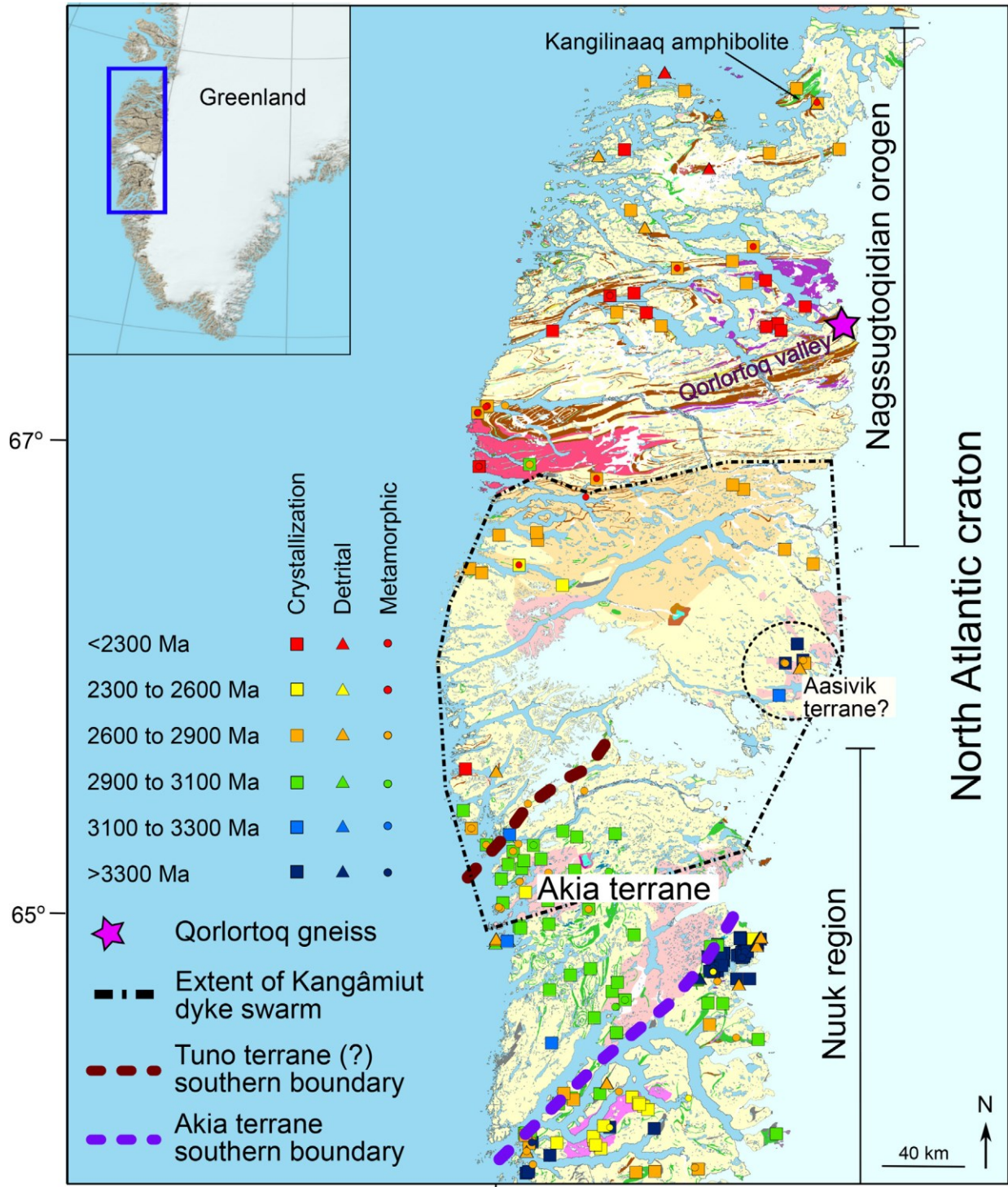
Fig. 2-1. Geologic map of the northern margin of the NAC in West Greenland showing the location of the Qorlortoq gneiss and Qorlortoq valley (base map is from Pedersen et al. (2013)). The area of study (region under the purple star) is expanded in Fig. 2-3. Also shown are the distribution and ages of different terranes and areas discussed in text. Point data represent grouped rock ages or individual zircon grains presented as the crystallization age of the rocks, the distribution of detrital components, or metamorphic overprint. Data sources are from Kalsbeek & Nutman (1996), Kirkland et al. (2016, 2018), Gardiner et al. (2019), and Steenfelt et al. (2020). The Aasivik terrane is Eoarchean crust discovered by Rosing et al. (2001). The Tuno terrane was proposed by Steenfelt et al. (2021) to be an allochthonous terrane encompassing the Archean Nagssugtoqidian area rocks; the proposed southern boundary of the terrane is shown. Also shown are the extent of the Kangâmiut dykes (Connelly and Mengel, 2000) and the location of the Kangilinaaq amphibolite (Hollis et al., 2006).
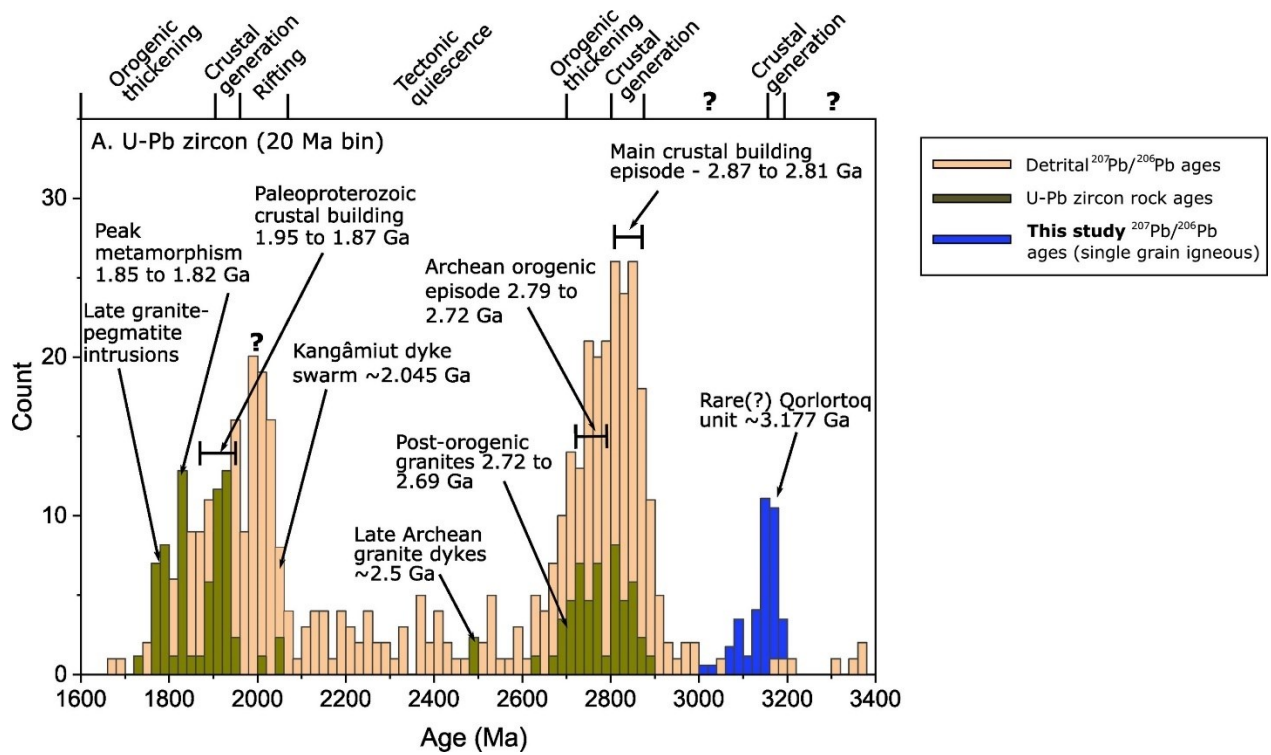
Fig. 2-2. U-Pb ages from crustally derived zircons showing the history of the NO. Rock ages are either weighted mean $^{206}Pb/^{207}Pb$ ages or upper concordia intercepts from igneous zircon. Literature U-Pb zircon ages are from Kalsbeek et al. (1987), Kalsbeek & Nutman (1996), Whitehouse et al. (1998), Nutman et al. (1999), Connelly & Mengel (2000), Connelly et al. (2000), Hollis et al. (2006), and Thrane & Connelly (2006).
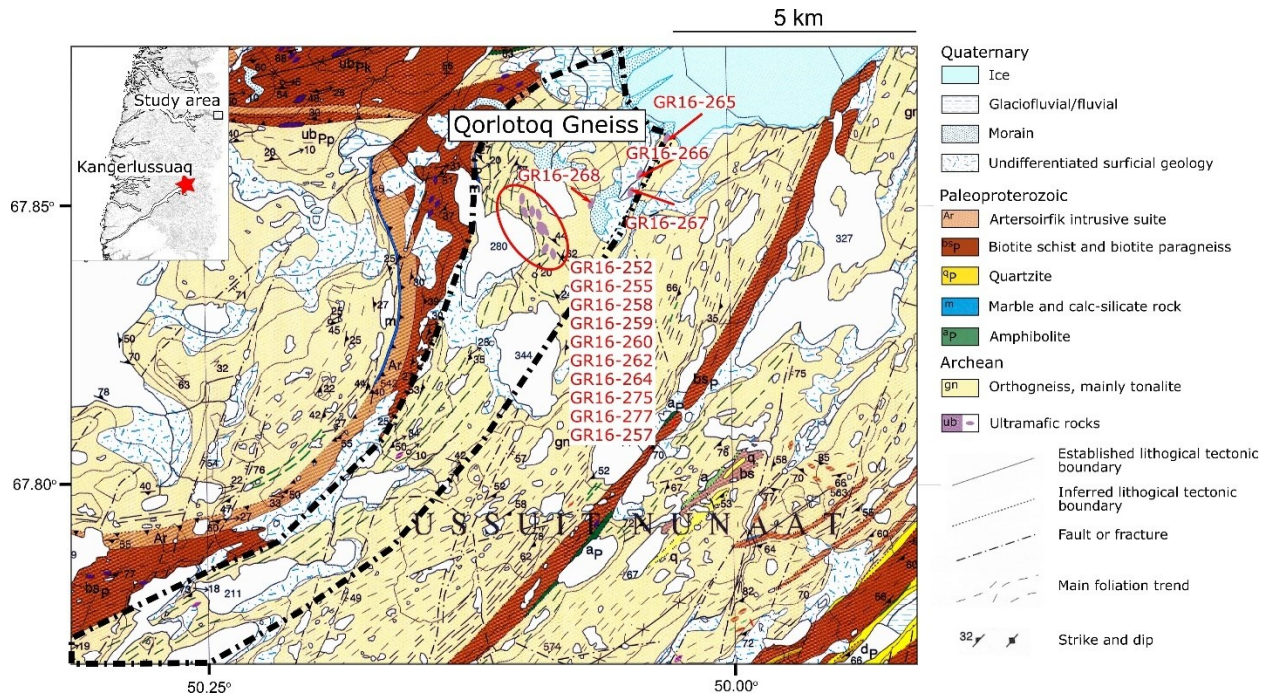
Fig. 2-3. Geological map of the study area for Chapter 2, after van Gool & Marker (2004). The map shows the location of the Qorlortoq gneiss and samples. The stippled outline shows the approximate known extent of the Qorlortoq gneiss (Manatschal et al., 1998).
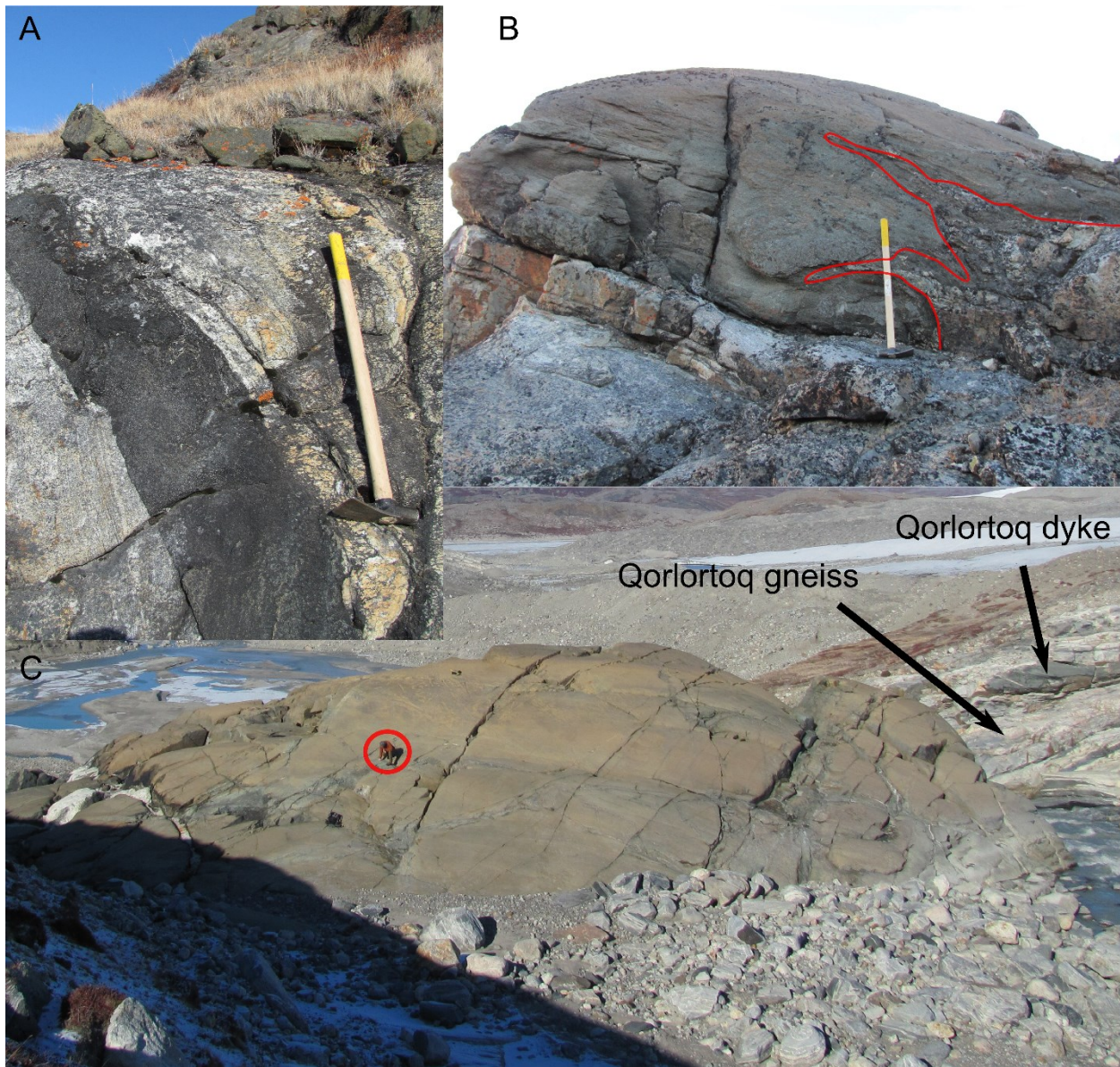
Fig. 2-4. Outcrop photos of the Qorlortoq gneiss, cumulates, and dykes. A) a Qorlortoq dyke shown with sharp contacts with the Qorlortoq gneiss. B) and C) are Qorlortoq cumulate enclaves. In B the red outline denotes the irregular contact with the host gneiss. Red outline in C shows a geologist for scale. The hammer in A and B is 76 cm in length.

Sample GR16-256
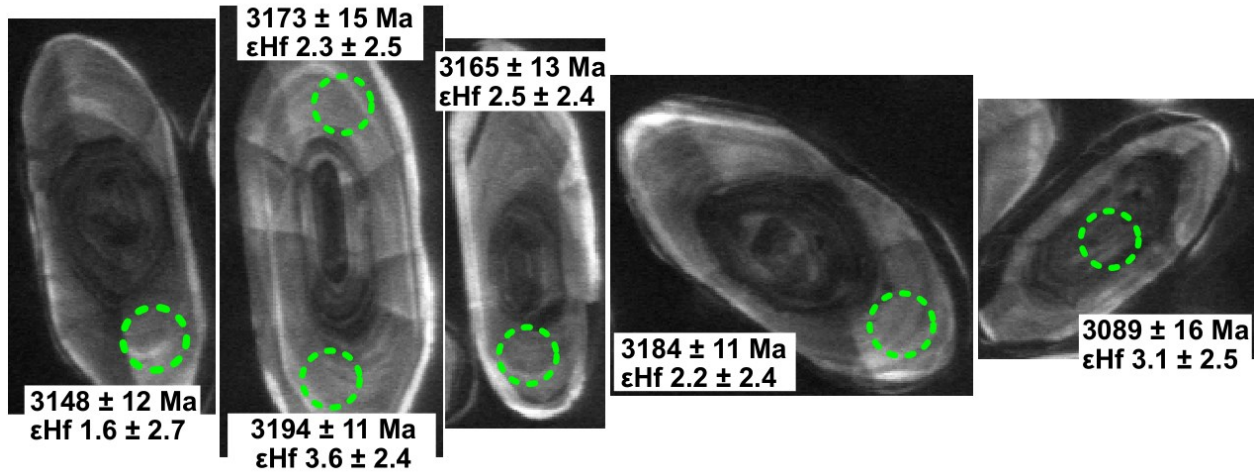
Sample GR16-261
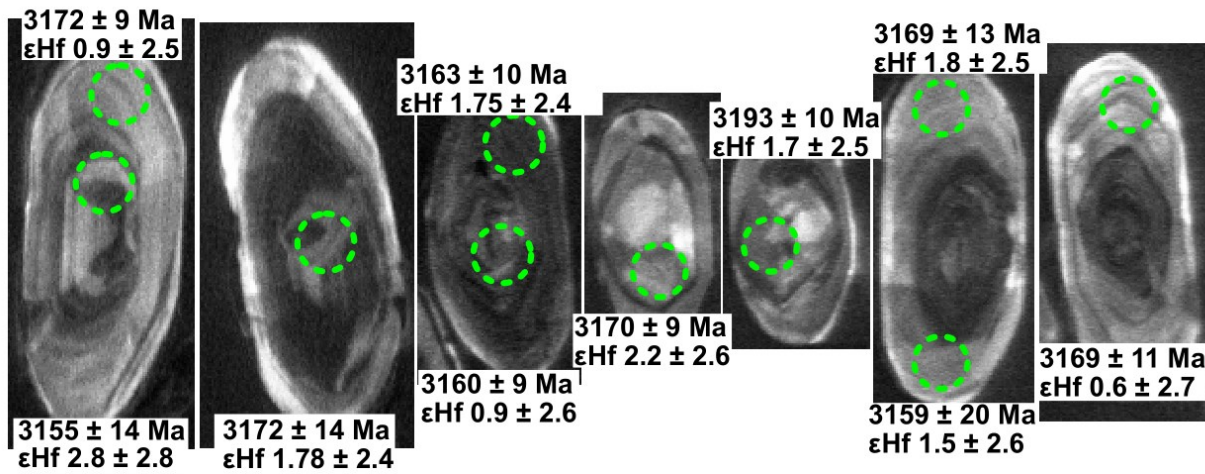
Fig. 2-5. Representative cathodoluminescence images of zircons from the Qorlortoq gneiss showing analysis spots and ^{207}Pb/^{206}Pb ages and εHf values at that age. Spot sizes are 33 μm.
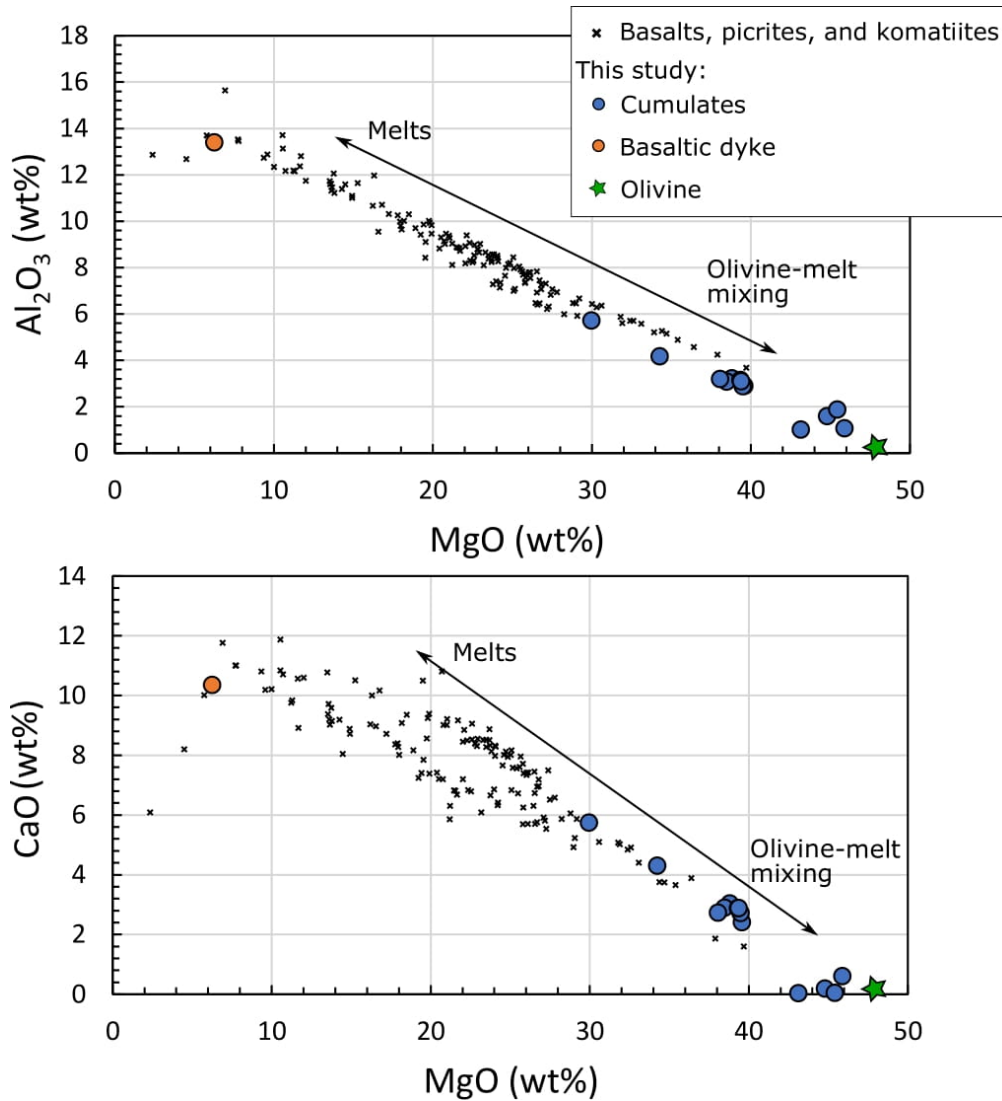
Fig. 2-6. CaO and Al$_2$O$_3$ vs MgO of Qorlortoq cumulates and basalt dyke in this study and basalts, picrites, and komatiites from the literature. The plot shows that the cumulates in this study fall along mixing lines between olivine (48 wt% MgO, 0 wt% Al$_2$O$_3$, and 0.2 wt% CaO) and high MgO melts. Data for basalts, picrites, and komatiites are from Puchtel et al. (2004), Ireland et al. (2009), Pitcher et al. (2009), and Waterton et al. (2020).
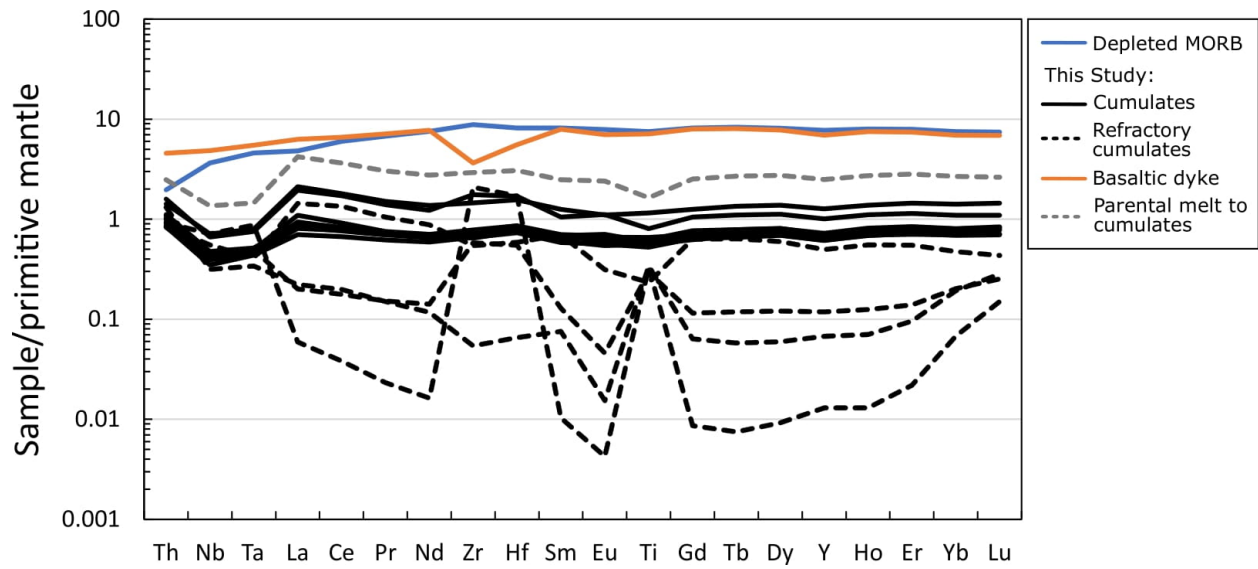
Fig. 2-7. Primitive mantle (PM) normalized plots of the samples in this study and depleted MORB (Gale et al., 2013). The Qorlortoq cumulates and basaltic dykes are not related due to the lower Th/Nb and La/Yb ratios of the dykes despite them being more evolved. The primitive mantle values are from McDonough & Sun (1995).
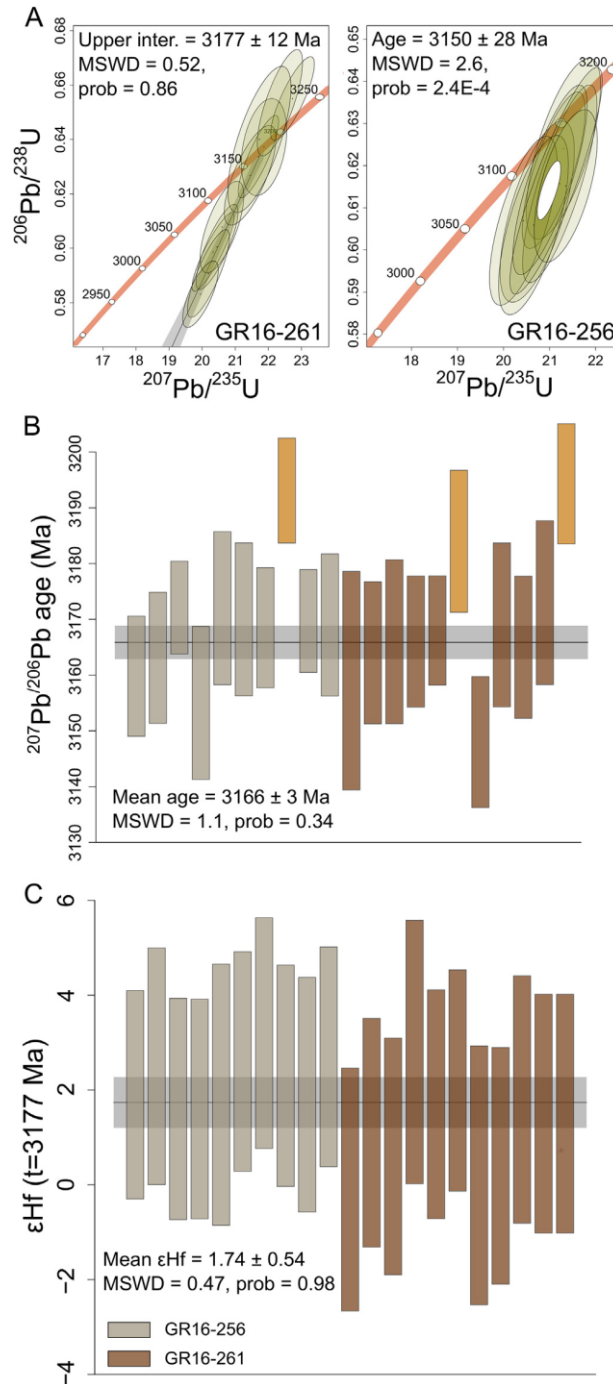
Fig. 2-8. Age and εHf plots for the Qorlortoq gneiss samples from laser ablation split stream U-Pb/Lu-Hf isotopic analyses of zircon. Error ellipses and bars are 2 standard deviations. A) Concordia plots, B) ^{206}Pb/^{207}Pb ages, and C) εHf at 3177 ± 12 Ma. Propagated into the error in εHf are the uncertainty in the age of the sample, ^{176}Lu decay constant (Söderlund et al., 2004), and CHUR composition (Bouvier et al., 2008). Diagrams constructed using IsoplotR (Vermeesch, 2018). MSDW for the concordia plots refer to concordance and equivalence.
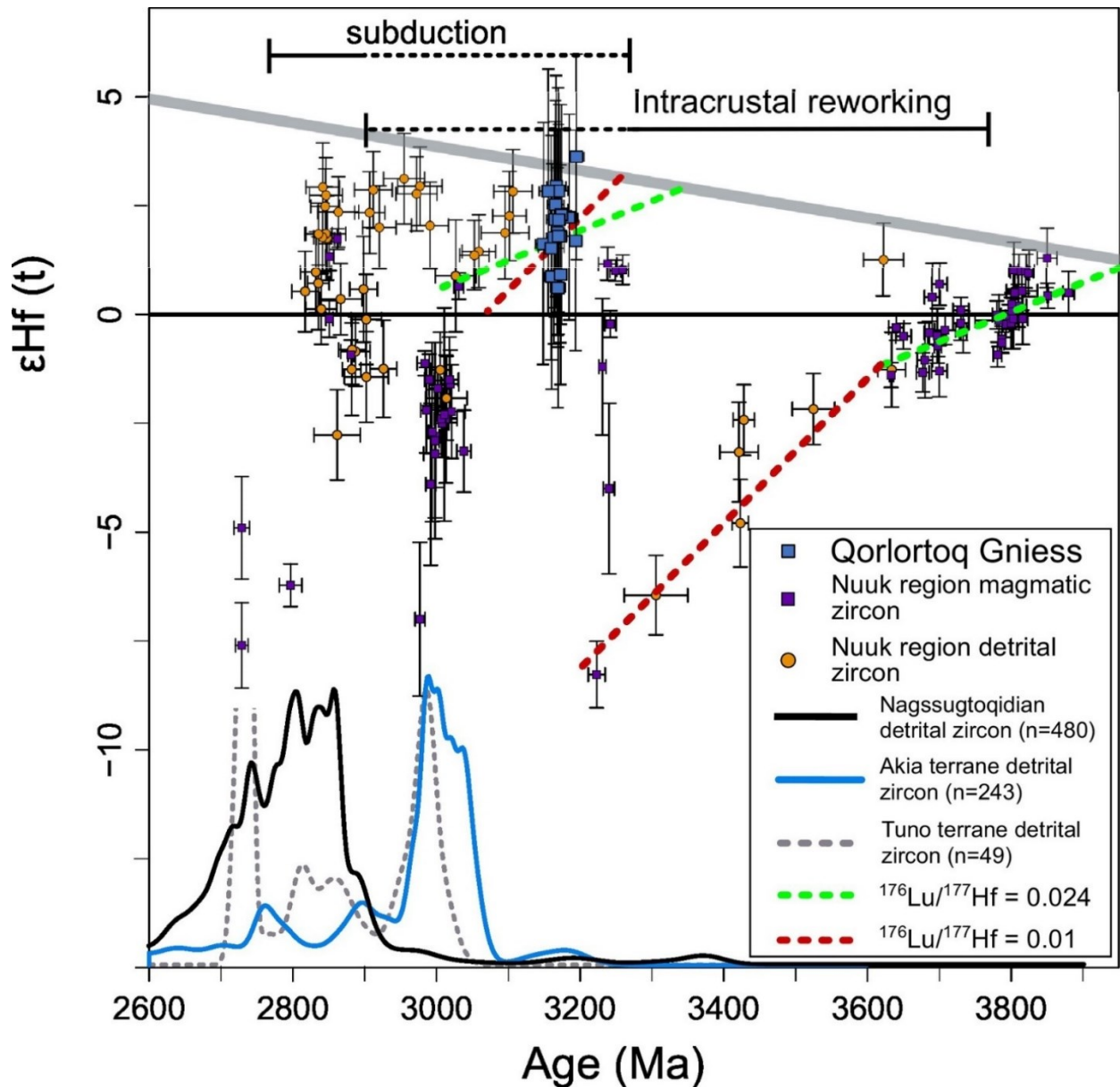
Fig. 2-9. εH vs time for the Qorlortoq gneiss (^{207}Pb/^{206}Pd ages) and rocks and detrital zircon from the Nuuk region (includes large component from the Akia terrane). The depleted mantle curve (grey line) is that of Næraa et al. (2012). Lu-Hf decay constant is from Söderlund et al. (2004) and CHUR value from Bouvier et al. (2008). εH evolution curves for mafic (^{176}Lu/^{177}Hf = 0.024) and continental (^{176}Lu/^{177}Hf = 0.01) crust are also displayed. At the base of the figure, kernel density estimates of ^{207}Pb/^{206}Pb ages of detrital zircon from the Nagssugtoqidian, Akia, and Tuno areas are shown. The kernel density estimates were made using IsoplotR (Vermeesch, 2018). Notice there are no significant population of detrital zircon in the Nagssugtoqidian area that are >2900 Ma. Nagssugtoqidian references from Kalsbeek et al. (1987), Kalsbeek & Nutman (1996),

49

Whitehouse et al. (1998), Nutman et al. (1999), Connelly & Mengel (2000), Connelly et al. (2000), Hollis et al. (2006), and Thrane & Connelly (2006). Nuuk and Akia area references from Garde et al. (2000), Hiess et al. (2009), Amelin et al. (2011), Næraa et al. (2012), Fisher & Vervoort (2018), Kirkland et al. (2018), and Gardiner et al. (2019). Tuno terrane references are from Nutman et al. (2004) and Gardiner et al. (2019). For clarity, only εHf values for detrital zircons of Næraa et al. (2012) are shown.
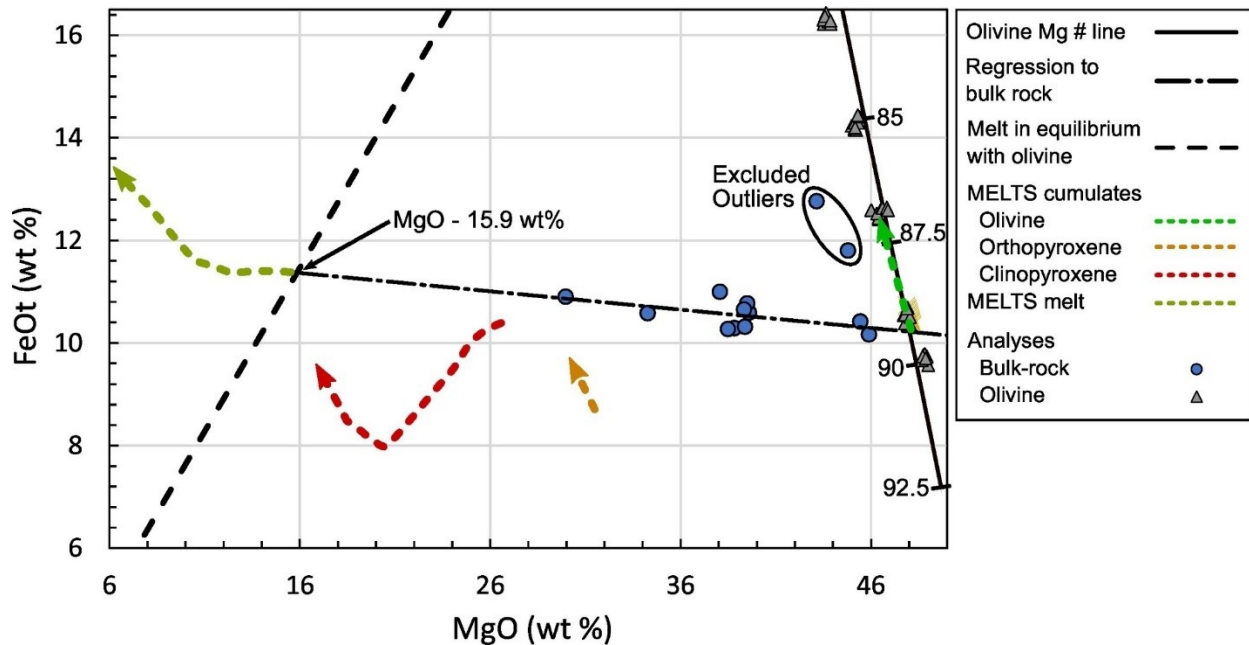
Fig. 2-10. FeO$_t$ vs MgO for bulk-rock and EPMA data, compared to MELTS modelling. The plot shows the intersection of bulk-rock analyses with idealized olivine compositions (olivine Mg # line) giving an initial olivine composition for all samples of 48.2 wt% and FeO concentration of 10.2 wt %. Also shown is the intersection of the bulk-rock analyses with melt in equilibrium with this olivine giving the parental melt composition of the cumulates (15.9 wt% MgO). To calculate the melt in equilibrium with olivine, the FeO-MgO exchange coefficient used for olivine ($K_{d,Fe2+-MgO}$=(FeO/MgO)^{ol}/(FeO/MgO)^L) was from Herzberg & O'hara (2002). Fe^{2+}/ΣFe of the parental melt was estimated from V/Sc ratios of the cumulates (Lee et al., 2005). Extrapolation of V and Sc over any terrestrial range in magmatic MgO content, yields variations of V/Sc ratios of <0.1, and V/Sc of the melt can be confidently taken as 5.3. This approximates an oxygen fugacity of about FMQ-1 (cf. Lee et al., 2005) and Fe^{2+}/ΣFe ratio of 0.9 during mantle melting. The two samples with high FeO$_t$ were excluded from the analysis. In the MELTS model initial oxygen fugacity of the melt was set to FMQ-1 and pressure was constant at 0.2 GPa. The MELTS melt composition is the estimated parental melt to the cumulates in this study.

51
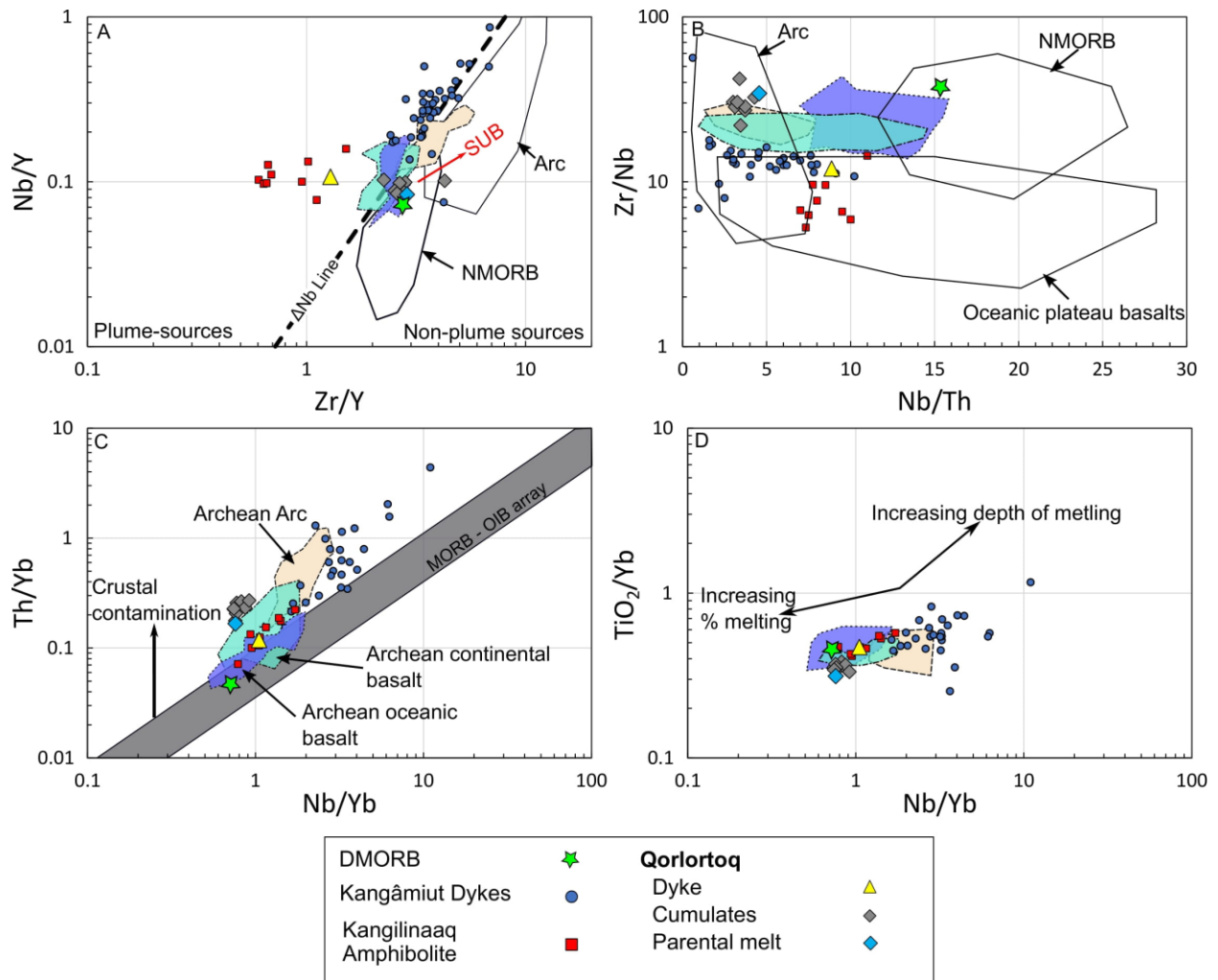
Fig. 2-11. A) and B) are the basalt trace element discrimination diagrams for distinguishing tectonic setting of (Condie, 2005) with their vector for subduction trajectory (SUB) and fields for normal MORB (NMORB), arc basalts, and oceanic plateau basalts. The ΔNb line in A) is from Fitton et al. (1997) separating plume from non-plume sources in Phanerozoic basalts. C) and D) are discrimination diagrams of Pearce (2008), showing their MORB-OIB array in C), with displacement above this array indicative of crustal contamination by assimilation or subduction, and in D) their trajectories of melting of increasing depleted sources and melting at increasing depths. Fields for Archean basalts and komatiites from different tectonic environments are from the literature; Continental setting (Xie et al., 1995; Tomlinson et al., 1999; Green et al., 2000; Cadman et al., 2001; Bolhar et al., 2003; Shimizu et al., 2005; Said et al., 2010), oceanic (Puchtel et al., 1998, 1999; Kerrich & Xie, 2002; Chavagnac, 2004), arc (Puchtel et al., 1999; Polat & Hofmann, 2003; Smithies et al., 2005; Jenner et al., 2009; Szilas et al., 2015). Literature values

52

were highly skewed and filtered for outliers by removing data that were greater or lower than 1.5 times the interquartile range plus or minus the median. Sources for other data are as follows; DMORB (Gale et al., 2013), Kangâmiut dykes (Cadman et al., 2001; Mayborn & Lesher, 2006), and Kangilinaaq amphibolite (Hollis et al., 2006).

Chapter 3

Juvenile lithospheric mantle formed beneath oceanic arcs underpins mobile belts cratonized during Paleoproterozoic supercontinent assembly

T. McIntyre[1], P. Waterton[1,2], L. Li[1], B. Gong[3], X. Zha[3], K. Szilas[2], & D.G. Pearson[1]

[1]Department of Earth & Atmospheric Sciences, University of Alberta, Edmonton, Alberta, Canada

[2]Department of Geosciences and Natural Resource Management, University of Copenhagen, Copenhagen, Denmark

[3]Laboratory of Crust-Mantle Materials and Environments, School of Earth and Space Science, University of Science and Technology of China, Hefei, China

Abstract

While the refractory composition of cratonic lithospheric mantle is understood to reflect significant melt depletion, the variety of early Earth tectonic melting regimes responsible for this depletion remains unclear. Rare mantle tectonites hosted in tectonic mélanges of Paleoproterozoic mobile belts, now composite portions of cratons, may provide complementary information to mantle xenoliths on which most models of cratonic mantle formation are built. Here we present the first mineral, bulk-rock major, trace, and platinum group elements, Re-Os isotopes, and olivine oxygen isotopes of a Paleoproterozoic orogenic peridotite in West Greenland - the Ussuit peridotite. The Ussuit peridotite was emplaced in the crust during the Nagssugtoqidian orogeny, between 1870 Ma and 1775 Ma. The most refractory peridotites have geochemical characteristics reflecting > 30% melting. Some primary signatures suggest melting was facilitated by peridotite interaction with hydrous melts or fluids (e.g. spinel Cr #'s > 65, Os/Ir ratios between 0.3 and 6, and olivine $\delta^{18}O$ values outside the normal mantle range). Together, the high degree of melt depletion and signatures of sub-arc hydrous fluxing suggest the Ussuit peridotite formed in a forearc or sub-arc environment. Re-Os isotopic systematics show the Ussuit peridotite experienced melt depletion at ~2 Ga overlapping the juvenile oceanic arc crust that hosts the peridotites. Furthermore, this age is coincident with the global production of juvenile cratonic lithosphere recorded in the crustal

portions of Paleoproterozoic mobile belts and underlying lithospheric mantle. Global Paleoproterozoic cratonic mantle has strong geochemical similarities with the Ussuit peridotites. Thus, it is suggested that subduction zone peridotites form key components of Paleoproterozoic cratonic lithospheric mantle and indicate that high degrees of melt extraction facilitated by hydrous fluxing played a role in forming the refractory compositions that are in part responsible for the long-term stability of cratons.

3.1 Introduction

Paleoproterozoic mobile belts form thick cratonic keels with highly refractory compositions (Janney et al., 2010; Ionov, et al., 2010; 2015a,b; Liu et al., 2018; Scott et al., 2021; Pearson et al., 2021). Like the Archean nuclei of cratons, the petrogenetic melting environments responsible for the formation Paleoproterozoic cratonic mantle lithosphere in these regions is unclear. The tectonic melting regimes inferred from studies of Paleoproterozoic mantle xenoliths largely revolve around contributions from anhydrous melting at hot mid-ocean ridges vs hydrous melting in sub-arc regions (Janney et al., 2010; Wittig et al., 2010; Ionov, et al., 2010; 2015a,b; Liu et al., 2018). However, mantle xenoliths sample only a small portion of the vast areas comprising these cratonic terranes and other opportunities for direct study of the mantle beneath them are rare.

Tectonically emplaced peridotite bodies provide superb opportunities for studying mantle lithosphere (Menzies, 1990) due to their size. In the Phanerozoic, mantle tectonites are often sub-arc or oceanic mantle lithosphere formed outboard of continental lithosphere (Bodinier & Godard, 2013). If the same is true for Paleoproterozoic mantle tectonites, mantle peridotites in tectonic mélanges of Paleoproterozoic mobile belts may offer a picture of mantle lithosphere formed in early earth melting environments prior to incorporation into cratonic mantle lithosphere and the subsequent metasomatism that affects many cratonic mantle xenoliths (cf. Menzies and

Hawkesworth, 1987). In order to understand better the melting environments that may have contributed to building Paleoproterozoic cratonic mantle we present a geochemical study of the Ussuit peridotite, a Paleoproterozoic orogenic peridotite in West Greenland, (Kalsbeek & Manatschal, 1999). The geochemical systematics of this portion of "proto cratonic mantle" allow us to clearly constrain that melt depletion occurred in a hydrous environment, highlighting the key importance of depleted arc mantle in building the lithosphere beneath the Paleoproterozoic terranes of some cratons.

3.2 The Ussuit peridotites - their geological and tectonic context

The Nagssugtoqidian Orogen (NO) of West Greenland is a deeply eroded orogenic belt recording a complex history of continental collision that occurred between ~1870 and 1775 Ma, resulting in the amalgamation of Archean continental blocks and Paleoproterozoic calc-alkaline plutonic suites and supracrustal assemblages (Kalsbeek et al., 1987; Kalsbeek & Nutman, 1996; Manatschal et al., 1998; Whitehouse et al., 1998; Nutman et al., 1999; Connelly et al., 2000; Connelly & Mengel, 2000; van Gool et al., 2002; Connelly et al., 2006; Thrane & Connelly, 2006; St-Onge et al., 2009; Garde & Hollis, 2020; McIntyre et al., 2021). Though most studies of the NO have focused on the felsic rocks, here we focus on the Ussuit peridotites hosted within Paleoproterozoic supracrustal rocks of the Ussuit Unit in the central Nagssugtoqidian orogen (CNO; Fig. 3-1).

The Ussuit unit is divided into an upper and lower sequence separated by a tectonic contact (Fig. 3-2 A; Manatschal et al., 1998; Kalsbeek & Manatschal, 1999). The lower sequence is 10s to a few 100 m thick comprising siliciclastic metasedimentary gneisses with minor metavolcanic rocks, carbonates, and the peridotites of this study (Manatschal et al., 1998; Kalsbeek & Manatschal, 1999). The upper sequence is >1000 m thick, consisting of the Arfersiorfik quartz diorite (AQD) suite which intrudes into and is overlain by siliciclastic metasedimentary gneisses with minor

metavolcanic rocks (Manatschal et al., 1998; Kalsbeek & Manatschal, 1999; Nutman et al., 1999). Based on similar detrital zircon geochronology in the siliciclastic sediments, the supracrustal rocks from the upper and lower sequence are grouped together as the Nordre Strømfjord supracrustal suite (Nutman et al., 1999). The depositional age of the supracrustal suite is dated to between 1950 and 1920 Ma, and the detrital zircons record a major age population at ~2050 Ma, a minor age population at ~2125 Ma, and very few Archean zircons (Nutman et al., 1999). The 2050 Ma and 2125 Ma detrital zircon populations do not correlate with any known proximal crustal lithology and are derived from an unrecognized or missing crustal fragment in the NO (Nutman et al., 1999). The AQD suite is dated to between 1920 and 1870 Ma, its Sm-Nd isotopic systematics show limited to no contamination by Archean crust (Whitehouse et al., 1998), and its geochemical characteristics are calc-alkaline in nature (Kalsbeek et al., 1987). Based on the limited Archean detrital zircon in the Nordre Strømfjord supracrustal suite and chondritic Sm-Nd isotopic systematics of the AQD, the Ussuit unit is interpreted to be a juvenile Paleoproterozoic oceanic arc accreted to the North Atlantic Craton shortly before or during the Nagssugtoqidian orogeny (Nutman et al., 1999; van Gool et al., 2002).

Peridotites within the lower sequence of the Ussuit unit – the Ussuit peridotite bodies of this study – have been argued to be refractory mantle peridotites and interpreted to be a dismembered ophiolite (Kalsbeek & Manatschal, 1999).

3.2.1 Peridotite samples – Field relationships and Petrography

One location of outcropping peridotite of the Ussuit unit lower sequence (Manatschal et al., 1998; Kalsbeek & Manatschal, 1999) was sampled in this study (Fig. 3-2 B). Peridotites in this area outcrop as low-lying mounds up to 50 m in diameter that likely make up portions of larger peridotites bodies up to 800 m in width. These larger sections of peridotite are hosted in marine

carbonates, siliciclastic metasediments, and metavolcanic rocks of the Nordre Strømfjord supracrustal suite.

At the west and north side of the larger peridotite body (Fig. 3-2 B) peridotites are relatively pristine dunite and harzburgites but cut by serpentine veins in areas (Fig. B3-1 A). Where sections are exposed on the east side of the main ultramafic body (Fig. 3-2 B), meter-scale blocks of pristine peridotite (Fig. B3-1 B and C) are separated by a sharp contact from sheared porphyroclastic peridotite or orthopyroxenite (Fig. B3-1 C and D) that is gradational in some areas to amphibole pyroxenite. The porphyroclastic peridotite and orthopyroxenite are characterized by a weathered foliation consisting of platy fine-grained green amphibole anastomosing around ~0.5 to 3 cm orthopyroxene porphyroclasts. Even in the pristine blocks the strain effects are manifest as a lineation of spinel grains. In thin section, the high strain is recorded as sub-grain development on the grain margins of olivine in coarse dunites (olivine up to 15 mm) and porphyroclastic harzburgites and sometimes by the complete recrystallization of dunite to a fine-grained granoblastic texture (olivine neoblasts typically <1 mm exhibiting polygonal grain boundaries). Similar strain characteristics are found in the Pyrenean orogenic ultramafic bodies (Fabries et al., 1991), the Beni Bousera massif (Pearson, 1989; Frets et al., 2014), Ronda massif (Van Der Wal & Bodinier, 1996), and the peridotites of the Josephine ophiolite (Kelemen & Dick, 1995). In addition to the effects of strain, throughout the peridotites there are locally pervasive 5 to 10 cm veins of amphibole orthopyroxenite.

The peridotites studied here include dunites and harzburgites showing minimal strain effects and sampled away from areas of intrusive melts (Fig. 3-2 B; Table 3-1).

3.3 Methods

3.3.1 Mineral chemistry, bulk-rock major, trace, and platinum group element chemistry, and Re-Os isotopes.

Procedural and analytical methods for determining the mineral chemistry, bulk-rock major, trace, and platinum group element chemistry, and Re-Os isotopes of the Ussuit peridotites are only briefly summarized here, as these data were produced together with those of ultramafic cumulates in the same analytical campaign in which previously published methods and quality control data were presented and discussed in detail (McIntyre et al., 2021). Some relevant reference material data, run as quality controls, are summarized below.

The mineral chemistry of the Ussuit peridotites was determined by electron microprobe analysis at the Electron Microprobe Laboratory, University of Alberta, Canada using wave-length dispersive methods. Standards and further analytical details are given in Appendix C. Sample results are given in Appendix C and some key compositional feature in Table 2-1.

Bulk-rock major and minor element concentrations were determined by X-ray fluorescence at Franklin Marshall College, US. Results are given in Appendix C. For ultramafic reference material MUH-1 most elements had relative standard deviations of <7 % and measured concentrations within 7% of the reference values (Appendix C). However, concentrations of K_2O and Na_2O were shown to be unreproducible due to the low concentrations of these elements in the reference material (Appendix C). As the measured concentration of these elements in the ultramafic rocks of this study were similarly low, K_2O and Na_2O are not reported. Long-term reproducibility for ultramafic reference materials analysed by this method are extensively documented in Waterton et al. (2020).

Trace elements were measured by inductively coupled plasma mass spectrometry at the Arctic Resources Laboratory (ARL), University of Alberta, Canada using a Nu Plasma Attom instrument. Results are given in Appendix C. All reference material data (OKUM, MUH-1, BCR-2) reported here are within 10 % of the reference values or otherwise within their estimated uncertainty (Appendix C). The exception is Hf which was measured to within 8 % of the reference values in OKUM and BCR-2 where both have Hf > 0.5 ppm, but about 40 % lower than the accepted value in MUH-1 in which Hf < 0.5 ppm. Thus, no Hf data are reported where it was measured as < 0.5 ppm. Results for reference material and unknowns are given in Appendix C, respectively.

Re-Os isotopes and platinum group elements (PGE) were measured by isotope dilution at the ARL following the method outlined in Pearson & Woodland (2000), except that solutions were run on a Nu Plasma Attom ICPMS instrument with peltier-cooled spray chamber. Results are given in Table 3-2 for unknowns, whereas reference material data can be found in Appendix C. Six repeat analyses of OKUM were performed to monitor accuracy and precision. Most measurements fall within uncertainty of the literature compilation values for OKUM (GeoReM; Jochum et al., 2005) and the long term average values for the ARL (n=56; Appendix C). The exception is one analysis of Ru where there is a significant deviation from the spike-natural isotope mixing line in $^{101}Ru/^{99}Ru$ vs $^{100}Ru/^{99}Ru$ space as discussed by McIntyre et al. (2021). For this reason, we report no data where unknowns do not plot on this mixing line.

3.3.2 Oxygen isotope compositions of olivine

Oxygen isotope compositions of handpicked olivine grains were measured via laser fluorination and dual-inlet isotope ratio mass spectrometry at the University of Science and Technology of China following the method of Sharp (1990). Olivine separates were placed in a Ni sample block under vacuum and pre-fluorinated at room temperature to remove surface adsorbed H_2O. A 25 W

MIR-10 CO_2 laser was used to heat the olivine grains in a BrF_5 atmosphere to release O_2. The liberated O_2 was transferred directly to a Finnegan Delta XP mass spectrometer for measurement of $^{18}O/^{16}O$ ratios. The results are given in ‰ expressed as $\delta^{18}O$ in relation to Vienna Standard Mean Ocean Water (Table 3-1). To monitor quality control, oxygen isotope compositions were measured in zircon 91500, garnet UWG-2, and an internal garnet standard 04BXL07 (Gong et al., 2007) alongside the olivine of the Ussuit peridotite.

3.4 Results

3.4.1 Mineral and bulk-rock geochemical characteristics

The petrographic and geochemical characteristics of the Ussuit peridotites can be subdivided into two categories – low Al-Ca peridotites and, for reasons described in the discussion, metasomatized peridotites. The key properties of these groups are summarized in Table 3-1 and briefly described below.

Low Al-Ca peridotites are dunitic to harzburgitic (Table 3-1). Their major element compositions reveal a similarly refractory nature in nearly all aspects; the rocks have highly forsteritic olivine (Mg # from 92.2 to 93.0; Fig. 3-3 A and B), Cr-rich spinel (Cr # from 58.6 to 90.4; Fig. 3-3 B and C), low bulk-rock Al_2O_3 (<0.43 wt%; Fig. 3-3 D) and CaO (<0.27 wt%), high bulk-rock Mg # (92.0 to 93.0), form U-shaped primitive mantle normalized REE patterns (Fig. 3-4), and are depleted in Pt and Pd relative to Os and Ir (Fig. 3-5).

Although also refractory in nature, metasomatized peridotites are distinguished from low Al-Ca peridotites by a variable enrichment in FeO and some incompatible elements. They are all harzburgites and have olivine Mg # between 90.8 and 91.9 (Fig. 3-3 A and B; excluding certain olivine Mg # >94 discussed in Section 3.5.6). Spinel core Cr # ranges from 49 to 91(Fig. 3-3 B and C) but rims are Al-rich with Cr # down to 28 (Fig. B3-2). Relative to low Al-Ca peridotites,

these peridotites are selectively enriched in SiO_2, FeO, Al_2O_3, (Figs 3-3 B and D and B3-3). For instance, the metasomatized peridotites have higher average orthopyroxene contents (Table 3-1; Fig. B3-3), olivine Mg # are systematically lower, and bulk-rock Al_2O_3 is highly variable (0.51 to 5.39 wt %; Fig. 3-3 D) but at uniformly low CaO contents (<0.89 wt%). Primitive mantle normalized REE patterns are highly variable, but HREE depleted (Yb between 0.006 and 0.06 ppm) and form U-shaped primitive mantle normalized patterns characterized by middle REE depleted to flat patterns (Fig. 3-4). Metasomatized peridotites are depleted in Pt and Pd relative to Os and Ir (Fig. 3-5), yet their Pd contents are systematically higher than those of the low Al-Ca group. Other notable enrichments are seen in bulk rock Hf and Zr (Fig. B3-4).

3.4.2 Re-Os isotopic characteristics

Combined low Al-Ca and metasomatized peridotites have bulk-rock $^{187}Os/^{188}Os$ ratios between 0.1127 and 0.1161 and $^{187}Re/^{188}Os$ ratios typically <0.029 (Table 3-2). Relative to Phanerozoic abyssal peridotites that reflect present day upper convective upper mantle isotopic compositions and have heterogeneous $^{187}Os/^{188}Os$ ratios ranging between 0.114 and 0.1587 (Brandon et al., 2000; Harvey et al., 2006; Lassiter et al., 2014; Day et al., 2017), the low Al-Ca and metasomatized Ussuit peridotites have an extremely narrow range in Os isotopic compositions.

3.4.3 Oxygen isotopic characteristics

In the low Al-Ca peridotites, olivine $\delta^{18}O$ values range between 5.45 and 6.21 ‰, whereas in the metasomatized peridotites they range between 4.44 and 6.17 ‰ (Table 3-1). This range in olivine $\delta^{18}O$ values is significantly outside the range of typical mantle olivine (Fig. 3-6 A). There is no correlation between olivine $\delta^{18}O$ values and loss on ignition which is < 2.1 wt% in these peridotites. However, olivine $\delta^{18}O$ values form a broad negative correlation with bulk-rock Ti contents (Fig. 3-6 B).

3.5 Discussion

3.5.1 Evidence for a mantle origin for the Ussuit peridotites

Crustally-hosted peridotites are found throughout West Greenland typically as enclaves and lenses within orthogneiss or ancient supracrustal belts (Dymek et al., 1988; Nutman et al., 1996; Bennett et al., 2002; Friend et al., 2002; Rollinson, 2002, 2007; Friend & Nutman, 2011; Szilas et al., 2015, 2017; McIntyre et al., 2019, 2021). In the Nuuk region, such peridotites were initially suggested to be mantle peridotite (Nutman et al., 1996; Bennett et al., 2002; Friend et al., 2002; Friend & Nutman, 2011; van de Löcht et al., 2018) but a progressive understanding of the geochemistry of olivine-rich cumulates led to the realization that many compositional discrimination schemes used to differentiate mantle and cumulate peridotites were in fact ineffective for this purpose (Szilas et al., 2015; McIntyre et al., 2019; Waterton et al., 2022). This led to debate and uncertainty regarding the petrogenesis of these rocks. Using a broader geochemical suite of discrimination tools and leaning on a growing database of olivine-rich cumulates, most peridotite bodies in the Nuuk region were later shown to be cumulates (Szilas et al., 2015; McIntyre et al., 2019; Waterton et al., 2022). To avoid the confusion and debate which surrounded the origin of peridotites in areas like the Nuuk region, we evaluate the origin of the Ussuit peridotite as either being derived from melting or crystal accumulation with an updated understanding of the geochemical characteristics that can be used to differentiate ancient cumulate and mantle peridotites.

The most refractory cumulate peridotites in West Greenland contain a few characteristics like that of similarly refractory mantle peridotites, e.g., bulk-rock Mg # > 88, Al_2O_3 < 1 wt%, or even depletions in Pt and Pd relative to Ir (Dymek et al., 1988; Szilas et al., 2015, 2017; McIntyre et al., 2019, 2021; Waterton et al., 2022). However, most cumulates do not show the consistently refractory geochemical characteristics that are often found in residues from high degrees of melt

depletion (McIntyre et al., 2019; Waterton et al., 2022). For example, cumulate dunites with high bulk-rock Mg # of >88 might be accompanied by primitive mantle normalized REE trends that are flat or have Ir/Pd ratios <1, characteristics that are inconsistent with the high degrees of melt depletion required to produce harzburgite or dunite compositions (Szilas et al., 2015; McIntyre et al., 2021; Waterton et al., 2022). In addition, cumulate rocks tend to have higher or more variable Ni than mantle rocks at a given measure of refractory character (Fig. 3-7). For example, highly fractionated HREEs characterized by high Lu/Yb ratios is a characteristic of highly melt depleted peridotitic mantle resulting from the increasing compatibility of REEs from Dy to Yb (Fig. 3-4). However, such REE fractionation is also found in highly refractory cumulate dunites (e.g. Szilas et al., 2017), but in these instances such rocks are also characterized by Ni contents typically >2700 ppm clearly differentiating them from mantle rocks (Fig. 3-7). As such, mantle rocks may be differentiated from cumulate rocks by a consistently high degree of depletion in all aspects, other than perhaps the most incompatible elements prone to metasomatic enrichment, e.g., LREEs and large ion lithophile elements, or where highly refractory characteristics exist in cumulates may be differentiated from melt residues by their high Ni contents (Fig. 3-7).

3.5.1.1 The Ussuit low Al-Ca peridotites as highly depleted residues from shallow (<5 GPa) melting

In contrast to Precambrian West Greenland cumulate peridotites, the low Al-Ca Ussuit peridotites are highly refractory in all characteristics and plot along modelled melt depletion trends at consistently high degrees of depletion (Figs. 3-3 to 3-5, 3-7, B3-3, and B3-4). Lu/Yb ratios are typically outside of the cumulate fields when plotted against Ni (Fig. 3-7 A). Furthermore, the concentration of some incompatible elements, e.g., Ti and Yb, are much more depleted than any cumulates in West Greenland (Fig. 3-7 B and C). Regarding Ti, igneous olivine typically has Ti

64

contents >70 ppm (Foley et al., 2013). Thus, cumulate dunite and harzburgite cannot have the very low Ti contents exhibited in the low Al-Ca peridotites, i.e., between 4 and 36 ppm, and this is reflected in refractory West Greenland cumulate peridotites that have Ti contents typically >70 ppm (Fig. 3-7 B). In contrast, mantle olivine can reach sub-ppm levels of Ti (Barrett et al., in press) and is thus more likely to comprise the low Al-Ca Ussuit peridotites. The very depleted compositions of the low Al-Ca Ussuit peridotites that are consistent in nearly all aspects, in combination with Ni contents between ~2000 and 3000 ppm and Ti contents <40 ppm, are only found in mantle peridotites (Fig. 3-3 to 3-5 and 3-7), clearly marking them as having been derived from partial melting.

When compared against the products of experimental peridotite melting (Table 3-3) and modelling (Arai, 1994; Pearce et al., 2000; Kubo, 2002; Bernstein et al., 2007; Wittig et al., 2008; Aulbach et al., 2016; Figs. 3-3, 3-4, and 3-7), the refractory characteristics of the low Al-Ca Ussuit peridotites reflect melting of fertile peridotite to > 30 % , or alternatively, they are two-stage melt depletion products whose sum effect is equivalent to this very high melt fraction removal.

This depleted nature is unlike Phanerozoic abyssal peridotites – samples of modern oceanic lithosphere which show much less refractory compositions (Dick et al., 1984; Niu, 2004; Warren, 2016; Figs. 3-3 and 3-4). Instead, the low Al-Ca peridotites are most similar to cratonic mantle lithosphere in West Greenland (Bernstein et al., 1998, 2006; Wittig et al., 2008; Figs. 3-3, 3-4, and 3-5), Paleoproterozoic cratonic mantle (Chesley et al., 1999; Pearson et al. 2004; Luguet et al., 2009; Janney et al., 2010; Ionov et al., 2015a,b; Liu et al., 2018; Fig. 3-3), and Phanerozoic forearc peridotites (Ishii et al., 1992; Parkinson & Pearce, 1998; Ulrich et al., 2010; Uysal et al., 2012; Scott et al., 2019; Figs. 3-3, 3-4, 3-5, and 3-7). The Ussuit peridotites are particularly similar, in their major element and mineral chemistry, to the Iwanaidake forearc peridotites, Japan, and

peridotites from the Papua New Guinea ophiolite (Kubo, 2002; Barrett et al., in press; Fig. 3-3 A and C).

The Ussuit low Al-Ca peridotites have very depleted HREE contents, with MREE/HREE fractionations and Al-HREE systematics similar to those observed in residues of melting in relatively low-pressure environments, where melt extraction takes place predominantly in the spinel stability field (e.g., Kelemen et al., 1998; Stachel et al., 1998; Figs. 3-3, 3-4, and 3-7), as is clearly the case for the forearc peridotites described above and as has been suggested for Paleoproterozoic peridotites (e.g., Janney et al., 2010; Ionov et al., 2015a,b; Liu et al., 2018). As such, the Ussuit low Al-Ca peridotites are shallow melt products whose refractory compositions may have been derived from hydrous melting in a forearc environment or the less well understood melting environment responsible for generating CLM.

3.5.1.2 The Ussuit metasomatized peridotites as refertilized highly depleted mantle

The origin of the Ussuit peridotites, that are characterized as enriched in some elements relative to the low Al-Ca peridotites, are more complex because these do not consistently exhibit refractory compositions. The high spinel Cr # of > ~70 found in most of the Ussuit metasomatized peridotites (Fig. 3-3 B and C), in experimental and natural samples are shown to record melt depletion of ~40% (Arai, 1994; Hirose & Kawamoto, 1995; Pearce et al., 2000; Bernstein et al., 2007; Condamine & Médard, 2014; Mitchell & Grove, 2015; Scott et al., 2019) and combined with low spinel TiO_2 contents clearly plot in fields defined by highly refractory mantle peridotites (Fig. 3-3 C). This is unlikely to be the result of secondary alteration because, as discussed below, Ti has been added to these peridotites. In addition, in West Greenland crustally hosted peridotites there is a positive correlation between spinel Cr # and spinel TiO_2 with spinel $Fe^{3+}/\Sigma Fe$ (Fig. 3B-5), which is an index of crustal alteration (Szilas et al., 2015; McIntyre et al., 2019). All Ussuit

peridotites clearly plot outside of this trend and in the fields of mantle peridotites (Fig. 3B-5). Similar to spinel chemistry, some of Ussuit metasomatized peridotite have very low bulk rock Al (Al_2O_3 as low as 0.51 wt%) and severely MREE depleted REE patterns that are similar to those of the low Al-Ca peridotites (Figs. 3-3 D and 3-4).

Despite these refractory characteristics, all of the metasomatized peridotites are more enriched in Fe than can be accounted for by the high degrees of depletion recorded in spinel Cr # or the low bulk-rock Al_2O_3 and MREE concentrations exhibited by some of the samples (Figs. 3-3 A and B and Fig. 3-4). Similarly, some of the samples display additional enrichment in Ti and Yb, which are not characteristic of high degrees of melt depletion (Fig. 3-7 B and C). These characteristics are inconsistent with an origin solely attributed to melt depletion. However, many of these samples have geochemical characteristics that clearly separate them from cumulate peridotites in West Greenland (Fig. 3-7).

As an alternative to crystal accumulation, the selective enrichment in some elements could be the result of the interaction with fluids or melts. Bulk-rock enrichment in Fe is recorded in some orogenic peridotites as being the result of interaction with basaltic melts (e.g. Ackerman et al., 2009; Bodinier & Godard, 2014). In the Ussuit metasomatized peridotites, such a process may be responsible for the displacement of olivine Mg # to lower values when plotted against Cr #, i.e., bulk-rock Fe enrichment plus sub-solidus mineral re-equilibration strongly affecting olivine (Fig. 3-3 B). In addition, the estimated modal proportion of orthopyroxene is significantly higher in the metasomatized peridotites relative to the low Al-Ca peridotites, averaging 0.33 vs 0.13, which could signify secondary melt- or fluid- fluid rock reactions (e.g. Wang et al., 2016; Varas-Reus et al., 2016; Nishio et a., in press; Fig. B3-3). Such a process combined with the retention of small amounts of residual metasomatic melts (1-5%) could be responsible for most of the variation in Ti

that causes these samples to have apparent low degrees of depletion or that places a few of the samples in the field of cumulates when plotted against Ni (Fig. 3-7). Similarly, the addition of < 1 to 3 % basaltic melts (Fig. 3-7 A and C) or ~1 to 6 % partial melts of basalts or sediments (Rapp et al., 1999; Hermann & Rubatto, 2009), the lithologies which host the Ussuit peridotites, could be responsible for the entire range of Lu/Yb and Yb concentrations that are inconsistent with the high degrees of depletion in these samples suggested by other mineral and bulk-rock elemental systematics (Figs. 3-3 C, 3-4, and Fig. 3-7). Finally, the metasomatized peridotites consistently plot in the field of mantle rather than cumulate peridotites (Fig. 3-7 and B3-5). That these peridotites have some highly refractory characteristics suggesting partial melting to > 30 %, that the more enriched characteristics can be shown to reflect secondary metasomatic processes, and that the peridotites consistently plot in the field of mantle peridotite, we interpret these peridotites as the products of metasomatism in peridotites that were as depleted as the Ussuit low Al-Ca peridotites.

3.5.1.3 The Ussuit peridotite as an orogenic peridotite

Given the above constraints, we agree with the initial proposal by Kalsbeek & Manatschal (1999) that the composition of the most refractory Ussuit peridotites are best explained by melt depletion rather than a crystal accumulation origin. That the metasomatized peridotites are likely products of melt- or fluid- rock interactions with more depleted mantle protoliths, the Ussuit peridotite as whole is not unlike Phanerozoic orogenic peridotites, i.e., such peridotites show a significant range of lithologies from highly to only moderately refractory, with the least refractory samples being the result of secondary melt-rock reactions (e.g. Le Roux et al., 2007; Varas-Reus et al., 2016).

Originally, Kalsbeek & Manatschal (1999) suggested these peridotites are a dismembered ophiolite. Because there are no other ophiolitic components associated with the peridotites other than mantle tectonite, we refer to these as orogenic peridotites and classify them as an intermediate pressure massif (terminology of Bodinier & Godard, 2014).

3.5.2 Hydrous vs anhydrous melting – the significance of the Ussuit peridotite as a shallow Precambrian melt residue

There remains uncertainty in the contribution of anhydrous vs hydrous melting to the petrogenesis of Paleoproterozoic and older cratonic mantle (Pearson et al., 2021). Understanding the extent to which such processes were responsible for generating the refractory compositions of this mantle domain is critical for understanding the formation and evolution of cratons. In part, this uncertainty is due to the secular cooling of the earth which has inherently changed the way in which the mantle lithosphere formed through time (Herzberg et al., 2010; Herzberg & Rudnick, 2012; Pearson et al., 2021). The average composition of Paleoproterozoic and older peridotites is more refractory than Phanerozoic peridotites (Pearson et al., 2021), which only reach the more refractory compositions of the former when a hydrous component is available to enhance melting, i.e., secondary melting in a forearc or sub-arc environment (e.g. Ishii et al., 1992; Parkinson & Pearce, 1998; Kubo, 2002; Ulrich et al., 2010; Uysal et al., 2012; Scott et al., 2019). In the Paleoproterozoic and Archean, a hotter younger earth may have given rise to the refractory compositions that comprise cratonic lithospheric mantle (CLM) at mid-ocean ridges and without the aid of subduction zones (e.g. Bernstein et al., 1998; Herzberg & Rudnick, 2012; Lee & Chin, 2014; Pearson & Wittig, 2014). As such, no natural analogues of hydrous vs anhydrous melting from the early Earth exist with which to make comparisons.

Because the Ussuit peridotites are similar to shallow (<5 GPa) Precambrian melt residues and products of hydrous melting in the Phanerozoic, constraining whether their melting environment was anyhydrous (e.g. a ridge / rifting environment) or hydrous (e.g. an arc environment), is an important step in understanding the petrogenetic melting environments of Paleoproterozoic cratonic mantle lithosphere. Below we examine this issue, considering constraints from potential melt-rock reaction effects and the Re-Os geochronology of the Ussuit peridotite.

3.5.2.1 *Cryptic signatures of melting environment recorded in the primary melting characteristics of the Ussuit peridotite*

Considering a Paleoproterozoic mid-ocean ridge environment, our modelling using pMELTS (Ghiorso et al., 2002; Smith & Asimow, 2005; Fig. 3-3) and other approaches (Iwamori et al., 1995; Herzberg, 2004; Wittig et al., 2008), the polybaric fractional melting of asthenospheric mantle by upwelling along a mantle adiabat with a mantle potential temperature of ~1550 ºC, considered likely in early Proterozoic times (Herzberg et al., 2010), will initiate at ~3.5 to 4.5 GPa and result in ~30 to 40% total melting at the base of the crust depending on crustal thickness and the shape of the melting regime (Fig. B3-6). The geochemical characteristics of the low Al-Ca Ussuit peridotites that are consistent with anhydrous melting in this environment include olivine Mg #'s between 92 and 93 and bulk-rock Al_2O_3 < 0.5 wt% (Table 3-3).

Other characteristics of the Ussuit low Al-Ca peridotites lean more in support of a hydrous flux melting regime rather than anhydrous melting at a ridge. For example, the combination of olivine Mg # >92 and spinel Cr # >60 has only been reported in hydrous flux melted peridotites from experimental (e.g. Hirose & Kawamoto, 1995; Condamine & Médard, 2014; Mitchell & Grove, 2015) and natural settings (e.g. Pearce et al., 2000; Ulrich et al., 2010; Uysal et al., 2012; Scott et al., 2019; Barrett et al., 2022). No anhydrous peridotite melting studies have reported spinel

compositions at >30 % melting (e.g. Baker & Stopler, 1994; Walter, 1998; Falloon et al., 1999, 2001, 2008; Pickering-Witter & Johnston, 1999). An additional line of evidence supporting a hydrous flux melting origin for the most depleted Ussuit peridotites is the Al_2O_3 content of orthopyroxene, which is uniformly low in the low Al-Ca Ussuit peridotite, i.e., between 0.4 and 0.7 wt%, whereas that from anhydrous melting experiments is >3 wt% for melting of fertile peridotite (Table 3-3). In contrast, Al_2O_3 in orthopyroxenite from hydrous melting experiments reaches as low as 0.9 wt% and slightly lower (0.7 wt%) in 2-stage hydrous melting experiments (Table 3-3). To summarize, several lines of evidence suggest a hydrous flux melt origin to explain the characteristics of the most depleted Ussuit peridotites, consistent with additional evidence for a sub-arc petrogenesis presented below.

3.5.2.2 Platinum group element constraints on peridotite-fluid interactions and implications for melting environment

Prior to sulfide exhaustion at ~25% partial melting, PGEs may not significantly fractionate (Pearson et al., 2004; Mungall & Brenan, 2014; Aulbach et al., 2016) or may be moderately fractionated due to the incongruent melting of sulfide phases (Alard et al., 2000; Luguet & Reisberg, 2016). Post sulfide exhaustion, PGE behaviour is controlled by the stability of platinum group minerals (Mungall & Brenan, 2014; Aulbach et al., 2016; Luguet & Reisberg, 2016). Partial melting, even beyond sulfide exhaustion, is not expected to significantly fractionate Os, Ir, or Ru from one another, whereas Pt and Pd may become depleted relative to the other PGEs after extensive melting (Aulbach et al., 2016; Luguet & Reisberg, 2016). The melt-depleted Ussuit peridotites show such P-PGE depletion where Pd and sometimes Pt are depleted relative to Os, Ir, and Ru (Fig. 3-5). In contrast, Os and Ir show significant fractionations from one another that are inconsistent with partial melting trends. For example, Os/Ir ratios expected from partial melting

are ~1 (Aulbach et al., 2016), whereas those in the Ussuit peridotite range from 0.3 to 5.8 in the low Al-Ca peridotites and 0.6 to 5.9 in the metasomatized peridotites.

Non-chondritic Os/Ir ratios are likely the result of reactive transport of melts or fluids through peridotites destabilizing PGE alloy phases and redistributing Os and Ir (Büchl et al., 2002; Lorand et al., 2004; Delpech et al., 2012; Luguet & Reisberg, 2016; Xu et al., 2021; Barrett et al., in press). Variations in Os/Ir ratios are common in forearc peridotites where ratios are 1.2 ± 0.8 and can reach up to 10 (Büchl et al., 2002; O'Driscoll et al., 2012, 2018; Scott et al., 2019; Chen et al., 2020; Secchiari et al., 2020; Xu et al., 2021; Barrett et al., in press). Regarding supra-chondritic Os/Ir ratios, forearc peridotites additionally show significant depletions in Pd like those of the Ussuit peridotites (e.g. Secchiari et al., 2020; Fig. 3-5). This is important because in non-arc settings where metasomatism may elevate Os/Ir ratios up to 3, these variations are accompanied by elevated Pd (Lorand et al., 2004; Delpech et al., 2012; Luguet & Reisberg, 2016). Thus, the very elevated Os/Ir ratios of the Ussuit low Al-Ca peridotites may be related to forearc processes.

In other forearc settings, such as those that formed the Papua New Guinea and New Caledonia ophiolitic peridotites (Secchiari et al., 2020; Barrett et al., in press), Os concentrations are reduced to sub-ppb levels, as observed in some Ussuit peridotites (Fig. 3-5). The resulting sub-chondritic Os/Ir ratios can reach values <0.2 (Scott et al., 2019; Secchiari et al., 2020; Xu et al., 2021; Barrett et al., in press). Although in some non-arc settings, where peridotites have interacted with large volumes of S-undersaturated melts, Os/Ir ratios may reach as low 0.7 (Lorand et al., 2003), which is consistent with many of the Ussuit low Al-Ca peridotites with sub-chondritic Os/Ir ratios (Table 3-2). However, Pd concentrations in these non-arc peridotites are > 1 ppb (Lorand et al., 2003), and thus distinct from the much lower Pd concentrations of the Ussuit low Al-Ca peridotites with sub-chondritic Os/Ir (Pd concentrations as low as 0.02 ppb).

To summarize, although sub- and supra-chondritic Os/Ir ratios can be produced by subduction and non-subduction related processes, the wide range of supra- and sub-chondritic Os/Ir ratios in the Ussuit low Al-Ca peridotites, the low Os concentrations in some samples combined with the overall depletion in Pd are consistent with PGE inter-element fractionations that occur typically in subduction-related settings.

3.5.2.3 Oxygen isotopic constraints on peridotite-fluid interactions and implications for melting environment

Canonical mantle peridotite $\delta^{18}O$ values are 5.5 ± 0.2 ‰ (Eiler, 2001), with olivine $\delta^{18}O$ values of 5.2 ± 0.2 ‰ (Mattey et al., 1994; Regier et al., 2018). The Ussuit peridotite olivines with $\delta^{18}O$ values between 4.4 and 6.4 ‰ are significantly outside this range (Table 3-1; Fig. 3-6 A). The low Al-Ca peridotites have the highest olivine $\delta^{18}O$ values ranging between 5.45 and 6.39 ‰ (Table 3-1). If considering melts from clastic sediments or altered basalts it would require a melt/rock ratio of ~0.1 to increase the olivine $\delta^{18}O$ values to 6.39 ‰ from a mantle olivine value of 5.2 ‰ (Fig. 3-6 B). This would cause significant changes in incompatible elements, outside the range found in the low Al-Ca Ussuit peridotites (Figs. 3-6 B and 3-7). As such, these values are likely derived from the primary melting environment of these peridotites.

The metasomatized peridotites have a greater range in olivine $\delta^{18}O$ values, 4.44 to 6.17 $\delta^{18}O$ (Table 3-1). These peridotites have clearly interacted with metasomatizing fluids or melts (Figs. 3-3 B, 3-7, B3-2 and B3-3). The fact that they have olivine with $\delta^{18}O$ values extending lower than mantle olivine, whereas the more refractory unmodified peridotites have olivine $\delta^{18}O$ values higher than the mantle, may suggest the lower olivine $\delta^{18}O$ are the result of secondary processes. Supporting this is the broad negative correlation between bulk-rock Ti contents and olivine $\delta^{18}O$ values which suggests the metasomatism responsible for the high Ti contents altered the $\delta^{18}O$ values of the

samples. This would be consistent with some orogenic peridotites where olivine with sub-mantle $\delta^{18}O$ values are the result of interactions with deeply derived orogenic fluids (e.g. Li et al., 2018). As such, we focus on the $\delta^{18}O$ values of the low Al-Ca peridotites which show the least evidence for metasomatism.

Fractional melting is unlikely to cause the high olivine $\delta^{18}O$ values of the low Al-Ca Ussuit peridotites because this process produces only nominal changes in initial olivine $\delta^{18}O$ values, i.e., typical variation in olivine $\delta^{18}O$ of < 0.1 ‰ (Eiler et al., 2000; Eiler, 2001) and measurements in very depleted rocks confirm this (Regier et al., 2018). Alternative mechanisms to alter $\delta^{18}O$ values include interaction with surface waters or crustal recycling (Eiler et al., 2000; Eiler, 2001; Laouar et al., 2017; Wang et al., 2018a; Li et al., 2018; Dallai et al., 2019).

A mechanism for alteration by surface water may be along detachment faults at mid-ocean ridges (Tao et al., 2020). However, this relatively high temperature hydrothermal alteration (Tao et al., 2020) would most likely cause a decrease in the $\delta^{18}O$ values of the peridotites (Boschi et al., 2008). Nevertheless, a minority of serpentinized oceanic peridotites have $\delta^{18}O$ values above 5.5 ‰ (Boschi et al., 2008). Furthermore, such detachment faults may be the loci of subduction initiation and provide a pathway for the obduction of peridotite into the crust (Maffione et al., 2015).

Other observations that may support alteration at a mid-ocean ridge are serpentinization and dehydration effects recorded in olivine in two samples of the metasomatized peridotites. Despite the olivine in the Ussuit metasomatized peridotites likely having its $\delta^{18}O$ values altered by late fluids, the timing of serpentinization and dehydration affects are not constrained to this event and could have occurred prior to secondary metasomatism. Serpentinization results in an increase in bulk-rock $Fe^{3+}/\Sigma Fe$ and the production of magnetite, lowering the availability of Fe for recrystallized olivine which consequently will have an increased forsterite content (Moody, 1976;

Evans, 2008; Debret et al., 2014; Majumdar et al., 2016). Near-complete prograde loss of serpentine minerals can preserve magnetite and produce high-Mg olivine (e.g. Szilas et al., 2015; Padron-Navarta et al., 2011). Two Ussuit metasomatized peridotites (GR16-109 and GR16-208), with olivine forsterite contents >95 % and modal magnetite abundances >5 % (Table 3-1) clearly record such a process. As such, hydrothermal alteration along detachment faults in a mid-ocean ridge, followed by supra-subduction zone processing and obduction may provide a viable mechanism to explain the variable oxygen isotopic compositions and subduction-related geochemical characteristics recorded in the Ussuit peridotite.

An alternative mechanism to alter olivine $\delta^{18}O$ values of the Ussuit peridotite is fluxing by melts or fluids generated from subducted crust. Clastic sediments, pelagic sediments, and altered oceanic crust have high $\delta^{18}O$ values and if recycled into the mantle can produce changes in $\delta^{18}O$ in this domain (Eiler et al., 2000; Eiler, 2001; Li et al., 2018; Wang et al., 2018a; Dallai et al., 2019; Fig. 3-6). Recycling of crustal components has been shown to be responsible for olivine $\delta^{18}O$ values from Paleoproterozoic and younger mantle dunites that are higher than typical mantle (e.g. Wang et al., 2018a; Dallai et al., 2019). In addition, recycling of clastic and pelagic material may be responsible for variations in $\delta^{18}O$ in glasses and olivine in arc lavas (Eiler et al., 2000). Furthermore, arc magmas that show deviations to positive $\delta^{18}O$ values in phenocrystic olivine are associated with depleted mantle domains, in that the magmas show significant depletions in bulk-rock Ti (Eiler et al., 2000), providing a possible correlation with the highly refractory sub-arc compositions that might be like that of the Ussuit peridotite.

To summarize, olivine $\delta^{18}O$ values outside of the mantle range, such as those observed in the Ussuit peridotites require unique mechanisms of formation. These may include mid-ocean ridge seawater alteration, subduction processes, or both. However, when such variations in $\delta^{18}O$ occur

in orogenic peridotites, they are typically associated with subduction processes and fluid fluxing related to crustal recycling (e.g. Li et al., 2018; Wang et al., 2018a; Dallai et al., 2019). As such, the oxygen isotopic composition of olivine in the Ussuit peridotite are possibly indicative of subduction zone processes, either in their initial or mature phases. This interpretation is consistent with the local crustal geology representing a subduction setting (Kalsbeek et al., 1987; Whitehouse et al., 1998; Nutman et al., 1999; Connelly et al., 2000; van Gool et al., 2002).

3.5.2.4 Timing of melt depletion and temporal relationship with local calc-alkaline magmatism

Defining the timing of melt removal from the Ussuit peridotites provides further constraints on their genesis. Given an isotopically homogenous starting material, efficient Re extraction during melting, and in the absence of secondary modification, Re-Os model ages (T_{RD} and T_{MA}) predict the approximate timing of melt depletion in refractory peridotites (Walker et al., 1989). The low $^{187}Re/^{188}Os$ ratios and relatively narrow range of $^{187}Os/^{188}Os$ ratios of the low Al-Ca Ussuit peridotites largely meets these requisite conditions. Despite secondary alteration recorded by the Ussuit metasomatized peridotites, these show a limited range in $^{187}Os/^{188}Os$ ratios suggesting Os isotopic compositions were unaltered by metasomatism. The resulting T_{RD} minimum Re-Os model ages for all the low Al-Ca and metasomatized peridotites are thus tightly distributed between ~1.7 and 2.1 Ga (Table 3-2), with T_{MA} ages being very similar. Such a tight range in ages is unlikely to be the result of re-enrichment / re-setting of older Archean peridotites that underpin the Archean cratonic nucleus to the south (Wittig et al., 2010), especially considering the highly melt depleted character of the low Al-Ca suite and the absence of sulfide within them. These ages are also considerably younger than the age of ultramafic cumulates found within the older Akia and Itsaq terranes (Bennett et al., 2002; Szilas et al., 2015, 2017; McIntyre et al., 2019; Waterton et al., 2022).

The prominent mode in Ussuit peridotite melt depletion ages, centered around 2 Ga (Fig. 3-8) overlaps the well-defined ~2050 Ma ^{207}Pb/^{206}Pb age peak for detrital zircons from the Nordre Strømfjord supracrustal suite (Scott & Gauthier, 1996; Kalsbeek et al., 1998; Scott, 1999; Nutman et al., 1999; Connelly et al., 2000, 2006; Thrane & Connelly, 2006; Fig. 3-8) and the 1920 to 1870 Ma age of the calc-alkaline Arfersiorfik quartz diorite (AQD) suite (Kalsbeek et al., 1987; Kalsbeek & Nutman, 1996; Whitehouse et al., 1998; Connelly et al., 2000; Fig. 3-8). In addition to this temporal association, the AQD suite formed from a juvenile source, with chondritic initial Nd isotope compositions, with no Archean melt or crustal influence (Kalsbeek et al., 1987; Whitehouse et al., 1998). Similarly, there is no indication of Archean inheritance in the tight clustering of Re-Os T_{RD} ages of the Ussuit peridotites at ~1950 Ma (Table 3-2; Fig. B3-7). Thus, there is a clear and direct temporal and isotopic relationship between the mantle peridotites and the local / regional Paleoproterozoic oceanic arc crust in the Nagssugtoqidian orogen, strengthening the case for a forearc origin for the Ussuit peridotites.

3.5.3 The nature of lithospheric mantle underlying Paleoproterozoic mobile belts and implications for Paleoproterozoic cratonization

The Laurentia supercraton, comprising much of what is now North America, records a history of lateral convergence and the assembly of Archean cratonic nuclei between 2000 and 1800 Ma (Hoffman, 1988). Within the southern West Greenland portion of the North Atlantic craton, defined as a rifted portion of the Laurentia supercraton by Pearson et al (2021), the Nagssugtoqidian orogen (NO) is also the suture between two Archean nuclei, the Rae and North Atlantic cratons (van Gool et al., 2002; Connelly et al., 2006; St-Onge et al., 2009; Garde & Hollis, 2020). The components within this mobile belt included Archean crust, Paleoproterozoic continental arc crust, and juvenile Paleoproterozoic oceanic arc crust (Kalsbeek et al., 1987;

Kalsbeek & Nutman, 1996; Whitehouse et al., 1998; Nutman et al., 1999; Connelly & Mengel, 2000; Connelly et al., 2000; van Gool et al., 2002). The continental arc, represented by the Sisimuit charnockite suite (Kalsbeek et al., 1987; Whitehouse et al., 1998; Fig. 3-1), records the modification of Archean lithosphere, whereas the Ussuit unit records the incorporation of juvenile oceanic arc crust into the suture zone. The Re-Os melt depletion ages from Ussuit peridotite along with similar ages from mantle xenoliths underlying the NO (Wittig et al., 2010) records the addition of Paleoproterozoic juvenile lithospheric mantle to the lithospheric section.

Peridotite xenolith thermobarometry constrained the depth of the underlying lithospheric keel of the NO to at least 215 km at the time of their eruption, ~ 580 Ma (Sand et al., 2009), consistent with present-day seismic estimates (Artemieva, 2019) and clearly qualifying this area as "cratonic" from the perspective of its long-term stability and lithospheric thickness (Pearson et al., 2021). As such, the NO records the production of cratonic lithosphere in the Paleoproterozoic through the lateral accretion of various lithospheric components which include Archean cratonic nuclei, arc-modified Archean lithosphere, and juvenile arc lithosphere.

The NO forms part of the vast network of Paleoproterozoic mobile belts that suture the Archean cratonic nuclei of Laurentia (van Gool et al., 2002; Wardle, et al., 2002a,b; St-Onge et al., 2009). Like the NO, the crustal portions of these mobile belts are characterized by arc plutonic and supracrustal suites whose age is coincident with the Paleoproterozoic lateral convergence of the Laurentia sub-components and whose isotopic systematics imply both juvenile and recycled provenances (Hoffman, 1988; Thériault & Ermanovics, 1997; Scott, 1998; Wardle, et al., 2002a,b). Globally a similar story emerges where juvenile arc-related crust forms large parts of cratonic lithosphere, particularly in Paleoproterozoic mobile belts that suture or surround Archean cratonic nuclei. For example, the Paleoproterozoic sutures of the Siberian craton include significant

portions of juvenile arc crust or otherwise Paleoproterozoic arc modified lithosphere (Rosen, 2002). In another example, the crustal architecture of the Paleoproterozoic lithospheric segments surrounding the Kaapvaal craton is characterized by crustal ages between 1700 Ma and 2100 Ma with indicators juvenile provenance in the form of Sm-Nd depleted mantle model ages that range between 2000 to 2400 Ma (Reid, 1997; Robb et al., 1999; Janney et al., 2010).

Where sampled as xenoliths, the underlying lithospheric mantle of many Paleoproterozoic mobile belts is characterized by Paleoproterozoic Re-Os melt depletion ages that overlap the Ussuit unit (e.g. Janney et al., 2010; Wittig et al., 2010; Ionov, et al., 2015a,b; Liu et al., 2018; Fig. 3-8 A). Similarly, many of these samples show highly refractory compositions like those of the Ussuit peridotite (Fig. 3-3) and with geochemical indices, such as spinel Cr #'s >75 and variable Os/Ir ratios averaging 1.4 ± 1.5 (Janney et al., 2010; Ionov, et al., 2010; 2015a,b; Liu et al., 2018), that suggest sub-arc influences. Finally, goethermobarometry and seismic tomography show the lithosphere underlying many of these mobile belts to extends to >150 km depth and along with their billion year-scale longevity the mobile belts and underlying lithosphere are classified as cratonic lithosphere (Ionov et al., 2015a,b; Pearson et al., 2021).

Clearly, the Paleoproterozoic must have been a key period for the growth of cratons, as is recorded by the significant proportion of juvenile Paleoproterozoic crust and lithospheric mantle characterizing the Paleoproterozoic mobile belts of composite cratons (Pearson et al., 2021). The underlying lithospheric mantle of these mobile belts are likely to be highly complex domains characterized by pristine and sub-arc modified Archean mantle lithosphere intercalated with Paleoproterozoic juvenile mantle lithosphere (Fig. 3-9). That the juvenile crust of these mobile belts is largely dominated by Paleoproterozoic arcs and that the underlying lithospheric mantle has

compositional similarities with the Ussuit peridotites, illustrates that sub-arc mantle underlying mobile belts is a likely a fundamental component of Paleoproterozoic cratonic lithosphere.

3.6 Conclusions

The Ussuit peridotites of the Nagssugtoqidian Orogen are compositionally distinct from Precambrian cumulate rocks in West Greenland. In contrast, the compositions of the peridotites clearly plot in fields largely occupied by mantle peridotites whose refractory compositions were derived from partial melting.

The Ussuit peridotites record the melting of forearc mantle to a cumulative melt fraction of > 30%. The resulting compositional characteristics are similar to those of Phanerozoic forearc peridotites and Paleoproterozoic CLM (Figs. 3-3 to 3-5 and 3-7). Primary characteristics recorded in the most pristine and melt-depleted rocks, i.e., Cr #'s up to 90 at olivine Mg # of 92-93 and orthopyroxenes containing <0.7 wt% Al_2O_3, require hydrous melting to generate these extreme compositions, suggesting arc-related processes in their petrogenesis. Similarly, PGE and oxygen isotopic characteristics show signatures akin to peridotites that have reacted with fluids in subduction zone settings. The rather uniform Re-Os isotope systematics of the Ussuit peridotites indicate their formation at ~ 2 Ga, coincident with local oceanic arc lithologies that comprise the Ussuit unit. Together, these characteristics strongly suggest that the Ussuit peridotite formed in a forearc or sub-arc setting and via melting that was facilitated by hydrous fluids.

The Re-Os geochronology of the Ussuit peridotites is coincides with drift and convergence events recorded regionally and globally (e.g. Hoffman, 1988; Reid, 1997; Robb et al., 1999; Rosen, 2002; van Gool et al., 2002; Wardle et al., 2002a,b; St-Onge et al., 2009) and during a period of major growth in cratons (Pearson et al., 2021). These events ultimately led to the formation of supercratons from smaller Archean nuclei and newly formed Paleoproterozoic cratonic

lithosphere. The crustal portions of Proterozoic cratonic lithosphere show a compositional diversity of continental and juvenile oceanic arcs (e.g. Hoffman, 1988; Reid, 1997; Robb et al., 1999; Rosen, 2002; van Gool et al., 2002; St-Onge et al., 2009). The underlying highly depleted lithospheric mantle of the latter are represented by the Ussuit peridotite – a rare snap-shot of this type of mantle emplaced as a large fragment, rather than as small xenoliths, into the crust. The characteristics and origin of the Ussuit peridotites indicate that sub-arc mantle may constitute an important component of Paleoproterozoic cratonic lithosphere. Supporting this, the composition and geochronology of mantle xenoliths from other Paleoproterozoic cratonic lithosphere domains have compositional and temporal similarities with Ussuit peridotites (e.g. Janney et al., 2010; Ionov et al., 2015a,b; Liu et al., 2018; Pearson et al., 2021).

Differentiating between residues melted at mid-ocean ridges and those formed by sub-arc hydrous flux melting in the Paleoproterozoic or earlier earth is difficult. Despite numerous Paleoproterozoic mantle xenoliths having similarities with Ussuit peridotite, in some instances these geochemical characteristics may result from melting in a hot ridge environment. For example, highly refractory compositions from up to 40% melting are likely to form from melting in the hot mid-ocean ridges which likely characterized the Paleoproterozoic (Fig. B3-6; Herzberg, 2004; Herzberg et al., 2010; Pearson & Wittig, 2014). In other instances, Paleoproterozoic xenoliths are less refractory, possibly signifying a lower degree of melt depletion than those of the Ussuit peridotite (cf. Wittig et al., 2008, 2010b; Janney et al., 2010; Ionov et al., 2010; 2015a,b; Czas et al., 2020). Likely, the lithospheric mantle underlying Paleoproterozoic lithosphere that form parts of broader cratonic masses is an amalgamation of residual mantle formed at mid-ocean ridges, mantle hydrous flux melted in sub-arc regions, mantle that has experienced metasomatism implicit in both environments, and potentially minor additions from mantle plumes. The hot mantle in the

Paleoproterozoic (Herzberg et al., 2010) likely led to overall high degrees of melt depletion in residual mantle lithosphere (Pearson & Wittig, 2014) but following that time, high melt fractions could only be achieved in mantle plumes and in arcs. Depleted lithospheric peridotite formed at Paleoproterozoic hot mid-ocean ridges and whose refractory characteristics were enhanced through sub arc melting, has the refractory properties like that of Archean cratonic mantle, with a viscosity and buoyancy that are critical to craton stability and protection from thermal erosion from the convective asthenosphere for billions of years.

3.7 Tables and Figures

Table 3-1 Samples, modal proportions, and key compositional characteristics.

Samples	Ol	Opx	Spinel	Amph	Mt	Rock Type	Bulk-rock Mg #	Bulk-rock Al$_2$O$_3$	Ol Mg #	Spinel Cr #	Olivine δ^{18}O (σ)
Low Al-Ca peridotites											
GR16-131	84.3	15.0	0.7			Harzburgite	92.0	0.39	92.3	69.9	5.45 (0.19)
GR16-141	86.6	11.6	0.4	1.4		Harzburgite	92.5	0.31	92.7	74.1	6.12 (0.04)
GR16-158	94.4	4.2	0.5			Dunite	92.1	0.20	92.4	83.3	5.70 (0.01)
GR16-160	65.5	34.0	0.4			Harzburgite	92.5	0.43	92.5	86.2	6.39 (0.18)
GR16-165	98.7	1.3	trace			Dunite	93.0	0.13	93.0	81.2	6.21 (0.04)
Metasomatized peridotites											
GR16-109	43.5	49.3	1.6	trace	5.6	Harzburgite	90.1	2.14	96.4		5.45 (0.05)
GR16-121	57.1	39.6	1.6	1.2	0.6	Harzburgite	90.1	1.66	91.1	87.0	
GR16-191	61.3	30.1	8.6	trace		Harzburgite	89.0	3.96	90.9	90.6	4.47 (0.16)
GR16-197	63.2	32.8	4.0	trace		Harzburgite	91.3	3.14	91.8	49.0	4.57 (0.37)
GR16-208	70.1	23.3	trace		6.6	Harzburgite	90.9	0.51	96.8		4.51 (0.08)
GR16-225	82.6	16.2	1.2			Harzburgite	90.4	0.51	90.8	78.9	6.17 (0.20)
GR16-231	57.9	40.8	0.2	0.6		Harzburgite	90.6	0.73	91.0	84.7	5.64 (0.19)

*Modal abundances were calculated from bulk-rock and mineral chemistry using MINSQ (Herrmann & Berry, 2002). Where minerals are indicated as occurring in trace abundances, the MINSQ spreadsheet did not detect these minerals, but they were found in thin section.
**Abbreviations are as follows: ol, olivine; Opx, orthopyroxene; Amph, amphibole; Mt, magnetite.

Table 3-2 Platinum group element and Re-Os isotopes for the Ussuit peridotites.

Samples	Os (ppb)	Ir (ppb)	Ru (ppb)	Pt (ppb)	Pd (ppb)	Re (ppb)	$^{187}Re/^{188}Os$	Abs. 2σ	$^{187}Os/^{188}Os$	Abs. 2σ	T_{RD} (Ma)	Os/Ir	Pd/Ir
Low Al-Ca peridotites													
GR16-131	0.23	0.3	4.96	3.00	0.19	0.005	0.10	0.015	0.11537	0.0003	1790 (180)	0.77	0.63
GR16-141	2.79	1.56	7.21	2.22	0.02	0.004	0.007	0.0005	0.11408	0.0002	1960 (160)	1.8	0.01
GR16-158	6.55	1.12	5.46	2.05	0.02	0.012	0.008	0.0006	0.11402	0.00032	1970 (160)	5.8	0.02
GR16-160	5.52	8.44	19.9	7.39	0.02	0.022	0.02	0.0006	0.11412	0.00024	1960 (160)	0.65	0.002
GR16-165	1.33	3.95	7.8	2.12	0.04	0.007	0.024	0.003	0.11371	0.00016	2010 (160)	0.34	0.01
Metasomatized peridotites													
GR16-109	3	1.58		1.03	0.54	0.002	0.004	0.002	0.11442	0.00019	1920 (170)	1.9	0.34
GR16-121	3.58	1.55		0.93	0.77	0.022	0.03	0.002	0.11609	0.00023	1690 (180)	2.3	0.50
GR16-191	3.04	1.49		2.27	2.87	0.002	0.003	0.0009	0.1127	0.00015	2160 (150)	2.0	1.9
GR16-197	2.29	1.07	5.16	1.95	0.76	0.002	0.005	0.0005	0.11425	0.00025	1940 (160)	2.1	0.7
GR16-208	2.57	0.57	6.3	2.97	0.84	0.002	0.004	0.001	0.11281	0.00015	2140 (150)	4.5	1.5
GR16-225	13	21.9	20.3	11.4	0.92	0.003	0.001	0.00004	0.1129	0.0002	2130 (150)	0.59	0.04
GR16-231	1.9	0.32	3.7	5.19	1.52	0.005	0.012	0.002	0.11398	0.00021	1980 (160)	5.9	4.8

* T_{RD} ages use enstatite chondrite compositions (Walker et al., 2002) and the decay constant used for ^{187}Re was 1.6689×10^{-11} (Selby et al., 2007). Bracketed numbers are the uncertainty estimated from the difference in ages when using ordinary vs carbonaceous chondrites as a reference frame.

Table 3-3 Comparison of key compositional features of the Ussuit peridotites with the products of peridotite melting experiments in hydrous and anhydrous environments.

Melting %	Olivine Mg #		Spinel Cr #		bulk-rock Al_2O_3		Orthopyroxene Al_2O_3	
	Hydrous	*Anhydrous*	*Hydrous*	*Anhydrous*	*Hydrous*	*Anhydrous*	*Hydrous*	*Anhydrous*
50	N/A	93.0 - 93.4	N/A	N/A	N/A	Trace	N/A	N/A
40	91.8 - 92.9	92.0 - 93.1	69.5 - 83.4	N/A	0.02 - 0.08	<0.2	0.9 - 2.6	3.3 - 4.4
30	90.5 - 92.2	92.0 - 92.4	55.6 - 63.6	22.6 - 60.2	0.1 - 1.1	0.3 - 0.7	1.0 - 3.6	2.2 - 6.0
20	90.2 - 92.3	91.0 - 91.8	37.4 - 58.8	18.9 - 56.2	0.5 - 1.8	1.0 - 1.8	2.0 - 4.3	2.8 - 6.0
10	89.6 - 91.2	90.4 - 91.3	11.5 - 34.5	13.1 - 31.3	1.3	1.7 - 3.1	4.0 - 5.3	4.5 - 6.3
2-stage melting	90.0 - 91.5	94.4 - 94.9	42.3 - 83.4	N/A	0.04 - 0.9	0.07 - 0.2	0.7 - 4.0	0.3 - 0.5
Low Al-Ca Ussuit peridotite	92.3 - 93.0		69.9 - 86.2		0.1 - 0.4		0.4 - 0.7	
Metasomatized Ussuit peridotite	90.8 - 91.9		41.1 - 90.6		0.5 - 5.4		0.5 - 1.7	

*Hydrous melting experiments: Hirose & Kawamoto (1995), Condamine & Médard (2014), and Mitchell & Grove (2015)
**Anhydrous melting experiments: Baker & Stopler (1994), Walter (1998), Falloon et al. (1999, 2008), and Pickering-Witter & Johnston, (1999)
***2-stage melting experiments: Falloon et al. (2001) and Mitchell & Grove (2015)
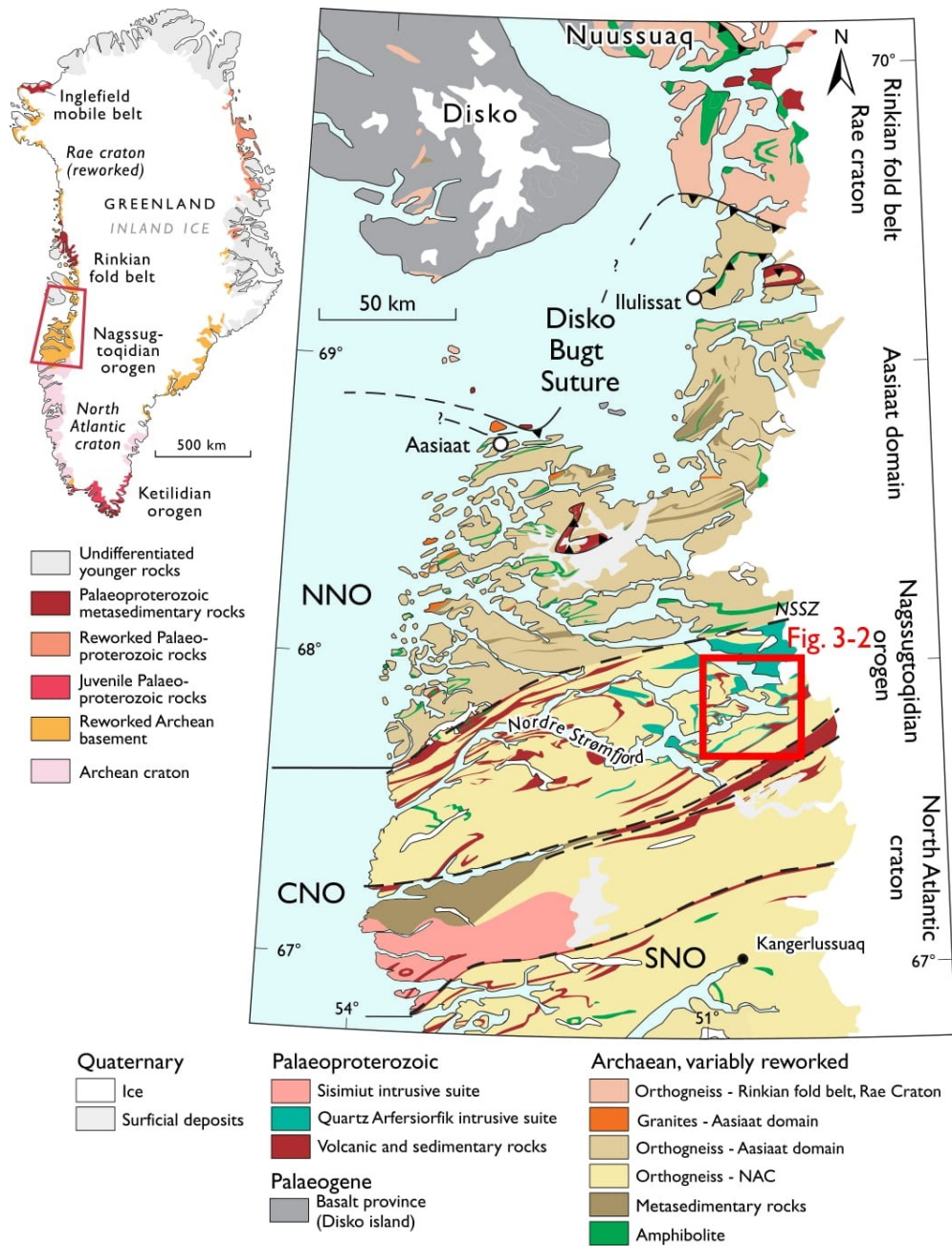
Fig. 3-1. A) Generalized geological map of Greenland showing the location of the Nagssugtoqidian orogen in the red rectangle and B) geological map of the Nagssugtoqidian orogen. Maps are modified from Garde & Hollis (2020). The Disko Bugt suture is that separating the Rae craton from the Aasiaat domain (Connelly et al., 2006). The central Nagssugtoqidian orogen (CNO) is the postulated location of an additional suture that separates the Aasiaat domain from the North Atlantic Craton (Garde & Hollis, 2020). Within this suture is the Ussuit peridotites and Ussuit Unit. NNO and SNO refer to the northern and southern Nagssugtoqidian orogen, respectively.

86
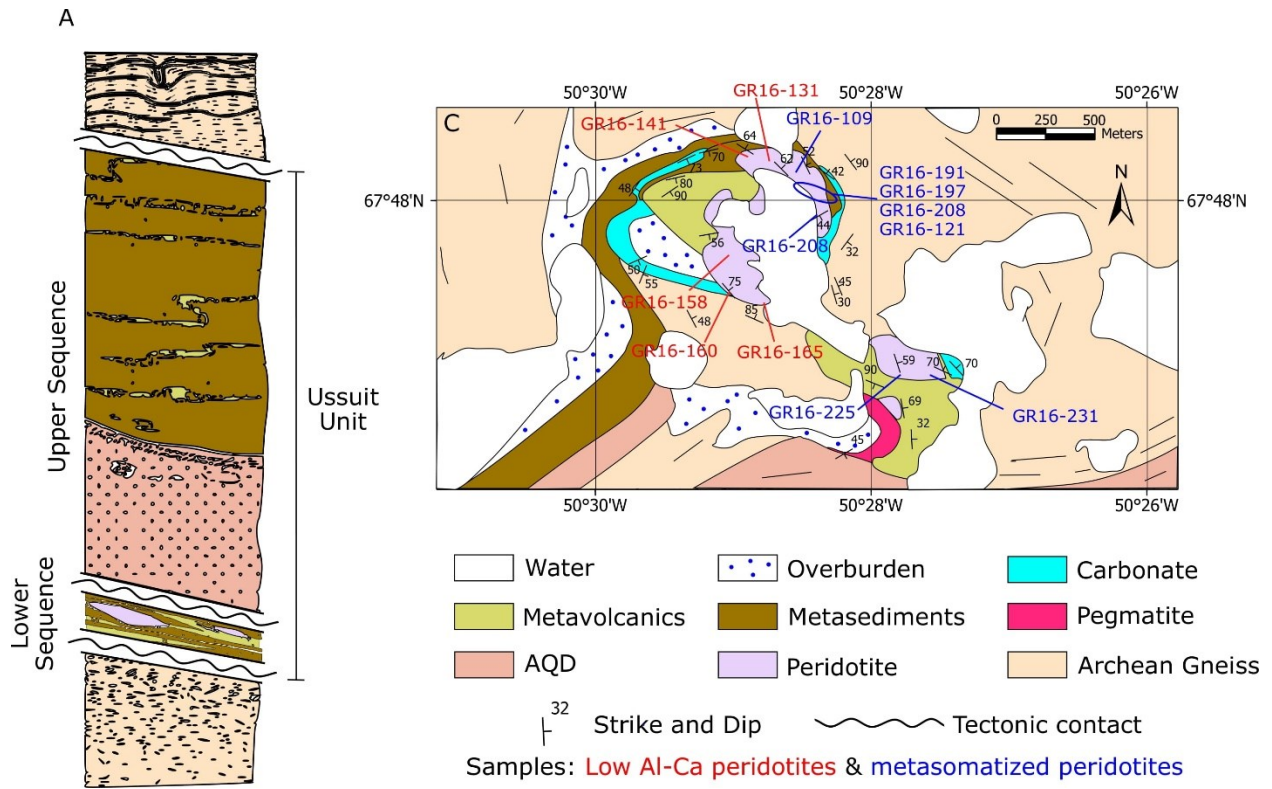
Fig. 3-2. A) Stratigraphic section of the Ussuit unit (Manatschal et al., 1998). B) Geological map of the study area after van Gool & Marker (2004) showing the locations of samples in this study.
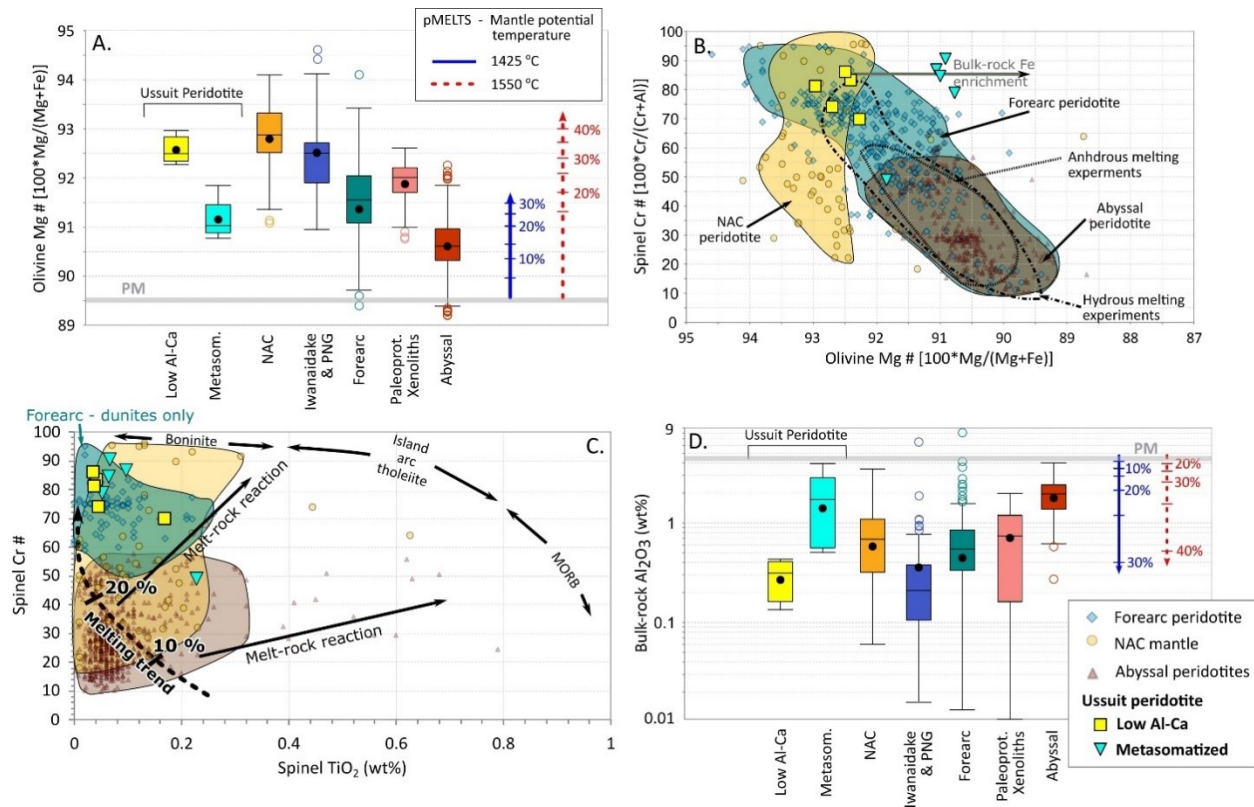
Fig. 3-3. Key compositional features of the Ussuit peridotites compared with mantle peridotites and showing their highly refractory nature. A) Box and whisker plots of olivine Mg # for the Ussuit peridotites compared with natural peridotites from various tectonic environments and modelling using pMELTS. B) Spinel Cr # vs olivine Mg # of the Ussuit peridotite compared with natural peridotites and peridotites from melting experiments. C) Spinel Cr # vs spinel TiO_2 contents showing the Ussuit peridotites overlap only the most highly refractory mantle peridotites. D) Bulk-rock Al_2O_3 for the Ussuit peridotites compared with those from other natural settings. Melting, modelled using pMELTS (Ghiorso et al., 2002; Smith & Asimow, 2005), is done for isentropic polybaric near fractional melting of primitive mantle (McDonough & Sun, 1995) from 4 to 0.2 GPa for mantle potential temperatures of 1425 and 1550 °C. pMELTS is not calibrated for melting at >4 GPa and for a mantle potential temperature of 1550 °C some melting would occur at greater depths. As a result, in the model ~11% melting occurred by batch melting at 4 GPa for a mantle potential temperature of 1550 °C. Bulk-rock Fe enrichment is discussed in text in Section 3.5.1.2. Spinel data are filtered to include only spinel with $Fe^{3+}/\Sigma Fe$ to be <0.15. References are as follows: abyssal peridotites are from Niu (2004) and Warren (2016); NAC peridotites are from Bernstein et al. (1998), Bizzarro & Stevenson (2003), and Wittig et al. (2008); forearc peridotites are from

Ishii et al. (1992), Parkinson & Pearce (1998), Pearce et al. (2000), Ishimaru et al. (2007), Ionov (2010), Ulrich et al. (2010), Uysal et al. (2012), Scott et al. (2019); Iwanaidake and Papua New Guinea (PNG) peridotites are from Kubo (2002) and Barrett et al. (in press), respectively; Paleoproterozoic peridotites are from Chesley et al. (1999), Pearson et al. (2004), Luguet et al. (2009), Janney et al. (2010), Ionov et al. (2015a,b), and Liu et al. (2018); Cumulate peridotites are from Rollinson et al (2002), Szilas et al. (2015,2017), and McIntyre et al. (2019,2021). References for melting experiments are summarized in Table 3-3.
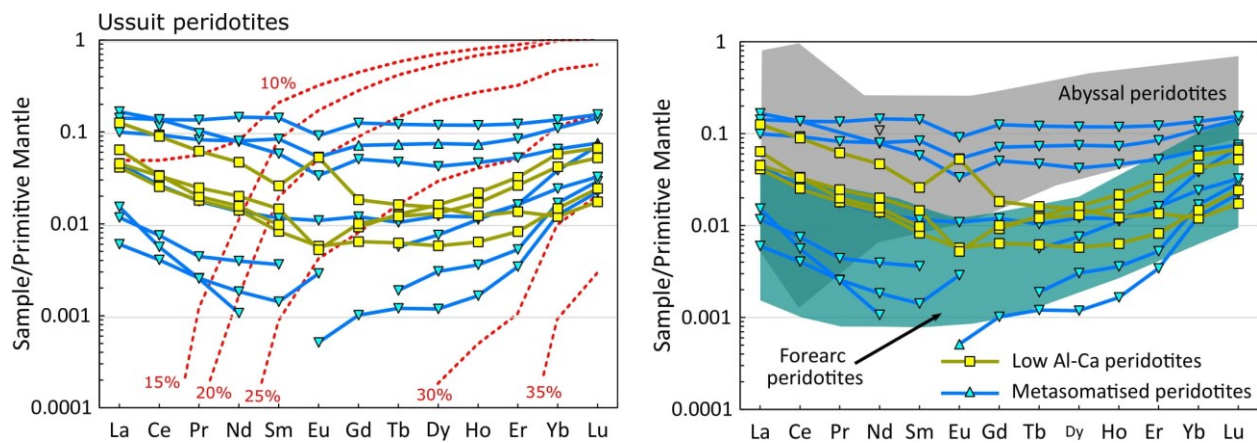
Fig. 3-4. Primitive mantle normalized REE patterns of the Ussuit peridotites. Also shown are the results from pMELTS modelling discussed in Fig. 3-3 for mantle potential temperatures of 1550 ºC (red dashed lines where the labels are melting percent). References for forearc and abyssal peridotites are as in Fig. 3-3. Note: Papua New Guinea peridotites are excluded because of the broad range in trace element patterns that overlap all Ussuit peridotites but mask the HREE fractions highlighted by other forearc peridotites that are mirrored by the Ussuit peridotite.
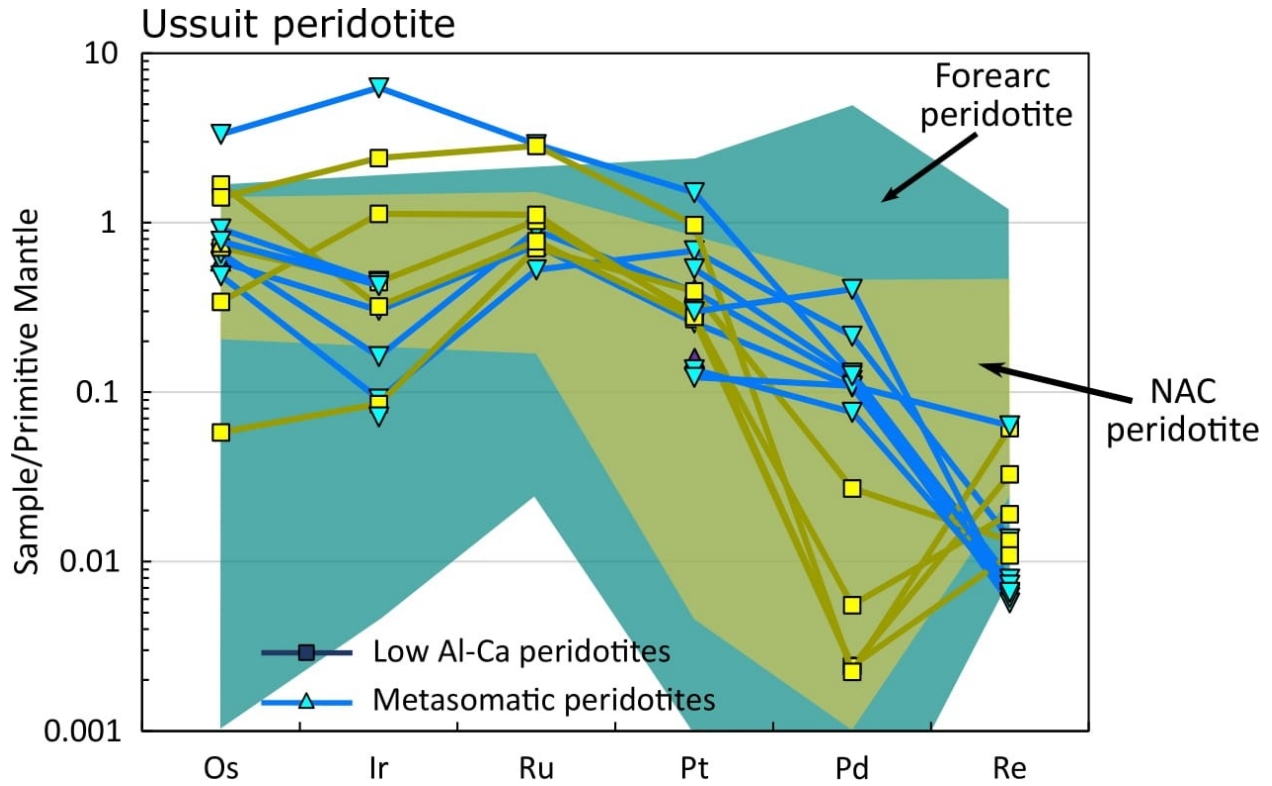
Fig. 3-5. Primitive normalized PGE patterns of the Ussuit peridotites categorized by type, as discussed in text. For comparison, forearc peridotites and CLM xenoliths from the NAC are shown. References for forearc peridotites are from Scott et al. (2019), Xu et al. (2021), O'Driscoll et al. (2012, 2018), Chen et al. (2020), and Secchiari et al. (2020), and for NAC peridotites are from Wittig et al. (2010).
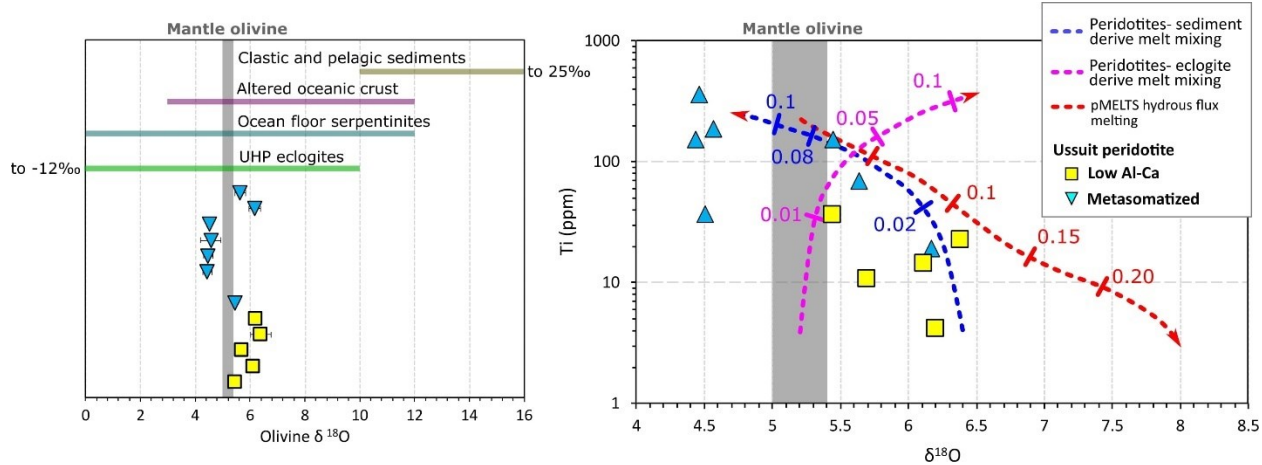
Fig. 3-6. A) Olivine $\delta^{18}O$ from the Ussuit peridotites compared with mantle olivine (Mattey et al., 1994) and potential contaminants. B) Bulk-rock TiO_2 vs olivine $\delta^{18}O$ for the Ussuit peridotites showing a broad negative correlation. Also shown are peridotite-melt reaction calculations with different melt/peridotite ratios. For reactions with clastic sediment as a contaminant, $\delta^{18}O$ were estimated as 15 ‰ and Ti contents were taken from experimental melts of clastic sediments from Hermann & Rubatto (2009). The results illustrate that the high olivine $\delta^{18}O$ values of the low Al-Ca peridotites cannot be derived from melt metasomatism without causing notable increases incompatible elements like Ti. In contrast, similar calculation for late orogenic fluids or melts with low $\delta^{18}O$ could cause the negative correlation between olivine $\delta^{18}O$ value and Ti if the initial olivine $\delta^{18}O$ values were like that of the most refractory low Al-Ca peridotite, i.e., ~6.4 ‰. In these calculations the $\delta^{18}O$ of the infiltrating fluid was estimate to be -10 ‰, Ti contents were taken from eclogitic melts (Wang et al., 2014), and the temperature was estimated to be 1000 ºC. A pMELTS model of hydrous flux melting is also shown. The model takes residual mantle from polybaric melting at ambient mantle temperatures of 1550 ºC modelled in Fig. 3-3 but stalled at 1 GPa. This residual mantle is then fluxed with hydrous melts derived from clastic sediments with $\delta^{18}O$ of 15 ‰ and with Ti contents from Hermann & Rubatto (2009). The pMELTS reactions are modelled at 1 GPa and 1200 ºC. $\Delta_{melt-olivine}$ values for melt-olivine reactions were taken from Eiler (2001). $\delta^{18}O$ for clastic and pelagic sediments and altered oceanic crust are from Eiler, (2001), for ultrahigh-pressure eclogites from Zheng (2012), and for ocean floor serpentinites from Boschi et al. (2008).
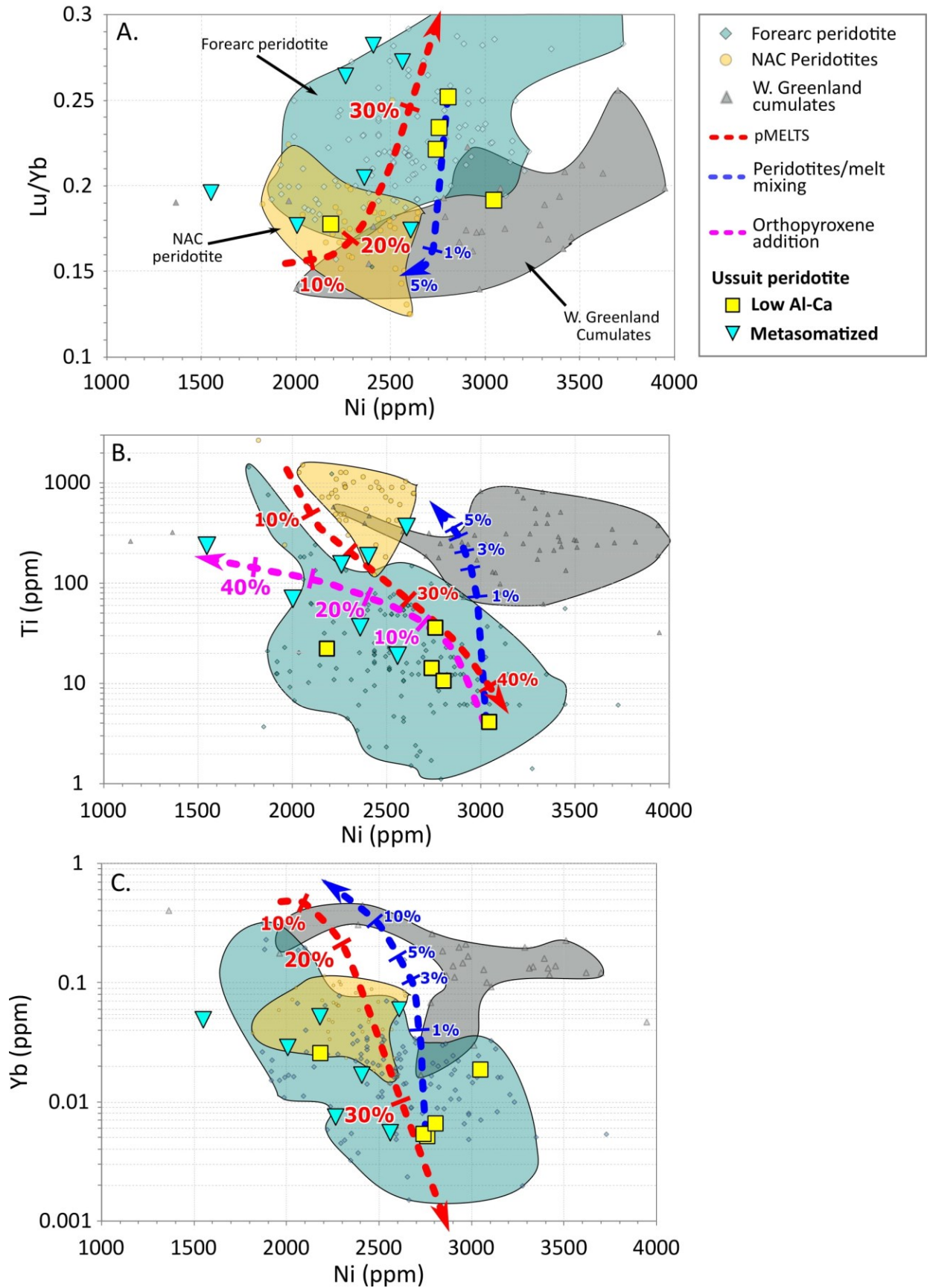
Fig. 3-7. Discrimination diagrams highlighting compositional differences between the Ussuit peridotites and cumulate peridotites in West Greenland. These diagrams show that the Ussuit peridotites plot consistently in the fields of refractory mantle rather than cumulate peridotites. Also shown are pMELTS modelling discussed in Fig. 3-3 for mantle potential temperature of 1550 ºC. and mixing relationships between the most refractory composition of the Ussuit peridotite and basalt (Rapp et al., 1999) and the average orthopyroxene from the Ussuit metasomatized peridotites. The Ussuit metasomatized peridotites with compositional enrichments relative to the low Al-Ca peridotites can be the result of < ~5 % addition of basalt to more refractory peridotites. References are as in Fig. 3-3 for forearc and NAC mantle peridotites. Data for West Greenland cumulates are from McIntyre et al. (2019, 2021), those data summarized by Waterton et al. (2022), and included the ultra-refractory cumulates of the Seqi ultramafic complex from Szilas et al. (2017). All data are filtered to have bulk-rock Mg # > 88.
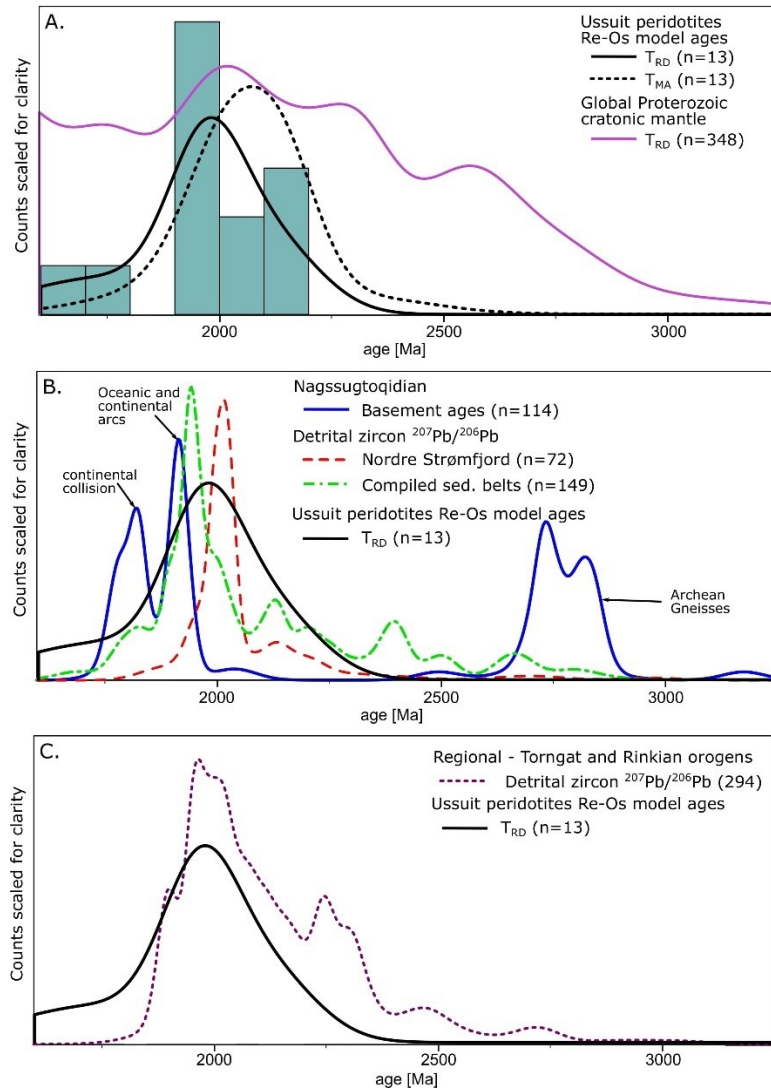
Fig. 3-8. A) Re-Os T_{RD} and T_{MA} histogram and kernel density estimates for the low Al-Ca and metasomatized Ussuit peridotites and Proterozoic cratonic mantle (Pearson et al., 2021). Bandwidth is 100 Ma. B) Kernel density estimates of rock ages for all dated rocks in the NO and detrital zircon ages from the Nordre Strømfjord supracrustal suite and other Paleoproterozoic supracrustal belts in the NO compared with T_{RD} ages of the Ussuit peridotites. Bandwidth is 20 Ma for U-Pb ages. C) Kernel density estimates for regional Paleoproterozoic supracrustal belts compared with T_{RD} ages from the Ussuit peridotites. In all NO and regional Paleoproterozoic supracrustal suites significant age population occur between ~1900 Ma to 2200 Ma reflecting the age of calc-alkaline intrusive suites in these areas and showing that such populations overlap with the age of melt depletion in the Ussuit peridotite. Additional smaller populations of zircons ages occur at ~2100 Ma in the supracrustal suites, overlapping with the oldest T_{RD} ages in the Ussuit

peridotites. The results suggest a wide representativeness of the Ussuit peridotite as the residues underlying the supracrustal belts that makeup the Paleoproterozoic sutures resulting from supercontinent assembly and cratonization in the Paleoproterozoic. References for global Proterozoic cratonic mantle are from (Pearson et al., 2021). References for the NO are from Kalsbeek et al. (1987), Kalsbeek & Nutman (1996), Whitehouse et al. (1998), Nutman et al. (1999) Connelly & Mengel (2000), Connelly et al. (2000 and 2006), Thrane & Connelly (2006), and McIntyre et al. (2021). Detrital zircon from Paleoproterozoic belts in the Torngat and Rinkian orogens are from Scott & Gauthier (1996), Kalsbeek et al. (1998), and Scott, (1999).

A. Drift and the formation of oceanic lithospheric mantle.

B. The development of ocean island arcs.

C. Continental convergence and lithospheric thickening to form Paleoproterozoic cratonic lithosphere.
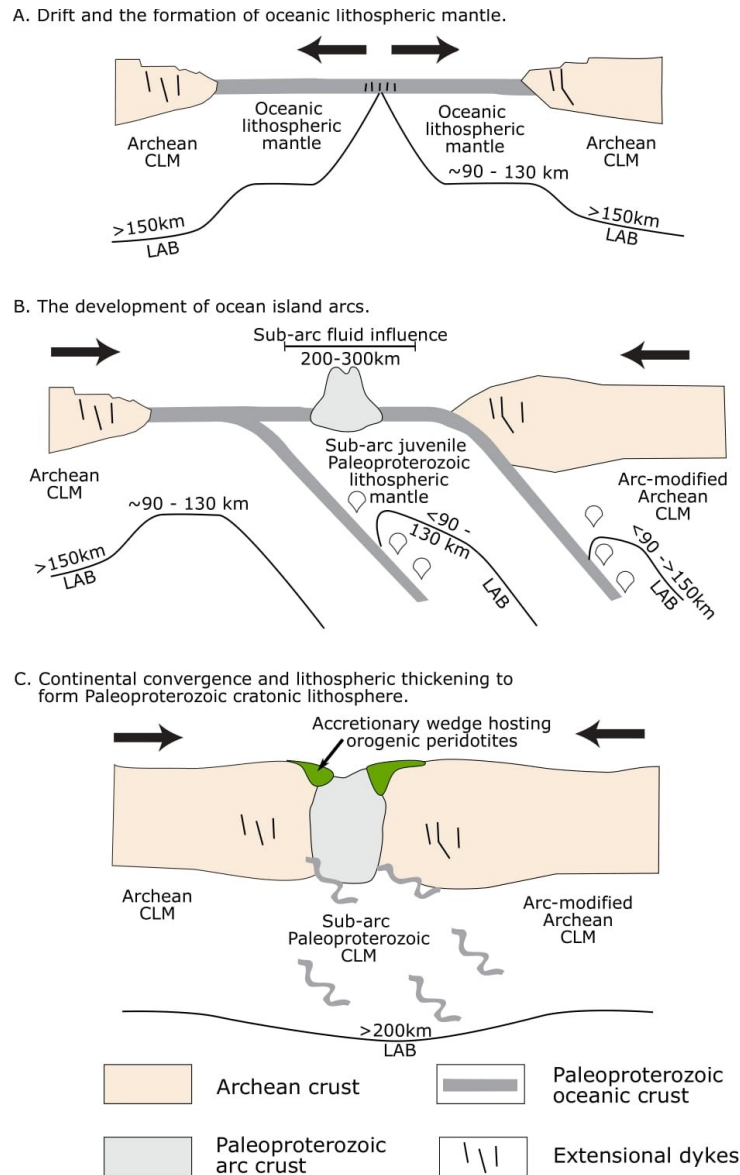
Fig. 3-9. Simplified schematic illustration of the formation of Paleoproterozoic cratonic lithosphere. A) An initial rifting and drift phase results in a residual oceanic lithospheric mantle 90 to 130 km thick (e.g. Herzberg et al., 2010; Pearson & Wittig, 2014; Wang et al., 2018). Subduction zones may form along detachment faults at mid-ocean ridges (Maffione et al., 2015). B) Dehydration of down going slabs release water into the arc wedge down to >120 km (~3.8 GPa) and the migration of water extends for 100's of km horizontally into the surrounding mantle (Wang et al., 2019). Secondary melting as a result of hydrous melt fluxing enhances the refractory compositions which characterize much of the Paleoproterozoic CLM (e.g. Janney et al., 2010; Ionov, et al., 2010; 2015a,b; Liu et al., 2018). C) Continental collision results in lateral compressions and formation of thick cratonic roots (Wang et al., 2018).

Chapter 4
Heat generation in cratonic mantle roots – new trace element constraints from mantle xenoliths and implications for cratonic geotherms

T. McIntyre, K. Kublik, C. Currie, & D.G. Pearson

Department of Earth & Atmospheric Sciences, University of Alberta, Edmonton, Alberta, Canada.

Abstract

Heat generation within the cratonic lithospheric mantle (CLM) is an important but poorly determined parameter for constructing cratonic geotherms. Direct measurement of heat producing element (HPE: K, U, and Th) concentrations in bulk-rock samples of cratonic mantle roots – provided as xenoliths in volcanic rocks such as kimberlites – is mostly compromised by infiltration of host melt into the xenoliths, resulting in over-estimates of heat production. Here we use in-situ methods (laser ablation inductively coupled plasma mass spectrometry) on minerals from a variety of cratonic mantle peridotites to avoid host-magma contamination enabling new, more accurate determinations of heat production for a wide spectrum of model mantle lithologies. The most melt-depleted, least metasomatized peridotites indicate that heat generation in un-metasomatized depleted cratonic lithospheric mantle is negligible, at ~ 0.00004 $\mu W/m^3$, 10^2 to 10^3 times less than models that use more enriched or metasomatized compositions. Refertilized cratonic peridotites, typical of many kimberlite hosted xenoliths, have more elevated, but still low heat generation, of 0.006 $\mu W/m^3$. We propose that the heat generation of typical cratonic mantle peridotite lies between these two bounds, i.e., between 0.006 and 0.00004 $\mu W/m^3$. Both values produce lower estimates of lithospheric thickness, by ~10 to up to 80 km, depending on model assumptions, than estimates using higher HPE concentrations measured on bulk-rock xenolith material.

4.1 Introduction

Modelled geothermal gradients, built from estimated thermal properties of the cratonic lithosphere, provide important insight into the thermal structure of Archean continental lithosphere. An important and yet poorly determined parameter affecting estimates of geothermal gradients within cratonic lithosphere, is the heat production in the cratonic lithospheric mantle (CLM) due to the decay of heat producing elements (HPE: K, U, and Th). Heat production in the CLM has been estimated by direct measurements of HPEs in mantle material (Rudnick et al., 1998; Russell et al., 2001; Goes et al., 2020) or by projecting geothermal models through pressure and temperature estimates from cratonic mantle xenoliths and varying heat production and other lithospheric properties to estimate the best-fits to the data (Rudnick & Nyblade, 1999; Russell et al., 2001; Michaut et al., 2007; Mather et al., 2011). Direct bulk-rock measurements of HPEs in xenoliths have yielded some elevated estimates for heat production and using these values produces unrealistic cratonic geotherms (Rudnick et al., 1998; Russell et al., 2001; Goes et al., 2020). The high heat production in such samples is, in part, due to the infiltration of relatively high-HPE kimberlite magmas, metasomatism, and sampling bias from both the kimberlite and the researchers (McDonough, 1990; Rudnick et al., 1998). An improved estimate of ~ 0.02 $\mu W/m^3$ for CLM heat production was derived from HPE concentrations in off-craton cratonic-like xenoliths (Rudnick et al., 1998). However, elemental mapping shows that even in basalt hosted mantle xenoliths melt infiltration is pervasive and bulk-rock analyses will result in overestimates of HPE concentrations (Emo & Kamber, 2021). The alternative approach to estimating mantle heat generation (i.e. from best-fit geotherm models to P-T arrays from cratonic mantle xenoliths) has produced variable estimates from 0 to 0.07 $\mu W/m^3$, a range that produces significant variation in estimated lithospheric thickness and temperature (Rudnick & Nyblade, 1999; Russell et al., 2001; Michaut

et al., 2007; Goes et al., 2020). Mantle heat production values employed in previously published cratonic geotherm models range from 0 to 0.084 $\mu W/m^3$ (Pollack & Chapman, 1977; Chapman, 1986; Jordan, 1988; Rudnick et al., 1998; Rudnick & Nyblade, 1999; Russell et al., 2001; Michaut et al., 2007; Hieronymus & Goes, 2010; Hasterok & Chapman, 2011; Mather et al., 2011; Goes et al., 2020), resulting in drastically different estimates of geothermal gradients within cratons (Fig. 1-1).

In this study, we estimate heat production in CLM through direct in-situ measurements of HPEs in a suite of cratonic mantle xenoliths. By using laser ablation inductively coupled plasma mass spectrometry (LA-ICPMS) to measure the abundance of K, U, and Th in mantle phases, we have avoided the effects of host-magma infiltration related overprints. The HPE data are combined with electron microprobe and broader trace element analyses to assess the effects of mantle metasomatism on the distribution of HPEs. The new database can be used to construct HPE concentrations of mantle peridotites with a wide variety of mineral modes if desired. Our results, supplemented by in-situ HPE analyses from the literature, provide new bounds on heat production within the CLM. We use the new HPE constraints to assess the consequences for lithospheric geotherm models in a variety of scenarios.

4.2 Samples

We selected a variety of cratonic mantle peridotite xenoliths from kimberlites, variously located in the Kaapvaal and North Atlantic cratons. The selection represents a range in melt depletion and melt metasomatism, reflecting a likely range of HPE concentrations.

For this study, peridotites from South Africa are largely from the North Lesotho kimberlite field – Letseng, Matsoku, Liqhobong, Thaba Putsoa, and Mothae pipes – with some peridotites from the Louwernsia (Namibia), Jagersfontein, Premier, and Bultfontein kimberlites (South Africa). Many of the samples have been well characterised for petrography and chemistry (Pearson & Nowell, 2002; Simon et al., 2003; Boyd et al., 2004; James et al., 2004; Pearson et al., 2004). Geothermobarometry indicates that these samples originated at depths ranging from <100km to ~145km depth (Table B4-1). The samples are largely lherzolitic spinel- to garnet- facies peridotites. Most samples are coarse peridotites and classify as coarse Mg-rich, low-T peridotites (Type AI terminology of Pearson et al. (2003)) and some samples classify as modally metasomatized phlogopite peridotites (Type AIII). Sample BR-1, the most metasomatically altered sample from the Kaavpvaal craton, contains significant proportions of both amphibole (12%) and phlogopite (8%). Additional Type AIII samples (FRB1350, M9, M13, LQ6, and LQ8) are all less metasomatized and contain only minor phlogopite (<1%).

Samples from the North Atlantic craton (NAC) are from the Pyramidefjeld kimberlite dykes in southern West Greenland. Two are coarse garnet peridotites with only minor phlogopite alteration (G-6-18 and G-6-UA). Two other samples are extensively metasomatized phlogopite-wehrlites (G-6-4C and G-6-14B). These Pyramidefjeld mantle xenoliths have been well studied (Wittig et al., 2008, 2010) and, along with others from the area (Aulbach, et al., 2017a), have been shown to be derived from mantle that has been significantly metasomatized by hydrous melts.

A literature compilation of in-situ analyses of clinopyroxene and garnet from cratonic peridotites supplements the data in this study. These samples are from the Siberian (Ionov et al., 2010, 2017, 2018; Agashev et al., 2013), Kaapvaal (Gregoire et al., 2003; Simon et al., 2003; Rehfeldt et al., 2008; Lazarov et al., 2012; le Roex & Class, 2016), North China (Sun et al., 2012), Rae (Liu et al.,

2016), Slave (Yaxley et al., 2017), and the North Atlantic (Aulbach, et al., 2017a) cratons. A compilation was also made of phlogopite and amphibole from cratonic mantle xenoliths (Ionov & Hofmann, 1995; Grégoire et al., 2002; Coltorti et al., 2004; Powell et al., 2004; Rehfeldt et al., 2008; Giuliani et al., 2016; Alemayehu et al., 2017; Aulbach, et al., 2017; Fitzpayne et al., 2018).

4.3 Analytical Methods

4.3.1 Electron probe micro analysis (EPMA)

Measurements of major elements in all phases were made by EPMA at the Electron Microprobe Laboratory, University of Alberta, Canada. Analytical conditions and standards are given in Appendix C and are briefly summarized here. A 2 μm beam was used with an accelerating potential of 20 kV and current of 20 nA. On- and off-peak times were 20-30s for all elements. Matrix corrections were done using ZAF or Phi-Rho-Z algorithms. Interference corrections were applied to Mn for interference by Cr, Ti for interference by Ba, Cr for interference by V, V for interference by Ti, and Ba for interference by V. Analyses are given in Appendix C.

4.3.2 Laser ablation inductively coupled mass spectrometry (LA-ICPMS)

LA-ICPMS was used to measure K, U, Th, and trace elements in olivine, orthopyroxene, clinopyroxene, and garnet together with U, Th, and trace elements in phlogopite and amphiboles, at the Arctic Resources Laboratory (ARL), University of Alberta, Canada. The instrumentation consists of a RESOlution ArF 193nm excimer laser ablation system coupled with a Thermo Scientific Element XR2 sector field ICPMS. Two ablation cell set-ups were used in the analyses; RESOlution M50A and S-155 Laurin Technic 2, both of which are "two-volume" cells. In these cells, ablated material is removed from the cell in a He flow and mixed with Ar and N_2 down-stream to the mass spectrometer. Instrument parameters are given in Table B4-2. The complete K, U, and Th data set is given in Appendix C.

Potassium was measured separately from U, Th, and trace elements. Measurements were performed on ^{39}K, in medium resolution mode (R = M/ΔM = ~4000). However, at this mass resolution significant interferences from ^{1}H^{38}Ar and the tail of the ^{40}Ar peak remain, requiring careful monitoring on the compound peak shape. Long (90 s) count times of the background were used to obtain improved limits of detection (LOD) and limits of quantification (LOQ), typically yielding LOQs between 0.1 and 0.3 ppm for K. Variations in inter- and intra-day changes in instrument behaviour and settings cause variability in the LOQ, which, in some instances reached 2 ppm in sessions where small spot sizes or lower laser frequencies were used.

Data were only considered reliable for calculations of heat production if above LOQ, whereas analyses lower than LOQs were used in a qualitative manner because they are subject to larger uncertainty. LODs and LOQs were calculated for each individual analysis using the method of Currie (1968) and Pettke et al. (2012) that defines LOQ as:

[EQN 1] $LOQ = 50*(1+[1+(R_{bkg,an}*DT_{an}*N_{ab,an}*(1+N_{ab,an}/N_{bkg,an}))/25]^{0.5})/DT_{an}*N_{ab,an}*S$

where R is signal in counts per second, DT is dwell time, N is the number of measurements, ab refers to measurements during ablation, bkg refers to background measurements, and an references the element of interest. S is the sensitivity (counts per second per unit of concentration) of the instrument to the analyte deduced from measurements of a calibration standard and sample signal. Two measurements of the calibration standard bracket every 5 to 10 unknown analyses. The sensitivity, S, is given by:

[EQN 2] $S = (R_{an,cal}/C_{an,cal})(R_{is,sam}/R_{is,cal})(C_{is,cal})/(C_{is,sam})$.

where *cal* is the calibration material, *is* is the internal standard, *sam* is the sample, and C is the concentration.

The internal standard used in the analyses of K was Si and the reference material used for calibration was NIST610 or NIST612. Reference material NIST614 was measured as a secondary standard for quality assurance (see Fig. B4-1 for summary). The accepted concentration of K in NIST614 is 30 ppm (Jochum et al., 2011) and the average and 2 standard deviations of 298 analyses of NIST614 for K over this analytical campaign was 29.2 ± 1.6 ppm.

Concentrations of U, Th, and other trace elements were measured in low mass resolution mode (M/ΔM ~ 400) using Si as an internal standard. For minerals very low in U and Th, such as olivine and orthopyroxene, measurements were made with only these two elements in the analyte list to maximize counting statistics, improving LOQs. In addition, some clinopyroxene and garnet measurements were performed only for U and Th. In these instances, NIST614 or NIST616 were used as secondary standards to assess accuracy and precision (Fig. B4-2; Appendix C). The average of U and Th measurements for these reference materials have relative standard deviations of ≤4.5% and are within ≤1.5% the compiled literature values from the GeoReM database (Jochum et al., 2005). Measurements of U, Th, and other trace elements in garnet, clinopyroxene, phlogopite, and amphibole used BIR-1G as a secondary standard for quality assurance (Fig. B4-2; Appendix C). Compiled values from GeoReM for U in BIR-1G are variable, with a median of 0.02 ppm and range of 0.011 to 0.214 ppm. The analyses of BIR-1G in this study have an average and two standard deviations of 0.018 ± 0.005 within error of median of compiled values from GeoReM. Thorium is less variable in BIR-1G with an average and two standard deviations of 0.030 ± 0.009 ppm from GeoReM. Our analyses of Th in BIR-1G fall within this range having 0.025 ± 0.004

ppm Th. Other trace element analyses of BIR-1G have relative standard deviations of ≤5% and all fall within the reference ranges for this material from GeoReM.

4.4 Results:

4.4.1 Geothermobarometry

Temperature and pressure estimates were made for previously uncharacterised samples to supplement available literature data (Table B4-1). Pressure estimates were made using the two-pyroxene and Al-in-OPX formulations (P_{BKN}/T_{BKN}) of Brey & Köhler (1990), which allows comparison to other samples in this study previously characterized by Simon et al. (2003) and James et al. (2004). Pressure and temperature estimates using the P_{BKN}/T_{BKN} thermobarometer range from 2.5 to 4.5 GPa and 656 to 1150 ºC, respectively. Spinel lherzolites were assigned a pressure of 2 GPa.

4.4.2 Heat producing elements

For optimal HPE data quality, ideal LA-ICPMS analyses should have steady time-resolved signals, with an absence of significant signal spikes, reflecting homogeneous distribution of the elements in the measured phases (Fig. B4-3 A and B). Irregular time resolved signals, resulting typically in systematically higher values of K, U, and Th were found if the ablation intercepted intragranular fractures or grain boundaries enriched in these elements compared to the host silicate phase (Fig. B4-3 C and D). Thus, all the data used here were filtered by removing analyses which had irregular time-resolved signals and/or clearly intercepted fractures/grain boundaries. The data set is given in Appendix C.

Despite careful assessment of time resolved signals, some abnormally high K measurements still occurred in low K-phases. These outliers are difficult to quantify when LOQs are similar to or exceed the likely typical concentration of an analyte in a phase (i.e. some analytical sessions had relatively high LOQs, above the concentrations of K found in phases measured during sessions where LOQs were low). To quantify K in olivine, orthopyroxene, and garnet, the data were filtered for outliers by accounting for variable LOQ of each analysis – which is largely a function of the measured backgrounds. Such filtering was done separately for each phase using measurements acquired with ≥130 μm spot sizes. Where sample analyses were below LOQ, the LOQ value was assigned as the concentration of the analyte, producing a maximum estimate for the concentration K in these phases. This procedure is viewed as not unduly biasing the data because most of the LOQ values assigned are within the range of data values obtained when signals did pass the > LOQ filtering. Using these combined measurements, the upper limit for outliers for K was defined as 1.5 times the interquartile range plus the median. There were no outliers in the lower part of the concentration range for any minerals. Using the above constraints, box and whisker plots for K in all minerals are given in Fig. 4-1.

4.4.2.1 Potassium

After filtering, 79 of 80 remaining measurements of K in olivine were below LOQ (Fig. 4-1 and Appendix C), the remaining analysis had a measured concentration of 0.22 ± 0.04 ppm. Excluding some analyses which were run on days that produced poor LOQs (0.41 to 0.8 ppm) due to high and variable backgrounds, K in olivine analyses yielded an average LOQ of 0.08 ppm. The average LOD for these analyses was 0.03 ppm and 78% of the measurements fell below LOD.

Many peridotites had K concentrations in orthopyroxene above LOQ (Fig. 4-1). These samples (G-6-UA, FRB135, LET29, LET30, LET38, LET64, LQ8, and M9) tend to have measured mineral equilibration temperatures and pressures greater than or equal to ~1027 °C and ~3.8 GPa (Table 4-1). The average K content for orthopyroxene measurements above LOQ was 0.22 ± 0.08 ppm. Of 136 analyses, 74% were below LOQ (averaging an LOQ of 0.18 ppm), and many samples (59%) had detectable signal above an average LOD of 0.06. If spinel lherzolites are compared with other lithologies, only 33% have K contents in orthopyroxene with detectable signals above the average LOD, significantly lower than 67% for all other samples.

Some peridotites (M13, FRB135, JJG2513, and LET64) had no detectable K signals in garnet, at an average LOD of 0.09 ppm. During sessions which yielded particularly low LOQs, samples LET29 and LET30 can be shown to have between 0.06 to 0.09 ppm K in garnet. Similarly, analyses that are above LOQ in sample BR-1 yielded K concentrations of 0.1 ± 0.02 ppm. In contrast, samples LQ6 and LQ8 have significantly higher and variable K in garnet, with an average of 0.31 ± 0.16. Thus, K in garnet was found to be low in all samples, typically < 0.1 ppm, with some higher values extending up to 0.31 ppm (Fig. 4-1).

Analyses of K in clinopyroxene are highly variable, ranging from 1.7 to 110 ppm. The range correlates strongly with pressure (Fig. 4-2) supporting findings from experimental studies (Harlow, 1997). Published analyses of K in clinopyroxene are of mantle xenoliths, diamond inclusions, and high P and T experiments (Fig. 4-2). These data, along with the "lower" pressure experimental data (5 to 7 GPa), generally fall along the K versus P trend defined by samples in this study (Fig. 4-2). However, experimental data (Harlow, 1997) at >7 GPa fall away from this trend with K increasing less drastically and linearly with pressure, up to concentrations of ~40 000 ppm (i.e., 4 wt% K) at 10 GPa and 1500 ºC. The discrepancy is likely the result of K reaching an approximate

maximum saturation that clinopyroxene can hold regardless of pressure in the experimental study (Harlow, 1997). Overall, the trajectory of K in clinopyroxene with increasing depth from this study is broadly consistent with the K contents of clinopyroxene in mantle xenoliths, diamond inclusions, and experimental results (Fig. 4-2). As there is clear pressure dependency of K in clinopyroxene, the average of the curve of pressure plotted against K in clinopyroxene in garnet peridotites was solved using the mean value theorem for pressures between 1 and 6 GPa. This gives an average value of K in clinopyroxene of 310 ppm for the cratonic lithospheric mantle.

Primary phlogopite (i.e. texturally equilibrated, pre-kimberlite phlogopite identified using textural and chemical criteria discussed by Erlank et al. (1987)) in peridotites studied here contains 9.9 ± 0.4 wt% K_2O (Appendix C). Together with published mantle phlogopite data, we estimate primary mantle phlogopite to have an average and 2 standard deviations K_2O concentration of 10 ± 1.1 wt%.

Only one sample (BR-1) from this study contains amphibole, classifying as kataphorite (after Locock (2014)) and has an average K_2O of 1.39 ± 0.02 wt% (2 standard deviations). Measurements of K_2O in mantle amphibole from the literature show variable K_2O, from 0.14 to 5.86 wt%. However, mantle xenoliths of the mica-amphibole-rutile-ilmenite-diopside (MARID) suite have the highest K_2O in amphibole (Grégoire et al., 2002; Fitzpayne et al., 2018), whereas amphibole-bearing peridotites make up the lower end of the data (Ionov & Hofmann, 1995; Coltorti et al., 2004; Powell et al., 2004).

4.4.2.2 Uranium and thorium

Concentrations of U and Th in all minerals tend to have tails in their distributions skewed to high concentrations (Fig. 4-1) and thus the median of these analyses was used. For olivine, most analyses above LOQ have a median of $0.06\,^{0.13}/_{0.02}$ ppb U and $0.41\,^{0.76}/_{0.18}$ ppb Th (where the super

107

and subscripts define the range in data less outliers (i.e. they are the median plus or minus 1.5 times the interquartile range or the max/min data point, whichever is the less extreme). Some peridotites (e.g. FRB1350) have olivines with much higher concentrations of up to 5 ppb U and 20 ppb Th and sample TP5 has olivine with up to 0.34 ppb U but has similar Th to olivine in other peridotites. These peridotites with enriched U and or Th in olivine also have enriched Th and/or U in orthopyroxene and clinopyroxene.

For orthopyroxene, most peridotites have median concentrations of $0.7\ ^{1.1}/_{0.2}$ ppb U and $1.0\ ^{1.9}/_{0.3}$ ppb Th. Like olivine, orthopyroxene in FRB1350 is enriched in U and Th relative to other peridotites, having median concentrations of $14\ ^{16}/_{13}$ ppb and $22\ ^{25}/_{20}$ ppb, respectively. Orthopyroxene from TP5, TP6, and FRB135 are also relatively enriched in U and Th with concentrations of $2.6\ ^{7.4}/_{0.7}$ ppb and $3.8\ ^{12.4}/_{1.5}$ ppb, respectively. FRB1007 and FRB1434 have U concentrations below median LODs of 0.07 ppb of 0.02 ppb, respectively, and Th concentrations like that of other samples.

Most cratonic peridotites have U and Th in garnet with medians of $58\ ^{100}/_{10}$ ppb and $20\ ^{44}/_{3}$ ppb, respectively. However, in certain peridotites from the Kaapvaal craton, garnets have abnormally high concentrations of U and Th (e.g. garnets in LQ6, LQ8, and M13 have U up to 150 ppb and Th up to 112 ppb). Most NAC peridotites tend to have low U and Th in garnet with U concentrations of $7.5\ ^{8.6}/_{4.7}$ ppb and Th contents below a median LOD of 1.3 ppb. Previously published U (0.3 to 650 ppb; median 34 ppb) and Th (0.1 to 830 ppb; median 18 ppb) for garnets in cratonic peridotite xenoliths have a larger range than measurements made in this study, but similar median and average concentrations (Fig. 4-3).

Most peridotites analysed in this study have median U and Th concentrations in clinopyroxene of $13\ ^{19}/_{7}$ ppb and $41\ ^{67}/_{14}$ ppb, respectively. Clinopyroxene from FRB1350 is enriched in U (400

$^{406}/_{394}$ ppb) and Th (1580 $^{1620}/_{1550}$ ppb), having even higher concentrations than clinopyroxene in metasomite sample BR-1 (U = 106 $^{106}/_{105}$ ppb; Th = 1290 $^{1320}/_{1250}$ ppb) but in general the range of clinopyroxene Th and U in our dataset falls within those of previously published kimberlite-borne peridotites (Fig. 4-3), i.e., U = 2 to 224 ppb; median = 10 ppb, and Th =15 to 1200 ppb; median = 50 ppb.

U and Th contents in phlogopite are variable. Phlogopite, occurring as a minor phase in Kaapvaal peridotites (M13 and M9) has U and Th contents ranging from 1 to 30 ppb and 6 to 74 ppb, respectively. Phlogopite in the amphibole-bearing sample BR-1 has much higher U and Th contents of 186 $^{200}/_{172}$ ppb and 3690 $^{3860}/_{3535}$ ppb, respectively. Similar enrichments in U and Th in more metasomatized peridotites are found in the NAC samples. Phlogopite-garnet lherzolites of the NAC have phlogopites with U of 7 $^{9}/_{5}$ ppb U and 32 $^{42}/_{26}$ ppb Th. In contrast, phlogopite in wehrlite samples from this area has 530 $^{1850}/_{250}$ ppb U and 14 600 $^{25\,200}/_{11\,200}$ ppb Th. These ranges cover the concentration of U (3.5 to 1880 ppb; median = 50 ppb) and Th (3.6 to 77 000 ppb; median = 260 ppb) in phlogopite from most mantle xenoliths from the literature (Fig. 4-3).

Only one sample in this study contained amphibole (BR-1), which had U and Th contents of 99 $^{100}/_{96}$ ppb and 1270 $^{1320}/_{1210}$ ppb, respectively. These concentrations are relatively close to the median U in amphibole in most mantle samples from the literature, which have a median of 120 $^{430}/_{10}$ ppb, and are relatively high regarding Th in amphibole from the literature (Fig. 4-3) which have a median of 410 $^{1580}/_{14}$ ppb.

4.5 Discussion:

4.5.1 Limitations of reconstructed bulk-rock elemental concentrations from mineral chemistry

There are two critical uncertainties in reconstructing bulk-rock heat producing element (HPE) concentrations from mineral chemistry – the concentration of these elements along grain boundaries prior to transport in a melt and the extent of modal metasomatism in cratonic lithospheric mantle (CLM). Experimental and empirical investigations suggest that grain boundaries in peridotites may be reservoirs for some incompatible elements in the mantle (Hiraga et al., 2004) and HPEs have been shown to be concentrated along grain boundaries in cratonic mantle peridotites (e.g. Eggins et al., 1998; Hiraga et al., 2004; Wittig et al., 2009; Emo & Kamber, 2021). However, in most cases it is impossible to determine if grain boundary enrichment is primary or due to a combination of groundwater infiltration (post-eruption), host melt-infiltration, low-T alteration, or recent metasomatism (Wittig et al., 2009; Emo & Kamber, 2021). The relative contribution of primary versus secondary grain boundary enrichment of HPEs cannot be easily deconvoluted and enrichment in HPEs by late eruption/post eruption fluids has been shown to artificially increase heat generation values derived from bulk-rock analyses of CLM xenoliths to unrealistically high values (e.g. Rudnick et al., 1998). Thus, except in rare cases where secondary grain boundary enrichment can be ruled out (e.g. Ionov and & Wang, 2021), in-situ analyses should be used in evaluating the HPE budget of lithospheric domains. Such an approach is probably acceptable for U and Th when considering their ionic radii, from which thermodynamic modelling suggests grain boundaries may not be significant hosts for these elements in CLM (cf. Hiraga et al., 2004). However, the concentration of K along grain boundaries remains a critical unknown for bulk-rock reconstructed K concentrations.

Clear evidence of metasomatism in CLM is found in the modal mineral proportions of xenoliths. Cratonic mantle formed by high degrees (>30%) of partial melting to produce a dunite or harzburgite residue (Boyd, 1989; Pearson et al., 1995; Bernstein et al., 2006, 2007; Griffin et al., 2009). In contrast, the modal abundances of orthopyroxene, clinopyroxene, garnet, and/or hydrous phases are too high in most cratonic mantle xenoliths to have originated by melt depletion (e.g. Gregoire et al., 2003; Pearson et al., 2003; Simon et al., 2003; Bernstein et al., 2007; Griffin et al., 2009). Instead, the high modal abundance of these phases is the result of modal metasomatism of depleted cratonic mantle (Gregoire et al., 2003; Pearson et al., 2003; Simon et al., 2003; Bernstein et al., 2007; Griffin et al., 2009). Such metasomatic phases have high abundances of HPEs and can raise heat production locally where present and their distribution within CLM is important to consider.

The overprinting of melt-depleted peridotites by modal metasomatism evident in cratonic mantle xenoliths is generally accepted to represent severe sampling bias by kimberlites that preferentially sample metasomatized wall rocks of repeatedly used melt pathways that most easily facilitate melt transport through CLM (O'Reilly & Griffin, 2013). Additional bias towards metasomatic lithologies may come from researchers preferentially sampling metasomatized xenoliths that appear more interesting in their mineralogical diversity than dunites (Rudnick et al., 1998). Thus, most studied CLM xenoliths are likely more metasomatized than the bulk CLM, a hypothesis that is supported by geophysical studies (e.g. Griffin et al., 2009; Artemieva, 2019) and by the occurrence of highly refractory basalt hosted CLM xenoliths erupted during major rifting events (e.g. Hanghøj et al., 2001; Bernstein et al., 2006, 2007). Also, the spatial variability of mantle metasomatism is striking, with xenoliths from some regions, such as the mantle sampled around Kimberley, South Africa, being considerably more metasomatized than that beneath other

locations on the same craton, such as Murowa, Zimbabwe (Pearson et al., 2018). Although this may imply that CLM contains less HPE-enriched metasomatic phases than most of the xenoliths derived from it, because of the sampling bias of melts and possibly researchers, the extent of metasomatism and hence the average modal mineralogy of CLM remains unknown. Nevertheless, the fact that some minimally metasomatized mantle lithologies are erupted as xenoliths, combined with the variety of metasomatic lithologies present in xenolith suites (from our samples and literature compilation), provides a powerful view of the range in HPE contents of cratonic mantle and allows us to evaluate the impact of varying modal mineralogy on heat generation and geotherms.

4.5.2 Lithological endmembers for evaluating mantle heat generation

To evaluate metasomatic variability and its potential effects on heat generation and geotherms, we constrain the heat generation of different endmember lithologies within CLM (Fig. 4-4). Using the database we have assembled (Table 4-1), it is possible to construct any desired mantle lithology, with or without metasomatic phases. Hence if the reader prefers other lithological variants than those we present, they are free to construct their own.

The different model cratonic mantle lithologies in which we evaluated heat generation are:

- *Depleted CLM:* Representing mantle that has experienced extensive melt depletion and minimal metasomatism and is generally unsampled by magmas erupting through it.
- *Refertilized CLM:* Characteristic of CLM peridotite xenoliths hosted in kimberlites and basalts that have experienced some enrichment by addition of clinopyroxene and/or garnet, with the possible presence of minor hydrous phases.
- *Enriched CLM:* A low-volume highly metasomatized endmember of refertilized CLM with 5 to 15% hydrous phases, akin to phlogopite-K-richterite-peridotites (e.g. Erlank et al.,

1987; Waters & Erlank, 1988), phlogopite-wehrlites (e.g. Aulbach, et al., 2017a), and mica-amphibole-rutile-ilmenite-diopside assemblages (MARID; e.g. Fitzpayne et al., 2018).

- *Mafic components:* Some sections of cratonic lithospheric mantle sampled by kimberlite contain evidence of meta-basalt components such as eclogite, present at ~ 1 volume % (Schulze, 1989), or crystallised high-pressure melts such as pyroxenites (e.g. Aulbach et al., 2020).

Below, we estimate the bulk HPE contents in these different categories of mantle components and calculate the resulting heat generation.

4.5.3 Metasomatic enrichment of HPEs and lithospheric structure

For typical metasomatized cratonic mantle – the "refertilized" and "enriched" endmembers – it is important to understand the controls on modal and cryptic metasomatism that can locally concentrate CLM domains in HPEs. Metasomatizing melts in the lithospheric mantle fractionate as they move towards the surface and become increasingly enriched in incompatible elements and volatiles (Waters & Erlank, 1988; McKenzie, 1989; Ionov et al., 2002; Aulbach, et al., 2017b). This melt enrichment would cause consequent enrichment in U and Th in any phase interacting with or crystallizing from the more fractionated melts (Fig. B4-4 and B4-5) and drive an increase in the modal abundance of hydrous phases with decreasing depth (e.g. Waters & Erlank, 1988; Aulbach, et al., 2017a).

Cratonic peridotites equilibrated at mid-lithospheric depths (~2.5 to 3.8 GPa) commonly contain high proportions of metasomatic lithologies (Waters & Erlank, 1988; Griffin et al., 2003; Aulbach, et al., 2017a,b; Perchuk et al., 2020; Özaydın et al., 2021) and in this study olivine, orthopyroxene, and clinopyroxene from these depths are more enriched in U and Th than those from peridotites

equilibrated in the deep CLM (Fig. B4-5). Thus, the HPE distribution in cratonic mantle, as recorded by xenoliths, appears to track trends expected for fractionating metasomatic melts. For instance, the non-hydrous peridotite with the greatest levels of U and Th enrichment – FRB1350 – is a graphite-bearing spinel-garnet lherzolite from Premier, equilibrated at ~ 2.5 to 3 GPa. Similarly, phlogopite- and amphibole-rich peridotites, or those containing the MARID assemblage, also originate from ~ 3 GPa (Waters & Erlank, 1988). Hence, the infiltration and freezing of these metasomatic melts at mid-lithospheric depths likely produce localized highly metasomatized enriched lithologies (our "enriched" CLM endmember) that may be related to mid-lithospheric seismic discontinuities and magnetotelluric anomalies (Waters & Erlank, 1988; Selway et al., 2015; Aulbach et al., 2017a,b; Özaydın et al., 2021). The combination of the high abundance of K-rich phases and the high levels of enrichment in U and Th in all phases generated by this metasomatism create localized zones of higher heat production because metasomatized enriched peridotites have heat production values that are orders of magnitude greater than peridotites whose HPE concentrations are controlled only be melt depletion (melt-depleted CLM endmember) or even "refertilized" CLM. As such, these metasomatic lithologies may be important local heat generating sources in the cratonic mantle underlying kimberlite provinces.

4.5.4 Radiogenic heat production from highly depleted cratonic peridotite – an estimate

The main HPE in Earth's mantle – K, Th and U – are all highly incompatible during mantle melting. This, combined with the geochemical and geophysical indications that typical cratonic peridotite forming the deep mantle roots beneath cratons are residual from the extraction of very large melt-fractions (> 30%; Boyd, 1989; Pearson et al., 1995; Bernstein et al., 2007), means that the heat production from such depleted, un-metasomatized mantle should be very low. Partial melting calculations (Fig. 4-5 A and B) indicate that after only 20% melting, the abundances of

the HPE should be $<<10^{-10}$ ppb, even in clinopyroxene, the phase with the highest solid/melt distribution coefficient for these elements. The concentration of HPE in minerals measured in this study far exceeds concentrations expected from partial melting (Fig. 4-5 A and B) and thus likely exceed that in depleted CLM. However, we note that 100% efficient melt extraction in all peridotite melt residues is unlikely and that some degree of metasomatism by small-degree mantle melts may affect most of lithosphere to varying extents, even in areas that contain primary depleted CLM that exist away from regions pervaded by kimberlitic melts.

We can use measured HPE concentrations in the most depleted peridotites in combination with mineral modes to make estimates of the heat generation in highly depleted CLM. For the most highly depleted cratonic peridotites, modal proportions were assumed to be dunite/harzburgite, with 95 % (by mass) olivine and 5 % orthopyroxene, similar to those from West Greenland and Zimbabwe (e.g. Hanghøj et al., 2001; Bernstein et al., 2006, 2007; Pearson et al., 2018). In olivine, the maximum K value was taken from the detection limits (i.e. 0.03 ppm K) and the average K in orthopyroxene was taken to be 0.22 ppm (the average orthopyroxene analyses above LOQ). To constrain U and Th concentrations in olivine and orthopyroxene, the median of analyses in peridotites with equilibration pressures >4 GPa were used (Table 1) because, as discussed in Section 4.5.3, this portion of the lithosphere is likely to have been metasomatized by less fractionated (enriched) fluids, with lower concentrations of HPE relative to those that reach mid - lithospheric depths. Given these constraints, ~69 % U and 49 % Th of the total peridotite is hosted in olivine and 31 % U and 51 % Th is hosted in orthopyroxene (Fig. 4-6).

The applied K, U, and Th concentrations, combined with the estimated mineral modes for depleted cratonic mantle (Table 4-2), give a heat generation of 0.00004 $\mu W/m^3$. Relative to most previously published estimates for the heat production in cratonic mantle lithosphere, this estimate is between

240 to 2000 times lower (Fig. 4-7), largely because of our focus on in-situ analyses and modal estimates of un-metasomatized lithologies. Clearly, the contribution of depleted, un-metasomatized cratonic peridotite to heat production beneath cratons is negligible.

4.5.5 Radiogenic heat production from refertilized CLM

Estimating K in moderately metasomatized peridotites (i.e. those typical of much of the mantle sampled by kimberlites) is difficult due to the overwhelming addition of K to the bulk-rock from trace additions of phlogopite. Considering that ~0.02 % modal phlogopite would overwhelm the contribution of 5% modal clinopyroxene with an average K of 310 ppm, such small amounts of modal phlogopite could be present (and overlooked) in most mantle xenoliths and would dominate the K budget throughout the metasomatized lithospheric mantle. Because of the significant uncertainty in the modal abundance of phlogopite we defer to bulk-rock rock analyses of K in metasomatized peridotites. Recent bulk-rock analyses of basalt-hosted lightly metasomatized xenoliths yield bulk-rock K concentrations of 291 ppm (Ionov and & Wang, 2021), similar to previous estimated K concentrations in basalt-hosted bulk-rock peridotites (Rudnick et al., 1998). Consequently, if this K was taken up in phlogopite it would be equivalent to ~0.3 % modal phlogopite. In this study, many peridotites have low (<1 vol %) modal phlogopite and 0.3 % phlogopite is approximately consistent with these observed modal abundances. However, we note that the unknown concentration of K along grain boundaries and the variability in phlogopite contents in refertilized peridotites remains a source of error for estimating bulk-rock K in refertilized CLM.

Because of the surprisingly large variation in U and Th found in the anhydrous peridotite minerals, we use the median of all data to counter skew from outlier data (Figs. 4-1 and 4-3; Table 4-1). We use 0.3 % modal phlogopite in refertilized CLM to test the impact of this mineral on the bulk-rock

budget of U and Th and concentration data from moderately metasomatized peridotites (phlogopite bearing garnet peridotites) in this study and Gregoire et al. (2003). Due to the low concentration of U and Th in phlogopite from peridotites with low phlogopite abundances (<1%), phlogopite contributes <2% of the bulk-rock U and Th budget (Fig. 4-6). Amphibole is present only in relatively advanced stages of metasomatism (e.g. Erlank et al., 1987; Waters & Erlank, 1988; Grégoire et al., 2002; Fitzpayne et al., 2018), and is therefore ignored in typical refertilized cratonic peridotites.

 U and Th are sufficiently high in apatite for trace amounts of this phase to impact heat production (Ionov et al., 1997; O'Reilly & Griffin, 2000), making it a potentially important metasomatic heat generating mineral in the refertilized mantle. Because micron-scale apatite is easy to miss during petrographic examination, the La-Th systematics of clinopyroxene can be used to track the abundance and composition of apatite (Fig. 4-5 A and B). Clinopyroxene in refertilized peridotite is almost entirely of metasomatic origin (Gregoire et al., 2003; Simon et al., 2003) and its precipitation will result in the fractionation of the metasomatic melts (McKenzie, 1989; Harte et al., 1993). However, modelled trends in La and Th in clinopyroxene cannot be accounted for solely by fractionation of clinopyroxene and require the presence of trace apatite (Fig. 4-5 A and B). Hence apatite may be more common in peridotites than previously thought.

Although the exact amount of apatite is not possible to constrain, as metasomatism is unlikely to be a homogenous process throughout the lithosphere, modelling of fractionating melts, following the approach of Vernières et al. (1997) allows an approximate estimate of ~0.02% apatite for every 1% modal addition of metasomatic clinopyroxene (Fig. 4-5 A and B). The concentration of U and Th in apatite can be constrained using the theoretical compositions of apatite in equilibrium with clinopyroxene in refertilized peridotites and comparing this to the concentrations from in-situ

studies of mantle apatite (e.g. Ionov et al., 1997; O'Reilly & Griffin, 2000). Using a $D^{ap/cpx}$ of 355 for both U and Th (Chazot et al., 1996) apatite in equilibrium with clinopyroxene in refertilized peridotites (Table 4-1) should contain approximately 28 ppm Th and 16 ppm U, comparable to "magmatic mantle apatite" from other studies (O'Reilly & Griffin, 2000). For heat production calculations, U and Th in apatite is taken as the median of magmatic mantle apatite concentrations given by O'Reilly & Griffin (2000) and its modal abundance is taken as 0.02 % of the total modal clinopyroxene (Tables 4-1 and 4-2).

Using these constraints, the proportions that minerals contribute to the bulk-rock HPE budget of refertilized CLM are shown in Fig. 4-6 and bulk-rock HPE concentrations are given in Table 2. Including apatite yields a present-day radiogenic heat production of 0.006 $\mu W/m^3$ for typical "refertilized" cratonic peridotite. The presence of apatite, in amounts calculated from the above approach (~ 0.04%), accounts for ~0.001 $\mu W/m^3$ of this estimate. Like the depleted mantle endmember, the bulk-rock heat generation for refertilized peridotite is a low estimate for the cratonic mantle (Fig. 4-7) compared to previous estimates (~2 to 14 times lower).

4.5.6 Radiogenic heat production from enriched CLM

Highly metasomatized lithologies from the lithospheric mantle considered here are those containing abundant phlogopite and/or amphibole (e.g. phlogopite-K-richterite-peridotite (PKP) and phlogopite-wehrlite rocks). As these lithologies are exceptionally high in HPE, they may be important local sources of heat generation in the lithospheric mantle.

In these enriched endmember lithologies, high modal contents of phlogopite (8%) and amphibole (12%) will account for >99.7% of the K content in the bulk-rock (Fig. 4-6). Other metasomatic phases containing high concentrations of K (e.g. priderite, lindsleyite-mathiasite, and hawthornite-yimengite; Haggerty, 1983; Foley et al., 1994; Harlow & Davies, 2004; Safonov et al., 2019) have

been recorded in highly metasomatized lithologies within cratonic mantle and may contribute to heat production locally. No such minerals were analysed in this study and they are not considered further. They will only be important to consider if their modal abundance is on a similar order of magnitude as phlogopite, which likely precedes their precipitation from metasomatic (Safonov et al., 2019) and has a higher concentration of K (cf. Haggerty, 1991).

For the enriched endmember metasomite, significant metasomatic enrichment in U and Th is identified using the constraints of La >8 ppm in clinopyroxene and >0.1 ppm in garnet, as such La concentrations mark the most metasomatized samples from this study and the literature (Fig 4-5 A and C). For olivine and orthopyroxene, only samples with equilibration pressures between 2.5 and 4 GPa were used in constraining bulk compositions to approximate the depth of the most enriched interval of the lithosphere, from our studied xenoliths (Fig. B4-5). This is consistent with previous findings (e.g. Waters & Erlank, 1988; Aulbach, et al., 2017a; Özaydın et al., 2021), and the melt-metasomatism model described in Section 4.5.3. Phlogopite analyses used in heat production calculations for the "enriched" CLM endmember are from highly metasomatized lithologies only. For apatite, the modal composition was estimated using the approach applied to refertilized cratonic peridotites. The composition of apatite in equilibrium with clinopyroxene from enriched peridotite (Table 4-1) is ~188 ppm Th and ~50 ppm U. This is similar to that found in highly metasomatized, amphibole-bearing, off-craton, lherzolites (O'Reilly & Griffin, 2000) and hence we use the latter estimate (Table 4-1). The proportion of the bulk-rock HPE concentrations that different minerals contribute is shown in Fig. 4-6. These combined constraints give an estimated heat production of 0.18 and 0.27 $\mu W/m^3$ for PKP and phlogopite-wehrlite lithologies, respectively (Table 4-2). Unlike refertilized peridotites, apatite is a large contributor to heat generation in the

metasomites, significantly increasing the heat generation in hydrous lithologies by ~0.1 $\mu W/m^3$. As such, it would be important to constrain its presence in any detailed study.

Additional lithologies enriched in HPEs that may be important sources of heat generation are the mica-amphibole-rutile-ilmenite-diopside (MARID) and phlogopite-ilmenite-clinopyroxene (PIC) suites. For MARID and PIC suites, the average reconstructed bulk-rock compositions from Fitzpayne et al. (2018) were used, yielding heat generation of 1.12 $\mu W/m^3$ and 1.04 $\mu W/m^3$, respectively for these lithologies (Tables 4-1 and 4-2). Although these lithologies have exceptionally high heat generation, they are often relatively young components of the lithosphere (e.g. Hamilton et al., 1998; Konzett et al., 1998, 2000), which limit their impact on geotherms as discussed below (Section 4.5.8).

4.5.7 Radiogenic heat production from eclogite

To estimate heat generation in eclogite components residing in the cratonic lithospheric mantle root we use the average bulk-rock reconstructed U and Th contents in eclogite of Aulbach & Jacob (2016) (Table 4-2). We use the K contents of clinopyroxene deduced from this study to account for pressure dependence of K in this mineral. Similarly, K is typically at or below detection in eclogitic garnets (Stachel & Harris, 2008) and we use the K content from this study. The modal proportions of clinopyroxene and garnet were taken as 55% and 45 %, respectively. Using these constraints eclogite has a heat generation of 0.006 $\mu W/m^3$. As discussed below, a value of 0.006 $\mu W/m^3$, the same heat generation as refertilized mantle, has a negligible impact on geotherms. Thus, unless significant K is distributed along grain boundaries, eclogite is not an important heat generating source in CLM.

4.5.8 The timing of mantle metasomatism and impacts on lithospheric geotherms

The addition of heat to the mantle lithosphere from the radiogenic decay of HPE hosted within metasomatic lithologies or eclogite components would only impact geothermal gradients preserved in xenoliths if these components existed in the lithospheric mantle on time scales similar to the rate of thermal diffusion through the lithosphere. The time required for diffusive heat transfer through the 250 km thick continental lithosphere is ~2 Gyr (Michaut & Jaupart, 2004; Michaut et al., 2007). Ancient cryptic metasomatism, where incompatible element concentrations are enriched without necessarily adding new minerals, is likely to have occurred early in the history of cratons, as recorded in garnet inclusions from Archean diamonds (e.g. Richardson et al., 1984) and in the complex radiogenic isotope record of the peridotites themselves (e.g. Pearson et al., 1995). However, on the whole, evidence for early metasomatism in cratons is rare and numerous isotopic studies have outlined significant metasomatism occurring in the cratonic mantle that does not significantly predate the host kimberlite (e.g. Pearson & Nowell, 2002; Simon et al., 2007; Aulbach, et al., 2017a). Although their age and longevity are similarly complex, hydrous metasomes such as PKP, PIC and MARID lithologies are likely relatively young or short-lived. These lithologies are composed of phases precipitated at temperatures and pressures close to geothermal gradients (McKenzie, 1989), such that they are likely to melt during thermal perturbation (e.g. plume events and rifting). Thus, hydrous metasomes may not be well preserved in the mantle lithosphere, although some examples have been documented (Carlson & Irving, 1994). Despite the apparent young age of metasomatism in many CLM xenoliths, isotopic systematic of CLM xenoliths are complex and metasomatism is likely to have been a continuous process affecting CLM throughout the history of cratons. If CLM was progressively metasomatized throughout its history, we assume extant CLM is at a metasomatic maximum, in

which case, the heat generation levels recorded in metasomatic lithologies (refertilized and enriched CLM endmembers) are maximum values. In contrast, some eclogites, tectonically emplaced into cratonic mantle lithosphere, have Archean ages (e.g. Pearson et al., 1995; Tappe et al., 2011; Aulbach & Viljoen, 2015). Although, the relatively low heat generation of eclogite, in combination with proportions typically <1% (Schulze, 1989), implies such lithologies likely have little impact on cratonic geotherms.

4.5.9 Implications for steady-state cratonic geotherms – peridotite-dominated lithosphere, no significant local metasomes

The values for lithospheric mantle heat generation used in the literature produce extremely variable geotherms for a given surface heat flow (Fig. 1-1). However, the most widely used estimate of mantle heat production in geothermal models is ~0.02 $\mu W/m^3$ (e.g. Rudnick et al., 1998; Hasterok & Chapman, 2011). To compare a mantle heat generation of 0.02 $\mu W/m^3$ to the depleted CLM endmember of this study (0.00004 $\mu W/m^3$) we construct model geotherms for different scenarios expected for cratonic lithosphere (complete model details are in Appendix A). First, we use such scenarios to explore the impacts of different mantle heat generating estimates on families of geotherms (e.g. Hasterok & Chapman, 2011; Jaupart & Mareschal, 2015; Goes et al., 2020) followed by an exercise in fitting geotherms to P and T data by allowing some free parameters (e.g. Mather et al., 2011).

The first scenario has an unconstrained depth to the lithosphere-asthenosphere boundary (LAB), where the heat flux at the Mohorovičić boundary (moho) accounts for 36% of the total surface heat flux of geotherms (Figs. 4-8 A and B). This ratio of moho to surface heat flux is needed to produce a 185 km thick lithosphere for a geotherm with a surface heat flow of 0.045 W/m^2. We chose a lithospheric thickness of 185 km because the median heat flow at the surface of Archean cratons

is 0.048 W/m^2 (cf. Jaupart & Mareschal, 2015) and the total lithospheric thickness is typically >180 km (Hasterok & Chapman, 2011). This approach is similar to that of Hasterok & Chapman (2011). The second scenario uses a fixed depth to the LAB of 210 km, denoted here as the intercept of the geotherms with the mantle adiabat (Figs. 4-8 C and D). This scenario is used because the high variance in surface heat flow above cratons can be due to variations in heat production in the upper crust and not representative of changes in lithospheric thickness (Jaupart & Mareschal, 2015). The third scenario examines geotherms with fixed moho heat flux of 0.016 W/m^2 (Figs. 4-8 E and F), approximately consistent with that in cratons (Jaupart & Mareschal, 2015). Like the scenario with fixed depth to the LAB, this value is probably relatively constant, whereas upper crustal heat generation is not (Jaupart & Mareschal, 2015). All these scenarios are presented as families of geotherms with surface heat flux that varies from 0.035 to 0.060 W/m^2 (Fig. 4-8) and the different scenario constraints are achieved by varying upper crustal heat generation.

The difference between geothermal models using a mantle heat generation of 0.02 μW/m^3 and heat generation in depleted mantle from this study (0.00004 μW/m^3) is significant where lithospheric thicknesses are characteristic of cratons (Fig. 4-8). Modelled geotherms with unconstrained depth to the LAB and mantle heat generation of 0.02 μW/m^3 may be up to 230 ºC colder and intersect the mantle adiabat at ~83 km deeper than a model using a mantle heat generation of 0.00004 μW/m^3 for a given surface heat flow (Fig. 4-8 A and B). The counterintuitive result in this scenario, where greater heat generation leads to an ultimately colder geotherm, is because without significant heat generation in the CLM, maintaining the observed surface heat flow requires greater heat flow through the cratonic lithosphere that is only achieved by a thinner insulating layer of peridotite (i.e. thinner CLM). Having a higher heat generation of 0.02 μW/m^3 in CLM adds

additional heat flow, requiring a thicker insulating layer to maintain the observed surface heat flow.

Geotherms using a fixed depth to the LAB result in temperatures ~45 ℃ hotter at mid-lithospheric depths for a lithospheric mantle with 0.02 $\mu W/m^3$ heat generation (Fig. 4-8 C and D) compared to 0.00004 $\mu W/m^3$. Geotherm models using fixed heat flow across the moho constrained to 0.016 W/m^2 (Jaupart & Mareschal, 2015) yield, on average, geotherms that are ~110 ℃ colder and intersect the mantle adiabat ~20 km deeper when using lithospheric mantle heat generation of 0.02 $\mu W/m^3$ versus 0.00004 $\mu W/m^3$. A similar exercise carried out by constructing geotherms that use the refertilized mantle endmember and eclogite with a mantle heat generation of 0.006 $\mu W/m^3$ compared with geotherms using the literature value of 0.02 $\mu W/m^3$, give similar results (Fig. B4-6) and the impact of significantly more metasomatic lithologies on geotherms is discussed in Appendix D.

To evaluate how using the heat generation of depleted CLM found in this study vs a value of 0.02 $\mu W/m^3$ may impact our geothermal model when fitted to pressure and temperature constraints, a Monte Carlo simulation was performed by randomly varying surface heat flow and heat generation in the upper crust (Fig. 4-9). In the output of the simulation, we evaluate how the depth to the LAB is related to the goodness of fit of temperature at pressure ($\chi^2 = \Sigma[(T(P)_{xenolith} - T(P)_{geotherm})^2/T(P)_{geotherm}]$) between xenolith data and geotherm (Fig. 4-9). In addition, we use two sets of data (Kopylova et al., 1999; Mather et al., 2011) that fall along cold (surface heat flow of ~0.035 W/m^2) and warm (surface heat flow of ~0.045 W/m^2) cratonic geotherms. At the lowest χ^2 from simulations using the cold geotherm, depth to the LAB is ~30 km deeper when using a heat generation of 0.02 $\mu W/m^3$ vs 0.00004 $\mu W/m^3$ (Fig. 4-9). For the warmer geotherm at the lowest χ^2 the LAB is ~10 km deeper for the higher heat generating value (Fig. 4-9). However, acceptable

solutions to fitting geotherms to the P and T arrays give estimated depths to the LAB above and below these optimal solutions at lowest χ^2. It is additionally important to note that such an exercise cannot be reversed to precisely determine CLM heat generation by fitting geotherms to P and T data due to uncertainties in model parameters and scatter in P and T arrays (e.g. Russell et al., 2001; Michaut et al., 2007).

Clearly, the different mantle heat generating estimates used in the literature (Fig. 4-7) result in significant differences in deep lithosphere temperatures (Figs. 1-1, 4-8, and 4-9). Using common values (e.g. 0.02 $\mu W/m^3$) may overestimate the diamond window (the portion of the lithosphere in the diamond stability field) and depth to the LAB by 10's of km for very cold geotherms with a surface heat flow of 0.035 W/m^2. Even for geotherms with surface heat flows of 0.040 to 0.050 W/m^2, the diamond stability field and depth to LAB may be overestimated by >10 km when using mantle heat generation of 0.02 $\mu W/m^3$.

4.6 Conclusions

Despite the carefully considered heat production estimates for CLM from past studies (Rudnick et al., 1998; Rudnick & Nyblade, 1999; Russell et al., 2001; Michaut et al., 2007; Hieronymus & Goes, 2010; Hasterok & Chapman, 2011; Goes et al., 2020), there has been little agreement on an accurate value for typical melt-depleted compositions, with anomalously high and widely varying values being used in geotherm models (Figs. 1-1 and 4-7). The use of in-situ analytical methods in this study circumvents the bias to high HPE contents evident in bulk-rock trace element data that can reflect kimberlite and basalt infiltration (e.g. Rudnick et al. 1998; Emo & Kamber, 2021). Our new database and literature compilation for HPE concentrations in cratonic mantle peridotites refines the constraints on the radiogenic heat production inherent within cratonic mantle and allows a re-evaluation of cratonic lithospheric mantle HPE concentrations. Moreover, the new data,

combined with published data, allow estimates of HPE concentrations in wide-ranging lithological models of cratonic mantle lithologies.

For the most melt-depleted cratonic lithosphere, minimally affected by metasomatism, we estimate a radiogenic heat production value of 0.00004 $\mu W/m^3$, which is ~2 to 3 orders of magnitude lower than most previous estimates (Fig. 4-7). Similarly, heat generation in metasomatized CLM, more typical of the compositions sampled by kimberlite-borne xenoliths (0.006 $\mu W/m^3$) is significantly lower than past estimates (Fig. 4-7). Although the extent of these lithologies is unknown within the cratonic mantle, we note that sampling bias by melts results in higher proportions of metasomatized lithologies available for study than may be present in CLM and that a portion of the metasomatism in these lithologies is too recent (e.g. Pearson & Nowell, 2002; Simon et al., 2007; Aulbach et al., 2017a; Pearson et al., in press) to impact geotherms. Thus, we suggest that 0.006 $\mu W/m^3$ is a maximum and unlikely value for heat generation to dominate bulk CLM. In contrast, it is unlikely that CLM maintained a melt depleted composition for billions of years and 0.00004 $\mu W/m^3$ is a minimum heat generation of CLM. It is more likely that the average heat generation in cratonic mantle peridotites lies somewhere between these values. Model geotherms, using either of these new values for mantle heat generation, estimate a depth to the LAB that can be anywhere from ~10 to up to 80 km shallower than models using most previous estimates for mantle heat generation (Fig. 4-8, 4-9 and B4-6), depending on the model.

For higher heat generating metasomatic lithologies (PKP, phlogopite-wherlites, MARID, and PIC), the relatively young age of such metasomatism (e.g. Konzett et al., 1998, 2000; Aulbach et al., 2017a) mean that their presence is unlikely to impact the geotherms reflected in the coexisting less metasomatized peridotites on billion-year timescales. Even eclogite, with heat generation of 0.006 $\mu W/m^3$, is unlikely to impact geotherms over the life of the mantle root.

Overall, we conclude that when radiogenic heat production in bulk cratonic mantle lithosphere is being examined in regions away from extensive metasomatism, the mantle component of heat production can be considered negligible and geotherms should be modelled accordingly.

4.7 Tables and Figures

Table 4-1 Constraints on heat producing elements in various minerals of cratonic lithospheric mantle.

			Ol	OPX	Grt	CPX	Phl	Ap	Amph	Rut	Ilm
	K	Conc' (ppm)	<0.03	0.22	~0.1	310	83015		11539		
		St. Dev.		0.08			4980		166		
Depleted CLM[1]	U	Conc' (ppb)	0.07	0.6	20	11					
		Range	0.02 - 0.18	0.03 - 0.9	0.2 - 40	1 - 15					
	Th	Conc' (ppb)	0.05	1	7	34					
		Range	0.02 - 0.11	0.2 - 1.6	0.06 - 20	2 - 73					
Refertilized CLM[1]	U	Conc' (ppb)	0.1	0.8	40	44	6	4400			
		Range	0.02 - 0.3	0.03 - 1.6	0.2 - 70	1 - 200	1 - 15	1200 - 11 900			
	Th	Conc' (ppb)	0.33	1.1	20	80	32	12 200			
		Range	0.02 - 0.9	0.2 - 4	0.06 - 40	2 - 439	6 - 112	3500 - 30 000			
Enriched CLM[1]	U	Conc' (ppb)	0.2	4.3	76	140	119	83 000	106		
		Range	0.02 – 1	0.6 – 22	23 - 236	18 - 447	3 - 643	14 000 – 200 000	10 – 401		
	Th	Conc' (ppb)	0.5	7.7	62	530	1134	203 000	417		
		Range	0.1 – 1.8	0.7 - 34	13 - 180	48 - 1494	4 - 7448	50 000 – 509 000	14 - 1619		
MARID[2]	U	Conc' (ppb)				5.5	112		38	2580	24
		Range				0.4 – 22.8	5 – 425		10 - 90	424 - 6070	4 – 56
	Th	Conc' (ppb)				32	1037		118	26	8
		Range				0.2 – 164	10 - 5480		42 - 283	3 - 109	1 - 54

Table 4-1 continued

			Ol	OPX	Grt	CPX	Phl	Ap	Amph	Rut	Ilm
PIC[2]	*U*	Conc' (ppb)				24	8.2				8
		Range				14 – 242	3.6 – 21				3 - 16
	Th	Conc' (ppb)				78	21				1.7
		Range				64 - 464	1 - 83				1 – 3.7

[1]This study and references from Section 4.2.
[2]Grégoire et al. (2002) and Fitzpayne et al. (2018).
*Ranges are excluding outliers defined as the median plus/minus 1.5 times the interquartile range.

Table 4-2 Estimated bulk-rock contents and heat generation for endmember-compositions of CLM.

		Modal proportions							Bulk-rock compositions			Heat generation ($\mu W/m^3$)**
		Ol	OPX	Grt	CPX	Phl	Amph	Ap*	K_2O (wt%)	U (ppm)	Th (ppm)	
Depleted CLM		0.95	0.05						5×10^{-6}	0.0001	0.0001	4×10^{-5}
Refertilized CLM		0.61	0.32	0.042	0.021	0.003		0.0004	0.03	0.004	0.005	0.006
Enriched	*PKP*	0.56	0.07	0.12	0.05	0.08	0.12	0.001	0.97	0.12	0.38	0.18
CLM	*Phl-wehrlite*	0.75			0.12	0.13		0.002	1.1	0.11	0.39	0.27
Eclogite		Average reconstructed bulk-rock							0.02[1]	0.01[2]	0.01[2]	0.006
MARID		Average reconstructed bulk-rock[3]							7.9	0.19	1.63	1.12
PIC		Average reconstructed bulk-rock[3]							8.9	0.014	0.08	1.04

*The modal proportion of apatite is assumed to be 0.02*clinopyroxene above depleted CLM.
**Heat generation is calculated using the equation $A = 10^{-5}\rho(3.5*K_2O + 9.67*U + 2.63*Th)$, where K_2O is in wt% and U and Th are in ppm. P is the density of peridotite and given in Appendix A.
[1] From bulk-rock K concentrations in clinopyroxene and garnet from this study. See text for details.
[2]Aulbach & Jacob (2016)
[3]Fitzpayne et al. (2018)

130
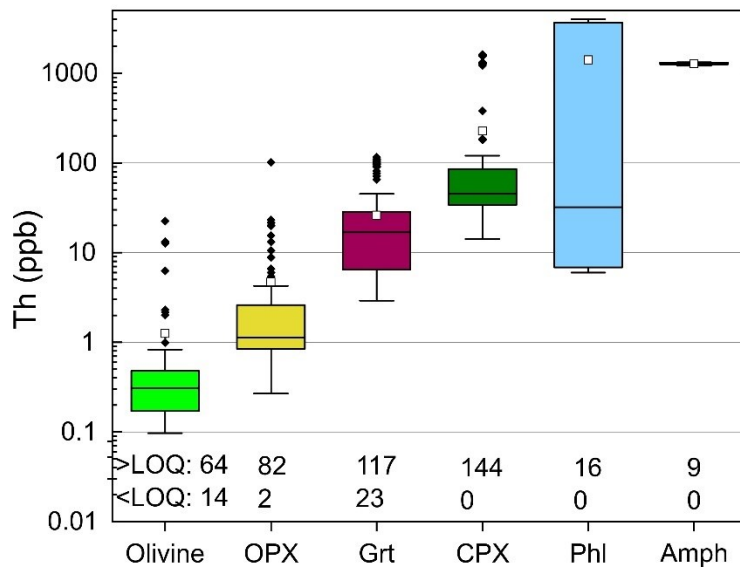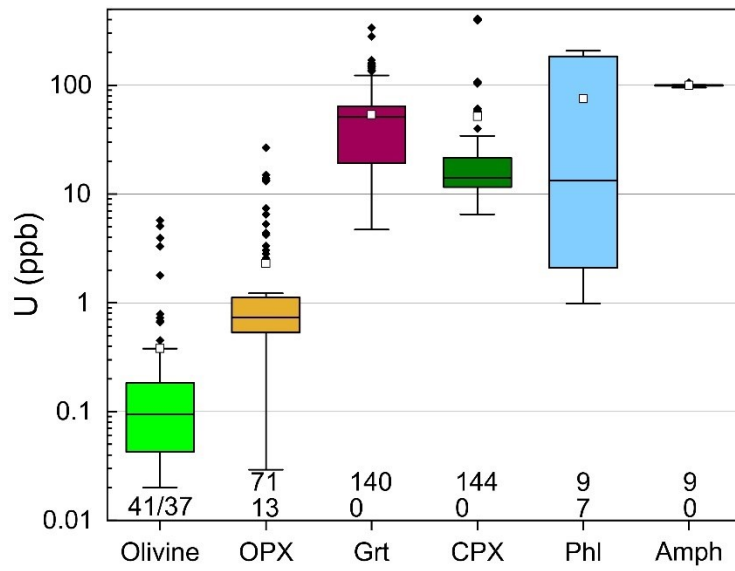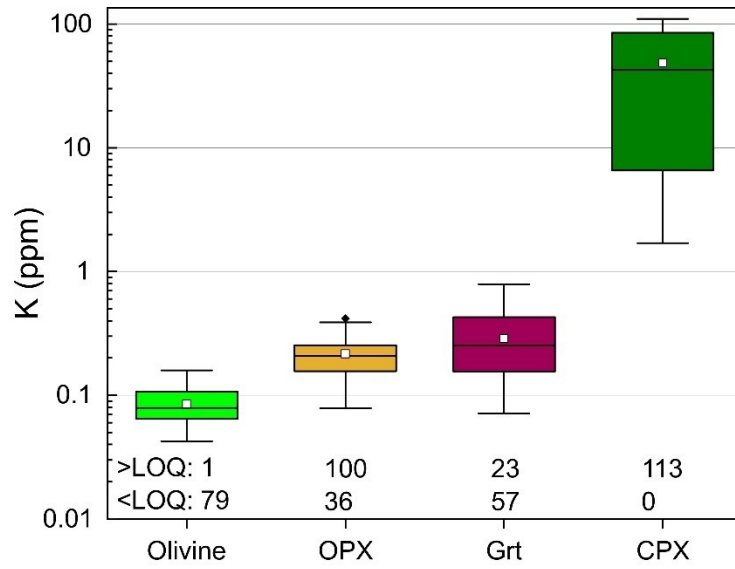
Fig. 4-1. Box and whisker plots of K, U, and Th concentrations in mantle peridotite minerals analysed in this study. White squares are average analyses, diamonds are outliers, the boxed areas represent the bounds of upper and lower quartiles, the median is the line through the box, and the whiskers are the median plus or minus l.5 times the interquartile range. Treatment of data follows that outlined in the Chapter 4 Results section, with a screen for the limit of quantification (LOQ) applied to each analysis. For analyses below the LOQ, the LOQ value is used. The number of analyses above and below LOQ are shown at the bottom of each plot.
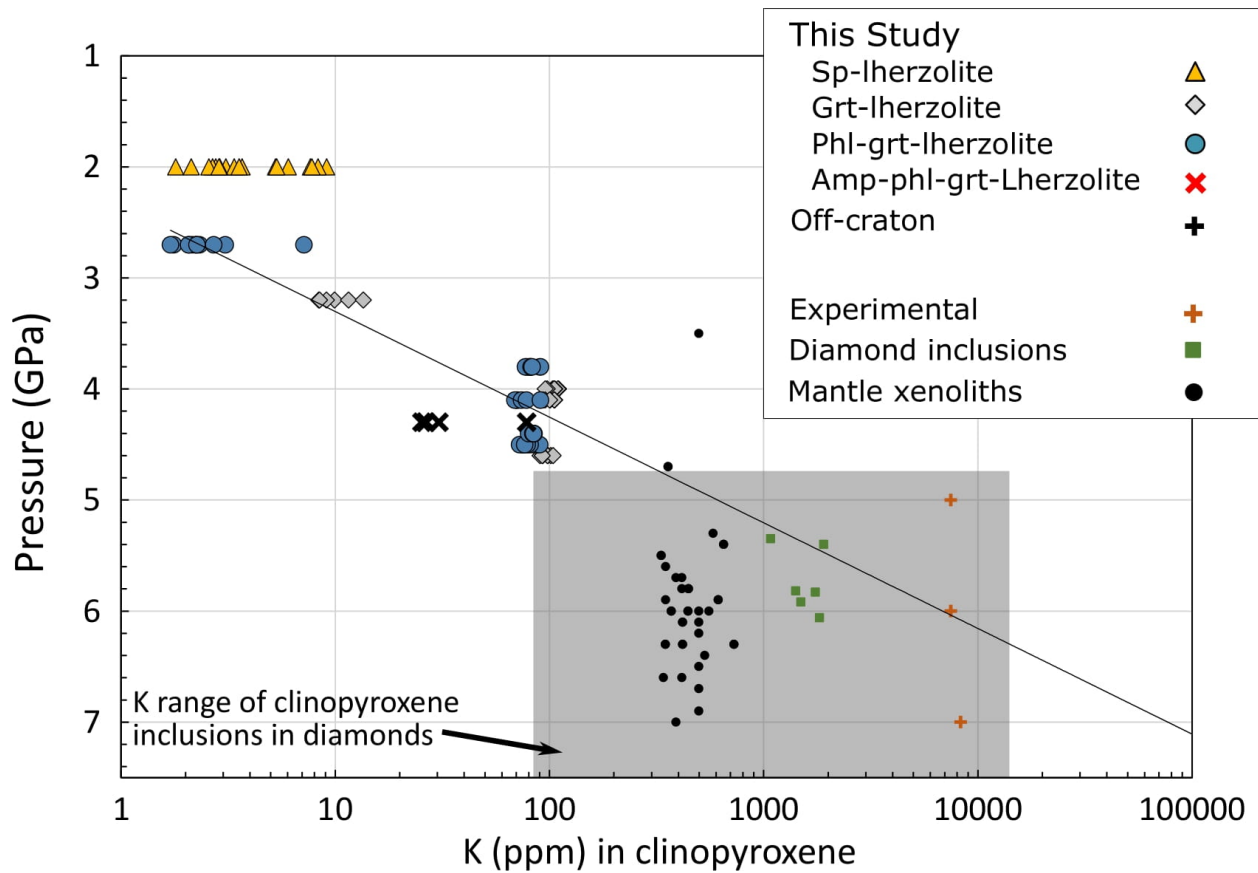
Fig. 4-2. Pressure vs K in clinopyroxene for mantle peridotites/metasomites analysed in this study and the literature showing a strong correlation. The black line is a logarithmic regression line to the garnet peridotites from this study. Shaded field of clinopyroxene inclusions in diamond are from Griffin et al. (1988) and Stachel & Harris (2008) and individual data points are from Wang & Gasparik (2001). Xenolith data are from cratonic mantle xenoliths (Section 4.2) and a 0.04 wt% K_2O cut off was used to approximate LOQ, avoiding potentially spurious data. Experimental data on K in clinopyroxene is from Harlow (1997) (high pressure experiments (10 to 11 GPa) are not shown but have up to 40 000 ppm K).
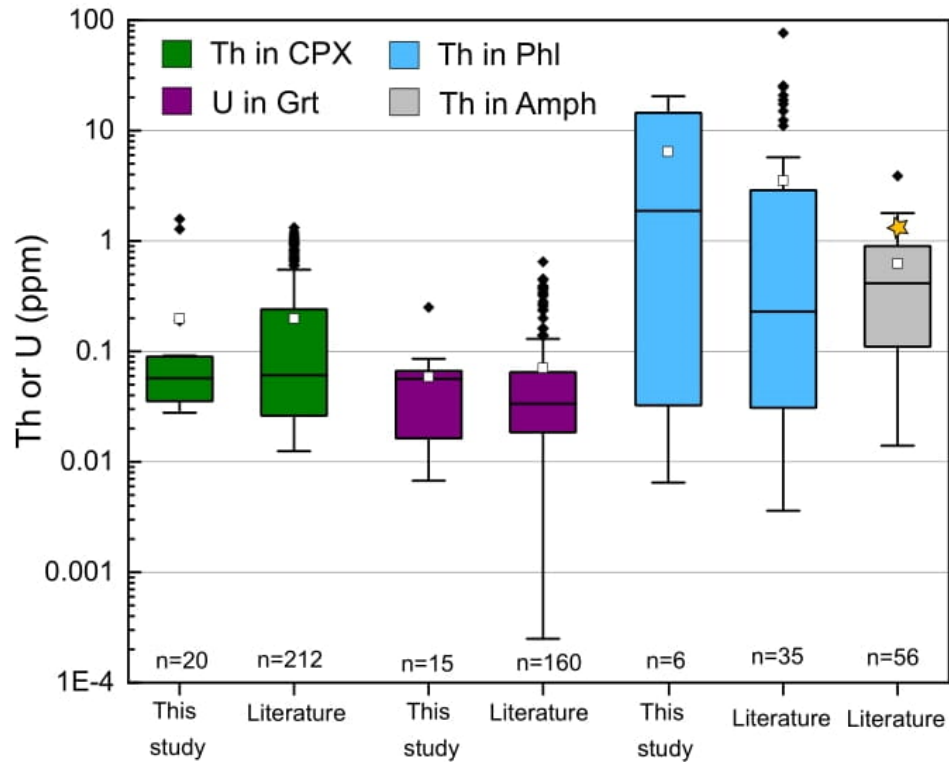
Fig. 4-3. Concentrations (in ppm) of U and Th in peridotite minerals in this study compared with a compilation of literature data (n is the number of samples included in the plot). The yellow star represents the value for the amphibole from metasomite BR-1 from this study. Literature data sources given in Section 4.2.
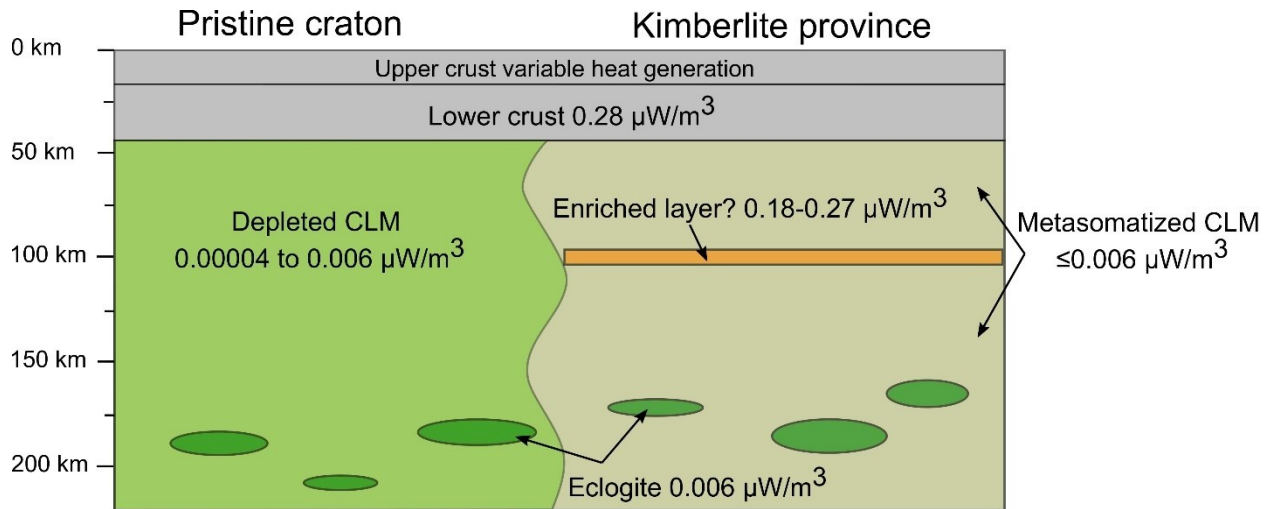
Fig. 4-4. Conceptual model of the likely variation in heat generation in cratonic mantle lithosphere including localized sources of heat generation from metasomatized peridotites/lithologies and eclogites. Lower crustal heat generation is from Hacker et al. (2015). Based on the original concept by Artemieva (2019).
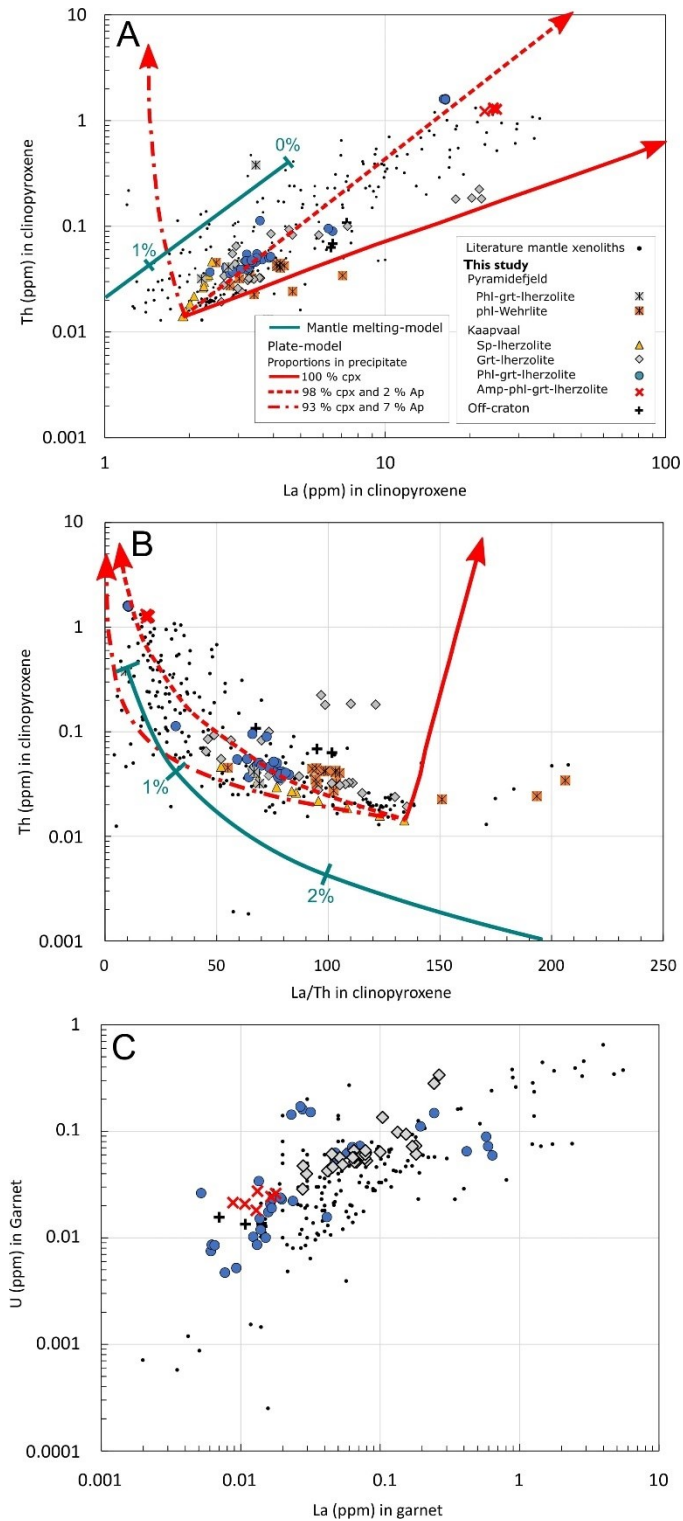
Fig. 4-5. Metasomatic enrichments of Th in clinopyroxene as function of La (A) and La/Th (B) and U in garnet as a function of La (C). The plate model (A and B) is that of Vernières et al. (1997) used for modelling melt migration in the mantle simulating a chromatographic column and tracks

metasomatic enrichment in La and Th in clinopyroxene by fractionating melts precipitating different proportions of clinopyroxene (cpx) and apatite (ap). Distribution coefficients used for clinopyroxene and apatite are from Chazot et al. (1996). For the plate model, 12 cells were used and the 11th increment shown in the figure. A constant porosity of 0.01 was used by setting dissolution equal to the volume of clinopyroxene and apatite precipitated. The different models resulted in a mass increase in clinopyroxene of ~5.1, 5.0, and 4.7% and in apatite of 0, 0.1, and 0.3% in the residual peridotite for 0, 2, and 7% apatite in the precipitate, respectively. Initial bulk-rock Th and La used in both models were deduced from LA-ICPMS analyses in this study and set to 0.0001 ppm and 0.011 ppm, respectively. Similarly, initial melt compositions were set by assuming clinopyroxene in sample M5 in equilibrium with a melt resulting in the initial fluids having 12.6 ppm Th and 17 ppm La. The plate model shows that clinopyroxene precipitation in the absence of apatite is unlikely to account for the observed trends in the data and the model in which the precipitate is 98% clinopyroxene and 2% apatite best tracks the overall distribution of samples from this study and the literature (see Section 4.2 for references). The melting model (A and B) is that of Johnson et al. (1990) modelling the fractional melting of peridotite. The initial peridotite composition was set to primitive mantle (McDonough & Sun, 1995). The distribution coefficients were from Johnson et al. (1990) and Salters et al. (2002). The percent values show the percent melting of primitive mantle. Considering that residual cratonic mantle forms by melting in excess of 30%, the model shows that the observed trends cannot be melting trends.
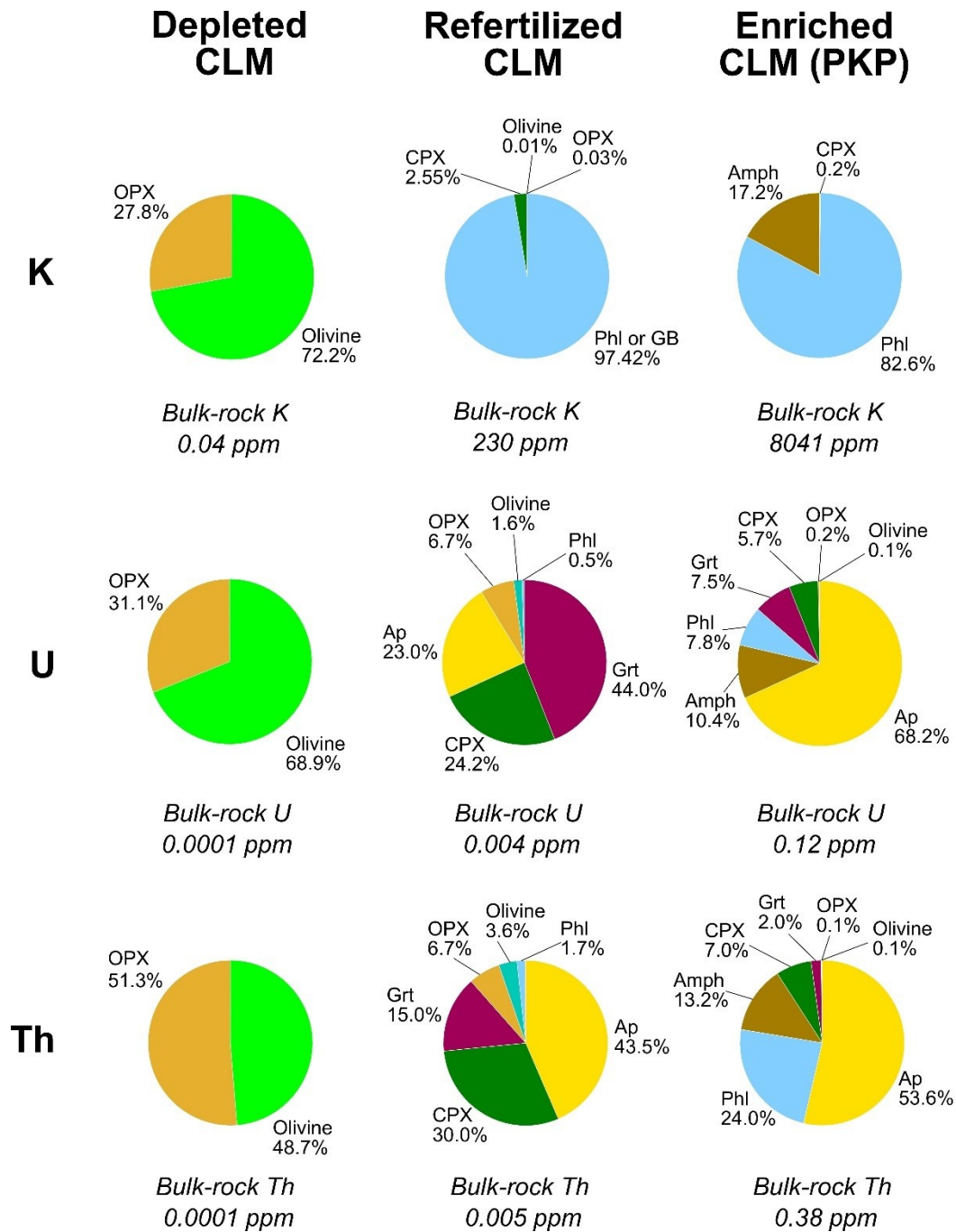
Fig. 4-6. Pie charts for different endmember lithologies discussed in text. Concentrations of elements in and modal proportions of minerals for the three endmember lithologies are given in Tables 4-1 and 4-2. Acronyms - OPX; orthopyroxene, grt; garnet, CPX; clinopyroxene, Phl; phlogopite, Amph; amphibole, and ap; apatite.
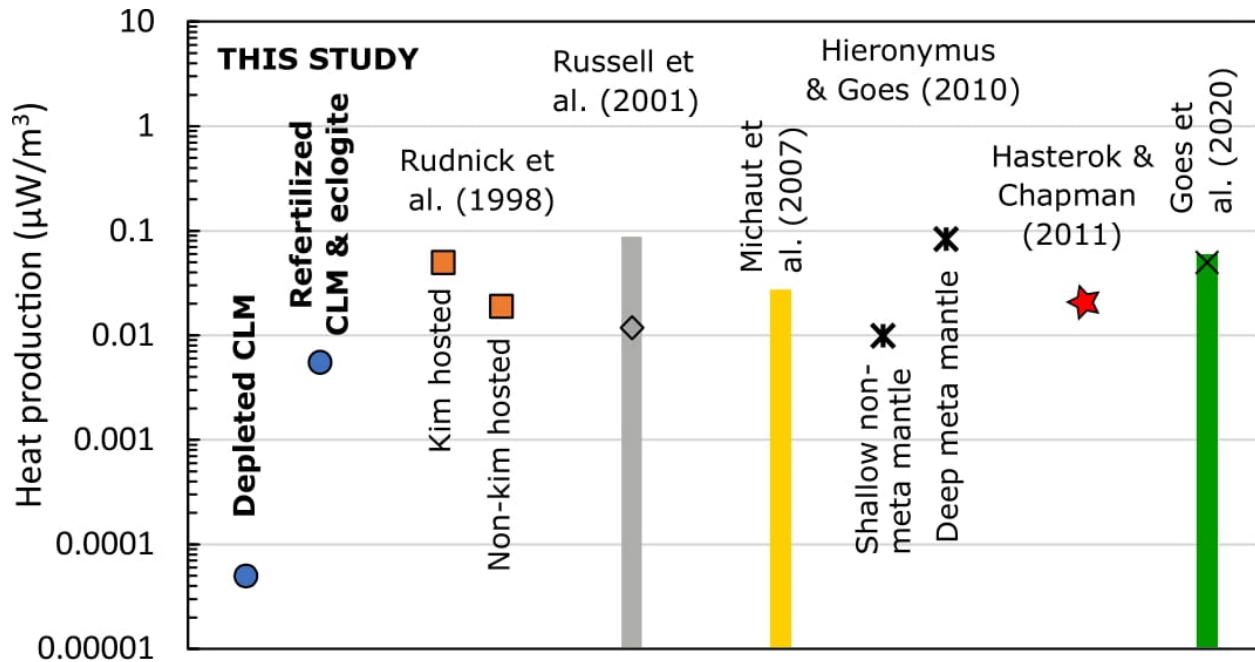
Fig. 4-7. Heat production estimates for cratonic lithospheric mantle derived from this study (Table 4-2) compared with published estimates. Depleted mantle values from this study are estimated from in-situ analyses of least metasomatized minerals and the refertilized mantle estimate is based on in-situ analyses of minerals typical of kimberlite hosted xenoliths. Data from Rudnick et al. (1998) are the median bulk-rock HPE measurements for kimberlite (kim) hosted and non-kimberlite hosted mantle xenoliths. The range (grey bar) estimate from Russell et al. (2001) is the range in heat production in the lithospheric mantle that best fits temperature and pressure arrays recorded in xenoliths and the data point in the range is their preferred value. The range (yellow bar) from Michaut et al. (2007) are Monte Carlo simulations to determine the range in geothermal parameters that best fit temperature and pressure arrays. Heat production values (black stars) from Hieronymus & Goes (2010) are estimates from the literature for deep (>120km depth) metasomatized (meta) mantle and shallow non-metasomatized mantle. The value (red star) from Hasterok & Chapman (2011) is derived from bulk-rock HPE measurements for mantle xenoliths. The range (green bar) from Goes et al. (2020) was used in their models and the black cross is their best estimate of heat generation for refertilized cratonic lithospheric mantle.
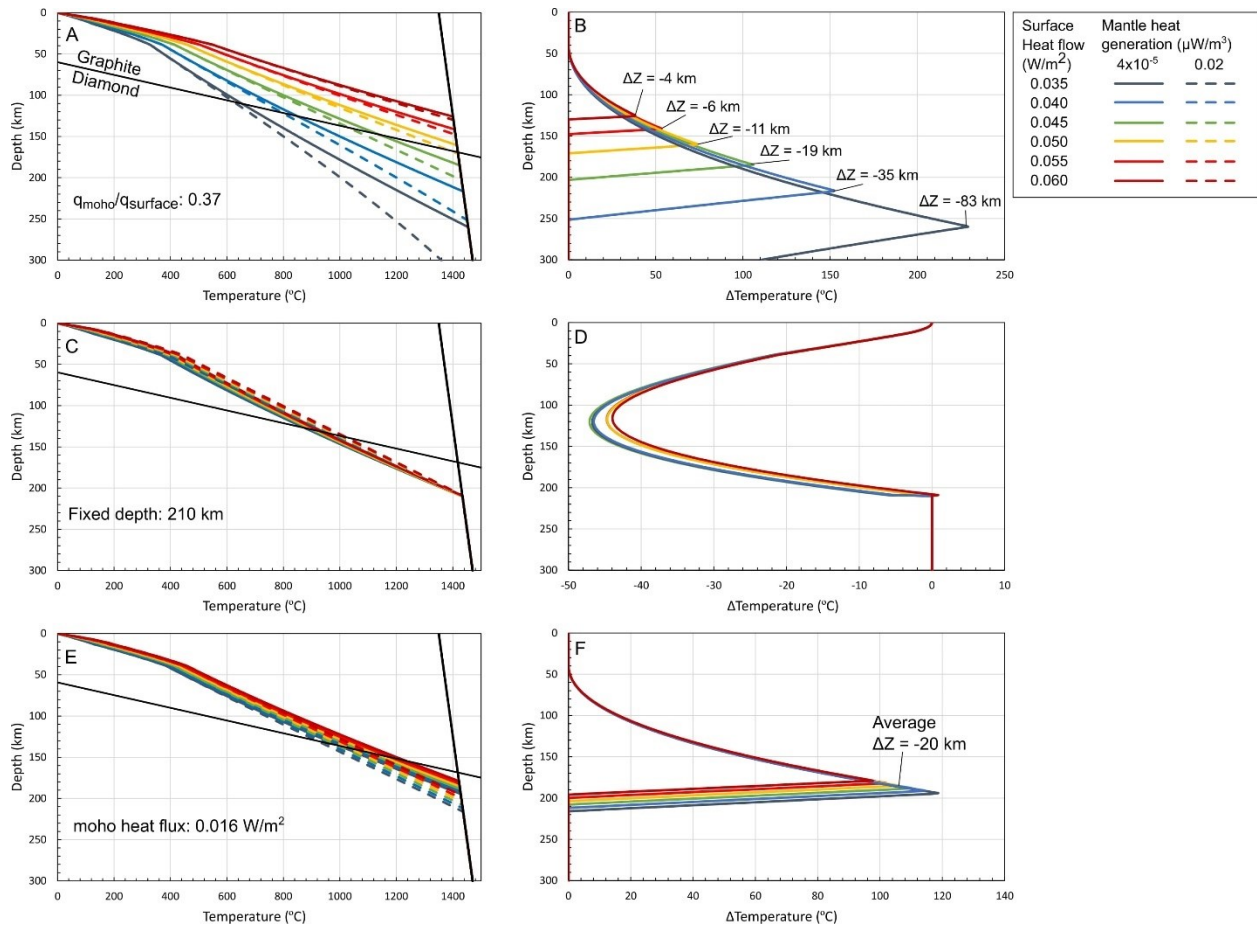
Fig. 4-8. Modelled geotherms comparing mantle heat generation of 0.00004 µW/m³ (the depleted CLM endmember in this study) to 0.02 µW/m³ (the value used by Hasterock & Chapman, 2011). Model details are given in Fig. 1-1 and Appenix A. Figures in the first column (Panels A, C, and E) are geotherms with different scenarios expected for cratons (unconstrained depth to the LAB and ratio of moho heat flux to surface heat flux of 0.37, fixed depth to the LAB, and fixed moho heat flux). These scenarios are discussed in Section 4.5.9.1. Figures in the second column (Panels B, D, and F) compare the difference in temperature at depth (ΔT: geotherm2(0.00004 µW/m³) – geotherm1(0.02 µW/m³)) for each scenario using the two different mantle heat generation estimates. ΔZ compares the depth the geotherms intersect the mantle adiabat when using the two different estimates for mantle heat generation. ΔZ for constant moho heat flux of 0.016 W/m² (Panel F) ranges from -18 to -23 km, with an average value of -20km. The inflection points in column 2 (Panels B and F) are the intercept of the geotherm using a mantle heat generation of 0.00004 µW/m³ with the mantle adiabat.

139
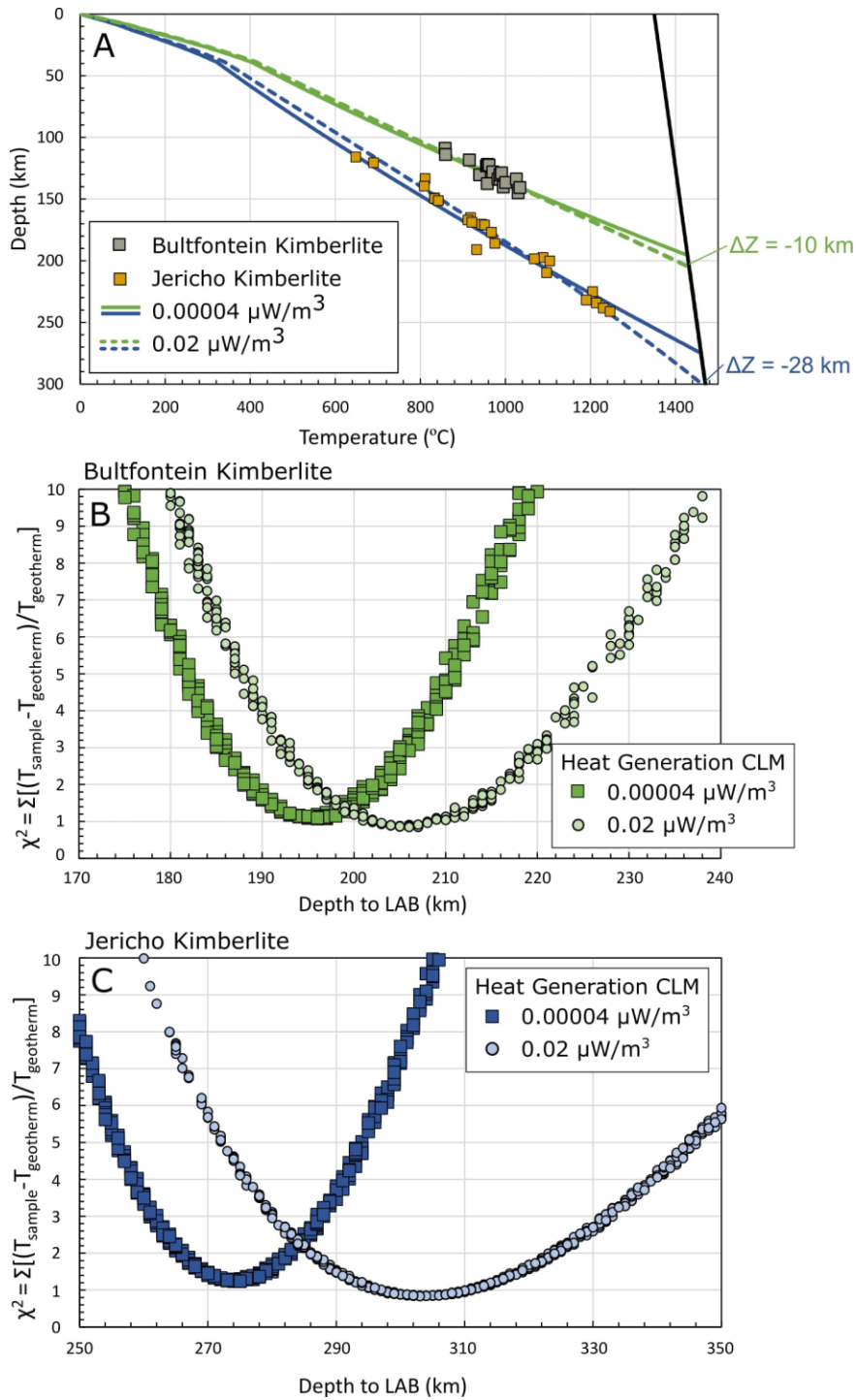
Fig. 4-9. A) Solutions for geotherms to pressure and temperature data using both mantle heat generation of 0.00004 µW/m³ and 0.02 µW/m³ where χ^2 ($\Sigma[(T(P)_{xenolith} - T(P)_{geotherm})^2/T(P)_{geotherm}]$) is lowest. The two pressure and temperature arrays approximate geotherms with surface heat flows of 0.035 W/m² (Jericho) and 0.045 W/m² (Bultfontein). B) and C) χ^2 vs depth to LAB for Monte

140

Carlo simulations for varying surface heat flux and upper crustal heat generation in the geotherm models from A). The results show that the best solution of geotherms to the xenolith data when using a mantle heat generation of 0.00004 vs 0.02 results in a ~30 km difference in depth to the LAB for the relatively cold geotherm (Jericho) and ~10 km difference for the warmer geotherm (Bultfontein). Other model details are given in Fig. 1-1 and Appendix A. Pressure and Temperature data are from Kopylova et al. (1999) and Mather et al. (2011).

Chapter 5
Conclusions

The purpose of the research in this thesis was to contribute to our knowledge of the current state of cratons and their evolution through time.

In **Chapter 2**, the research I present adds to our understanding of the crustal components that make up the Archean portions of cratons. I report the petrogenetic characteristics of an ancient fragment of crust, the ~3180 Ma Qorlortoq gneiss and its included components, i.e., cumulate enclaves and basaltic dykes. The Qorlortoq gneiss is significantly older than most other Archean components that comprise the Nagssugtoqidian orogen (NO) where the Qorlortoq gneiss exists. Like the episodic hiatus in the Nuuk region in the nucleus of the North Atlantic craton (NAC; Næraa et al., 2012), this may imply changes in local geodynamic processes over this time period. This would be largely consistent with the mantle peridotite Re-Os model ages that show the CLM of the NAC to have stabilized around ~2800 Ma rather than at the time in which the Qorlortoq gneiss formed (Wittig et al., 2010). This probably signifies a change in geodynamic processes from a style that does not preserve lithosphere as a whole to one that does at ~2900 Ma. It further likely signifies that such processes were not occurring during the formation of the Qorlortoq gneiss.

Chapter 3 contributes to the study of craton evolution by showing that sub-arc peridotites are likely components of Paleoproterozoic cratonic lithosphere. In this study I report an in-depth assessment of a mantle tectonite hosted in the Paleoproterozoic Nagssugtoqidian orogen, the Ussuit peridotite. The peridotites from this dismembered tectonite have primary and secondary geochemical signatures that strongly imply a sub-arc influence. In addition, the tightly clustered ~2000 Ma Re-Os model ages overlap the age of the spatially associated oceanic arc lithologies, the Ussuit unit. Moreover, this melt-depletion age for the peridotites overlaps a global increase in

the production of cratonic lithosphere at this time and mantle xenoliths from such lithosphere share geochemical similarities with the Ussuit peridotite. The inference that sub-arc processes may have played a role in generating portions of the cratonic lithosphere, including the refractory composition of its mantle keel, is an important milestone in understating the processes leading to formation and stabilization of cratons.

Chapter 4 provides important constraints on heat generation in the lithospheric mantle that will be valuable to the scientific community. Prior to this study, estimates of heat generation in the CLM used in modelling the thermal structure of cratonic lithosphere varied significantly (e.g. Rudnick et al., 1998; Michaut & Jaupart, 2004; Michaut et al., 2007; Hieronymus & Goes, 2010; Hasterok & Chapman, 2011; Jaupart & Mareschal, 2015; Goes et al., 2020). Some of these estimates were based on bulk-rock chemistry and subject to uncertainty regarding the infiltration of host melts (e.g. Rudnick et al., 1998; Hasterok & Chapman, 2011). The approach used here, i.e., in situ analysis of heat producing elements in mantle minerals, not only avoids this issue but also allows for the estimation of heat generation in a variety of mantle lithologies, not just a single value for the entire CLM. Using the concentration of heat producing elements in minerals measured in this study, the estimated heat generation in the cratonic mantle lithosphere ranges from 0.00004 to 0.006 $\mu W/m^2$, estimates which are 3 to 1000 times lower than commonly used mantle heat generation estimates. Using these new constraints, the depth to the lithospheric asthenospheric boundary may be estimated to be 10 to up to 80 km more shallow than when using heat generation values based on bulk-rock xenolith measurements of heat producing elements.

5.1 Future Directions

The studies in this thesis reveal several opportunities for future work that can significantly broaden our understanding of cratonic petrogenesis and evolution. The relatively small study of Chapter 2

highlights important missing information on the crustal architecture of the NAC. Importantly, a thorough crustal mapping initiative should be undertaken using modern geochemical methods for understanding geodynamic environments and magmatic evolution. This would include U-Pb/Lu-Hf split-stream laser ablation ICPMS in zircons from basement gneisses from across the NAC in West Greenland to reveal recycled components that may be similar between terranes. In addition, several new methods in zircon trace element geochemistry can be used to derive important information regarding magmatic processes, such as, temperature of formation (Fu et al., 2008) and oxygen fugacity (Loucks et al. 2020), which may highlight temporal changes related to changing Archean geodynamic environments. Such studies may provide information on how the many different Archean terranes in the NAC may have been related at the time of their formation.

In Chapter 3, it was suggested that sub-arc hydrous flux melting was in part responsible for the refractory compositions of Paleoproterozoic cratonic lithospheric mantle. However, further work is required to understanding the full extent of influence of hydrous flux melting on Paleoproterozoic cratonic mantle and the melting environment of Archean cratonic mantle. An approach to accomplish this is to consider modelling of residual mantle columns at midocean ridges, e.g., Scott & Stevenson (1989), using early earth mantle potential temperatures and compare this with models for lithospheric thickening, e.g., Wang et al. (2018), and data from mantle xenoliths that reflect the architecture of cratonic lithospheric mantle. This approach can be used to evaluate if melting at mid-ocean ridges combined with lithospheric thickening can account for the entire range of melt depletion recorded in cratonic lithospheric mantle or if other processes, like hydrous flux melting, are required to significantly facilitated melting throughout a residual mantle column. The results of such a study would be far reaching regarding our understanding early earth geodynamic regimes.

A significant number of potential studies can be derived from Chapter 4. Firstly, it was shown that there is a pressure dependence of K in clinopyroxene. It was outside the scope of this study to derive a mineral barometer for K in clinopyroxene. However, if such a barometer could be derived from further studies, it would provide a much-needed tool for determining pressure in mantle xenoliths derived from the spinel stability field. High potential impact studies from Chapter 4 would also include using the updated constraints on the concentration of heat producing elements in mantle minerals to model geotherms in cratonic lithosphere. Such studies could greatly improve our understanding of the heat flow in cratons which may have previously been derived from modelling using lithospheric mantle heat generation that is unrealistically high. Because of the diversity and global distribution of cratons, such studies would necessarily be numerous and require a reevaluation of geotherms on a global scale. Once complete, such studies could greatly improve our understanding of the heat generation within the cratonic lithospheric mantle and hence the thermal evolution of the earth.

References

References for Chapters 1-5 and Appendices A and B

Ackerman, L., Walker, R. J., Puchtel, I. S., Pitcher, L., Jelínek, E., & Strnad, L. (2009). Effects of melt percolation on highly siderophile elements and Os isotopes in subcontinental lithospheric mantle: A study of the upper mantle profile beneath Central Europe. *Geochimica et Cosmochimica Acta*, *73*, 2400–2414.

Agashev, A. M., Ionov, D. A., Pokhilenko, N. P., Golovin, A. V., Cherepanova, Y., & Sharygin, I. S. (2013). Metasomatism in lithospheric mantle roots: Constraints from whole-rock and mineral chemical composition of deformed peridotite xenoliths from kimberlite pipe Udachnaya. *Lithos*, 160–161, 201–215.

Alard, O., Griffin, W. L., Lorand, J. P., Jackson, S. E., & O'Reilly, S. Y. (2000). Non-chondritic distribution of the highly siderophile elements in mantle sulphides. *Nature*, *407*, 891–894.

Alemayehu, M., Zhang, H. F., & Aulbach, S. (2017). Persistence of fertile and hydrous lithospheric mantle beneath the northwestern Ethiopian plateau: Evidence from modal, trace element and Sr–Nd–Hf isotopic compositions of amphibole-bearing mantle xenoliths. *Lithos*, 284–285, 401–415.

Allwood, A. C., Walter, M. R., Kamber, B. S., Marshall, C. P., & Burch, I. W. (2006). Stromatolite reef from the Early Archaean era of Australia. *Nature*, *441*, 714–718.

Amelin, Y. (2009). Sm-Nd and U-Pb systematics of single titanite grains. *Chemical Geology*, 261, 53–61.

Amelin, Y., Kamo, S. L. & Lee, D. C. (2011). Evolution of early crust in chondritic or nonchondritic Earth inferred from U-Pb and Lu-Hf data for chemically abraded zircon from the Itsaq Gneiss Complex, West Greenland. *Canadian Journal of Earth Sciences*, 48, 141–160.

Arai, S. (1994). Characterization of spinel peridotites by olivine-spinel compositional relationships: Review and interpretation. *Chemical Geology*, *113*, 191–204.

Artemieva, I. M. (2019). Lithosphere thermal thickness and geothermal heat flux in Greenland from a new thermal isostasy method. *Earth-Science Reviews*, 188, 469–481.

Aulbach, S., Massuyeau, M., & Gaillard, F. (2017b). Origins of cratonic mantle discontinuities: A view from petrology, geochemistry and thermodynamic models. *Lithos*, 268–271, 364–382.

Aulbach, S., Mungall, J. E., & Pearson, D. G. (2016). Distribution and processing of highly siderophile elements in cratonic mantle lithosphere. *Reviews in Mineralogy and Geochemistry*, *81*, 239–304.

Aulbach, S., Sun, J. F., Tappe, S., Höfer, H. E., & Gerdes, A. (2017a). Volatile-rich metasomatism in the cratonic mantle beneath SW Greenland: Link to kimberlites and mid-lithospheric discontinuities. *Journal of Petrology*, 58, 2311–2338.

Aulbach, S., & Viljoen, K. S. (2015). Eclogite xenoliths from the Lace kimberlite, Kaapvaal craton: From convecting mantle source to palaeo-ocean floor and back. *Earth and Planetary Science Letters*, 431, 274–286.

Aulbach, Sonja, & Jacob, D. E. (2016). Lithos Major- and trace-elements in cratonic mantle eclogites and pyroxenites reveal heterogeneous sources and metamorphic processing of low-pressure protoliths. *Lithos*, 262, 586–605.

Aulbach, Sonja, Viljoen, K. S., & Gerdes, A. (2020). Diamondiferous and barren eclogites and pyroxenites from the western Kaapvaal craton record subduction processes and mantle metasomatism, respectively. *Lithos*, 368–369, 105588.

Baker, M. B., & Stopler, E. M. (1994). The Composition of High-Pressure Mantle Melts: Results from Diamond Aggregate Experiments. *Mineralogical Magazine*, *58*, 2811–2827.

Barrett, N, Jaques, A. L., González-Álvarez, I., Walter, M. J., & Pearson D. G. (2022 – in press). Ultra-refractory peridotites of Phanerozoic mantle origin: The Papua New Guinea ophiolite mantle tectonites. Journal of Petrology, XX, XX-XX.

Bauer, A., Reimink, J., Chacko, T., Foley, B., Shirey, B., & Pearson, D. G. (2020). Hafnium isotopes in zircons document the gradual onset of mobile-lid tectonics. *Geochemical Perspectives Letters*, *14*, 1-6.

Becker, H., Horan, M. F., Walker, R. J., Gao, S., Lorand, J.-P., & Rudnick, R. L. (2006). Highly siderophile element composition of the Earth's primitive upper mantle: Constraints from new data on peridotite massifs and xenoliths. *Geochimica et Cosmochimica Acta*, *70*, 4528–4550

Bennett, V. C., Nutman, A. P. & Esat, T. M. (2002). Constraints on mantle evolution from 187OS/188Os isotopic compositions of Archean ultramafic rocks from southern West Greenland (3.8 Ga) and Western Australia (3.46 Ga). *Geochimica et Cosmochimica Acta*, 66, 2615–2630.

Bernstein, S., Hanghøj, K., Kelemen, P. B., & Brooks, C. K. (2006). Ultra-depleted, shallow cratonic mantle beneath West Greenland: Dunitic xenoliths from Ubekendt Ejland. *Contributions to Mineralogy and Petrology*, 152, 335–347.

Bernstein, S., Kelemen, P. B., & Brooks, C. K. (1998). Depleted spinel harzburgite xenoliths in Tertiary dykes from East Greenland: Restites from high degree melting. *Earth and Planetary Science Letters*, *154*, 221–235.

Bernstein, S., Kelemen, P. B., & Hanghøj, K. (2007). Consistent olivine Mg# in cratonic mantle reflects Archean mantle melting to the exhauston of orthopyroxene. *Geology*, 35, 459–462.

Bizzarro, M., & Stevenson, R. K. (2003). Major element composition of the lithospheric mantle under the North Atlantic craton: Evidence from peridotite xenoliths of the Sarfartoq area, southwestern Greenland. *Contributions to Mineralogy and Petrology*, *146*, 223–240.

Bodinier, J. L., & Godard, M. (2013). Orogenic, Ophiolitic, and Abyssal Peridotites. In: Holland, H. D. & Turekian, K. K. (Eds.). *Treatise on Geochemistry: Third Edition*, Pergamon, 1-73.

Bolhar, R., Woodhead, J. D. & Hergt, M. H. (2003). Continental setting inferred for emplacement of the 2.9-2.7 Ga Belingwe Greenstone Belt, Zimbabwe: Comment. *Geology*, 31, 295–298.

Boschi, C., Dini, A., Früh-Green, G. L., & Kelley, D. S. (2008). Isotopic and element exchange during serpentinization and metasomatism at the Atlantis Massif (MAR 30°N): Insights from B and Sr isotope data. *Geochimica et Cosmochimica Acta*, *72*, 1801–1823.

Bouvier, A., Vervoort, J. D. & Patchett, P. J. (2008). The Lu-Hf and Sm-Nd isotopic composition of CHUR: Constraints from unequilibrated chondrites and implications for the bulk composition of terrestrial planets. *Earth and Planetary Science Letters*, 273, 48–57.

Boyd, F. R. (1989). Compositional distinction between oceanic and cratonic lithosphere. *Earth and Planetary Science Letters*, 96, 15–26.

Boyd, F. R., & Gurney, J. J. (1986). Diamonds and the african lithosphere. *Science*, *232*, 472–477.

Boyd, F. R., Pearson, D. G., Hoal, K. O., Hoal, B. G., Nixon, P. H., Kingston, M. J., & Mertzman, S. A. (2004). Garnet lherzolites from Louwrensia, Namibia: Bulk composition and P/T relations. Lithos, 77, 573–592.

Brandon, A. D., Snow, J. E., Walker, R. J., Morgan, J. W., & Mock, T. D. (2000). ^{190}Pt-^{186}Os and ^{187}Re-^{187}Os systematics of abyssal peridotites. *Earth and Planetary Science Letters*, *177*, 319–335.

Brey, G. P., & Köhler, T. (1990). Geothermobarometry in four-phase lherzolites II. new thermobarometers, and practical assessment of existing thermobarometers. *Journal of Petrology*, 31, 1353–1378.

Büchl, A., Brügmann, G., Batanova, V. G., Münker, C., & Hofmann, A. W. (2002). Melt percolation monitored by Os isotopes and HSE abundances: A case study from the mantle section of the Troodos Ophiolite. *Earth and Planetary Science Letters*, *204*, 385–402.

Cadman, A. C., Tarney, J., Bridgwater, D., Mengel, F., Whitehouse, M. J. & Windley, B. F. (2001). The petrogenesis of the Kangamiut dyke swarm, West Greenland. *Precambrian Research*, 105, 183–203.

Carlson, R. W., & Irving, A. J. (1994). Depletion and enrichment history of subcontinental lithospheric mantle: An Os, Sr, Nd and Pb isotopic study of ultramafic xenoliths from the northwestern Wyoming Craton. *Earth and planetary Science Letters*, 126, 457–472.

Chapman, D. S. (1986). Thermal gradients in the continental crust. *Geological Society Special Publication*, 24, 63–70.

Chazot, G., Menzies, M. A., & Harte, B. (1996). Determination of partition coefficients between apatite, clinopyroxene, amphibole, and melt in natural spinel lherzolites from Yemen: Implications for wet melting of the lithospheric mantle. *Geochimica et Cosmochimica Acta*, 60, 423–437.

Chesley, J. T., Rudnick, R. L., & Lee, C. T. (1999). Re-Os systematics of mantle xenoliths from the East African Rift: Age, structure, and history of the Tanzanian craton. *Geochimica et Cosmochimica Acta*, *63*, 1203–1217.

Chen, C., Su, B. X., Xiao, Y., Uysal, İ., Lin, W., Chu, Y., Jing, J. J., & Sakyi, P. A. (2020). Highly siderophile elements and Os isotope constraints on the genesis of peridotites from the Kızıldağ ophiolite, southern Turkey. *Lithos*, *368–369*.

Celli, N. L., Lebedev, S., Schaeffer, A. J., & Gaina, C. (2020). African cratonic lithosphere carved by mantle plumes. *Nature Communications*, *11*, 92.

Coggon, J. A., Luguet, A., Nowell, G. M. & Appel, P. W. U. (2013). Hadean mantle melting recorded by southwest Greenland chromitite 186 Os signatures. *Nature Geoscience*. Nature Publishing Group, 6, 871–874.

Coltorti, M., Beccaluva, L., Bonadiman, C., Faccini, B., Ntaflos, T., & Siena, F. (2004). Amphibole genesis via metasomatic reaction with clinopyroxene in mantle xenoliths from Victoria Land, Antarctica. *Lithos*, 75, 115–139.

Condie, K. C. (2005). High field strength element ratios in Archean basalts: A window to evolving sources of mantle plumes? *Lithos*, 79, 491–504.

Condamine, P., & Médard, E. (2014). Experimental melting of phlogopite-bearing mantle at 1 GPa: Implications for potassic magmatism. *Earth and Planetary Science Letters*, *397*, 80–92.

Connelly, J. N., Gool, J. A. M. Van & Mengel, F. C. (2000). Temporal evolution of a deeply eroded orogen: the Nagssugtoqidian Orogen, West Greenland. *Canadian Journal of Earth Sciences*, 37, 1121–1142.

Connelly, J. N. & Mengel, F. C. (2000). Evolution of Archean components in the Paleoproterozoic Nagssugtoqidian orogen, West Greenland. *Bulletin of the Geological Society of America*, 112, 747–763.

Connelly, J. N., Thrane, K., Krawiec, A. W. & Garde, A. A. (2006). Linking the Palaeoproterozoic Nagssugtoqidian and Rinkian orogens through the Disko Bugt region of West Greenland. *Journal of the Geological Society*, 163, 319–335.

Currie, L. A. (1968). Limits for Qualitative Detection and Quantitative Determination: Application to Radiochemistry. *Analytical Chemistry*, 40, 586–593.

Czas, J., Pearson, D. G., Stachel, T., Kjarsgaard, B. A., & Read, G. H. (2020). A Palaeoproterozoic diamond-bearing lithospheric mantle root beneath the Archean Sask Craton, Canada. *Lithos*, *356–357*, 105301.

Dallai, L., Bianchini, G., Avanzinelli, R., Natali, C., & Conticelli, S. (2019). Heavy oxygen recycled into the lithospheric mantle. *Scientific Reports*, *9*, 1–7.

Davis, G. L. (1977). The ages and uranium contents of zircons from kimberlites and associated rocks. In: *2nd internation Kimberlite Conference* (Vol. 2, pp. 67–69). Santa Fe.

Davies, G. R., Spriggs, A. J., & Nixon, P. H. (2001). A Non-cognate Origin for the Gibeon Kimberlite Megacryst Suite, Namibia: Implications for the Origin of Namibian Kimberlites. *Journal of Petrology*, 42, 159–172.

Day, J. M. D., Walker, R. J., & Warren, J. M. (2017). 186Os–187Os and highly siderophile element abundance systematics of the mantle revealed by abyssal peridotites and Os-rich alloys. *Geochimica et Cosmochimica Acta*, *200*, 232–254.

Debret, B., Andreani, M., Muñoz, M., Bolfan-casanova, N., Carlut, J., Nicollet, C., Schwarts, S., & Trcera, N. (2014). Evolution of Fe redox state in serpentine during subduction. *Earth and Planetary Science Letters*, *400*, 206–218.

Delpech, G., Lorand, J. P., Grégoire, M., Cottin, J. Y., & O'Reilly, S. Y. (2012). In-situ geochemistry of sulfides in highly metasomatized mantle xenoliths from Kerguelen, southern Indian Ocean. *Lithos*, *154*, 296–314.

Dick, H. J. B., Fisher, R. L., & Bryan, W. B. (1984). Mineralogic variability of the uppermost mantle along mid-ocean ridges. *Earth and Planetary Science Letters*, *69*, 88–106.

Dymek, R. F., Brothers, S. C., & Schiffries, C. M. (1988). Petrogenesis of ultramafic metamorphic rocks from the 3800 ma isua supracrustal belt, West Greenland. *Journal of Petrology*, *29*, 1353–1397.

Eggins, S. M., Rudnick, R. L., & Mcdonough, W. F. (1998). The composition of peridotites and their minerals: a laser-ablation ICP – MS study. *Earth and Planetary Science Letters*, 154, 53–71.

Eickmann, B., Hofmann, A., Wille, M., Bui, T. H., Wing, B. A., & Schoenberg, R. (2018). Isotopic evidence for oxygenated Mesoarchaean shallow oceans. *Nature Geoscience*, *11*, 133–138.

Eiler, J. M. (2001). Oxygen isotope variations of basaltic lavas and upper mantle rocks. *Stable Isotope Geochemistry*, *43*, 319–364.

Eiler, J. M., Crawford, A., Elliott, T., Farley, K. A., Valley, J. W., & Stolper, E. M. (2000). Oxygen isotope geochemistry of oceanic-arc lavas. *Journal of Petrology*, *41*, 229–256.

Emo, R. B., & Kamber, B. S. (2021). Evidence for highly refractory, heat producing element-depleted lower continental crust: Some implications for the formation and evolution of the continents. *Chemical Geology*, 580, 120389.

Erlank, A. J., Waters, F. G., Hawkesworth, C. J., Haggerty, S. E., Allsopp, H. L., Rickard, R. S., & Menzies, M. A. (1987). Evidence for mantle metasomatism in peridotite nodules from the Kimberley pipes, South Africa. *Mantle Metasomatism*, 221–311.

Evans, B. W. (2008). Control of the Products of Serpentinization by the Fe 2 + Mg À 1 Exchange Potential of Olivine and Orthopyroxene. *Journal of Petrology*, *49*, 1873–1887.

Fabriès, J., Bodinier, J. L., Dupuy, C., Lorand, J. P., & Benkerrou, C. (1989). Evidence for modal metasomatism in the orogenic spinel lherzolite body from caussou (Northeastern Pyrenees, France). *Journal of Petrology*, *30*, 199–228.

Fabries, J., Lorand, J. P., Bodinier, J. L., & Dupuy, C. (1991). Evolution of the upper mantle beneath the pyrenees: Evidence from orogenic spinel lherzolite massifs. *Journal of Petrology*, *Special-Vol* 2, 55–76.

Falloon, T. J., Danyushevsky, L. V., & Green, D. H. (2001). Peridotite melting at 1 GPa: Reversal experiments on partial melt compositions produced by peridotite-basalt sandwich experiments. *Journal of Petrology*, *42*, 2363–2390.

Falloon, T. J., Green, D. H., Danyushevsky, L. V., & Faul, U. H. (1999). Peridotite melting at 1·0 and 1·5 GPa: An experimental evaluation of techniques using diamond aggregates and mineral mixes for determination of near-solidus melts. *Journal of Petrology*, *40*, 1343–1375.

Falloon, T. J., Green, D. H., Danyushevsky, L. V., & Mcneill, A. W. (2008). The composition of near-solidus partial melts of fertile peridotite at 1 and 1·5 GPa: Implications for the petrogenesis of MORB. *Journal of Petrology*, *49*, 591–613.

Fisher, C. M., Hanchar, J. M., Samson, S. D., Dhuime, B., Blichert-Toft, J., Vervoort, J. D. & Lam, R. (2011). Synthetic zircon doped with hafnium and rare earth elements: A reference material for in situ hafnium isotope analysis. *Chemical Geology*, 286, 32–47.

Fisher, C. M., Paton, C., Pearson, D. G., Sarkar, C., Luo, Y., Tersmette, D. B. & Chacko, T. (2017). Data Reduction of Laser Ablation Split-Stream (LASS) Analyses Using Newly Developed

Features Within Iolite: With Applications to Lu-Hf + U-Pb in Detrital Zircon and Sm-Nd +U-Pb in Igneous Monazite. *Geochemistry, Geophysics, Geosystems*, 18, 4604–4622.

Fisher, C. M. & Vervoort, J. D. (2018). Using the magmatic record to constrain the growth of continental crust—The Eoarchean zircon Hf record of Greenland. *Earth and Planetary Science Letters*, 488, 79–91.

Fitton, J. G., Saunders, A. D., Norry, M. J., Hardarson, B. S. & Taylor, R. N. (1997). Thermal and chemical structure of the Iceland plume. *Earth and Planetary Science Letters*, 153, 197–208.

Fitzpayne, A., Giuliani, A., Hergt, J., Phillips, D., & Janney, P. (2018). New geochemical constraints on the origins of MARID and PIC rocks: Implications for mantle metasomatism and mantle-derived potassic magmatism. *Lithos*, 318–319, 478–493.

Foley, S. F., Prelevic, D., Rehfeldt, T., & Jacob, D. E. (2013). Minor and trace elements in olivines as probes into early igneous and mantle melting processes. *Lithos*, *363*, 181-191.

Foley, S. F., Höfer, H., & Brey, G. (1994). High-pressure synthesis of priderite and members of the lindsleyite-mathiasite and hawthorneite-yimengite series. *Contributions to Mineralogy and Petrology*, 117, 164–174.

Förster, A., Fuchs, S., Förster, H. J., & Norden, B. (2021). Ambiguity of crustal geotherms: A thermal-conductivity perspective. *Geothermics*, 89, 101937.

Frets, E. C., Tommasi, A., Garrido, C., Vauchez, A., Mainprice, D., Kamaltarguisti, & Amri, I. (2014). The beni bousera peridotite (rif belt, morocco): An oblique-slip low-angle shear zonethinning the subcontinental mantle lithosphere. *Journal of Petrology*, *55*, 283–313.

Friend, C. R. L. & Nutman, A. P. (2005). New pieces to the Archaean terrane jigsaw puzzle in the Nuuk region, southern West Greenland: Steps in transforming a simple insight into a complex regional tectonothermal model. *Journal of the Geological Society*, 162, 147–162.

Fu, B., Page, F. Z., Cavosie, A. J., Fournelle, J., Kita, N. T., Lackey, J. S., Wilde S. A., & Valley, J. W. (2008). Ti-in-zircon thermometry: applications and limitations. *Contributions to Mineralogy and Petrology*, 156, 197-215.

Gale, A., Dalton, C. A., Langmuir, C. H., Su, Y. & Schilling, J. G. (2013). The mean composition of ocean ridge basalts. *Geochemistry, Geophysics, Geosystems*, 14, 489–518.

Garde, A. A., Friend, C. R. L., Nutman, A. R. & Marker, M. (2000). Rapid maturation and stabilisation of middle Archaean continental crust: The Akia terrane, southern West

Greenland. *Bulletin of the Geological Society of Denmark*, 47, 1–27.

Garde, A. A., & Hollis, J. A. (2020). A buried Palaeoproterozoic spreading ridge in the northern Nagssugtoqidian orogen , West Greenland. In: Kusky, T., Zhai, M. G., & Xiao, W. (Eds), The Evolving Continents: Understanding Processes of Continental Growth. *Geological Society, London, Special Publications, 338, 213–234,*

Gardiner, N. J., Kirkland, C. L., Hollis, J., Szilas, K., Steenfelt, A., Yakymchuk, C. & Heide-Jørgensen, H. (2019). Building Mesoarchaean crust upon Eoarchaean roots: the Akia Terrane, West Greenland. *Contributions to Mineralogy and Petrology*, 174, 1–19.

Ghiorso, M. S. & Gualda, G. A. R. (2015). An H2O–CO2 mixed fluid saturation model compatible with rhyolite-MELTS. *Contributions to Mineralogy and Petrology*, 169, 1–30.

Ghiorso, M. S., Hirschmann, M. M., Reiners, P. W., & Kress, V. C. (2002). The pMELTS: A revision of MELTS for improved calculation of phase relations and major element partitioning related to partial melting of the mantle to 3 GPa. *Geochemistry, Geophysics, Geosystems*, *3*, 1–35.

Giuliani, A., Phillips, D., Kamenetsky, V. S., & Goemann, K. (2016). Constraints on kimberlite ascent mechanisms revealed by phlogopite compositions in kimberlites and mantle xenoliths. *Lithos*, 240–243, 189–201.

Goes, S., Hasterok, D., Schutt, D., & Klocking, M. (2020). Continental lithospheric temperatures: a review. *Physics of the Earth and Planetary Interiors*, 306, 106509.

Gong, B., Zheng, Y. F., & Chen, R. X. (2007). TC/EA-MS online determination of hydrogen isotope composition and water concentration in eclogitic garnet. *Physics and Chemistry of Minerals*, *34*, 687–698.

Green, M. G., Sylvester, P. J. & Buick, R. (2000). Growth and recycling of early Archaean continental crust: Geochemical evidence from the Coonterunah and Warrawoona Groups, Pilbara Craton, Australia. *Tectonophysics*, 322, 69–88.

Grégoire, M., Bell, D., & Le Roex, A. (2002). Trace element geochemistry of phlogopite-rich mafic mantle xenoliths: Their classification and their relationship to phlogopite-bearing peridotites and kimberlites revisited. *Contributions to Mineralogy and Petrology*, 142, 603–625.

Gregoire, M., Bell, D. R., & Le Roex, A. P. (2003). Garnet Lherzolites from the Kaapvaal Craton (South Africa): Trace Element Evidence for a Metasomatic History. *Journal of Petrology*, 44, 629–657.

Griffin, W. L., Jaques, A. L., Sic, S. H., Ryan, C. G., Cousens, D. R., & Suter, G. F. (1988). Conditions of diamond growth: a proton microprobe study of inclusions in West Australian diamonds. *Contributions to mineralogy petrology*, 99, 143–158.

Griffin, W. L., O'Reilly, S. Y., Afonso, J. C., & Begg, G. C. (2009). The composition and evolution of lithospheric mantle: A re-evaluation and its tectonic implications. *Journal of Petrology*, 50, 1185–1204.

Griffin, W. L., O'Reilly, S. Y., Natapov, L. M., & Ryan, C. G. (2003). The evolution of lithospheric mantle beneath the Kalahari Craton and its margins. *Lithos*, 71, 215–241.

Gualda, G. A. R., Ghiorso, M. S., Lemons, R. V. & Carley, T. L. (2012). Rhyolite-MELTS: A modified calibration of MELTS optimized for silica-rich, fluid-bearing magmatic systems. *Journal of Petrology*, 53, 875–890.

Guillou-Frottier, L., Burov, E., Augé, T. & Gloaguen, E. (2014). Rheological conditions for emplacement of Ural-Alaskan-type ultramafic complexes. *Tectonophysics*, 631, 130–145.

Hacker, B. R., Kelemen, P. B., & Behn, M. D. (2015). Continental Lower Crust. *Annual Review of Earth and Planetary Sciences*, 43, 167–205.

Haggerty, S. E. (1983). The mineral chemistry of new titanates from the jagersfontein kimberlite, South Africa: Implications for metasomatism in the upper mantle. *Geochimica et Cosmochimica Acta*, 47, 1833–1854.

Haggerty, S. E. (1991). Oxide mineralogy of the upper mantle. In D. H. Lindsley (Ed.), *Oxide minerals: petrology and magnetic significance. Reviews in mineralogy and geochemistry*, *25*, 355–416.

Haggerty, S. E. (1991). Oxide mineralogy of the upper mantle. In D. H. Lindsley (Ed.), Oxide minerals: petrology and magnetic significance (pp. 355–416). Reviews in mineralogy.

Hamilton et al., 1998 Hamilton, M. A., Pearson, D. G., Stern, R. A., and Boyd, F. R., 1998, Constraints on MARID petrogenesis: SHRIMP II U-Pb zircon evidence for pre-eruption metasomatism at Kampfersdam: *Extended Abstracts, 7th International Kimberlite Conference, Cape Town*, p. 296-298.

Hammerli, J., Kemp, A. I. S. & Whitehouse, M. J. (2019). In situ trace element and Sm-Nd isotope

analysis of accessory minerals in an Eoarchean tonalitic gneiss from Greenland: Implications for Hf and Nd isotope decoupling in Earth's ancient rocks. *Chemical Geology*, 524, 394–405.

Hanghøj, K., Kelemen, P., Bernstein, S., Blusztajn, J., & Frei, R. (2001). Osmium isotopes in the Wiedemann Fjord mantle xenoliths: A unique record of cratonic mantle formation by melt depletion in the Archaean. *Geochemistry, Geophysics, Geosystems*, 2, 2000GC000085.

Harlow, G. E. (1997). K in clinopyroxene at high pressure and temperature: An experimental study. *American Mineralogist*, *82*, 259–269.

Harlow, G. E., & Davies, R. (2004). Status report on stability of K-rich phases at mantle conditions. *Lithos*, *77*, 647–653.

Harte, B., Hunter, R. H., & Kinny, P. D. (1993). Melt geometry, movement and crystallization, in relation to mantle dykes, veins and metasomatism. *Philosophical Transactions - Royal Society of London*, *342*, 1–21.

Harvey, J., Gannoun, A., Burton, K. W., Rogers, N. W., Alard, O., & Parkinson, I. J. (2006). Ancient melt extraction from the oceanic upper mantle revealed by Re–Os isotopes in abyssal peridotites from the Mid-Atlantic ridge. *Earth and Planetary Science Letters*, *244*, 606-621.

Hasterok, D., & Chapman, D. S. (2011). Heat production and geotherms for the continental lithosphere. *Earth and Planetary Science Letters*, *307*, 59–70.

Hermann, J., & Rubatto, D. (2009). Accessory phase control on the trace element signature of sediment melts in subduction zones. *Chemical Geology*, *265*, 512–526.

Herrmann, W., & Berry, R. F. (2002). MINSQ - a least squares spreadsheet method for calculating mineral proportions from whole rock major element analyses. *Geochemistry: Exploration, Environment, Analysis*, *2*, 361–368.

Herzberg, C. (2004). Geodynamic information in peridotite petrology. *Journal of Petrology*, *45*, 2507–2530.

Herzberg, C., Condie, K., & Korenaga, J. (2010). Thermal history of the Earth and its petrological expression. *Earth and Planetary Science Letters*, *292*, 79–88.

Herzberg, C. & O'hara, M. J. (2002). Plume-Associated Ultramafic Magmas of Phanerozoic Age. *Journal of Petrology*, 43, 1857–1883.

Herzberg, C., & Rudnick, R. (2012). Formation of cratonic lithosphere: An integrated thermal and petrological model. *Lithos*, *149*, 4–15.

Hieronymus, C. F., & Goes, S. (2010). Complex cratonic seismic structure from thermal models of the lithosphere: Effects of variations in deep radiogenic heating. *Geophysical Journal International*, *180*, 999–1012.

Hiess, J., Bennett, V. C., Nutman, A. P. & Williams, I. S. (2009a). In situ U-Pb, O and Hf isotopic compositions of zircon and olivine from Eoarchaean rocks, West Greenland: New insights to making old crust. *Geochimica et Cosmochimica Acta*, 73, 4489–4516.

Hiraga, T., Anderson, I. M., & Kohlstedt, D. L. (2004). Grain boundaries as reservoirs of incompatible elements in the Earth's mantle. *Nature*, 427, 699–703.

Hirose, K., & Kawamoto, T. (1995). Hydrous partial melting of lherzolite at 1 GPa: The effect of H2O on the genesis of basaltic magmas. *Earth and Planetary Science Letters*, *133*, 463–473.

Hoffman, P. F. (1988). United plates of America, the birth of a craton: Early Proterozoic assembly and growth of Laurentia. *Annual Review of Earth and Planetary Sciences*, *16*, 543–603.

Hoggard, M. J., Czarnota, K., Richards, F. D., Huston, D. L., Jaques, A. L., & Ghelichkhan, S. (2020). Global distribution of sediment-hosted metals controlled by craton edge stability. *Nature Geoscience*, *13*, 504–510.

Hollis, J. A., Keiding, M., Stensgaard, B. M., Gool, J. A. M. Van & Garde, A. A. (2006). Evolution of Neoarchaean supracrustal belts at the northern margin of the North Atlantic Craton, West Greenland. *Geological Survey of Denmark and Greenland Bulletin*, 11, 9–31.

Ionov, D. A. (2010). Petrology of mantle wedge lithosphere: New data on supra-subduction zone peridotite xenoliths from the andesitic Avacha volcano, Kamchatka. *Journal of Petrology*, *51*, 327–361.

Ionov, D. A., Bodinier, J. L., Mukasa, S. B., & Zanettie, A. (2002). Mechanisms and Sources of Mantle Metasomatism: Major and Trace Element Compositions of Peridotite Xenoliths from Spitsbergen in the Context of Numerical Modelling. *Journal of Petrology*, *43*, 2219–2259.

Ionov, D. A., Carlson, R. W., Doucet, L. S., Golovin, A. V., & Oleinikov, O. B. (2015a). The age and history of the lithospheric mantle of the Siberian craton: Re-Os and PGE study of peridotite xenoliths from the Obnazhennaya kimberlite. *Earth and Planetary Science*

Letters, *428*, 108–119.

Ionov, D. A., Doucet, L. S., & Ashchepkov, I. V. (2010). Composition of the lithospheric mantle in the siberian craton: New constraints from fresh peridotites in the Udachnaya-East Kimberlite. *Journal of Petrology*, *51*, 2177–2210.

Ionov, D. A., Doucet, L. S., Carlson, R. W., Golovin, A. V., & Korsakov, A. V. (2015b). Post-Archean formation of the lithospheric mantle in the central Siberian craton: Re-Os and PGE study of peridotite xenoliths from the Udachnaya kimberlite. *Geochimica et Cosmochimica Acta*, *165*, 466–483.

Ionov, D. A., Doucet, L. S., Pogge von Strandmann, P. A. E., Golovin, A. V., & Korsakov, A. V. Ionov, D. A., Doucet, L. S., Pogge von Strandmann, P. A. E., Golovin, A. V., & Korsakov, A. V. (2017). Links between deformation, chemical enrichments and Li-isotope compositions in the lithospheric mantle of the central Siberian craton. *Chemical Geology*, *475*, 105–121.

Ionov, D. A., Doucet, L. S., Xu, Y., Golovin, A. V., & Oleinikov, O. B. (2018). Reworking of Archean mantle in the NE Siberian craton by carbonatite and silicate melt metasomatism: Evidence from a carbonate-bearing, dunite-to-websterite xenolith suite from the Obnazhennaya kimberlite. *Geochimica et Cosmochimica Acta*, *224*, 132–153.

Ionov, D. A., Griffin, W. L., & O'Reilly, S. Y. (1997). Volatile-bearing minerals and lithophile trace elements in the upper mantle. *Chemical Geology*, *141*, 153–184.

Ionov, D. A., & Hofmann, A. W. (1995). NbTa-rich mantle amphiboles and micas: Implications for subduction-related metasomatic trace element fractionations. *Earth and Planetary Science Letters*, *131*, 341–356.

Ireland, T. J., Walker, R. J. & Garcia, M. O. (2009). Highly siderophile element and 187Os isotope systematics of Hawaiian picrites: Implications for parental melt composition and source heterogeneity. *Chemical Geology*, 260, 112–128.

Irvine, T. N., & Baragar, W. R. A. (1971). A Guide to the Chemical Classification of the Common Volcanic Rocks. *Canadian Journal of Earth Sciences*, *8*, 523–548.

Ishii, T., Robinson, P. T., Maekawa, H., & Richard, F. (1992). Petrological studies of peridotites from diapiric serpentinite seamounts in the Izu-Ogasawara-Mariana Forearc, Leg 125. In: Fryer, P., Pearce, J., & Stokking L. B. (Eds.). *Proceedings of the Ocean Drilling Program, Scientific Results, 125*, 445–485.

Ishimaru, S., Arai, S., Ishida, Y., Shirasaka, M., & Okrugin, V. M. (2007). Melting and multi-stage metasomatism in the mantle wedge beneath a frontal arc inferred from highly depleted peridotite xenoliths from the avacha volcano, Southern Kamchatka. *Journal of Petrology*, *48*, 395–433.

Iwamori, H., McKenzie, D., & Takahashi, E. (1995). Melt generation by isentropic mantle upwelling. *Earth and Planetary Science Letters*, *134*, 253–266.

Jacob, D. E. (2004). Nature and origin of eclogite xenoliths from kimberlites. *Lithos*, *77*, 295-316.

James, D. E., Boyd, F. R., Schutt, D., Bell, D. R., & Carlson, R. W. (2004). Xenolith constraints on seismic velocities in the upper mantle beneath southern Africa. *Geochemistry, Geophysics, Geosystems*, *5*, Q01002.

Janney, P. E., Shirey, S. B., Carlson, R. W., Pearson, D. G., Bell, D. R., Le Roex, A. P., … Boyd, F. R. (2010). Age, composition and thermal characteristics of South African off-craton mantle lithosphere: Evidence for a multi-stage history. *Journal of Petrology*, *51*, 1849–1890.

Jaupart, C., & Mareschal, J. C. (2015). Heat Flow and Thermal Structure of the Lithosphere. In G. Schubert (Ed.), *Treatise on Geophysics: Second Edition*, *6*, 217-253.

Jelsma, H., Barnett, W., Richards, S., & Lister, G. (2009). Tectonic setting of kimberlites. *Lithos*, 112, 155–165.

Jenner, F. E., Bennett, V. C., Nutman, A. P., Friend, C. R. L., Norman, M. D. & Yaxley, G. (2009). Evidence for subduction at 3.8 Ga: Geochemistry of arc-like metabasalts from the southern edge of the Isua Supracrustal Belt. *Chemical Geology*, 261, 83–98.

Jochum, K. P., Nohl, U., Herwig, K., Lammel, E., Stoll, B., & Hofmann, A. W. (2005). GeoReM : A New Geochemical Database for Reference Materials and Isotopic Standards. *Geostandards and Geoanalytical Research*, *29*, 333–338.

Jochum, K. P., Weis, U., Stoll, B., Kuzmin, D., Yang, Q., Raczek, I., … Enzweiler, J. (2011). Determination of Reference Values for NIST SRM 610-617 Glasses Following ISO Guidelines. *Geostandards and Geoanalytical Research*, *35*, 397–429.

Jordan, T. H. (1978). Composition and development of continental lithosphere. *Nature*, *274*, 544-548.

Jordan, T. H. (1988). Structure and formation of the continental tectosphere. *Journal of Petrology*, Special lithosphere issue, 11–37.

Kalsbeek, F. & Manatschal, G. (1999). Geochemistry and tectonic significance of peridotitic and metakomatiitic rocks from the Ussuit area, Nagssugtoqidian orogen, West Greenland. *Precambrian Research*, 94, 101–120.

Kalsbeek, F. & Nutman, A. P. (1996). Anatomy of the Early Proterozoic Nagssugtoqidian orogen, West Greenland, explored by reconnaissance SHRIMP U-Pb zircon dating. *Geology*, 24, 515–518.

Kalsbeek, F., Pidgeon, R. T. & Taylor, P. N. (1987). Nagssugtoqidian mobile belt of West Greenland: a cryptic 1850 Ma suture between two Archaean continents-chemical and isotopic evidence. *Earth and Planetary Science Letters*, 85, 365–385.

Kalsbeek, F., Pulvertaft, T. C. R., & Nutman, A. P. (1998). Geochemistry, age and origin of metagreywackes from the Palaeoproterozoic Karrat Group, Rinkian Belt, West Greenland. *Precambrian Research*, *91*, 383–399.

Kelemen. P. B. (1990). Reaction Between Ultramafic Rock and Fractionating Basaltic Magma I. Phase Relations, the Origin of Calc-alkaline Magma Series, and the Formation of Discordant Dunite. *Journal of Petrology*, *31*, 51-98.

Kelemen, P. B. & Dick, H. J. B. (1995). Focused melt flow and localized deformation in the upper mantle: juxtaposition of replacive dunite and ductile shear zones in the Josephine peridotite, SW Oregon. *Journal of Geophysical Research*, *100*, 423–438.

Kemp, A. I. S., Hawkesworth, C. J., Collins, W. J., Gray, C. M. & Blevin, P. L. (2009). Isotopic evidence for rapid continental growth in an extensional accretionary orogen: The Tasmanides, eastern Australia. *Earth and Planetary Science Letters*, 284, 455–466.

Kerrich, R. & Xie, Q. (2002). Compositional recycling structure of an Archean super-plume:Nb-Th-U-LREE systematics of Archean komatiites and basalts revisited. *Contributions to Mineralogy and Petrology*, 142, 476–484.

Kirkland, C. L., Hartnady, M. I. H., Barham, M., Olierook, H. K. H., Steenfelt, A. & Hollis, J. A. (2021). Widespread reworking of Hadean-to-Eoarchean continents during Earth's thermal peak. *Nature Communications*,12, 1–9.

Kirkland, C. L., Hollis, J. & Gardiner, N. (2016). Greenland U-Pb Geochronology Database.

www.greenmin.gl.

Kirkland, C. L., Yakymchuk, C., Hollis, J., Heide-Jørgensen, H. & Danišík, M. (2018). Mesoarchean exhumation of the Akia terrane and a common Neoarchean tectonothermal history for West Greenland. *Precambrian Research*, 314, 129–144.

Konzett, È., Armstrong, A., & Gu, D. (2000). Modal metasomatism in the Kaapvaal craton lithosphere : constraints on timing and genesis from U ± Pb zircon dating of metasomatized peridotites and MARID-type xenoliths. *Contributions to Mineralogy and Petrology*, 139, 704–719.

Konzett, È., Armstrong, R. A., Sweeney, R. J., & Compston, W. (1998). The timing of MARID metasomatism in the Kaapvaal mantle: An ion probe study of zircons from MARID xenoliths. *Earth and Planetary Science Letters*, *160*, 133–145.

Kopylova, M. G., Russell, J. K., & Cookenboo, H. (1999). Petrology of peridotite and pyroxenite xenoliths from the Jericho Kimberlite: Implications for the thermal state of the mantle beneath the Slave Craton, Northern Canada. *Journal of Petrology*, 40, 79–104.

Krystopowicz, N. J., & Currie, C. A. (2013). Crustal eclogitization and lithosphere delamination in orogens. *Earth and Planetary Science Letters*, 361, 195-207.

Kubo, K. (2002). Dunite formation processes in highly depleted peridotite: Case study of the Iwanaidake peridotite, Hokkaido, Japan. *Journal of Petrology*, *43*(3), 423–448.

Laouar, R., Satouh, A., Salmi-Laouar, S., Abdallah, N., Cottin, J. Y., Bruguier, O., Bosch, O., Ouabadi, A., Boyce, A. J., & Fallick, A. E. (2017). Petrological, geochemical and isotopic characteristics of the Collo ultramafic rocks (NE Algeria). *Journal of African Earth Sciences*, *125*, 59–72.

Lassiter, J. C., Byerly, B. L., Snow, J. E., & Hellebrand, E. (2014). Constraints from Os-isotope variations on the origin of Lena Trough abyssal peridotites and implications for the composition and evolution of the depleted upper mantle. *Earth and Planetary Science Letters*, *403*, 178–187.

LaTourrette, T., Hervig, R. L., & Holloway, J. R. (1995). Trace element partitioning between amphibole, phlogopite, and basanite melt. *Earth and Planetary Science Letters*, 135, 13–30.

Lazarov, M., Brey, G. P., & Weyer, S. (2012). Evolution of the South African mantle - A case study of garnet peridotites from the Finsch diamond mine (Kaapvaal craton); part 1: Inter-mineral trace element and isotopic equilibrium. *Lithos*, 154, 193–209.

le Roux, V., Bodinier, J. L., Tommasi, A., Alard, O., Dautria, J. M., Vauchez, A., & Riches, A. J. V. (2007). The Lherz spinel lherzolite: Refertilized rather than pristine mantle. *Earth and Planetary Science Letters*, *259*, 599–612.

le Roex, A., & Class, C. (2016). Metasomatic enrichment of Proterozoic mantle south of the Kaapvaal Craton, South Africa: origin of sinusoidal REE patterns in clinopyroxene and garnet. *Contributions to Mineralogy and Petrology*, 171, 1–24.

Lee, C. T. A., & Chin, E. J. (2014). Calculating melting temperatures and pressures of peridotite protoliths: Implications for the origin of cratonic mantle. *Earth and Planetary Science Letters*, *403*, 273–286.

Lee, C.-T. A., Leeman, W. P., Canil, D. & Li, Z.-X. A. (2005). Similar V/Sc Systematics in MORB and Arc Basalts: Implications for the Oxygen Fugacities of their Mantle Source Regions. *Journal of Petrology*, 46, 2313–2336.

Li, C., Arndt, N. T., Tang, Q. & Ripley, E. M. (2015). Trace element indiscrimination diagrams. *Lithos*, 232, 76–83.

Li, H. Y., Chen, R. X., Zheng, Y. F., Hu, Z., & Xu, L. (2018). Crustal Metasomatism at the Slab-Mantle Interface in a Continental Subduction Channel: Geochemical Evidence From Orogenic Peridotite in the Sulu Orogen. *Journal of Geophysical Research: Solid Earth*, *123*(3), 2174–2198.

Liu, J., Brin, L. E., Pearson, D. G., Bretschneider, L., Luguet, A., van Acken, D., Kjarsgaard, B., Riches A., & Mišković, A. (2018). Diamondiferous Paleoproterozoic mantle roots beneath Arctic Canada: A study of mantle xenoliths from Parry Peninsula and Central Victoria Island. *Geochimica et Cosmochimica Acta*, *239*, 284–311.

Liu, J., Pearson, D. G., Wang, L. H., Mather, K. A., Kjarsgaard, B. A., Schaeffer, A. J., Irvine, G. J., Kopylova, M. G., & Armstrong, J. P. (2021). Plume-driven recratonization of deep continental lithospheric mantle. *Nature*, *592*, 732–736.

Liu, J., Riches, A. J. V., Pearson, D. G., Luo, Y., Kienlen, B., Kjarsgaard, B. A., … Armstrong, J. P. (2016). Age and evolution of the deep continental root beneath the central Rae craton, northern Canada. *Precambrian Research*, 272, 168–184.

Locock, A. J. (2014). An Excel spreadsheet to classify chemical analyses of amphiboles following the IMA 2012 recommendations. *Computers and Geosciences*, 62, 1–11.

Lorand, J. P., Delpech, G., Grégoire, M., Moine, B., O'Reilly, S. Y., & Cottin, J. Y. (2004). Platinum-group elements and the multistage metasomatic history of Kerguelen lithospheric mantle (South Indian Ocean). *Chemical Geology*, *208*, 195–215.

Lorand, J. P., Reisberg, L., & Bedini, R. M. (2003). Platinum-group elements and melt percolation processes in Sidamo spinel peridotite xenoliths, Ethiopia, East African Rift. *Chemical Geology*, *196*, 57–75.

Loucks, R. R., Fiorentini, M. L., & Henriquez, G. J. (2020). New Magmatic Oxybarometer Using Trace Elements in Zircon. *Journal of Petrology*, 61, egaa034.

Luguet, A., Jaques, A. L., Pearson, D. G., Smith, C. B., Bulanova, G. P., Roffey, S. L., Rayner, M. J., & Lorand, J. P. (2009). An integrated petrological, geochemical and Re-Os isotope study of peridotite xenoliths from the Argyle lamproite, Western Australia and implications for cratonic diamond occurrences. *Lithos*, *112*, 1096–1108.

Luguet, A. & Reisberg, L. (2016). Highly Siderophile Element and 187Os Signatures in Non-cratonic Basalt-hosted Peridotite Xenoliths: Unravelling the Origin and Evolution of the Post-Archean Lithospheric Mantle. *Reviews in Mineralogy and Geochemistry*, *81*, 305–367.

Maffione, M., Thieulot, C., van Hinsberge, D. J. J., Morris, A., Plumper, O., & Spakman, W. (2015). Dynamics of intraoceanic subduction initiation: 1. Oceanic detachment fault inversion and the formation of supra-subduction zone ophiolites. *Geochemistry Geophysics Geosystems*, *16*, 1541–1576.

Majumdar, A. S., Vollmer, C., Berndt, J., Mondal, S. K., & Putnis, A. (2016). Formation of Mg-rich Olivine Pseudomorphs in Serpentinized Dunite from the Mesoarchean Nuasahi Massif, Eastern India: Insights into the Evolution of Fluid Composition at the Mineral–Fluid Interface. *Journal of Petrology*, *57*, 3–26.

Manatschal, G., Ulfbeck, D. & van Gool, J. (1998). Change from thrusting to syncollisional extension at a mid-crustal level: An example from the Palaeoproterozoic Nagssugtoqidian Orogen (West Greenland). *Canadian Journal of Earth Sciences*, 35, 802–819.

Mather, K. A., Pearson, D. G., McKenzie, D., Kjarsgaard, B. A., & Priestley, K. (2011). Constraints on the depth and thermal history of cratonic lithosphere from peridotite xenoliths, xenocrysts and seismology. *Lithos*, 125(1–2), 729–742.

Mattey, D., Lowry, D., & Macpherson, C. (1994). Oxygen isotope composition of mantle peridotite. *Earth and Planetary Science Letters*, *128*, 231–241.

Mayborn, K. R. & Lesher, C. E. (2006). Origin and evolution of the Kangâmiut mafic dyke swarm, West Greenland. *Geological Survey of Denmark and Greenland Bulletin*, 11, 61–86.

McDonough, W. F. (1990). Constraints on the composition of the continental lithospheric mantle. *Earth and Planetary Science Letters*, 101, 1–18.

McDonough, W. F. & Sun, S. s. (1995). The composition of the Earth. *Chemical Geology*, 120, 223–253.

McKenzie, D. (1989). Some remarks on the movement of small melt fractions in the mantle. *Earth and Planetary Science Letters*, 95, 53–72.

McIntyre, T., Pearson, D. G., Szilas, K. & Morishita, T. (2019). Implications for the origins of Eoarchean ultramafic rocks of the North Atlantic Craton: a study of the Tussaap Ultramafic complex, Itsaq Gneiss complex, southern West Greenland. *Contributions to Mineralogy and Petrology*. Springer Berlin Heidelberg, 174, 1–21.

McIntyre, T., Waterton, P., Vezinet, A., Szilas, K., & Pearson, D. G. (2021). Extent and age of Mesoarchean components in the Nagssugtoqidian orogen, West Greenland: Implications for tectonic environments and crust building in cratonic orogenic belts. *Lithos*, *396–397*, 106182.

Meisel, T., Walker, R. J., Irving, A. J. & Lorand, J. P. (2001). Osmium isotopic compositions of mantle xenoliths: A global perspective. *Geochimica et Cosmochimica Acta*, 65, 1311–1323.

Menzies M. A. (1990). Archean, Proterozoic, and Phanerozoic lithospheres. In: Menzies, M. A. (ed). *Continental mantle*, Clarendon Press, 67-86.

Menzies, M.A. & Hawkesworth C. (1987). Mantle Metasomatism. Academic Press Inc., 512.

Menzies, M., Xu, Y., Zhang, H., & Fan, W. (2007). Integration of geology, geophysics and geochemistry: A key to understanding the North China Craton. *Lithos*, *96*, 1–21.

Michaut, C., & Jaupart, C. (2004). Nonequilibrium temperatures and cooling rates in thick continental lithosphere. *Geophysical Research Letters*, 31, 1–4.

Michaut, C., Jaupart, C., & Bell, D. R. (2007). Transient geotherms in Archean continental lithosphere: New constraints on thickness and heat production of the subcontinental lithospheric mantle. *Journal of Geophysical Research: Solid Earth*, 112, 4408.

Mitchell, A. L., & Grove, T. L. (2015). Melting the hydrous, subarc mantle: the origin of primitive andesites. *Contributions to Mineralogy and Petrology*, *170*, 1–23.

Moody, J. B. (1976). An experimental study on the serpentinization of iron-bearing olivines. *Canadian Mineralogist*, *14*, 462–478.

Moyen, J. F. & Martin, H. (2012). Forty years of TTG research. *Lithos*, 148, 312–336.

Mungall, J. & Brenan, J. (2014). Partitioning of platinum-group elements and Au between sulfide liquid and basalt and the origins of mantle-crust fractionation of the chalcophile elements. *Geochimica et Cosmochimica Acta*, *125*, 265–289.

Næraa, T., Scherstén, A., Rosing, M. T., Kemp, A. I. S., Hoffmann, J. E., Kokfelt, T. F. & Whitehouse, M. J. (2012). Hafnium isotope evidence for a transition in the dynamics of continental growth 3.2 Gyr ago. *Nature*, 485, 627–630.

Nishio, I., Morishita, M., Itano, K., Guotana, J. M., Tamura, A., Szilas, K., Harigane, Y., Tani, K., & Pearson, D. G. (in press). Metasomatic modification of the Mesoarchean Ulamertoq ultramafic body, southern West Greenland. Journal of Petrology, XX, XXXX.

Niu, Y. (2004). Bulk-rock major and trace element compositions of abyssal peridotites: Implications for mantle melting, melt extraction and post-melting processes beneath Mid-Ocean ridges. *Journal of Petrology*, *45*, 2423–2458.

Nutman, A.P.; McGregor, V.R.; Friend, C.R.L.; Bennet, V.C.; Kinny, P. D. (1996). The Itsaq Gneiss Complex of southern West Greenland; the world's most extensive record of early crustal evolution (3900-3600 Ma). *Precambrian Research*, 78, 1–39.

Nutman, A. P., Friend, C. R. L., Barker, S. L. L. & McGregor, V. R. (2004). Inventory and assessment of Palaeoarchaean gneiss terrains and detrital zircons in southern West Greenland. *Precambrian Research*, 135, 281–314.

Nutman, A. P., Kalsbeek, F., Marker, M., Gool, J. A. M. Van & Bridgwater, D. (1999). U – Pb zircon ages of Kangamiut dykes and detrital zircons in metasediments in the Palaeoproterozoic Nagssugtoqidian Orogen (West Greenland) Clues to the pre-collisional history of the orogen 1. *Precambrian Research* 93, 87–104.

Nutman, A. P., Kinny, P. D., & Price, R. (1993). Complicated By Limited Exposure; the Best Exposures. *Tectonics*, *12*(4), 971–981.

O'Driscoll, B., Walker, R. J., Clay, P. L., Day, J. M. D., Ash, R. D., & Daly, J. S. (2018). Length-scales of chemical and isotopic heterogeneity in the mantle section of the Shetland Ophiolite Complex, Scotland. *Earth and Planetary Science Letters*, *488*, 144–154.

O'Driscoll, Brian, Day, J. M. D., Walker, R. J., Daly, J. S., McDonough, W. F., & Piccoli, P. M. (2012). Chemical heterogeneity in the upper mantle recorded by peridotites and chromitites from the Shetland Ophiolite Complex, Scotland. *Earth and Planetary Science Letters*, *333–334*, 226–237.

O'Neill, C., Lenardic, A., Moresi, L., Torsvik, T. H. & Lee, C. T. A. (2007). Episodic Precambrian subduction. *Earth and Planetary Science Letters*, 262, 552–562.

O'Reilly, S. Y., & Griffin, W. L. (2000). Apatite in the mantle: Implications for metasomatic processes and high heat production in Phanerozoic mantle. *Lithos*, 53, 217–232.

O'Reilly, S. Y., & Griffin, W. L. (2013). Mantle Metasomatism. In D. E. Harlov & H. Austrheim (Eds.), Metasomatism and the Chemical Transformation of Rock (pp. 471–533).

Paces, J. B. & Miller, J. D. (1993). Precise U-Pb Ages of Duluth Complex and Related Mafic Intrusions, Northeastern Minnesota' Geochronological Insights to Physical, Petrogenetic, Paleomagnetic, and Tectonomagmatic Processes Associated With the 1.1 Ga Midcontinent Rift System. *Journal of geophysical research*, 98, 13997–14013.

Padron-Nvarta, J. A., Sanchez-Vizcaino, V. L., Garrido, C. J., & Gomez-Pugnaire, M. . (2011). Metamorphic Record of High-pressure Dehydration of Antigorite Serpentinite to Chlorite Harzburgite in a Subduction Setting (Cerro del Almirez , Nevado-Filabride Complex, Southern Spain. *Journal of Petrology*, *52*, 2047–2078.

Palin, R. M., Santosh, M., Cao, W., Li, S. S., Hernández-Uribe, D. & Parsons, A. (2020). Secular change and the onset of plate tectonics on Earth. *Earth-Science Reviews*, 207, 103172.

Parkinson, I. J., & Pearce, J. A. (1998). Peridotites from the Izu-Bonin-Mariana forearc (ODP Leg

125): evidence for mantle melting and melt-mantle interaction in a supra-subduction zone setting. *Journal of Petrology*, *39*, 1577–1618.

Paton, C., Woodhead, J. D., Hellstrom, J. C., Hergt, J. M., Greig, A. & Maas, R. (2010). Improved laser ablation U-Pb zircon geochronology through robust downhole fractionation correction. *Geochemistry, Geophysics, Geosystems*, 11, Q0AA06.

Pearce, J. A. (1996). A User's Guide to Basalt Discriminant Diagrams. In: Wyman, D. (ed.) *Trace Element Geochemistry of Volcanic Rocks: Applications for Massive Sulphide Exploration, Geological Association of Canada, Short Course Notes*, 12, 79–113.

Pearce, J. A. (2008). Geochemical fingerprinting of oceanic basalts with applications to ophiolite classification and the search for Archean oceanic crust. *Lithos*, 100, 14–48.

Pearce, J. A., Barker, P. F., Edwards, S. J., Parkinson, I. J., & Leat, P. T. (2000). Geochemistry and tectonic significance of peridotites from the South Sandwich arc-basin system, South Atlantic. *Contributions to Mineralogy and Petrology*, *139*, 36–53.

Pearson, D. G. (1989). The petrogenesis of pyroxenites containing octahedral graphite and associated mafic ultramafic rocks of the Beni Bousera peridotite massif, North Morocco. *Unpublished PhD Thesis*, University of Leeds, p. 412.

Pearson, D. G., Canil, D., & Shirey, S. B. (2003). Mantle Samples Included in Volcanic Rocks: Xenoliths and Diamonds. Xenoliths and Diamonds. In: Holland, H. D. & Turekian, K. K. (Eds.). *Treatise on Geochemistry: Second Edition*, Pergamon, 171-275.

Pearson, D. G., Carlson, R. W., Shirey, S. B., Boyd, F. R., & Nixon, P. H. (1995). Stabilisation of Archaean lithospheric mantle: A Re–Os isotope study of peridotite xenoliths from the Kaapvaal craton. *Earth and Planetary Science Letters*, *134*, 341–357.

Pearson, D. G., Irvine, G. J., Ionov, D. A., Boyd, F. R., & Dreibus, G. E. (2004). Re-Os isotope systematics and platinum group element fractionation during mantle melt extraction: A study of massif and xenolith peridotite suites. *Chemical Geology*, *208*, 29–59.

Pearson, D. G., Lui, J., Smith, C. B., Mather, K. A., Krebs, M. Y., Bulanova, G. P., & Kobussen, A. (2018). Characteristics and origin of the mantle root beneath the Murowa diamond mine: Implications for craton and diamond formation. *Society of Economic Geologists Special publication*, *20*, 403–423.

Pearson, D. G., & Nowell, G. M. (2002). The continental lithospheric mantle: Characteristics and

significance as a mantle reservoir. *Philosophical Transactions of the Royal* Society, *360*, 2383–2410.

Pearson, D. G., Scott, J., Liu, J., Schaeffer, A. J., Wang, L. H., van Hunen, J., Szilas, K., Chacko, T., & Kelemen, T. (2021). Deep continental roots and cratons. *Nature*, 596, 199-210.

Pearson, D. G. & Wittig, N. (2014). The Formation and Evolution of Cratonic Mantle Lithosphere - Evidence from Mantle Xenoliths. In: Holland, H. D. & Turekian, K. K. (Eds.). *Treatise on Geochemistry: Second Edition*, Elsevier, 255-292.

Pearson, D. G. & Woodland, S. J. (2000). Solvent extraction/anion exchange separation and determination of PGEs (Os, Ir, Pt, Pd, Ru) and Re-Os isotopes in geological samples by isotope dilution ICP-MS. *Chemical Geology*, 165, 87–107.

Pedersen, M., Weng, W. L., Keulen, N. & Kokfelt, T. F. (2013). A new seamless digital 1:500 000 scale geological map of Greenland. *Geological Survey of Denmark and Greenland Bulletin*, 65–68.

Perchuk, A. L., Gerya, T. V, Zakharov, V. S., & Griffin, W. L. (2020). Building cratonic keels in Precambrian plate tectonics. *Nature*, 586, 396-401.

Pettke, T., Oberli, F., Audétat, A., Guillong, M., Simon, A. C., Hanley, J. J., & Klemm, L. M. (2012). Recent developments in element concentration and isotope ratio analysis of individual fluid inclusions by laser ablation single and multiple collector ICP-MS. *Ore Geology Reviews*, 44, 10–38.

Philipp, H., Eckhardt, J. D. & Putchelt, H. (2001). Platinum-Group Elements (PGE) in Basalts of the Seaward-Dipping Reflector Sequence, SE Greenland Coast. *Journal of Petrology*, 42, 407–432.

Pickering-Witter, J., & Johnston, A. D. (1999). The Effects of variable mineral proportions on the melting systematics of fertile peridotic assemblages. *Contributions to Mineralogy and Petrology*, *140*, 190–211.

Pitcher, L., Helz, R. T., Walker, R. J. & Piccoli, P. (2009). Fractionation of the platinum-group elments and Re during crystallization of basalt in Kilauea Iki Lava Lake, Hawaii. *Chemical Geology*, 260, 196–210.

Polat, A. & Hofmann, A. W. (2003). Alteration and geochemical patterns in the 3.7-3.8 Ga Isua greenstone belt, West Greenland. *Precambrian Research*, 126, 197–218.

Pollack, H. N., & Chapman, D. S. (1977). On the regional variation of heat flow, geotherms, and lithospheric thickness. *Tectonophysics*, 38, 279–296.

Powell, W., Zhang, M., O'Reilly, S. Y., & Tiepolo, M. (2004). Mantle amphibole trace-element and isotopic signatures trace multiple metasomatic episodes in lithospheric mantle, western Victoria, Australia. *Lithos*, *75*, 141–171.

Puchtel, I. S., Hofmann, A. W., Amelin, Y. V., Garbe-Schönberg, C. D., Samsonov, A. V. & Shchipansky, A. A. (1999). Combined mantle plume-island arc model for the formation of the 2.9 Ga Sumozero-Kenozero greenstone belt, SE Baltic Shield: Isotope and trace element constraints. *Geochimica et Cosmochimica Acta*, 63, 3579–3595.

Puchtel, I. S., Hofmann, A. W., Mezger, K., Jochum, K. P., Shchipansky, A. A. & Samsonov, A. V. (1998). Oceanic plateau model for continental crustal growth in the Archaean: A case study from the Kostomuksha greenstone belt, NW Baltic Shield. *Earth and Planetary Science Letters*, 155, 57–74.

Puchtel, I. S., Humayun, M., Campbell, A. J., Sproule, R. A. & Lesher, C. M. (2004). Platinum group element geochemistry of komatiites from the Alexo and Pyke Hill areas, Ontario, Canada. *Geochimica et Cosmochimica Acta*, 68, 1361–1383.

Rapp, R. P., Shimizu, N., Norman, M. D., & Applegate, G. S. (1999). Reaction between slab-derived melts and peridotite in the mantle wedge: Experimental constraints at 3.8 GPa. *Chemical Geology*, *160*, 335–356.

Regier, M. E., Miškovi, A., Ickert, R. B., Pearson, D. G., Stachel, T., Stern, R. A., & Kopylova, M. (2018). An oxygen isotope test for the origin of Archean mantle roots. *Geochemical Perspectives Letters*, *9*, 6–10.

Rehfeldt, T., Foley, S. F., Jacob, D. E., Carlson, R. W., & Lowry, D. (2008). Contrasting types of metasomatism in dunite, wehrlite and websterite xenoliths from Kimberley, South Africa. *Geochimica et Cosmochimica Acta*, *72*, 5722–5756.

Reid, D. L. (1997). Sm-Nd age and REE geochemistry of Proterozoic arc-related igneous rocks in the Richtersveld Subprovince, Namaqua Mobile Belt, Southern Africa. *Journal of African Earth Sciences*, *24*, 621–633.

Reimink, J. R., Davies, J. H. F. L., & Ielpi, A. (2021). Global zircon analysis records a gradual rise of continental crust throughout the Neoarchean. *Earth and Planetary Science Letters*, *554*,

116654.

Richardson, S. H., Gurney, J. J., Erlank, A. J., & Harris, J. W. (1984). Origin of diamonds in old enriched mantle. *Nature, 310*, 198–202.

Rizo, H., Walker, R. J., Carlson, R. W., Touboul, M., Horan, M. F., Puchtel, I. S., Boyet, M. & Rosing, M. T. (2016). Early Earth differentiation investigated through 142Nd, 182W, and highly siderophile element abundances in samples from Isua, Greenland. *Geochimica et Cosmochimica Acta*, 175, 319–336.

Robb, L. J., Armstrong, R. A., & Waters, D. J. (1999). The history of granulite-facies metamorphism and crustal growth from single zircon U-Pb geochronology: Namaqualand, South Africa. *Journal of Petrology*, *40*, 1747–1770.

Rollinson, H. (2007). Recognising early Archaean mantle: A reappraisal. *Contributions to Mineralogy and Petrology*, 154, 241–252.

Rollinson, H., Appel, P. W. U. & Frei, R. (2002). A Metamorphosed, Early Archaean Chromitite from West Greenland: Implications for the Genesis of Archaean Anorthositic Chromitites. *Journal of Petrology*, 43, 2143–2170.

Rosen, O. M. (2002). Siberian craton - A fragment of a Paleoproterozoic supercontinent. *Russian Journal of Earth Sciences*, *4*, 103–119.

Rosing, M. T., Nutman, A. P. & Løfqvist, L. (2001). A new fragment of the early earth crust: The Aasivik terrane of West Greenland. *Precambrian Research*, 105, 115–128.

Rudnick, R. L., McDonough, W. F., & O'Connell, R. J. (1998). Thermal structure, thickness and composition of continental lithosphere. *Chemical Geology*, *145*, 395–411.

Rudnick, R. L., & Nyblade, A. A. (1999). The thickness and heat production of Archean lithosphere: constraints from xenolith thermobarometry and surface heat flow. *Geochemical Society Special publication*, *6*, 3–12.

Russell, J. K., Dipple, G. M., & Kopylova, M. G. (2001). Heat production and heat flow in the mantle lithosphere, Slave craton, Canada. *Physics of the Earth and Planetary Interiors*, *123*, 27–44.

Safonov, O., Butvina, V., & Limanov, E. (2019). Phlogopite-forming reactions as indicators of metasomatism in the lithospheric mantle. *Minerals*, *9*, 1–18.

Said, N., Kerrich, R. & Groves, D. (2010). Geochemical systematics of basalts of the Lower Basalt Unit, 2.7 Ga Kambalda Sequence, Yilgarn craton, Australia: Plume impingement at a rifted

craton margin. *Lithos*, 115, 82–100.

Salters, V. J. M., Longhi, J. E., & Bizimis, M. (2002). Near mantle solidus trace element partitioning at pressures up to 3.4 GPa. *Geochemistry, Geophysics, Geosystems*, *3*, 1–23.

Sambridge, M. & Lambert, D. D. (1997). Propagating errors in decay equations: Examples from the Re-Os system. *Geochimica et Cosmochimica Acta*, 61, 3019–3024.

Sand, K. K., Waight, T. E., Pearson, D. G., Nielsen, T. F. D., Makovicky, E. & Hutchison, M. T. (2009). The lithospheric mantle below southern West Greenland: A geothermobarometric approach to diamond potential and mantle stratigraphy. *Lithos*, 112, 1155–1166.

Scherstén, A. & Garde, A. A. (2013). Complete hydrothermal re-equilibration of zircon in the Maniitsoq structure, West Greenland: A 3001 Ma minimum age of impact? *Meteoritics and Planetary Science*, 48, 1472–1498.

Schulze, D. J. (1989). Constraints on the abundance of eclogite in the upper mantle. Journal of

Simon, N. S. C., Carlson, R. W., Pearson, D. G., & Davies, G. R. (2007). The origin and evolution of the Kaapvaal Cratonic Lithospheric Mantle. *Journal of Petrology*, *48*, 589–625.

Scott, D. J. (1998). An overview of the U-Pb geochronology of the Paleoproterozoic Torngat Orogen, northeastern Canada. *Precambrian Research*, *91*, 91–107.

Scott, D. J. (1999). U-Pb geochronology of the eastern Hall Peninsula, southern Baffin Island, Canada: A northern link between the Archean of West Greenland and the Paleoproterozoic Torngat Orogen of northern Labrador. *Precambrian Research*, *93*, 5–26.

Scott, D. J., & Gauthier, G. (1996). Comparison of TIMS (U-Pb) and laser ablation microprobe ICP-MS (Pb) techniques for age determination of detrital zircons from paleoproterozoic metasedimentary rocks from northeastern Laurentia, Canada, with tectonic implications. *Chemical Geology*, *131*, 127–142.

Scott, J. M., Liu, J., Pearson, D. G., Harris, G. A., Czertowicz, T. A., Woodland, S. J., Riches, A J. V., & Luth, R. W. (2019). Continent stabilisation by lateral accretion of subduction zone-processed depleted mantle residues; insights from Zealandia. *Earth and Planetary Science Letters*, *507*, 175–186.

Scott, J. M., Pearson, D. G., Liu, J., Auer, A., Cooper, Al. F., Li, D., Palmaer, M. C., Read, S. E., Reid, M. R., & Woodland, S. (2021). Osmium isotopes in peridotite xenoliths reveal major

mid-Proterozoic lithosphere formation under the Transantarctic Mountains. *Geochimica et Cosmochimica Acta*, *312*, 25-43.

Scott, D. R. & Stevenson, D. J. (1989). A self-consistent model of melting, magma migration and buoyancy-driven circulation beneath mid-ocean ridges. *Journal of Geophysical Research*, 94, 2973-2988.

Secchiari, A., Gleissner, P., Li, C., Goncharov, A., Milke, R., Becker, H., Bosch, D., & Montanini, A. (2020). Highly siderophile and chalcophile element behaviour in abyssal-type and supra-subduction zone mantle: New insights from the New Caledonia ophiolite. *Lithos*, *354–355*, 105338.

Selby, D., Creaser, R. A., Stein, H. J., Markey, R. J. & Hannah, J. L. (2007). Assessment of the 187Re decay constant by cross calibration of Re-Os molybdenite and U-Pb zircon chronometers in magmatic ore systems. *Geochimica et Cosmochimica Acta*, 71, 1999–2013.

Selway, K., Ford, H., & Kelemen, P. (2015). The seismic mid-lithosphere discontinuity. Earth and Planetary Science Letters, 414, 45–57.

Sharp, Z. D. (1990). A laser-based microanalytical method for the in situ determination of oxygen isotope ratios of silicates and oxides. *Geochimica et Cosmochimica Acta*, *54*, 1353–1357.

Shimizu, K., Nakamura, E. & Maruyama, S. (2005). The geochemistry of ultramafic to mafic volcanics from the belingwe greenstone belt, Zimbabwe: Magmatism in an archean continental large igneous province. *Journal of Petrology*, 46, 2367–2394.

Simon, N. S. C., Irvine, G. J., Davies, G. R., Pearson, D. G., & Carlson, R. W. (2003). The origin of garnet and clinopyroxene in "depleted" Kaapvaal peridotites. *Lithos*, *71*, 289–322.

Simonetti, A., Heaman, L. M., Hartlaub, R. P., Creaser, R. A., MacHattie, T. G. & Böhm, C. (2005). U-Pb zircon dating by laser ablation-MC-ICP-MS using a new multiple ion counting Faraday collector array. *Journal of Analytical Atomic Spectrometry*, 20, 677–686.

Sláma, J. *et al.* (2008). Plešovice zircon - A new natural reference material for U-Pb and Hf isotopic microanalysis. *Chemical Geology*, 249, 1–35.

Sleep, N. H., Ebinger, C. J., & Kendall, J. M. (2002). Deflection of mantle plume material by cratonic keels. *Geological Society Special Publication*, *199*, 135–150.

Smith, P. M., & Asimow, P. D. (2005). Adiabat-1ph: A new public front-end to the MELTS,

pMELTS, and pHMELTS models. *Geochemistry, Geophysics, Geosystems*, *6*, 1–8.

Smithies, R. H., Champion, D. C., Van Kranendonk, M. J., Howard, H. M. & Hickman, A. H. (2005). Modern-style subduction processes in the Mesoarchaean: Geochemical evidence from the 3.12 Ga Whundo intra-oceanic arc. *Earth and Planetary Science Letters*, 231, 221–237.

Sobolev, A. V *et al.* (2007). Supporting Online Material for The Amount of Recycled Crust in Sources of Mantle-Derived Melts. *Science*, 316, 412–418.

Söderlund, U., Patchett, P. J., Vervoort, J. D. & Isachsen, C. E. (2004). The 176Lu decay constant determined by Lu-Hf and U-Pb isotope systematics of Precambrian mafic intrusions. *Earth and Planetary Science Letters*, 219, 311–324.

St-Onge, M. R., Van Gool, J. A. M., Garde, A. A., & Scott, D. J. (2009). Correlation of Archaean and Palaeoproterozoic units between northeastern Canada and western Greenland: Constraining the pre-collisional upper late accretionary history of the Trans-Hudson orogen. *Geological Society Special Publication*, *318*, 193–235.

Stachel, T., & Harris, J. W. (2008). The origin of cratonic diamonds — Constraints from mineral inclusions. *Ore Geology Reviews*, *34*, 5–32.

Stanley, J. R., & Flowers, R. M. (2016). Dating kimberlite emplacement with zircon and perovskite (U-Th)/He geochronology. *Geochemistry, Geophysics, Geosystems*, 17, 4517–4533.

Steenfelt, A., Hollis, J., Kirkland, C. L., Sandrin, A., Gardiner, N. J., K. H. Olierook, H., Szilas, K., Waterton, P. & Yakymchuk, C. (2021). The Mesoarchaean Akia terrane, West Greenland, revisited: New insights based on spatial integration of geophysics, field observation, geochemistry and geochronology. *Precambrian Research*, 105958.

Stern, R. A., & Bleeker, W. (1998). Age of the world's oldest rocks refined using Canada's SHRIMP: the Acasta Gneiss Complex, Northwest Territories, Canada. *Geoscience Canada*, *25*, 27–31.

Szilas, K., Kelemen, P. B. & Rosing, M. T. (2015). The petrogenesis of ultramafic rocks in the >3.7Ga Isua supracrustal belt, southern West Greenland: Geochemical evidence for two distinct magmatic cumulate trends. *Gondwana Research*. International Association for Gondwana Research, 28, 565–580.

Szilas, K., van Hinsberg, V., McDonald, I., Næraa, T., Rollinson, H., Adetunji, J. & Bird, D. (2017). Highly refractory Archaean peridotite cumulates: Petrology and geochemistry of

the Seqi Ultramafic Complex, SW Greenland. *Geoscience Frontiers*, 9, 689–714.

Sun, J., Liu, C. Z., Wu, F. Y., Yang, Y. H., & Chu, Z. Y. (2012). Metasomatic origin of clinopyroxene in Archean mantle xenoliths from Hebi, North China Craton: Trace-element and Sr-isotope constraints. *Chemical Geology*, *328*, 123–136.

Tang, M., Chen, K. & Rudnick, R. L. (2016). Archean upper crust transition from mafic to felsic marks the onset of plate tectonics. *Science*, 351, 372–375.

Tao, C., Seyfried, W. E., Lowell, R. P., Liu, Y., Liang, J., Guo, Z., … Li, W. (2020). Deep high-temperature hydrothermal circulation in a detachment faulting system on the ultra-slow spreading ridge. *Nature Communications*, *11*, 1300.

Tappe, S., Smart, K. A., Pearson, D. G., Steenfelt, A., & Simonetti, A. (2011). Craton formation in Late Archean subduction zones revealed by first Greenland eclogites. *Geology*, *39*, 1103–1106.

Tappe, S., Dongre, A., Liu, C. Z., & Wu, F. Y. (2018). "Premier" evidence for prolonged kimberlite pipe formation and its influence on diamond transport from deep Earth. *Geology*, 46(10), 843–846.

Thériault, R. J., & Ermanovics, I. (1997). Sm-Nd isotopic and geochemical characterisation of the Paleoproterozoic Torngat orogen, Labrador, Canada. *Precambrian Research*, *81*, 15–35.

Thrane, K. & Connelly, J. N. (2006). Zircon geochronology from the Kangaatsiaq – Qasigiannguit region , the northern part of the 1.9 – 1.8 Ga Nagssugtoqidian orogen , West Greenland. *Geological Survey of Denmark and Greenland Bulletin*, 11, 87–99.

Tomlinson, K. Y., Hughes, D. J., Thurston, P. C. & Hall, R. P. (1999). Plume magmatism and crustal growth at 2.9 to 3.0 Ga in the Steep Rock and Lumby Lake area, Western Superior Province. *Lithos*, 46, 103–136.

Ulrich, M., Picard, C., Guillot, S., Chauvel, C., Cluzel, D., & Meffre, S. (2010). Multiple melting stages and refertilization as indicators for ridge to subduction formation: The New Caledonia ophiolite. *Lithos*, *115*, 223–236.

Uysal, I., Ersoy, E. Y., Karslĩ, O., Dilek, Y., Sadĩklar, M. B., Ottley, C. J., Tiepolo, M., & Meisel, T. (2012). Coexistence of abyssal and ultra-depleted SSZ type mantle peridotites in a Neo-Tethyan Ophiolite in SW Turkey: Constraints from mineral composition, whole-rock geochemistry (major-trace-REE-PGE), and Re-Os isotope systematics. *Lithos*, *132–133*,

50–69.

van de Löcht, J., Hoffmann, J. E., Li, C., Wang, Z., Becker, H., Rosing, M. T., Kleinschrodt, R., & Münker, C. (2018). Earth's oldest mantle peridotites show entire record of late accretion. *Geology*, *46*, 199–202.

van der Wal, D., & Bodinier, J. L. (1996). Origin of the recrystallisation front in the Ronda peridotite by km-scale pervasive porous melt flow. *Contributions to Mineralogy and Petrology*, *122*, 387–405.

van Gool, J. A. M., Connelly, J. N., Marker, M. & Mengel, F. C. (2002). The Nagssugtoqidian Orogen of West Greenland: Tectonic evolution and regional correlations from a West Greenland perspective. *Canadian Journal of Earth Sciences*, 39, 665–686.

van Gool, J. A. M. & Marker, M. (2004). Geological map of Greenland, 1:100 000, Ussuit 67 V.2 Nord. *Geological Survey of Denmark and Greenland*.

van Gool, J. A. M. & Marker, M. (2007). Explanatory notes to the Geological map of Greenland, 1:100 000, Ussuit 67 V.2 Nord. *Geological Survey of Denmark and Greenland Map Series,* 3, 1–40.

Varas-Reus, M. I., Garrido, C. J., Marchesi, C., Bodinier, J. L., Frets, E., Bosch, D., Tommasi, W., Hidas, K., & Targuisti, K. (2016). Refertilization processes in the subcontinental lithospheric mantle: The record of the Beni Bousera orogenic peridotite (Rif Belt, northern Morocco). Journal of Petrology, 57, 2251–2270.

Varfalvy, V., Hébert, R., Bedard, J. H., & Laflèche, M. R. (1997). Petrology and geochemistry of pyroxenite dykes in upper mantle peridotites of the North Arm Mountain massif, Bay of Islands Ophiolite, Newfoundland: Implications for the genesis of boninitic and related magmas. *Canadian Mineralogist*, *35*, 543–570.

Vermeesch, P. (2018). IsoplotR: A free and open toolbox for geochronology. *Geoscience Frontiers*, 9, 1479–1493.

Vernières, J., Godard, M., & Bodinier, J.-L. (1997). A plate model for the simulation of trace element fractionation during partial melting and magma transport in the Earth's upper mantle. *Journal of Geophysical Research: Solid Earth*, *102*, 24771–24784.

Vezinet, A., Pearson, D. G., Thomassot, E., Stern, R. A., Sarkar, C., Luo, Y. & Fisher, C. M.

(2018). Hydrothermally-altered mafic crust as source for early Earth TTG: Pb/Hf/O isotope and trace element evidence in zircon from TTG of the Eoarchean Saglek Block, N. Labrador. *Earth and Planetary Science Letters*, 503, 95–107.

Walker, R. J., Carlson, R. W., Shirey, S. B., & F.R, B. (1989). Os, Sr, Nd, and Pb isotope systematics of southern African peridotite xenoliths: Implications for the chemical evolution of subcontinental mantle. *Geochimica et Cosmochimica Acta*, *53*, 1583–1595.

Walker, R. J., Prichard, H. M., Ishiwatari, A. & Pimentel, M. (2002). The osmium isotopic composition of convecting upper mantle deduced from ophiolite chromites. *Geochimica et Cosmochimica Acta*, 66, 329–345.

Walter, M. J. (1998). Melting of Garnet Peridotite and the Origin of Komatiite and Depleted Lithosphere. *Journal of Petrology*, *39*, 29–60.

Walter, M. J. (2014). Melt Extraction and Compositional Variability in Mantle Lithosphere. In: Holland, H. D. & Turekian, K. K. (Eds.). *Treatise on Geochemistry: Second Edition*, Elsevier, 393–419.

Wang, W., & Gasparik, T. (2001). Metasomatic clinopyroxene inclusions in diamonds from the Liaoning province , China. *Geochimica et Cosmochimica Acta*, *65*(4), 611–620.

Wang, C., Liang, Y., Dygert, N., & Xu, W. (2016). Formation of orthopyroxenite by reaction between peridotite and hydrous basaltic melt: an experimental study. *Contributions to Mineralogy and Petrology*, *171*, 1–18.

Wang, C. G., Xu, W. L., Yang, D. Bin, Liu, Y. S., Pei, F. P., Li, Q. L., & Zhou, Q. J. (2018). Olivine Oxygen Isotope Evidence for Intracontinental Recycling of Delaminated Continental Crust. *Geochemistry, Geophysics, Geosystems*, *19*, 1913–1924.

Wang, H., Huismans, R. S., & Rondenay, S. (2019). Water Migration in the Subduction Mantle Wedge: A Two-Phase Flow Approach. *Journal of Geophysical Research: Solid Earth*, *124*, 9208–9225.

Wang, H., van Hunen, J., & Pearson, D. G. (2015). The thinning of subcontinental lithosphere: The roles of plume impact and metasomatic weakening. *Geochemistry Geophysics Geosystems*, *18*, 1541–1576.

Wang, H., van Hunen, J., & Pearson, D. G. (2018). Making Archean cratonic roots by lateral compression: A two-stage thickening and stabilization model. *Tectonophysics*, *746*, 562–

571.

Wang, L., Kusky, T. M., Polat, A., Wang, S., Jiang, X., Zong, K., Wang, J., Deng, H., & Fu, J. (2014). Partial melting of deeply subducted eclogite from the Sulu orogen in China. *Nature Communications*, *5*, 1–11.

Wardle, R. J., Gower, C. F., James, D. T., St-Onge, M. R., Scott, D. J., Garde, A. A., … Hall, J. (2002). Correlation chart of the Proterozoic assembly of the northeastern Canadian - Greenland Shield. *Canadian Journal of Earth Sciences*, *39*, 895–896.

Wardle, R. J., James, D. T., Scott, D. J., & Hall, J. (2002). The southeastern Churchill Province: Synthesis of a Paleoproterozoic transpressional orogen. *Canadian Journal of Earth Sciences*, *39*, 639–663.

Warren, J. M. (2016). Global variations in abyssal peridotite compositions. *Lithos*, *248–251*, 193–219.

Waters, F. G., & Erlank, A. J. (1988). Assessment of the vertical extent and distribution of mantle metasomatism below kimberley, south africa. *Journal of Petrology*, *Special Volume*, 1, 185–204.

Waterton, P., Guotana, J. M., Nishio, I., Morishita, T., Tani, K., Woodland, S., … Szilas, K. (2022). No mantle residues in the Isua Supracrustal Belt. *Earth and Planetary Science Letters*, *579*, 117348.

Waterton, P. Hyde, W. R., Tusch, J., Hollis, J. A., Kirkland C. L., Kinney, C., Yakymchuk, C., Gardiner, N. J., Zakharov, D., Olierook, K. H., Lightfoot, P. C., and Szilas, K. (2020b). Geodynamic implications of synchronous norite and TTG formation in the 3 Ga Maniitsoq Norite Belt, West Greenland. *Frontiers in Earth Science*, 8, 562062.

Waterton, P., Pearson, D. G., Kjarsgaard, B., Hulbert, L., Locock, A., Parman, S. W. & Davis, B. (2017). Age, Origin, and Thermal Evolution of the ultra-fresh ~1.9 Ga Winnipegosis Komatiites, Manitoba, Canada. *Lithos*, 268–271, 114–130.

Waterton, P., Pearson, D. G., Mertaman, S. A., Mertzman K. R., & Kjarssgaard, B. A. (2020a). A fractional crystallization link between komatiites, basalts, and dunites of the Palaeoproterozoic Winnipegosis Komatiite Belt, Manitoba, Canada. *Journal of Petrology*, 61, 1–30.

Whitehouse, M. J., Kalsbeek, F. & Nutman, A. P. (1998). Crustal growth and crustal recycling in

the Nagssugtoqidian orogen of West Greenland: Constraints from radiogenic isotope systematics and U-Pb zircon geochronology. *Precambrian Research*, 91, 365–381.

Wittig, N., Pearson, D. G., Webb, M., Ottley, C. J., Irvine, G. J., Kopylova, M., … Nowell, G. M. (2008). Origin of cratonic lithospheric mantle roots: A geochemical study of peridotites from the North Atlantic Craton, West Greenland. *Earth and Planetary Science Letters*, *274*, 24–33.

Wittig, N., Webb, M., Pearson, D. G., Dale, C. W., Ottley, C. J., Hutchison, M., Jensen, S. M., & Luguet, A. (2010). Formation of the North Atlantic Craton: Timing and mechanisms constrained from Re-Os isotope and PGE data of peridotite xenoliths from S.W. Greenland. *Chemical Geology*, *276*, 166–187.

Wittig, Nadine, Pearson, D. G., Downes, H., & Baker, J. A. (2009). The U, Th and Pb elemental and isotope compositions of mantle clinopyroxenes and their grain boundary contamination derived from leaching and digestion experiments. *Geochimica et Cosmochimica Acta*, 73, 469–488.

Wlotzka, F. (2005). Cr spinel and chromite as petrogenetic indicators in ordinary chondrites: Equilibration temperatures of petrologic types 3.7 to 6. *Meteoritics and Planetary Science*, *40*, 1673–1702.

Woodhead, J. D. & Hergt, J. M. (2005). A preliminary appraisal of seven natural zircon reference materials for in situ Hf isotope determination. *Geostandards and Geoanalytical Research*, 29, 183–195.

Xie, Q., Campbell McCuaig, T. & Kerrich, R. (1995). Secular trends in the melting depths of mantle plumes: Evidence from HFSE/REE systematics of Archean high-Mg lavas and modern oceanic basalts. *Chemical Geology*, 126, 29–42. Xu, Y. & Liu, C. Z. (2019). Subduction-induced fractionated highly siderophile element patterns in forearc mantle. *Minerals*, *9*, 9–11.

Xu, Y., Li, D., Dong, G. C., Pearson, D. G., & Liu, J. (2021). Modification of Lithospheric Mantle by Melts/Fluids With Different Sulfur Fugacities During the Wilson Cycle: Insights From Lesvos and Global Ophiolitic Peridotites. *Journal of Geophysical Research: Solid Earth*, *126*.

Xu, Y. & Liu, C. Z. (2019). Subduction-induced fractionated highly siderophile element patterns

in forearc mantle. *Minerals*, *9*, 9–11.

Xu, Y., Shankland, T. J., Linhardt, S., Rubie, D. C., Langenhorst, F., & Klasinski, K. (2004). Thermal diffusivity and conductivity of olivine, wadsleyite and ringwoodite to 20 GPa and 1373 K. Physics of the Earth and Planetary Interiors, 143, 321–336.

Yakymchuk, C., Kirkland, C. L., Hollis, J. A., Kendrick, J., Gardiner, N. J. & Szilas, K. (2020). Mesoarchean partial melting of mafic crust and tonalite production during high-T–low-P stagnant tectonism, Akia Terrane, West Greenland. *Precambrian Research*, 339, 105615.

Yaxley, G. M., Berry, A. J., Rosenthal, A., Woodland, A. B., & Paterson, D. (2017). Redox preconditioning deep cratonic lithosphere for kimberlite genesis - Evidence from the central Slave Craton. *Scientific Reports*, *7*, 1–10.

Zheng, Y.-F., & Hermann, J. (2014). Geochemistry of continental subduction-zone fluids. *Earth, Planets and Space*, *66*, 93.

Zheng, Y. F. (2012). Metamorphic chemical geodynamics in continental subduction zones. *Chemical Geology*, *328*, 5–48.

Appendix A Geotherm calculations and model

The modelled steady-state geotherms were calculated from a top-down approach using the equation describing conductive heat transfer through a layer (e.g., Chapman, 1986):

[EQ 1] $T_i = T_{i-1} + (q_{i-1}\Delta z/k(T,P)) - (A\Delta z^2/2k(T,P))$.

The equation describes the temperature at the bottom of a layer (T_i: units K) of thickness $z_i - z_{i-1}$ (Δz; units m) as a function of the temperature at the top of a layer (T_{i-1}: set to 273 K at the surface), thermal conductivity (k), heat flow (q), and heat production (A: units W/m^3). The heat flow at the top of the layer (q_{i-1}: units W/m^2) is described as the heat flow at its base (q_i) plus the heat flow produced by the decay of radiogenic elements (i.e. heat production A; units W/m^3) within the layer:

[EQ 2] $q_{i-1} = q_i + A\Delta z$.

Thus, heat flow at the top of each new layer is q_i at the base of the overlying layer and is calculated using EQ 2.

Heat generation is calculated from the concentration of heat producing elements in the rock:

[EQ 3] $A = \rho_0 10^{-5}[3.5(K_2O \text{ wt}\%) + 9.67(U \text{ ppm}) + 2.63(Th \text{ ppm})]$.

A.1 Temperature and pressure dependent thermal conductivity in the crust

In the crust, we use temperature and pressure dependent thermal conductivity ($k(T,P)$; units W/mK) in the model and solved iteratively for each layer. The equations of Förster et al. (2021) are used where:

[EQ 4] $k(T,P) = k_0 + \Delta k(T) + \Delta k(P)$,

and

[EQ 5] $\Delta k(T) = k(T) - k_0$,

[EQ 6] $\Delta k(P) = k(P) - k^*_0$,

where equations for *k(T)* are lithology dependent and k_0 is the thermal conductivity at surface conditions (Table A-1). k^*_0 is a thermal conductivity term specific to pressure – it is the intercept of the linear function describing changes in *k* as a function of pressure (P; units GPa) for different rocks (see Förster et al. (2021) for discussion). *K(P)* functions take the form:

[EQ 7] $k(P) = k^*_0 (1 + \alpha P)$.

Rearranging eq 4 gives:

[EQ 8] $k(T,P) = k(T) + k^*_0 \alpha P$,

where α (GPa^{-1}) is an empirical constant. All equations and variables are given in Table A-1.

A.2 Temperature and pressure dependent thermal conductivity in the mantle

For the mantle, we additionally use temperature and pressure dependent thermal conductivity, but use the function for *k(T,P)* of Xu et al. (2004):

[EQ 9] $k(T,P) = k_0(298/T_i)^{0.439}(1 + \alpha P)$.

The use of the *k(T,P)* function of Xu et al. (2004) produces Moho heat fluxes between 0.014 and 0.017 W/m^2 for reasonable lithospheric thicknesses (180 to 220 km thick), consistent with the heat flux across the Moho in cratons, which is estimated from surface heat flow and crustal heat production to be between 0.015 and 0.018 W/m^2 (Jaupart & Mareschal, 2015). It should be noted that Förster et al. (2021) also provide temperature and pressure dependent thermal conductivity for the mantle. However, the use of these equations for *k(T,P)* in the mantle yield high *k* values such that heat is too efficiently transferred from the asthenosphere to the base of the crust. For example,

a geotherm with a 0.049 W/m^2 surface heat flow (the approximate average across Archean cratons (Jaupart & Mareschal, 2015; Goes et al., 2020)) requires a Moho heat flow of ~0.023 W/m^2 for a lithospheric thickness of 225 km (thinner lithosphere would require higher moho heat flux).

A.3 Pressure formulation and the mantle adiabat

Pressure in the crust and mantle is solved iteratively with temperature and thermal conductivity:

[EQ 10] $P_B = P_T + \rho(T)g/(1 \times 10^6)$,

where

[EQ 11] $\rho(T) = \rho_0[1 - \acute{\alpha}(T_i - T_0)]$,

g is the acceleration due to gravity (9.81 m/s^2), ρ_0 is the rock density at surface conditions, and T_0 is a reference temperature for each rock type (Table A-1; Krystopowicz & Currie, 2013).

The mantle adiabat is calculated as:

[EQ 12] $T_{adiabat} = 1623 + 0.4z$,

where z is depth (units km).

A.4 Crustal structure

Crustal thickness is held constant at a 39 km and composed of an upper and lower crust (13 and 26 km thickness, respectively). Lower crustal heat generation is held constant at 0.28xE-6 W/m^3 (Hacker et al., 2015). However, upper crustal heat generation has an exceptionally large influence on geotherms and is varied to produce appropriate geotherms used in Figs. 1-1, 4-8, 4-9, B4-6, and E-1; $q_{moho}/q_{surface} = 0.37$, fixed depth, and fixed q_{moho}. Mantle heat generation is varied as discussed in text and Figs. 1-1, 4-8, 4-9, B4-6, and E-1.

Table A-1 Properties of lithosphere used in geothermal models.

	Lithology	Thickness (km)	Density, ρ_0 (kg/m³)	k(T) or k(T,P)	α (GPa⁻¹)	k^*_0 (W/mK)	$\acute{a}$ (K⁻¹)	T_0 (K)	Heat generation (W/m³)
Upper crust	Felsic granulite	15	2800	[A]$k(T) = 1/(0.132 + 6.57 \times 10^{-4} T_B) + 0.524 \times 10^{-9} T_B^3$	[A]0.134	[A]3.6	[D]0.00003	[D]627	Variable
lower crust	Mafic granulite	24	3000	[A]$k(T) = 1/(0.344 + 3.27 \times 10^{-4} T_B) + 0.445 \times 10^{-9} T_B^3$	[A]0.044	[A]2.5	[D]0.00003	[D]627	[C]0.16xE-6
mantle	Peridotite	variable	3250	[B]$k(T,P) = k_0(298/T_B)^{0.439}(1 + \alpha P)$	[B]0.032	[B]4.1 (k_0)	[D]0.00003	[D]1344	Variable

[A](Förster et al., 2021)
[B](Xu et al., 2004)
[C](Hacker et al., 2015)
[D](Krystopowicz & Currie, 2013)

Appendix B Supplementary Tables and Figures

Chapter 2 Supplementary Figures
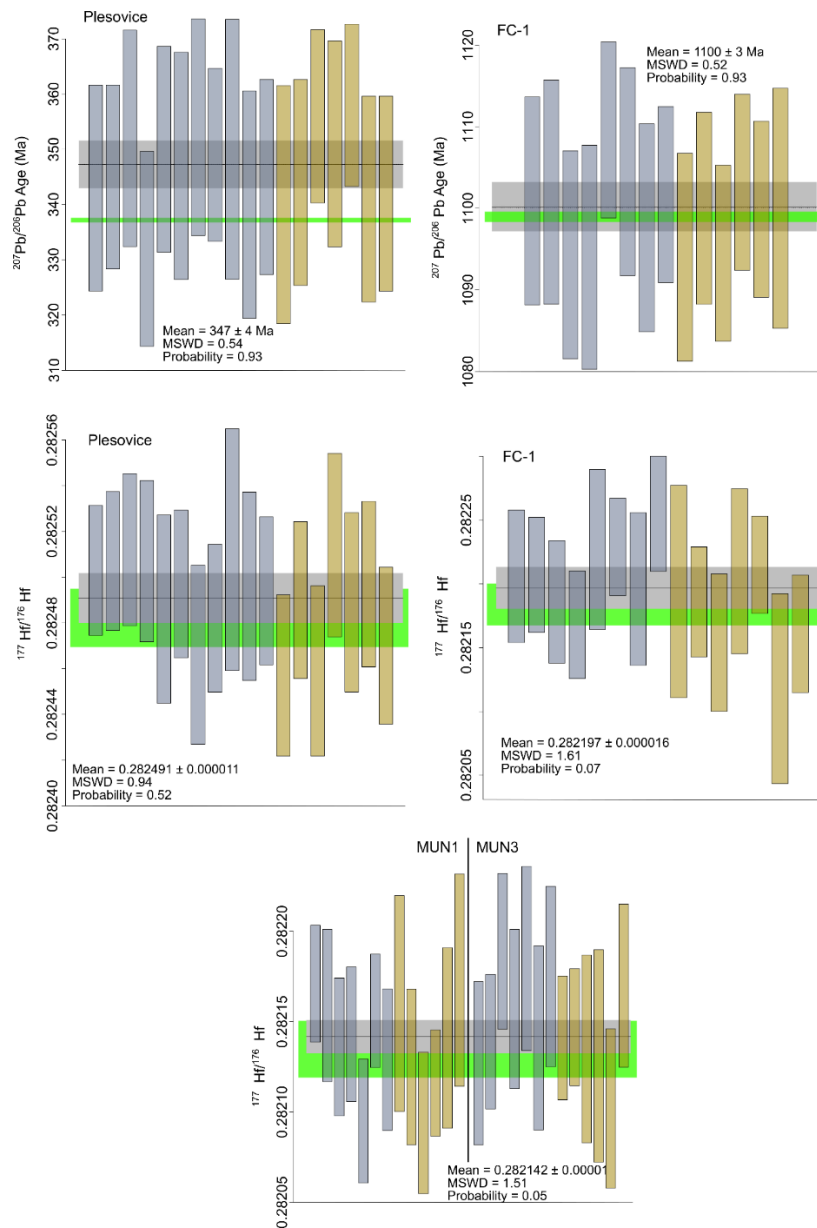
Fig. B2-1. Bar charts and weighted mean ^{207}Pb/^{206}Pd ages and ^{176}Hf/^{177}Hf for reference materials. Error in the analyses (bars) are 2 standard deviations. The grey bar and line are the weighted mean and its error of the analyses. The green bar is the mean and error of the reference value for the materials. Reference values are from Paces & Miller (1993), Woodhead & Hergt (2005), Sláma et

al. (2008), and Fisher et al. (2011). The two colours of bar represent the two difference analytical sessions.
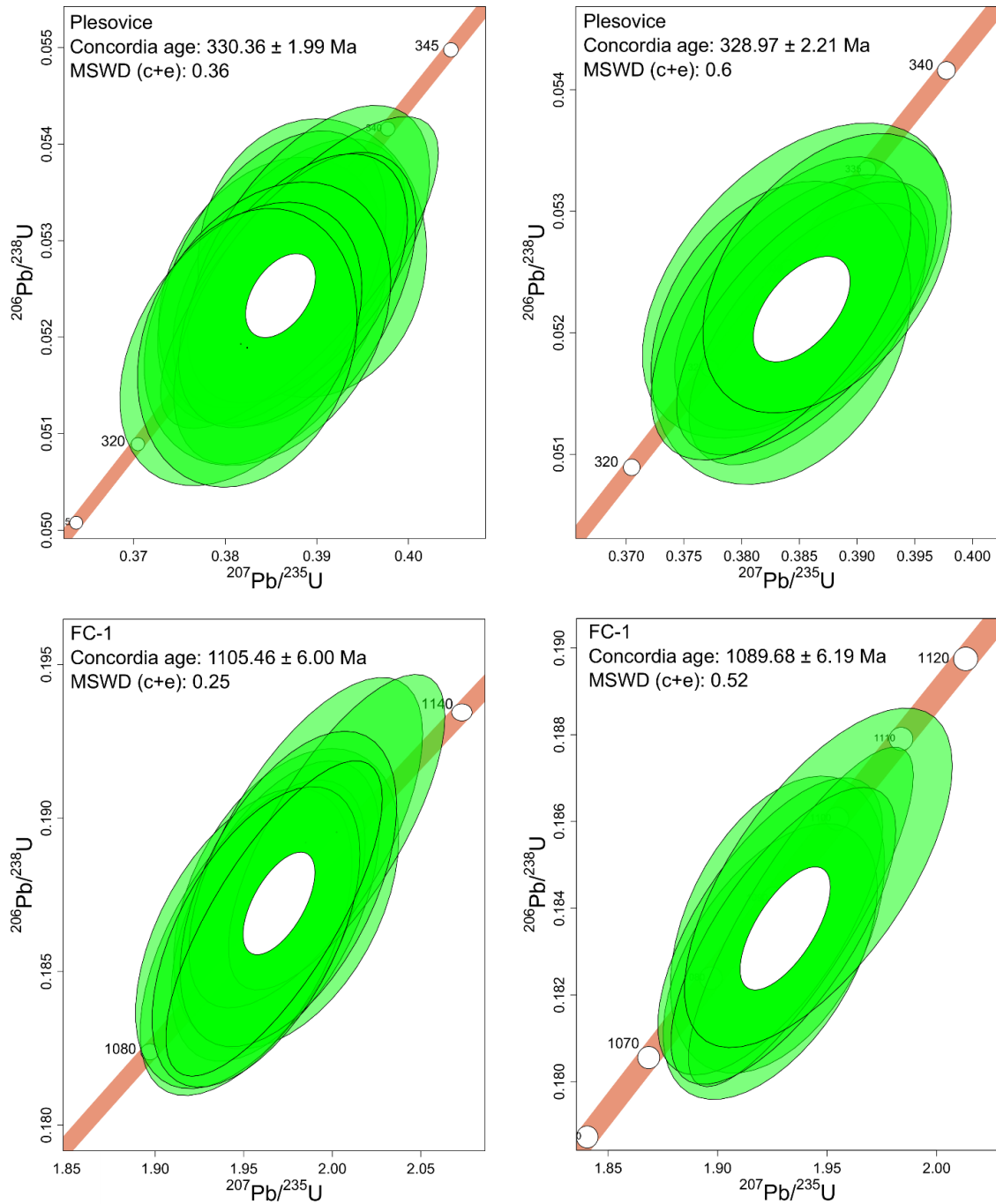
Fig. B2-2. Concordia plots for refence zircons from two analytical sessions undertaken in this study.
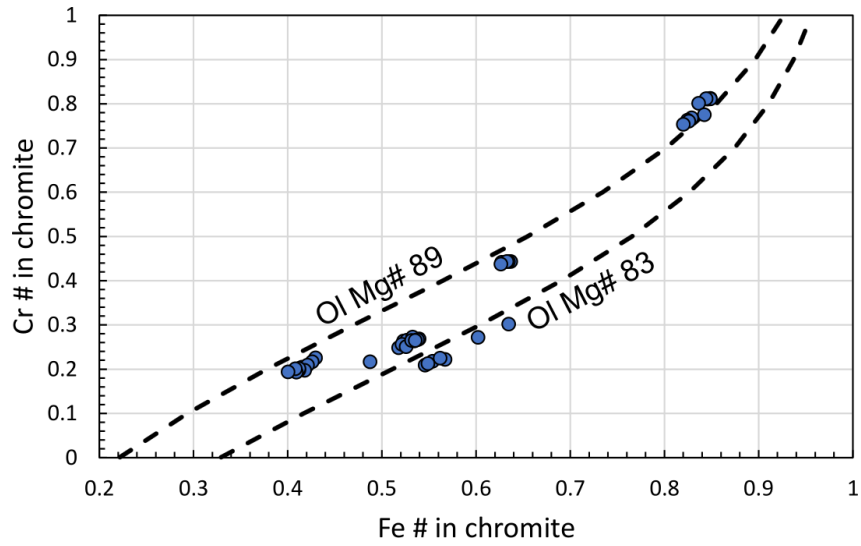
Fig. B2-3. Cr # vs Fe # in chromite for the Qorlortoq cumulates. The diagram shows that the chromite compositions follow lines of equilibration with olivine of different Mg # and temperature of 550 ºC. Olivine equilibration lines are from the thermometer of Wlotzka (2005).
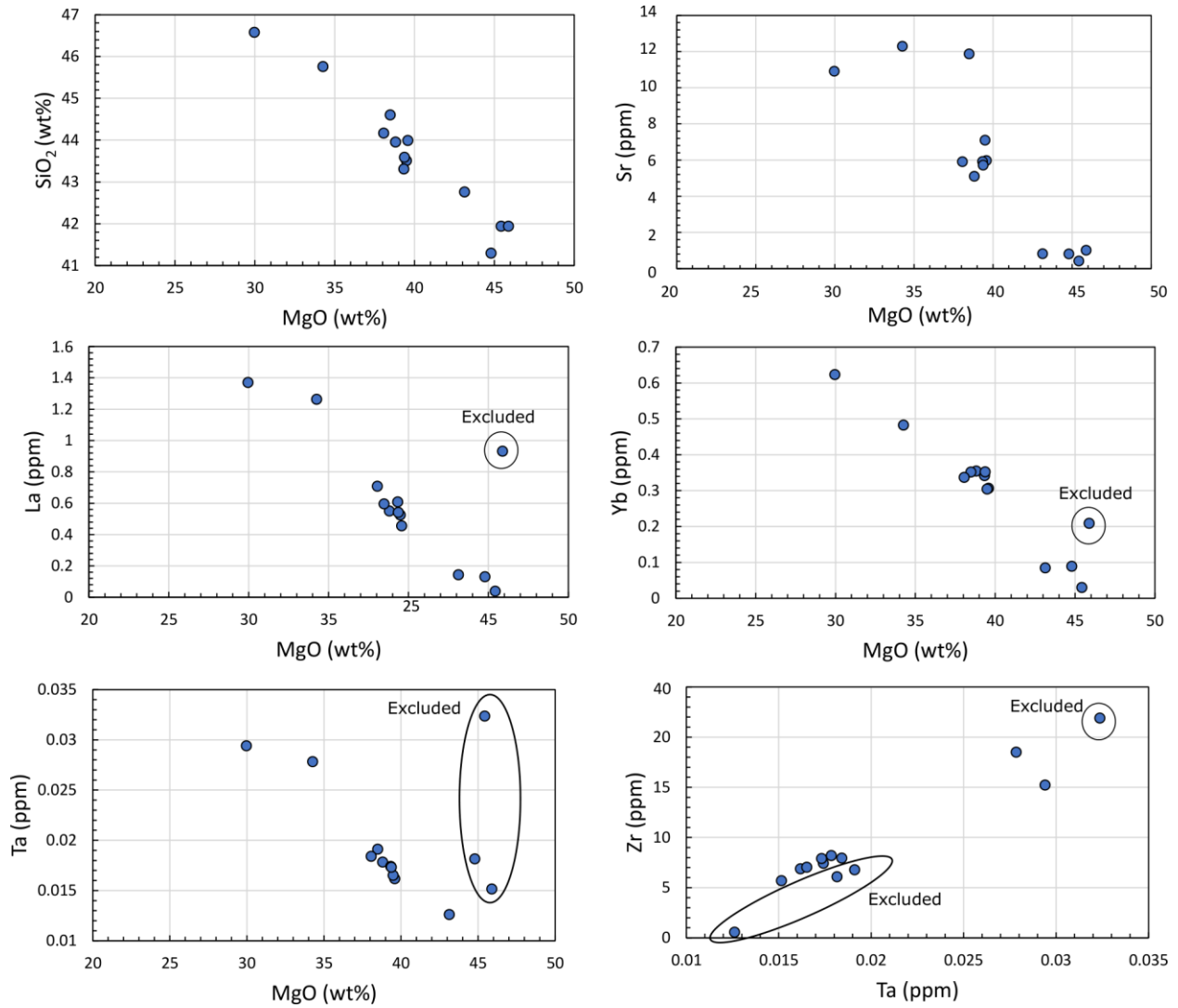
Fig. B2-4. Linear correlations between bulk-rock MgO wt% and other elements in the Qorlortoq cumulates, implying low degrees of alteration. Also, shown are samples excluded from the calculation of initial parental melt compositions determined by regressions of bulk-rock element concentrations to an MgO concentration of 15.9 wt% as discussed in text.
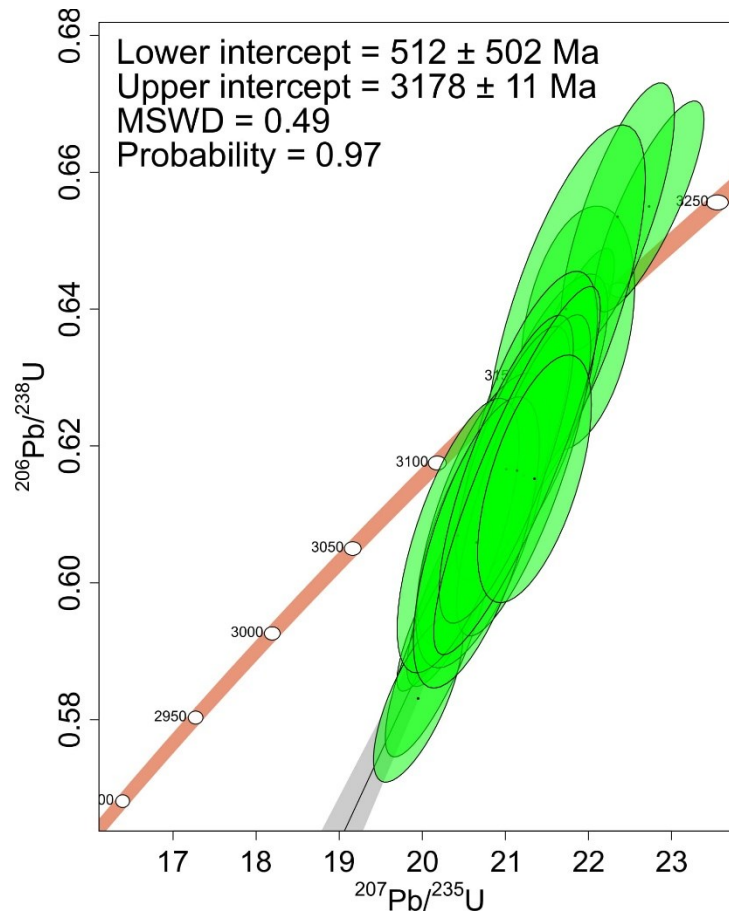
Fig. B2-5. Concordia plot of zircon U-Pb analyses for both Qorlortoq gneiss samples showing that the offset of GR16-256 falls along the discordia line of GR16-261 defining a single population.
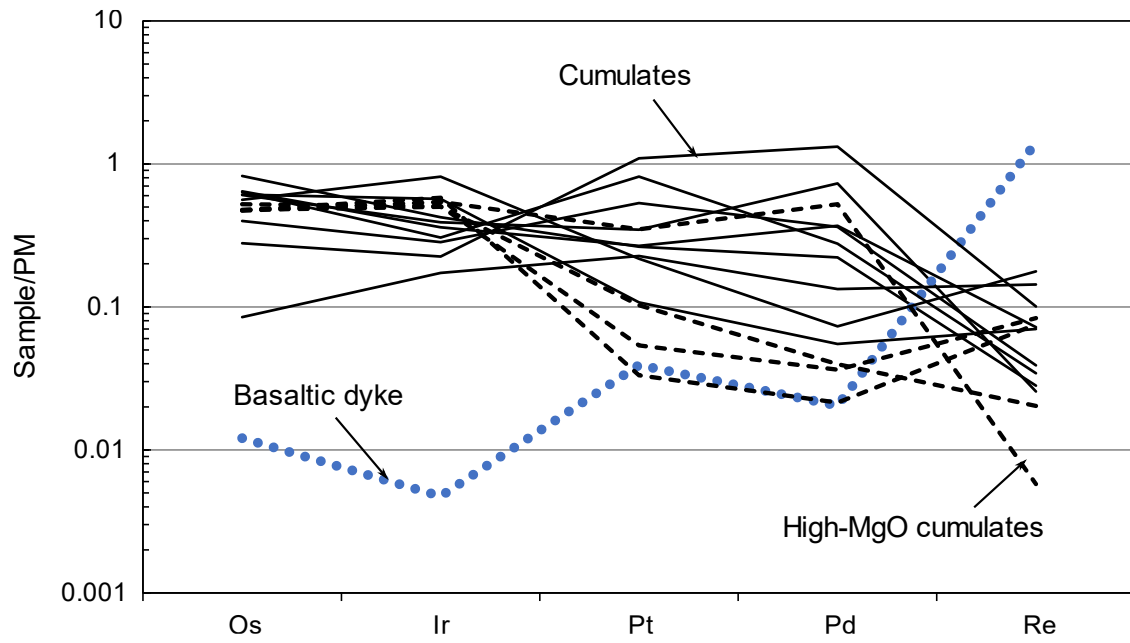
Fig. B2-6. Primitive mantle (PM) normalized PGE concentrations in the Qorlortoq cumulates and basaltic dykes. Normalization values are from Becker et al. (2006).
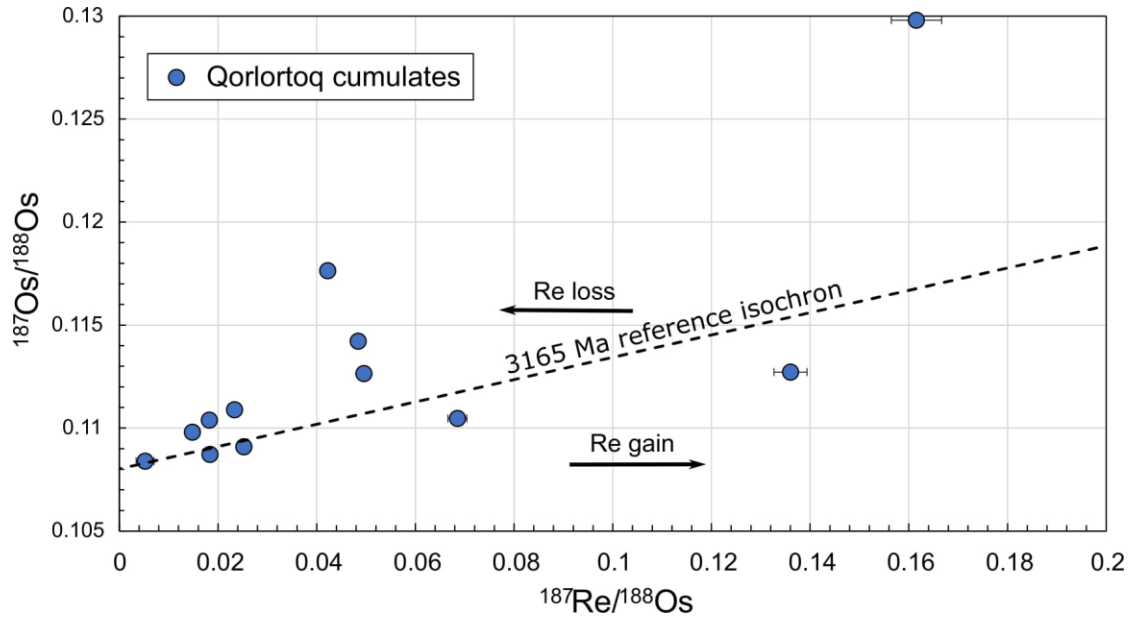
Fig. B2-7. ^{187}Os/^{188}Os vs ^{187}Re/^{188}Os for the cumulates in this study. Where not visible, error bars are smaller than the data markers. Decay constant was that of Selby et al. (2007).
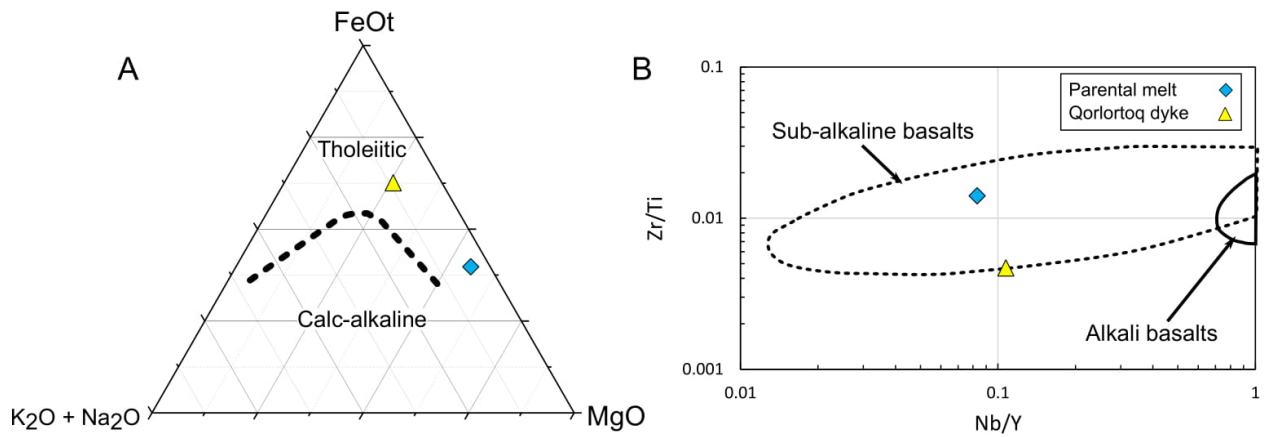
Fig. B2-8. Basalt iscrimination diagrams for the Qorlortoq dyke and parental melts of the Qorlortoq cumulates. Discriminations diagrams of Irvine & Baragar (1971) (A) and Pearce (1996) (B).

Chapter 3 Supplementary Figures
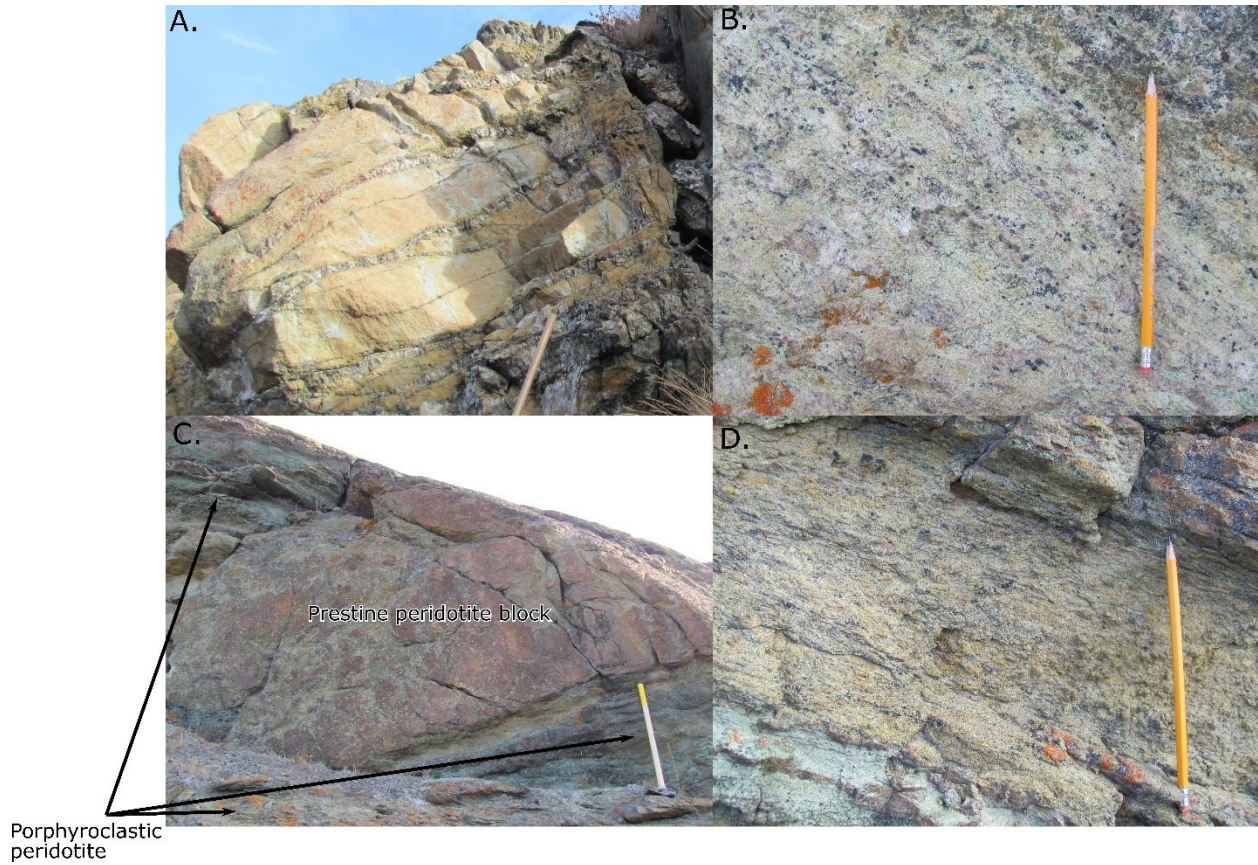
Fig. B3- 1. Outcrop photos of the Ussuit peridotites. A) Dunite with serpentinite veins. Outcrop is ~ 2 m in height. B) Close up of harzburgite from Ussuit metasomatized peridotites. C) Large competent harzburgite block surrounded by porphyroclastic peridotite (hammer is 76 cm long). D) porphyroclastic peridotite.
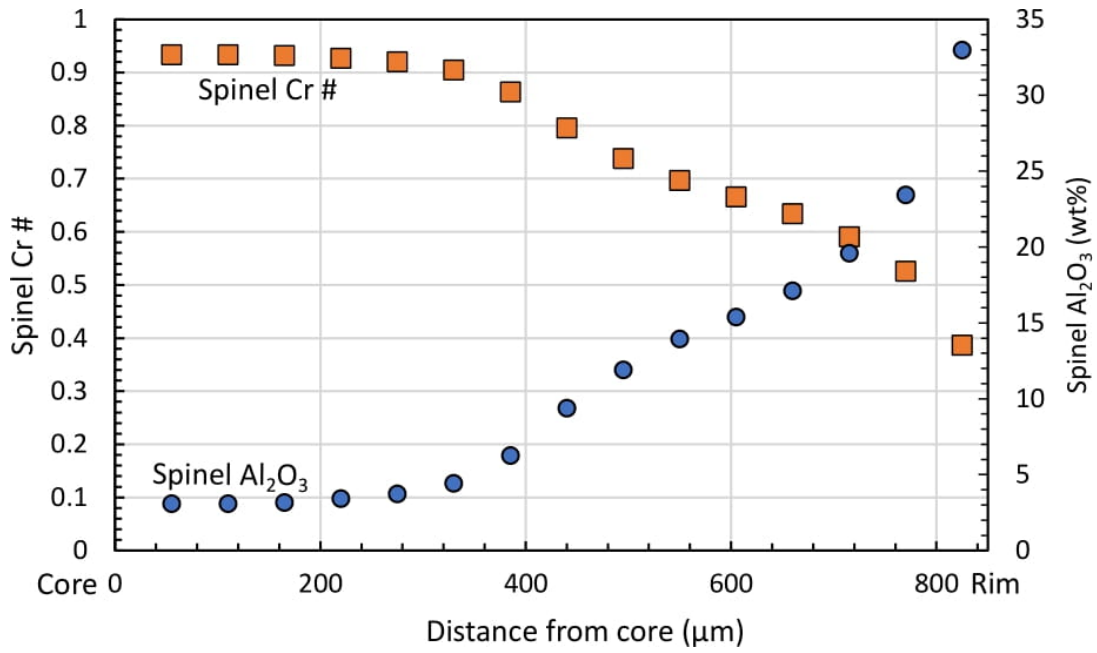
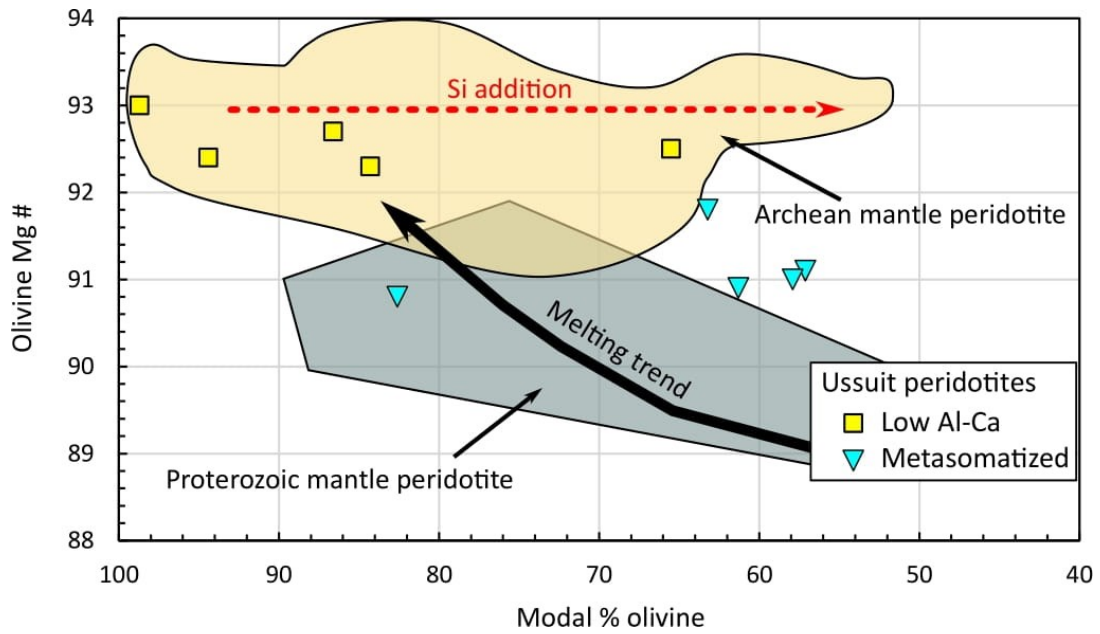Fig. B3-2. Example core to rim profile in spinel from Ussuit metasomatized peridotites showing decreasing Cr # in spinel rims as a result of Al_2O_3 enrichment.

Fig. B3-3. Olivine Mg # vs modal olivine content of the Ussuit peridotite showing that some samples likely have had Si added to them post melting. Diagram, field for Proterozoic and Archean mantle peridotite, and melting and Si addition trends are from Bernstein et al. (2007).
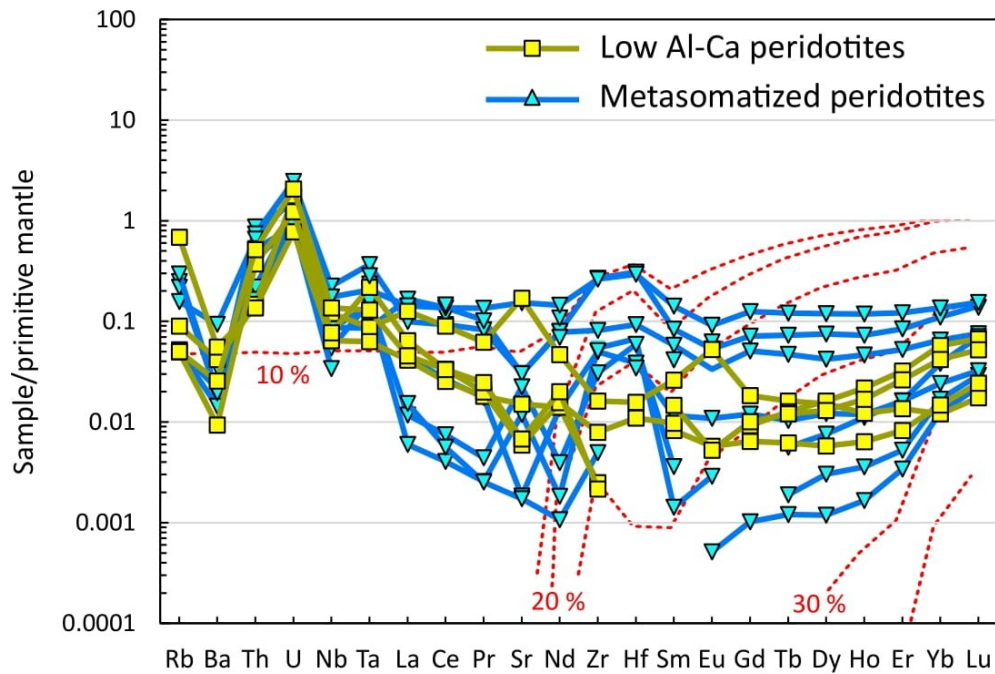
Fig. B3-4. Primitive mantle normalized trace element diagram with extended range of trace elements. As in Fig. 3-4, the pMELTS modelling discussed in Fig. 3-3 is shown for mantle potential temperatures of 1550 ºC (red dashed lines where the labels are melting percent). Primitive normalized values are from McDonough & Sun (1995).
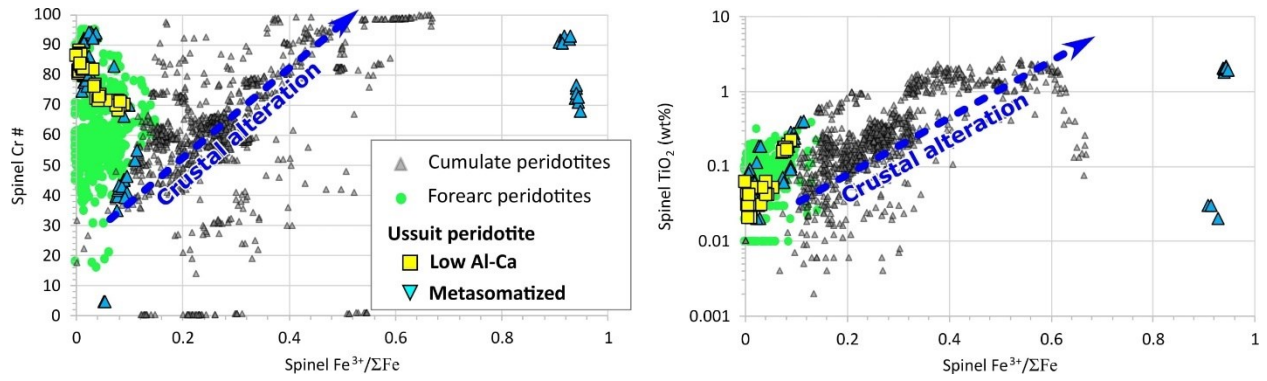
Fig. B3-5. The Ussuit peridotite spinel Cr # - TiO$_2$ - Fe$^{\#+}$/ΣFe systematics showing a clear distinction from cumulate processes and limited indicators of alteration. In both plots the Ussuit peridotite clearly plot in the field of forearc peridotites. References are as in Fig. 3-3.
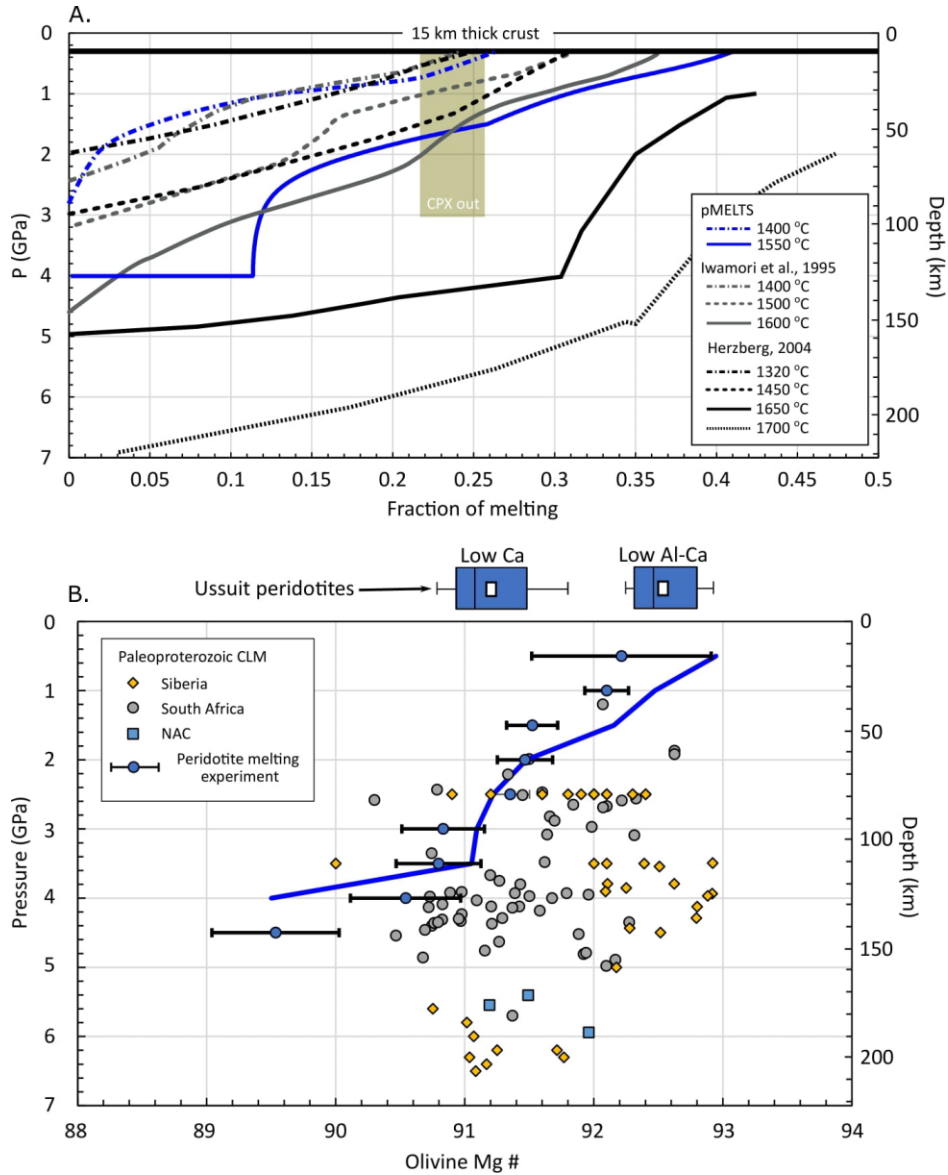
Fig. B3-6. A) Fractional decompression melting trends of fertile peridotite at different mantle potential temperatures. Modelling from pMELTS is as in Fig. 3. B) 1600 ºC melting path of Iwamori et al. (1995) fitted with olivine Mg #'s at 0.5 GPa intervals from anhydrous peridotite melting experiments where the degree of depletion matches within ± 2.5 % (Baker & Stopler, 1994; Walter, 1998; Falloon et al., 1999, 2001, 2008; Pickering-Witter & Johnston, 1999). Error bars reflect 1 standard deviation in the olivine Mg # from melting experiments. Also, shown are the pMELTS olivine Mg #'s for the model in A) at 0.5 GPa intervals. Olivine Mg #'s from experiments were not fitted to the pMELTS model due to anomalous behaviour between 3 and 4 GPa as can be seen in A). Data sources are from Janney et al. (2010), Ionov et al. (2010; 2015a,b), and Wittig et al. (2010).
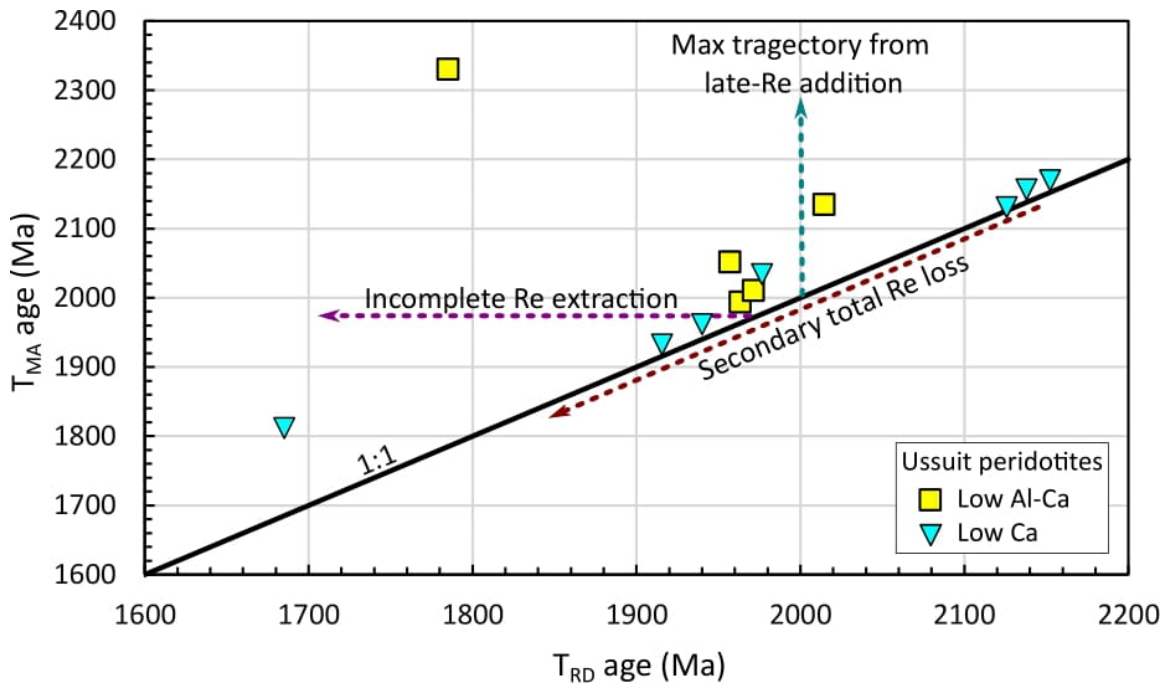
Fig. B3-7. Plot of T_{MA} vs T_{RD} showing the various paths that can alter model ages.

Chapter 4 Supplementary Tables and Figures

Table B4-1. Key information on samples used in this study.

Samples	Kimberlite	Reference	Modal proportions							T (°C)	P (Gpa)	TCa-in-OPX	Kimberlite age (Ma)
			Ol	*OPX*	*CPX*	*Grt*	*Sp*	Phl	Amph	(BKN/BKN)		(°C)	
W. Greenland													
Phlogopite-garnet lherzolite													
G-6-UA	Pyramidefjeld	3	93	3.3	1	0.7		2				968	150
G-8-18A	Pyramidefjeld	3	85	7	7	0.7		<1				945	150
phlogopite-wherlite													
G-6-14B	Pyramidefjeld	3	78		11			11					150
G-6-4C	Pyramidefjeld	3	73		14		1.2	11					150
Kaapvaal													
Amphibole-phlogoite-garnet-lherzolite													
Bos rd1	Boshof Rd. Dump (Bultfontein Kimberlite)	3	56	7	5	12		8	12			864	84
Phlogopite-garnet lherzolite													
LQ6	Liqhobong	1, 3, 7	60	32	2.9	5.5		<1%		1150	4.5	996	107
LQ8	Liqhobong	1, 3, 7	61	34	2.2	3.6		<1%		1085	3.8	997	107
LET64	Letseng	1, 6	54	37	1.6	7.7		<1%		1123	4.5	996	95
M9	Matsoku	1, 3, 4	53	38	3.9	5.1		<1%		1075	4.4	998	~90
M13	Matsoku	1, 3, 4	69	26	1.4	3.7		<1%		1026	4.1	983	~90
FRB1350	Premier	2, 3, 8	55.8	32.8	4.6	5.1	0.3	<1%		851	2.7	891	1153
Garnet-lherzolite													
LET29	Letseng	1, 3, 6	70	26	2.4	0.1	1.6			1081	4	986	95
LET30	Letseng	3,											95
LET38	Letseng	1, 3, 6	56	36	1.7	5.7				1027	4.1	997	95
PHN4265	Letseng	2, 3, 6	51.7	41.9	0.7	5.9				1131	4.63	1011	95

Sample	Locality	Refs											
TP5	Thaba Putsoa	1, 3, 4	67	27	1.2	5.2	0.2			907	3.2	934	~90
TP6	Thaba Putsoa	1, 3, 4	72	24	0.8	2.9	0.2			972	3.7	931	~90
FRB135	Mothae	2, 3, 5	54.4	39	0.3	5.9				973	3.76		87
FRB1007	Jagersfontein	2, 3, 5	70.3	23.8	1.8	2.6	0.32			656	2.49	1021	86
Spinel-Lherzolite													
M5	Matsoku	1, 3, 4	59	35	3.3	0	2.7					798	~90
M6	Matsoku	3										812	~90
FRB1434	Boshof Rd. Dump (Bultfontein Kimberlite)	2, 3, 6	60.7	39	0.5	0						1155	84
Off-craton garnet lherzolite													
JJG2513	Louwrencia Cores	2, 3, 5	62.7	25.5	4.8	7.5				1011	4.34	986	~72

1. Simon et al. (2003)

2. James et al. (2004)

3. This study

4. Davis (1977)

5. Davies et al. (2001)

6. Jelsma (2009)

7. Stanley & Flowers (2016)

8. Tappe et al. (2018)

Table B4-2. LA-ICPMS instrument operating parameters.

Measurement interval	
Background measurement	90s for K and 60s for trace elements
Ablation time	40s
wash out time	42s
Laser parameters	
Attenuation	26%
Laser fluence (at ablation site)	$3.5 - 3.8$ J/cm^2
Laser frequency	8 to 15 Hz
Spot size	33 to 193 μm
Carrier gases	
He	M50A: 1000ml/min S155: 350 to 500 ml/min
N	M50A: 0 ml/min S155: 2 to 4 ml/min
Ar	560 to 890 ml/min
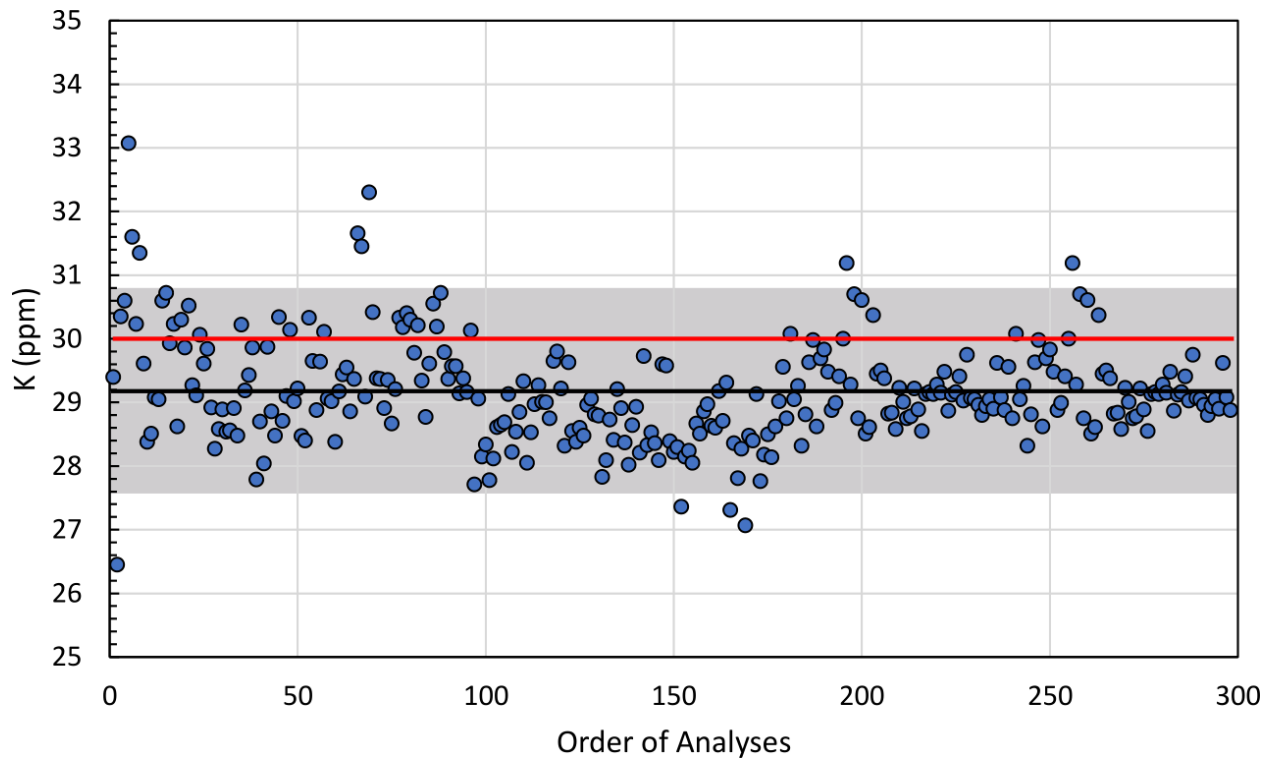
Fig. B4-1. Repeat measurements of K in reference material NIST614 which gave an average and 2 standard deviations of 29.2 ± 1.6 ppm outlined in the black line and grey field, respectively. The accepted value of K in NIST614 (red line) is 30 ppm (Jochum et al., 2011).
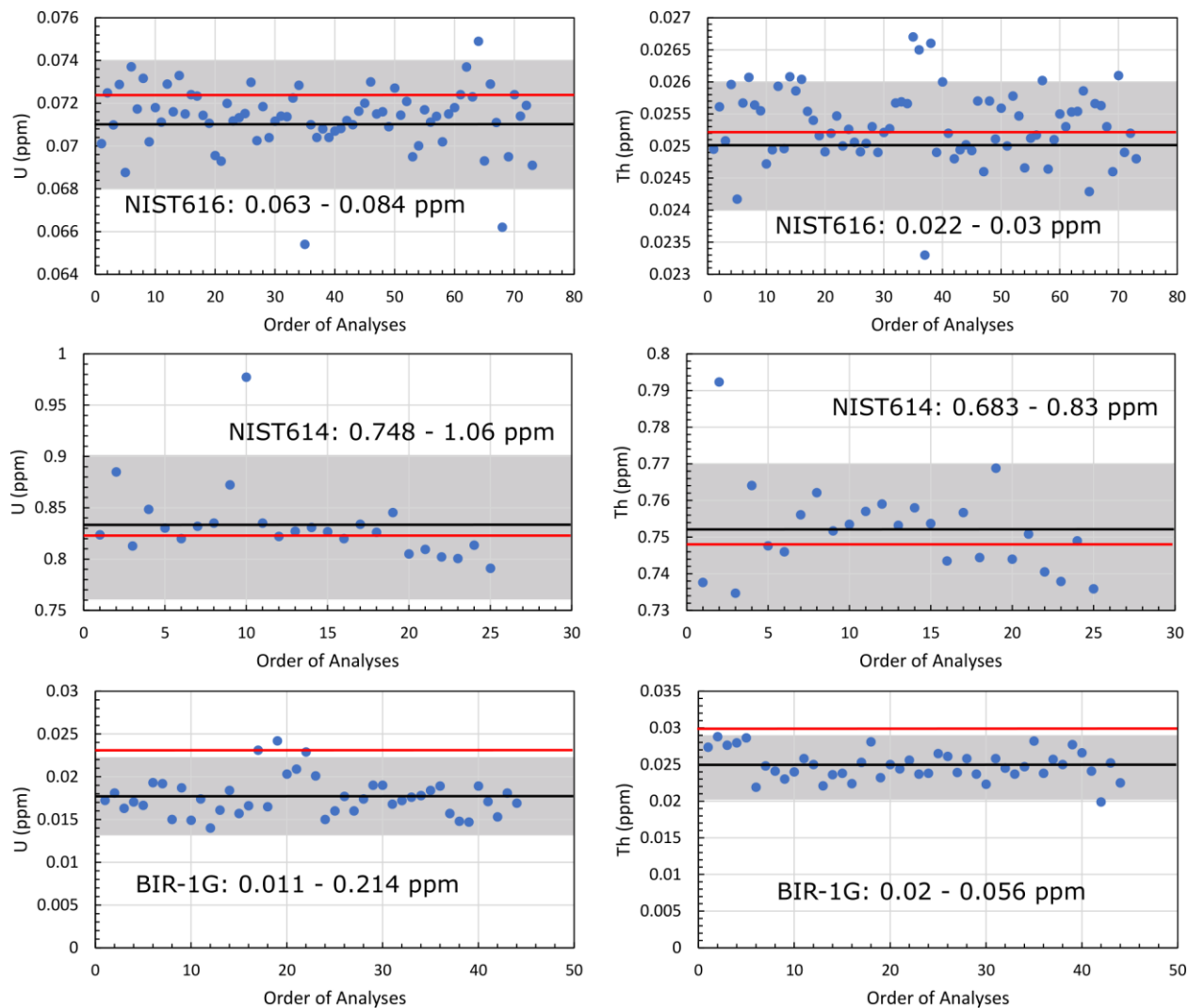
Fig. B4-2. Repeat U and Th analyses of reference materials. The range in values are the literature compiled values and the red lines represent the average compiled values from http://georem.mpch-mainz.gwdg.de/. The black lines and grey fields are the average and 2 standard deviations of analyses, respectively.
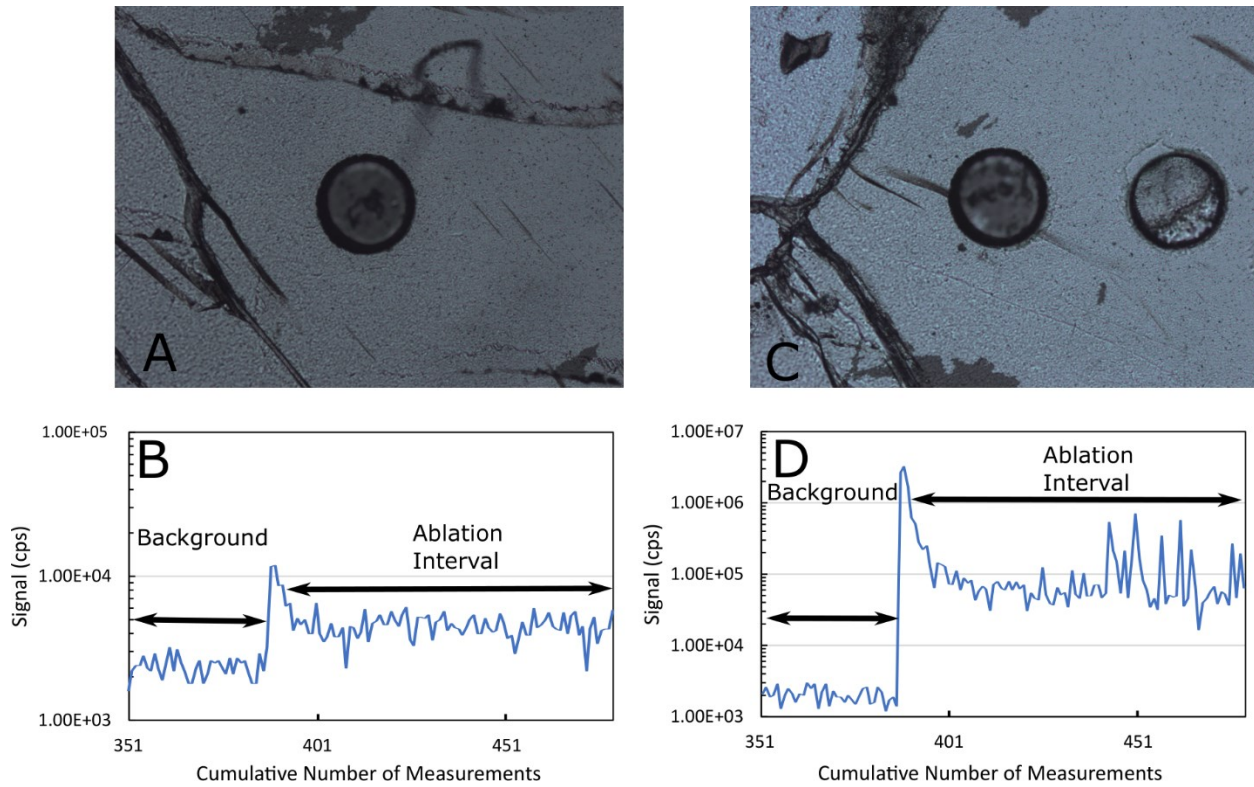
Fig. B4-3. Laser ablation spots of orthopyroxene in a clean, inclusion-free grain (A) with a steady time resolved signal of K (B) indicative of a homogenous distribution of K in orthopyroxene, and (C) ablation that overlaps a minor fracture in orthopyroxene, resulting in an erratic time resolved signal (D). The concentration of K in analyses in A and B was 0.28 ± 0.02 ppm and that in C and D was 8.6 ± 1.7 ppm. The spots in the figure are 193 μm in diameter and both from different orthopyroxene grains in sample M9.
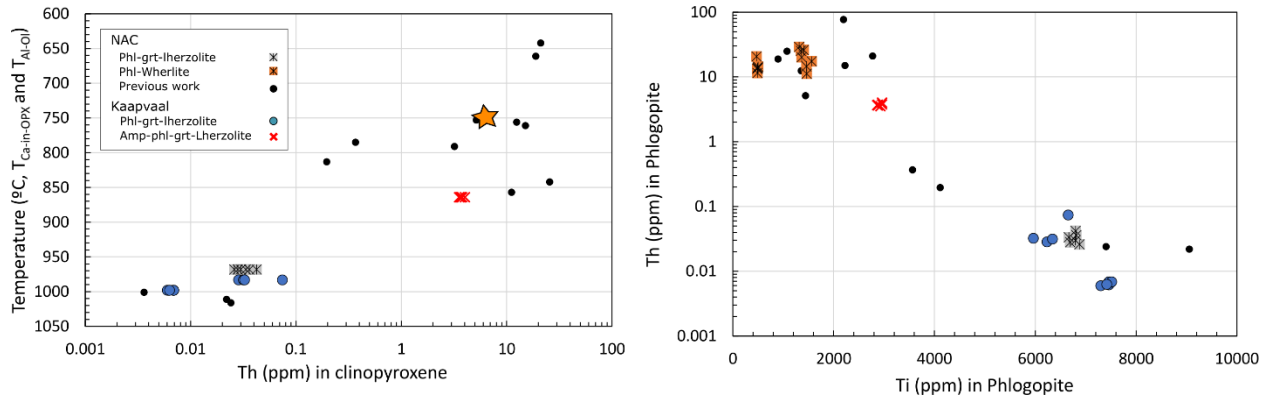
Fig. B4-4. A) U in phlogopite vs temperature and B) Th vs Ti trends in phlogopite. The data for this study use $T_{Ca-in-OPX}$ (Table B4-1) and "previous work" using T_{Al-Ol} are data from Aulbach et al. (2017a). The orange star in A is the location of the phlogopite wehrlites in this study inferred from Th vs Ti trends in B. The figures imply increasing Th in phlogopite with decreasing temperature due to fractionating melts in the lithospheric mantle moving towards the surface.
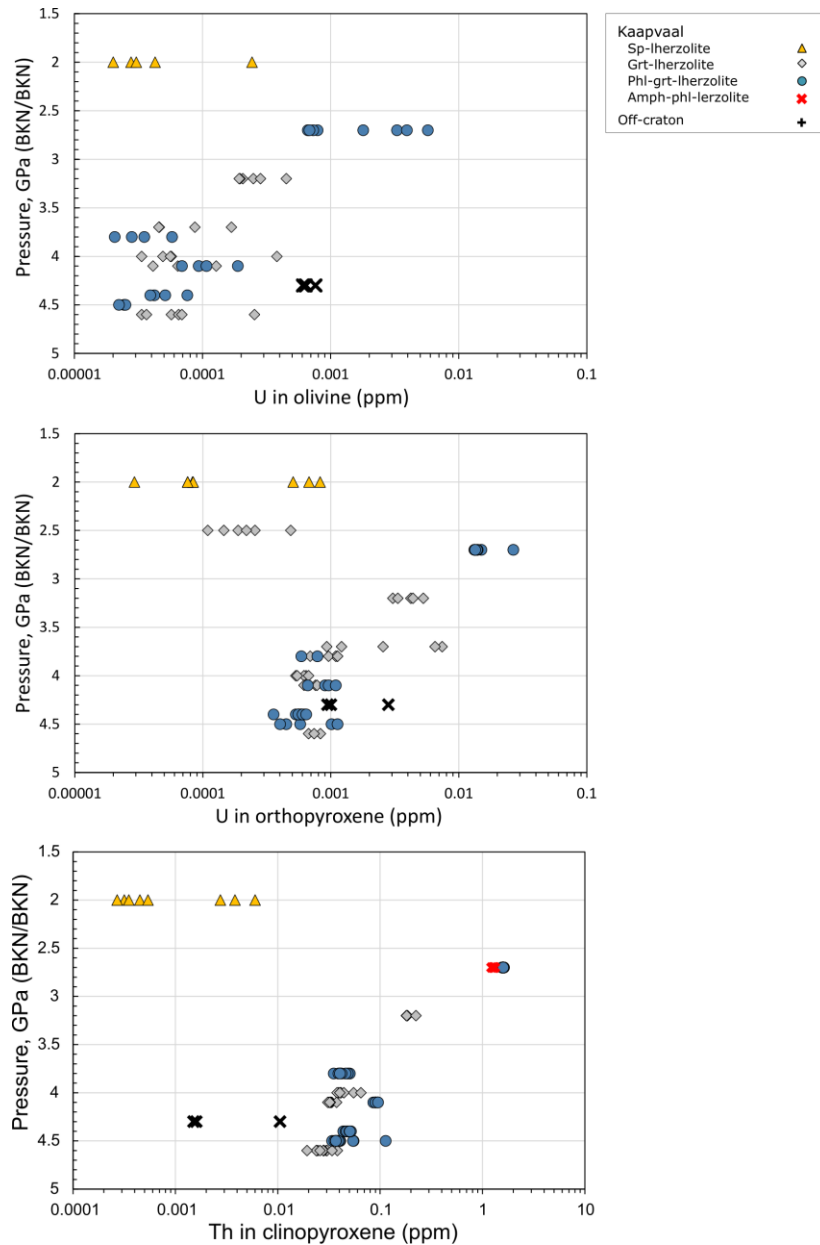
205

Fig. B4-5. Pressure vs U in orthopyroxene and olivine and pressure vs Th in clinopyroxene showing increasing U and Th contents in the minerals with decreasing pressure to 2.6 GPa in the Kaapvaal lithospheric mantle. The lack of U and Th enrichment in the upper lithospheric mantle (pressures <2.6 GPa) is interpreted to reflect a transition of metasomatic melts from porous flow at pressures >2.5 GPa to channelized flow at pressure <2.5 GPa, as described by Aulbach, et al. (2017b) with less fluid/rock interaction – and hence metasomatism – under channelized flow. Equilibrium pressures could not be obtain for the amphibole bearing sample, but were estimated from the Ca-in-orthopyroxene temperatures of 861˚C°.
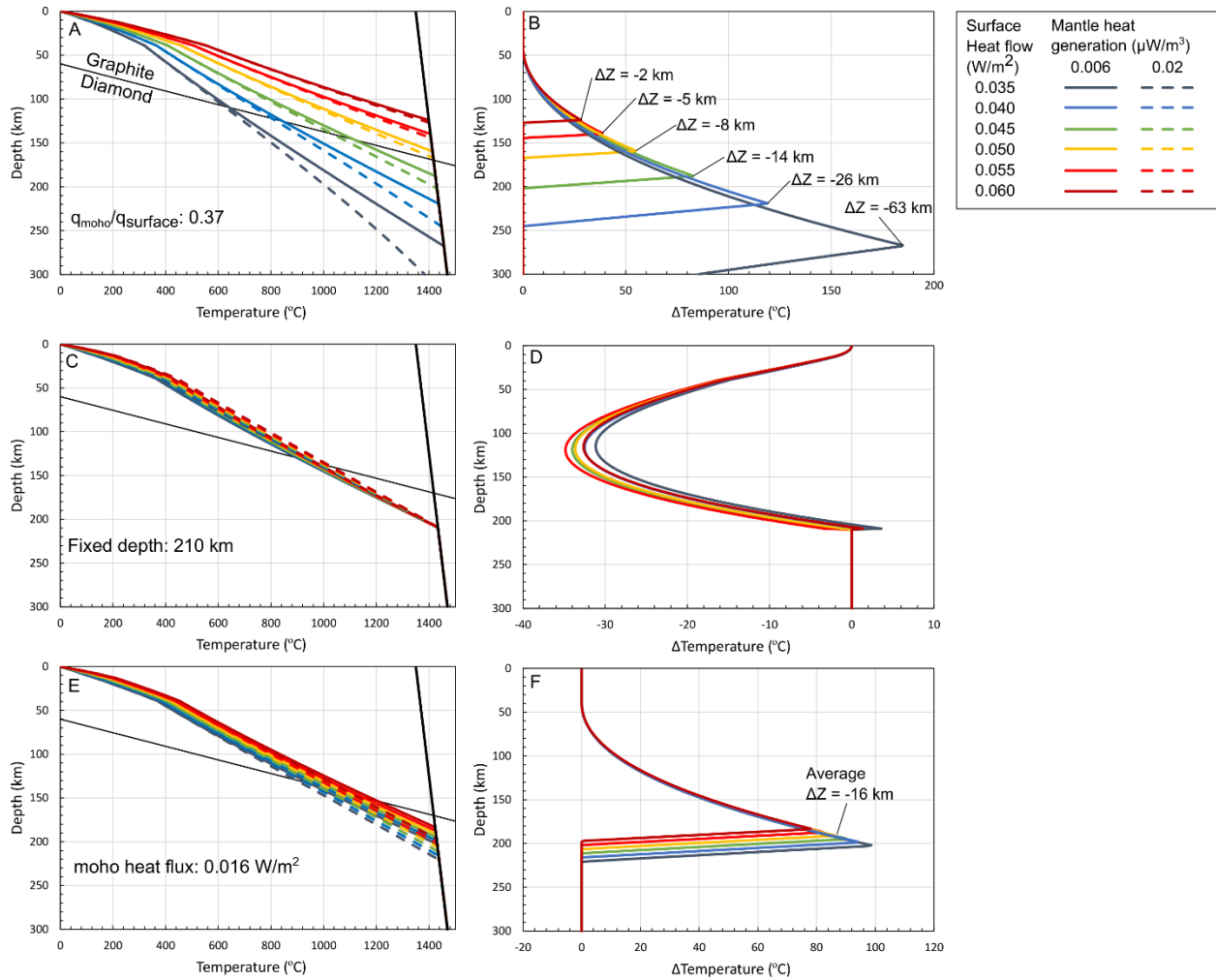
Fig. B4-6. Comparing geothermal models using a mantle heat generation of 0.006 $\mu W/m^3$ vs a mantle heat generation of 0.02 $\mu W/m^3$. The first column (Panels A, C, and E) are geotherms with different scenarios discussed in Section 4.5.9.1 and the second column (Panels B, D, and F) compares the difference in temperature at depth (ΔT: geotherm2(0.006 $\mu W/m^3$) – geotherm1(0.02 $\mu W/m^3$)) between models with mantle heat generation of 0.02 and 0.006 $\mu W/m^3$. ΔZ for fixed MOHO geotherms ranges from -18 for a 0.035 W/m^2 surface heat flow geotherm to -14 for a 0.60 W/m^2 surface heat flow geotherm. Model details are given in Fig. 1-1 and Appendix A.

Appendix D
Heat generation from hydrous mid-lithospheric metasomes

As mentioned in text, localized highly metasomatized layers, ~10 km in thickness, and composed of ~10 % hydrous phases are possible interpretation of seismic mid-lithospheric discontinuities in some cratons (Selway et al., 2015; Aulbach et al., 2017). Although we consider it unlikely that metasomes are long lived enough to impact geotherms, comparing a geothermal model with a heat generation of depleted mantle (0.00006 $\mu W/m^3$) and metasomatized layered mantle shows the maximum impact of present day metasomes on geotherms (. The HPE distribution in this metasomatized mantle is modelled as having a 10 km thick enriched layer (phlogopite wehrlite) at 95 km depth with a heat generation of 0.27 $\mu W/m^3$ and 0.006 $\mu W/m^3$ in the rest of the lithospheric mantle. The high heat generating layer (the metasome) produces a distinct anomaly at 95 km depth where geothermal models with unconstrained depth to the LAB are deflected to lower geothermal gradients (up to 200 ºC cooler at depth) and greater depths (up to 53 km) to the LAB (Fig. D-1 A and B). In fixed depth LAB geotherms, the metasomatized model causes a positive thermal anomaly at 100 km depth that is up to ~60 ºC hotter than a model using heat generation of depleted mantle (Fig. D-1 C and D). In geothermal models with fixed Moho heat flux the metasomatized geotherms are deflected to cooler geotherms by 100 – 120 ºC and intersect the mantle adiabat 18 to 22 km deeper than geotherms using heat generation of depleted mantle (Fig. D-1 E and F). The distinct differences between the metasomatized and depleted mantle models shows that if metasomes are both long lived and volumetrically extensive, they can have significant impact on geothermal gradients at a local scale.
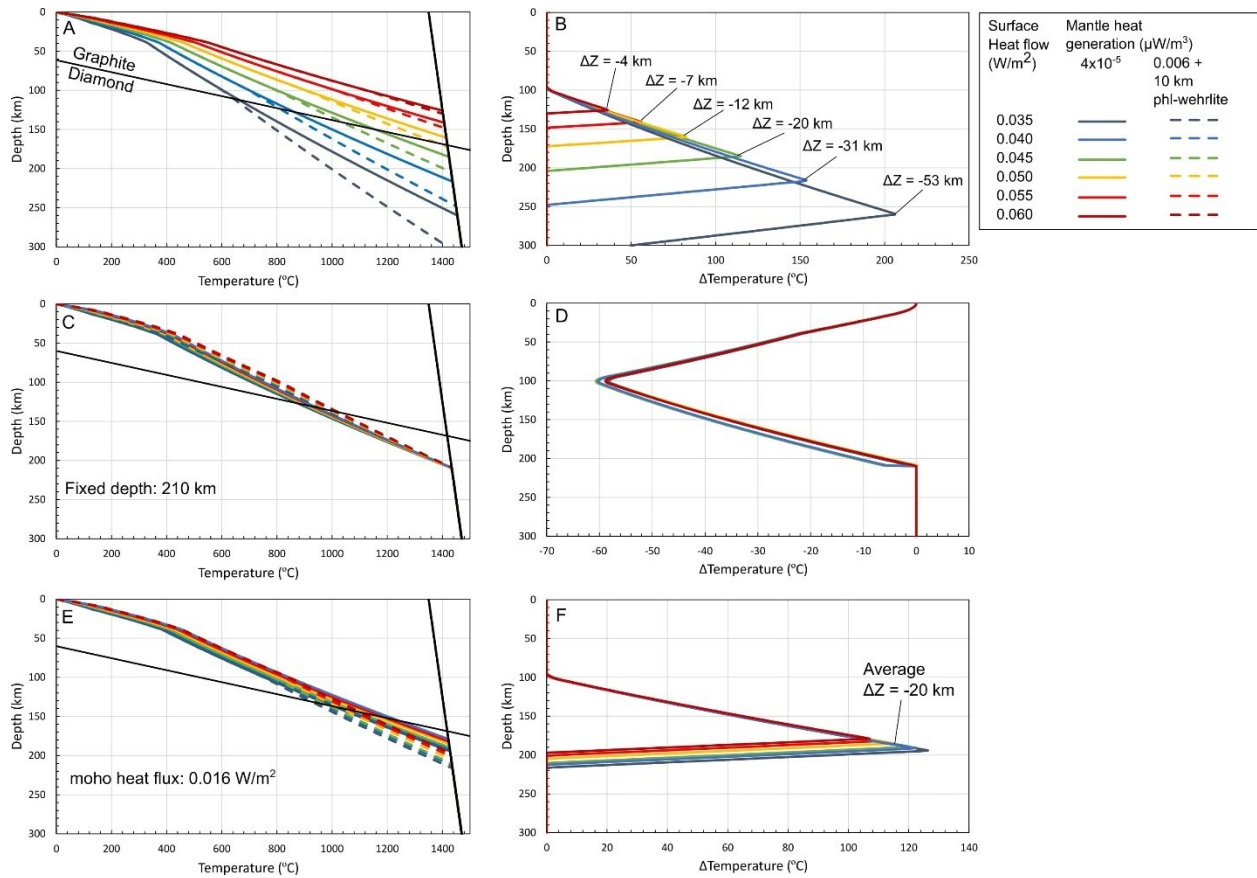
Fig. D-1. Comparing geothermal models using lithospheric mantle heat generation of 0.00004 $\mu W/m^3$ with a model for metasomatized mantle where the lithospheric mantle has a heat generation of 0.006 $\mu W/m^3$, but with a 10 km thick enriched layer at 95 km depth with a heat generation of phlogopite-wehrlite lithologies (0.27 $\mu W/m^3$). The first column (Panels A, C, and E) are geotherms with different scenarios discussed in Section 4.5.9 and Fig. 4-8 and the second column (Panels B, D, and F) compares the difference in temperature at depth (ΔT: geotherm2(0.00006 $\mu W/m^3$) – geotherm1(variable heat generation)) between models with mantle heat generation of metasomatized mantle and depleted mantle. ΔZ for fixed moho heat flux (Panel F) ranges from -22 for a 0.035 W/m^2 surface heat flow geotherm to -18 for a 0.60 W/m^2 surface heat flow geotherm. Other model details are given in Fig. 1-1 and Appendix A.